

VIABILITY STUDY OF THE BIPV-PCM MICROFACILITY
UNDER SEVERE WEATHER CONDITIONS

by

Amanda Gregory, A.S., B.S., M.S., M.B.A.

A dissertation submitted to the Graduate Council of
Texas State University in partial fulfillment
of the requirements for the degree of
Doctor of Philosophy
with a Major in Materials Science, Engineering, and Commercialization
May 2023

Committee Members:

Tongdan Jin, Chair

Jana Minifie

Yoichi Miyahara

Eduardo Perez

Byoung Hee You

COPYRIGHT

by

Amanda Gregory

2023

DEDICATION

For my dad, who would have been proud.

For Chance, I could not have finished this without your love, support, and constant encouragement.

ACKNOWLEDGEMENTS

I am forever grateful to everyone that assisted my learning, supported me through my struggles, and encouraged my efforts on this project.

TABLE OF CONTENTS

	Page
LIST OF TABLES.....	viii
LIST OF FIGURES	x
LIST OF ABBREVIATIONS.....	xii
ABSTRACT.....	xiii
CHAPTER	
I. INTRODUCTION	1
Research Motivation	1
The Problems	1
A Potential Solution	3
The State of the Art.....	4
Photovoltaics.....	4
Building Integrated Photovoltaics.....	10
Phase Change Materials	12
Research Scope	14
Research Questions	14
Selected PV.....	15
Selected PCM.....	15
Thermal Modeling and Simulation	16
Novelty and Contributions of this Work.....	17
II. THERMAL MODELING	20
Conduction.....	20
Conduction Basic Concepts	20
Thermal Conductivity	22
The Heat Diffusion Equation.....	23
Radiation.....	27
Radiation Basic Concepts	27
Blackbody Radiation.....	29
Radiation from Real Surfaces	30
Absorption, Reflection, and Transmission.....	31
Solar Radiation.....	33
Convection	35
Convection Basic Concepts	35
Convection Boundary Layers.....	38

Laminar and Turbulent Flow	42
Free Convection	45
Mixed Free and Forced Convection.....	46
Phase Change	47
The Mushy Zone	47
The Improved Enthalpy-Porosity Method	49
Summary	51
III. THE BIPV-PCM MICROFACILITY AND ENVIRONMENT.....	55
Factors Influencing PV Performance.....	55
Sunlight	55
Cloud Cover.....	61
Relative Humidity	63
Ambient Temperature	66
Wind.....	67
Panel Degradation.....	68
Extreme Weather Analysis.....	68
Overall Increasing Temperatures	69
Extreme Weather Events.....	71
BIPV-PCM Microfacility Specifications	73
Building.....	74
PV Panels	75
PCM.....	76
Summary	77
IV. THE THREE-BOX MODEL.....	80
Mathematical Modeling and Simulation Basic Concepts	80
Types of Models.....	80
General Simulation Abilities and Limitations	82
Finite Element Analysis	83
Matlab Software.....	83
Specifying the Model.....	85
Limitations and Approximations	85
Governing Equations.....	86
Physical and Thermal Properties.....	90
Boundary Conditions	91
Mesh and Initial Conditions.....	93
Simulation Results and Analysis	94
PCM of 5cm Thickness with Channel Spacing of 5cm	95
PCM of 50cm Thickness with Channel Spacing of 5cm	96
PCM of 5cm Thickness with Channel Spacing of 50cm	97
PCM of 50cm Thickness with Channel Spacing of 50cm	97
Summary	98

V. THE BIPV-PCM MICROFACILITY BUSINESS MODEL.....	108
Introduction.....	108
The Business Model Canvas	109
Customer Segments	110
Value Proposition.....	111
Channels.....	112
Customer Relationships	112
Revenue Streams.....	113
Key Resources.....	114
Key Activities	115
Key Partnerships	115
Cost Structures.....	116
The BIPV-PCM Microfacility BMC	117
Customer Segments	117
Value Proposition.....	120
Channels.....	122
Customer Relationships	123
Revenue Streams.....	125
Key Resources.....	126
Key Activities	126
Key Partnerships	128
Cost Structures.....	129
The Overall BMC for the BIPV-PCM Microfacility	131
VI. CONCLUSION AND FUTURE WORK.....	133
Conclusions	133
Future Research Opportunities.....	135
APPENDIX SECTION	137
REFERENCES	225

LIST OF TABLES

	Page
Table 1.1. PV types, their optimal efficiencies, and US manufacturers	15
Table 1.2. Phase change material, melting temperatures, and thermal conductivities	16
Table 1.3. Variables and Constants Used in Chapter 1.....	19
Table 2.1. Local coefficients for Laminar Flow Zone Parallel to a Flat Plate	43
Table 2.2. Local Coefficients for Turbulent Flow Zone Parallel to a Flat Plate.....	44
Table 2.3. Average Coefficient of Friction, Nusselt, and Sherwood Numbers for Turbulent Flow	44
Table 2.4. Average Nusselt Numbers for Horizontal Plates	45
Table 2.5. Parallel Plate Natural Convection Constants and Optimal Spacing	46
Table 2.6. Permeability variants and associated constants	49
Table 2.7. Variables and Constants Used in Chapter 2.....	51
Table 3.1. Cloud Coverage in Oktas	62
Table 3.2. The effect of relative humidity and ambient temperature changes for silicon PV panels	64
Table 3.3. Lesser Heat Wave Specifications.....	72
Table 3.4. Monocrystalline Silicon PV Panel Specifications	76
Table 3.5. PCM Specifications	77
Table 3.6. Variables and Constants Used in Chapter 3.....	78
Table 4.1. Governing Equations for Three-Box BIPV-PCM Microfacility Model	90
Table 4.2. PDE Coefficients for the Three-Box BIPV-PCM Microfacility Model.....	90
Table 4.3. Three-Box Model Geometric Dimensions	91
Table 4.4. Three-Box Model Thermal Properties	92

Table 4.5. Boundary Conditions for the Three-Box Model	94
Table 4.6. Real-world environmental data used to determine relevant values for simulation	95
Table 4.7. Representative environmental data used in simulation	95
Table 5.1. Interior Building Temperature for Transient Solution at 0.005s	131

LIST OF FIGURES

	Page
Figure 1.1. Diagram of the BIPV-PCM Microfacility	3
Figure 1.2. A typical p-n junction PV cell	5
Figure 1.3. Current vs. Voltage and Power vs. Voltage plots	7
Figure 1.4. Schematic of a basic BIPV system with exterior glazing	11
Figure 1.5. Energy stored by the PCM as a function of increasing temperature	13
Figure 2.1. Thermal flux in the n , x , and y directions from the surface of an isotherm	21
Figure 2.2. Control volume with energy transfer rates in Cartesian coordinates	24
Figure 2.3. Steradian, solid angle, and spherical coordinates.....	28
Figure 2.4. Blackbody and real surface emission	31
Figure 2.5. Rayleigh and Mie Scattering	33
Figure 2.6. Fluid moving over a stationary flat surface	35
Figure 2.7. Velocity boundary layer	39
Figure 2.8. Thermal boundary layer.....	40
Figure 2.9. Mass boundary layer.....	41
Figure 2.10. Laminar and turbulent flow	42
Figure 2.11. Liquid, solid, and mushy zones	48
Figure 3.1. The celestial sphere	59
Figure 3.2. Incident sunlight on the rooftop PV panels of the BIPV-PCM microfacility	60
Figure 3.3. Wind interaction with channels of BIPV-PCM facility	68
Figure 3.4. Temperature data for Austin, TX based on constructed data set	70
Figure 3.5. Idealized BIPV-PCM layers	74

Figure 4.1. Basic workflow for modeling and simulation in Matlab	84
Figure 4.2. Finite elements and nodes	84
Figure 4.3. Three-Box Model of the BIPV-PCM Microfacility	86
Figure 4.4. Three-Box Model and Mesh.....	93
Figure 4.5. Solid 5cm Thick PCM, 5cm Channel Spacing, 0 m/s Wind Speed, $T_{amb} = 323K$	99
Figure 4.6. Solid 5cm Thick PCM, 5cm Channel Spacing, 30 m/s Wind Speed, $T_{amb} = 323K$..	100
Figure 4.7. Solid 50cm Thick PCM, 5cm Channel Spacing, 30 m/s Wind Speed, $T_{amb} = 323K$	101
Figure 4.8. Melted 50cm Thick PCM, 5cm Channel Spacing, 30 m/s Wind Speed, $T_{amb} = 333K$	102
Figure 4.9. Solid 5cm Thick PCM, 50cm Channel Spacing, 0 m/s Wind Speed, $T_{amb} = 323K$	103
Figure 4.10. Solid 5cm Thick PCM, 50cm Channel Spacing, 30 m/s Wind Speed, $T_{amb} = 323K$	104
Figure 4.11. Solid 50cm Thick PCM, 50cm Channel Spacing, 30 m/s Wind Speed, $T_{amb} = 323K$	105
Figure 4.12. Solid 50cm Thick PCM, 50cm Channel Spacing, 50 m/s Wind Speed, $T_{amb} = 323K$	106
Figure 4.13. Melted 50cm Thick PCM, 50cm Channel Spacing, 50 m/s Wind Speed, $T_{amb} = 333K$	107
Figure 5.1. Visualization of the Business Model Canvas for the BIPV-PCM Microfacility.....	132

LIST OF ABBREVIATIONS

Abbreviation	Description
BIPV	Building Integrated Photovoltaics
PCM	Phase Change Materials
BMC	Business Model Canvas
PV	Photovoltaics
GHG	Greenhouse Gases
PDE	Partial Differential Equation
LST	Local Solar Time
LT	Local Time
EoT	Equation of Time
LSTM	Local Solar Time Meridian
UTC	Universal Coordinated Time
HRA	Hour Angle
RH	Relative Humidity
NOAA	National Oceanic and Atmospheric Administration
EPA	Environmental Protection Agency
PNW	Pacific Northwest
EVA	Ethylene Vinyl Acetate
FEA	Finite Element Analysis
CAD	Computer-Aided Design
ROI	Return on Investment

ABSTRACT

Developing new and improved building integrated photovoltaics (BIPV) materials that can withstand severe weather is critical to reversing climate change. BIPV coupled with phase change materials (PCM) is a promising technology that is so far not well-studied. Most PCM types that have been investigated are petroleum-based paraffin waxes which are not sustainable in the long term. Furthermore, there are few studies which examine the effects of high temperatures and severe weather on the temperature profile of BIPV-PCM microfacility. This work aims to investigate sustainable PCM incorporated into a small BIPV facility under extreme temperature and varying wind profile. A variety of extreme weather events are simulated to determine what building spacing, PCM type, and PCM thickness have the most significant effect on the temperature profile of the interior of the building.

Real-world weather data from the National Oceanic and Atmospheric Administration was adopted to reflect increasing ambient temperatures and include more frequent severe weather events. These real-world values were used to determine a realistic set of temperature, solar radiation, and wind speed representing worst-case climate scenarios. Mathematical models for conduction, radiation, convection, and phase change are assembled into a “three-box” model of the BIPV-PCM system, and the steady state solution is found for different BIPV-PCM geometries. The results of the model indicate that thicker PCM and wider channel spacing improve performance most. Although candelilla wax outperforms beeswax and soy wax, no BIPV orientation or sustainable PCM modeled could maintain interior building temperatures below 300K.

The two primary reasons that new products such as the BIPV-PCM microfacility fail to gain wide adoption are a lack of a business plan and poorly defined customer segments. This study leverages the business model canvas (BMC) to address these challenging issues and

proposes a pathway to facilitate the mass commercialization for the decades to come.

I. INTRODUCTION

Research Motivation

There is no question that climate change is taking place and that greenhouse gas (GHG) emissions from human activities are to blame [1], [2]. Indeed, as of 2006-2015 there has been an 0.87°C increase in global temperatures since the pre-industrial period [3]. 2016 and 2020 have been the warmest years on record, with average global temperature increases of 1.3°C and 1.25°C , respectively [4], and the six consecutive years from 2015 through 2020 have been the hottest ever recorded [5]. Although temperatures on both extremely hot and extremely cold days are expected to increase, in the continental United States average temperatures are expected to rise by approximately 1.4°C from 2021 to 2050 [6].

The Problems: As global climate changes and temperatures increase, so do the chances of extreme weather events such as heat waves and drought, intensified precipitation resulting in flooding, dangerously high local temperatures, and other types of severe storms [3], [5]. Warmer temperatures allow the atmosphere to store larger quantities of water, leading to more intense rainfall and subsequent flooding, as well as more intense and frequent formation of tropical storms and hurricanes [7]. Climate scientists and meteorologists agree that climate change is influencing global weather patterns, leading to more frequent and severe weather events like the historic freeze across Texas in February 2021 [8], or the heat wave across the Pacific Northwest [9], [10] and the flooding in China and Germany [11] during July of 2021. Although the exact mechanisms at play may not be precisely known, scientists worldwide agree that climate change is actively taking place and leading to a slew of negative effects, including higher temperatures and more extreme weather.

Extreme weather events have a variety of impacts, none of them positive. Of especially

grave concern is the fragility of the electric grid in the face of extreme weather coupled with aging utility infrastructure and cyber security threats, increasing the frequency and breadth of black- and brown-outs. Failure of the electric grid causes interruptions in wastewater treatment, the food supply chain, healthcare delivery, communications towers, and so on, leading to supply shortages, spreading of illnesses, and loss of human life [12]. Human dependency on electric power is unquestionable, hence the motivation to develop cleaner alternative energy generation and storage technologies, such as wind turbines, photovoltaic (PV) panels, and utility-scale energy storage.

As the global population continues to grow, so do water and food needs. Food insecurity has been a growing concern for decades but has increased steadily since 2014. A staggering 8.9% of the global population was undernourished as of 2019 [13]. The Covid-19 pandemic has further exacerbated this issue by putting incredible stress on the global supply chain as well as agricultural labor supply [13], [14]. The food supply chain is a major source of both greenhouse gas (GHG) emissions and deforestation. Without radical changes, the GHG emissions from the food supply chain will preclude the ability to avoid 2°C global temperature increases by 2050. In other words, an unchanged global food system means more than 2°C global warming even if every other emission source is eliminated today [15].

Higher temperatures caused by climate change require an increase in freshwater usage for agricultural purposes and human consumption. Higher evaporation rates and temperatures can increase the growth of dangerous bacteria and algae that make the water unsafe for use [7]. Freshwater supplies are dwindling rapidly in agricultural regions both in and outside of the US [16], and already “water commodities” are being traded on the stock market in the US like other precious commodities such as gold [17]. As of 2019 agriculture accounted for about 70%

freshwater usage globally, and this does not include human consumption or freshwater use in industrial sectors other than agriculture [18].

All this is, of course, in addition to ocean acidification, sea level rise, arctic ice melting, ecosystem collapse, and so on. Altogether these circumstances make one thing starkly clear: “something’s got to give” if human life is to continue thriving on this planet.

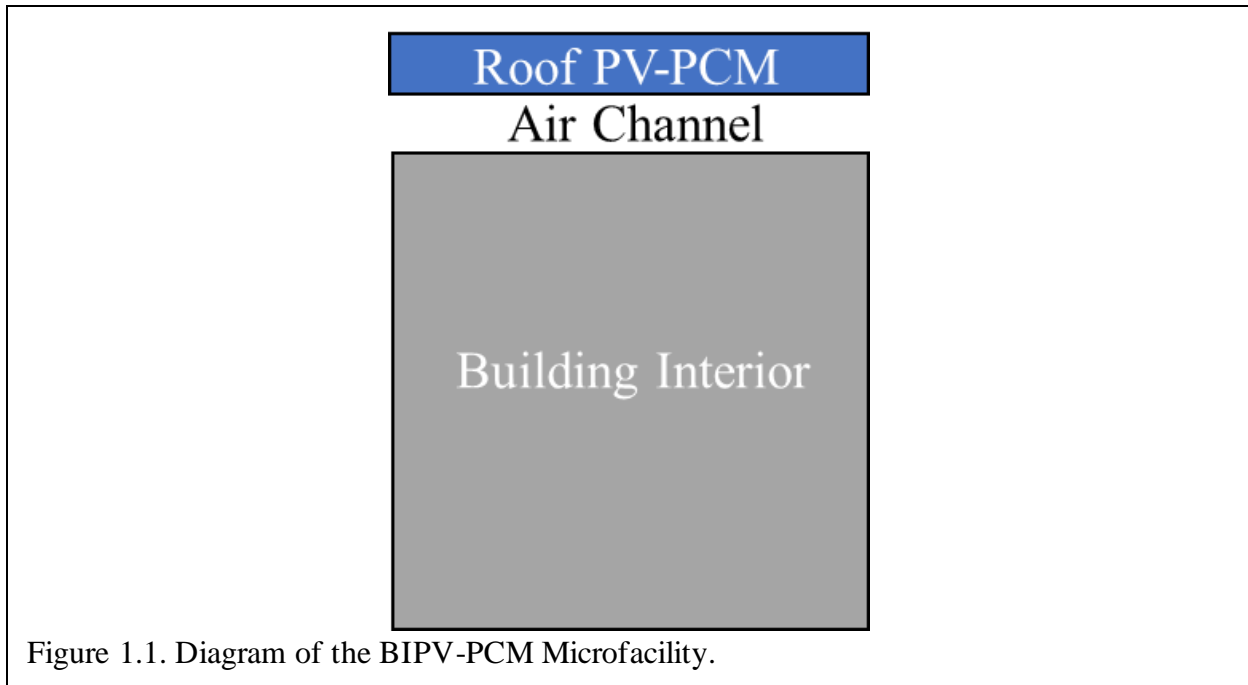


Figure 1.1. Diagram of the BIPV-PCM Microfacility.

A Potential Solution: Undoubtedly this array of problems is overwhelming and requires complimentary, innovative solutions across a plethora of technologies, such as vertical farming, building integrated photovoltaics (BIPV), geothermal and wind energy generation, sustainable materials, and many more. In this work, a hybrid solution is proposed: a grid-independent micro-facility powered by integrated PV enhanced with PCM.

As inclement weather events (such as the event in February 2021 that nearly caused catastrophic grid failure in the state of Texas), and natural disasters (such as the rash of wildfires across California, Washington, and Oregon in 2020 or the flooding in China and Germany in the summer of 2021) are expected to occur with increasing frequency as global temperatures

continue to rise and climate change effects continue to ramp up. There is a growing need for production facilities that utilize renewable energy sources and operate independently with respect to utility-scale grid infrastructure. In this work, the BIPV-PCM shipping container “microfacility” is investigated in-depth. First, the mathematical basis for a thermal model is developed, followed by an analysis of real-world weather and its overall impact on using real-world data. Next, an energy-based 2D “three-box model” of the BIPV-PCM microfacility is developed and the thermal behavior of a limited set of building designs is explored. Finally, a business model for the BIPV-PCM microfacility is developed using the BMC, a popular strategic management tool.

The State of The Art

The BIPV-PCM microfacility examined in this work combines building-integrated photovoltaics with phase change materials, and the following sections review the state of the art of these technologies.

Photovoltaics: Perhaps one of the most widely known renewable energy technologies is the photovoltaic cell, colloquially known as the solar panel. Harvesting energy from bountiful sunlight is an attractive pursuit both because of the abundance of this free energy and the ever intensifying need to reduce GHG emissions. Between 2010 and 2019 roughly US\$2.6 trillion have been invested in advancing renewable energy technology, and photovoltaics accounted for over 52% of these funds [19].

In the simplest terms, solar panels transform light into electricity. When a material absorbs a photon of light with the same energy as its bandgap, an electron-hole pair is formed. Although there are exceptions, typically a solar cell utilizes the electric field formed at a p-n junction to separate the electron-hole pairs. When a hole reaches the p-n junction the natural

electric field of the junction pulls the carrier across the junction to the p-type material. In essence, the p-n junction sorts electrons into the n-type material and holes into the p-type material. The collection probability of the p-n junction is dependent on the distance that the generated carrier must traverse. If the minority carrier (hole) is generated further from the junction than its diffusion length, it is more likely to recombine with the majority carrier (electron) before reaching the junction. When the circuit is open and current cannot flow, these light-generated carriers build-up on either side of the p-n junction, which induces an electric field that opposes that naturally formed at the p-n junction. The reduction in the net electric field allows a greater number of carriers to diffuse across the junction until a new equilibrium is reached and a voltage exists across the junction. Alternatively, if a load is placed across the shorted circuit, electrons traverse the circuit dissipating their energy before reaching the p-type material to recombine with a hole. Figure 1.2 provides a cross-sectional diagram of a solar cell [20].

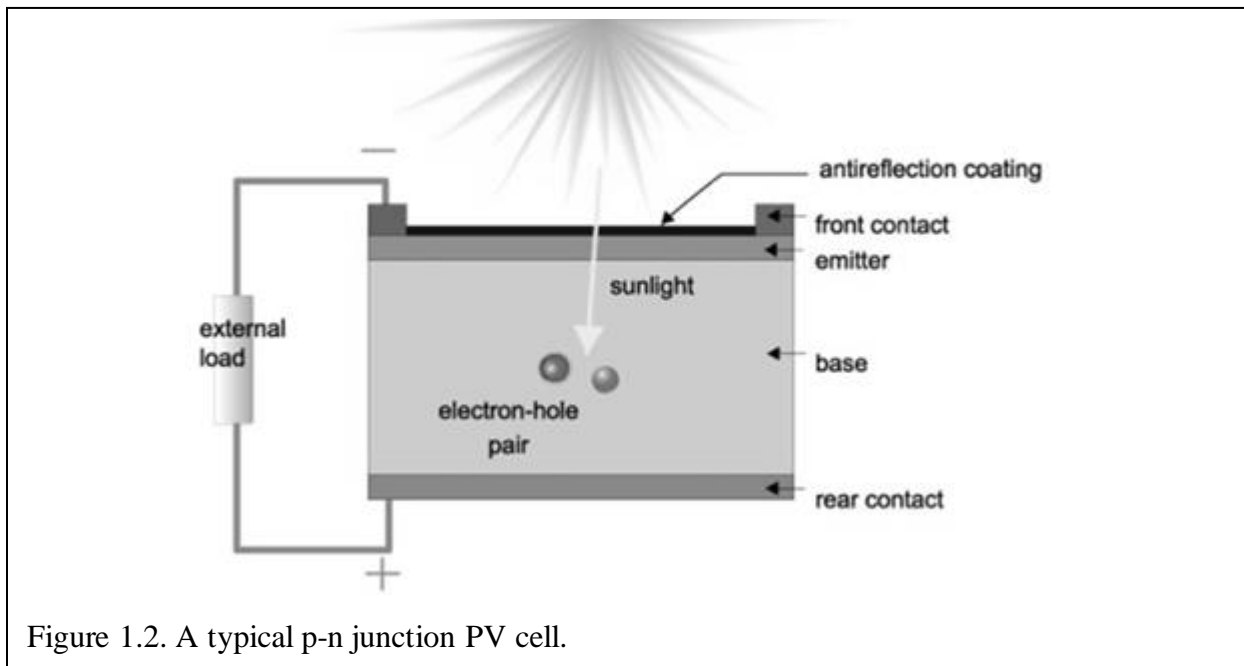


Figure 1.2. A typical p-n junction PV cell.

There are three basic modes of operation for any semiconductor p-n junction: thermal equilibrium, steady state operation, and transient operation. In thermal equilibrium there is no net

current in the device because there are no external inputs. Under steady state operation, inputs like light or applied voltage are constant and the device operates in either forward bias (decreased electric field at the junction that increases diffusion current) or reverse bias (increased electric field at the junction that decreases diffusion current). Under transient conditions the amplitude of the applied voltage rapidly changes over time.

In thermal equilibrium some charge carriers traverse the depletion region and recombine generating a “dark saturation current.” The dark saturation current, I_0 , is a property of the diode-like p-n junction and material quality and can be thought of as a measure of the recombination rate of a given device. As the temperature, T , of the device increases, individual charge carriers have higher velocities and thus have a higher probability of traversing the depletion region, so the value of I_0 also increases at higher temperatures. As the purity of the materials in the device increases (or the number of defects decreases), fewer charge carriers are available, and I_0 decreases. The net current, I_{net} , through the diode-like PV device at thermal equilibrium can be expressed as a function of applied voltage, V , using the ideal diode law adjusted by an ideality factor, n_{id} , that varies between 1 and 2, and is expressed as [20]:

$$I_{net} = I_0 \left(e^{\frac{qV}{n_{id}k_B T}} - 1 \right) \quad \text{Eq. 1.1}$$

where k_B is Boltzmann’s constant.

Under steady state conditions the net current must account for the light generated current, I_L , and thus the net current may be expressed:

$$I_{net} = I_0 \left(e^{\frac{qV}{n_{id}k_B T}} - 1 \right) - I_L \quad \text{Eq. 1.2}$$

The “-1” term in the expression is typically neglected because at higher applied voltages the exponential term, $e^{\frac{qV}{n_{id}k_B T}}$ is much larger than 1, while at lower voltages the light generated current

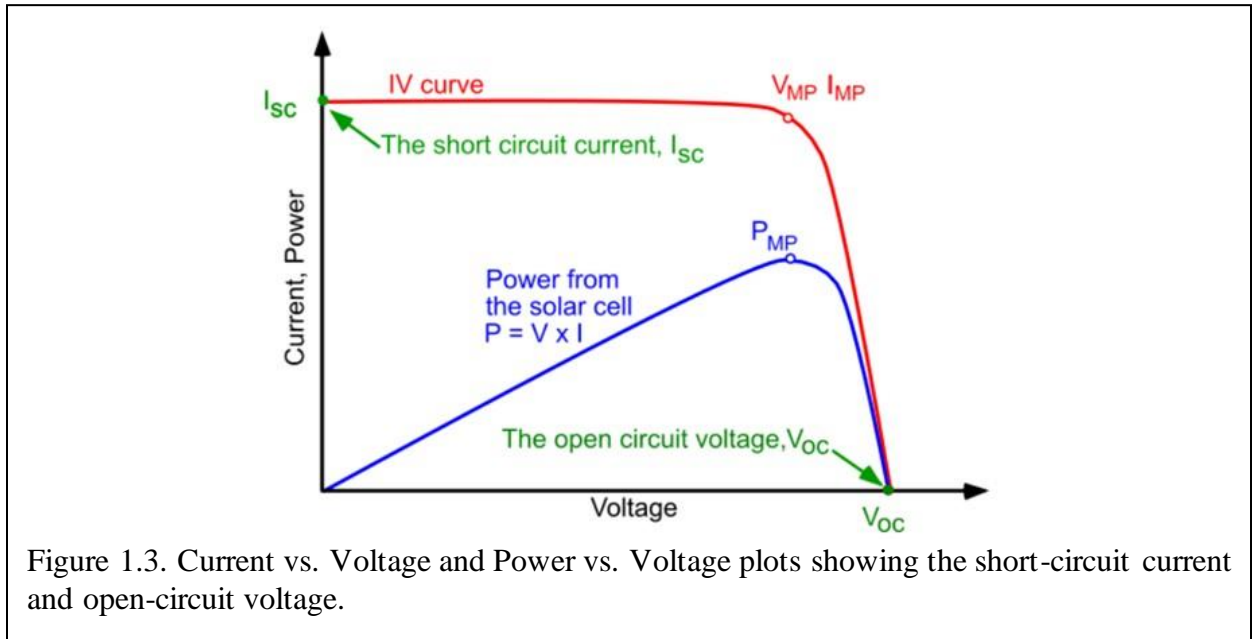
within the solar cell (I_L) dominates. By convention, this expression is reversed as shown in Equation 1.3 so that the I-V curve is flipped as shown in Figure 1.3 [20].

$$I_{net} = I_L - I_0 \left(e^{\frac{qV}{n_{id}kT}} \right) \quad \text{Eq. 1.3}$$

The short-circuit current, I_{sc} , is typically treated as equivalent to the light-generated current, I_L . However, I_{sc} is measured outside of the solar cell and thus subject to some deviation from I_L due to measurement and circuit resistances. The intensity and spectrum of incident light, the area of the PV cell, and the optical properties and collection probabilities of the PV cell all influence the value of I_{sc} . The open-circuit voltage, V_{oc} , is the maximum possible voltage of the PV cell and can be found by setting the net current equal to zero and solving for V :

$$V_{oc} = \frac{n_{id}k_B T}{q} \ln \left(\frac{I_L}{I_0} \right) \quad \text{Eq. 1.4}$$

Because I_0 increases as T increases, V_{oc} ultimately decreases with increasing temperature.



The relationship between power, voltage, and current is well-established. At both the short-circuit current and the open-circuit voltage the power is zero. The plot of the power versus

voltage is found by multiplying the I_{net} expression by V :

$$P = VI_{net} = VI_L - VI_0 \left(e^{\frac{qV}{n_{id}kT}} \right) \quad \text{Eq. 1.5}$$

By taking the derivative of this function with respect to voltage and setting it equal to zero, the maximum power can be determined:

$$V_{mp} = V_{oc} - \left(\frac{n_{id}k_B T}{q} \right) \ln \left[1 + \frac{qV_{mp}}{n_{id}k_B T} \right] \quad \text{Eq. 1.6}$$

This implicit equation converges rapidly to a V_{mp} value, which may then be used to find the current at maximum power, I_{mp} . A fill factor, commonly abbreviated “FF,” quantifies the maximum power of a given PV cell and is expressed:

$$FF = \frac{P_{mp}}{I_{sc}V_{oc}} = \frac{I_{mp}V_{mp}}{I_{sc}V_{oc}} \quad \text{Eq. 1.7}$$

The FF is a measure of the squareness of a PV cell’s I-V curve and is a ratio of the largest possible area under the I-V curve to the product of I_{sc} and V_{oc} , or the area if the I-V curve was perfectly square. Efficiency is measured under standard testing conditions so that different types of PV panels can be compared and is defined as the ratio of maximum output power to input power from the sun:

$$\eta = \frac{P_{mp}}{P_{in(solar)}} = \frac{I_{sc}V_{oc}FF}{P_{in(solar)}} \quad \text{Eq. 1.8}$$

Increased temperatures decrease the bandgap energy, and more charge carrier pairs are formed, increasing I_{sc} . The decrease in V_{oc} over this temperature rise is, however, more dramatic than the rise in I_{sc} , hence the overall effect is decreased PV cell efficiency [20].

The virtually unlimited energy from the sun and the fact that the power generated by solar panels does not emit GHG has driven intense study and continual improvement of PV technology. Solar energy research and commercialization has and is likely to continue to receive

the largest share of overall renewable energy investment funding [19]. Solar panels have also become more commercially available and affordable as semiconductor material cost, quality, and manufacturing processes and efficiency continue to improve [21]. Unique materials and combinations such as perovskites with caffeine [22] or capsaicin [23] are exciting areas of research. PV panel efficiency has overall been increasing [21], with maximum efficiency ranging from 21.1% to 22.8% under standard testing conditions [24].

Although PV panels do not generate any GHG emissions under operation, the procurement of the raw materials and the manufacturing process may be considered sources of emissions which enlarge the carbon footprint of this technology [25]. While PV research accounts for the largest portion of renewable energy investment funding, as of 2017 solar PV generation represented only 1.7% of electricity globally [26]. Furthermore, despite ongoing novel materials research, most commercialized PV panels are made of monocrystalline or polycrystalline silicon. Finally, PV performance drops with rising temperatures, with the power generation falling on the order of 0.4% per Celsius degree over ideal operating temperatures [27]. Increasing global temperatures mean higher local temperatures, which decrease PV efficiency and power conversion.

Finally, silicon PV panels are known to degrade over time and manufacturers report a degradation rate of roughly 0.5% efficiency loss per year. PV modules in operation experience power loss stemming from a variety of factors including high ambient temperatures, relative humidity, and extreme weather effects. For example, Scotland has much cooler average annual ambient temperatures than Australia or Thailand, thus silicon PV panels in these regions have different rates of degradation. Observations show that Scotland's lower annual average temperature leads a silicon PV degradation rate between 1.05% and 1.16% per year, while the

high annual average temperatures in Australia lead to a more rapid degradation rate ranging from 1.35% to 1.46% per year, and the combination of high temperatures and high relative humidity in Thailand lead to an even more dramatic degradation rate that ranges from 1.5% to 4.9% per year [28]. Although it can generally be assumed that higher temperatures will lead to greater degradation rates, this is not always the case and there is a good deal of variation between manufacturers of silicon solar panels [28], [29]. While assuming the degradation rate of a PV panel is constant vastly simplifying financial modeling, this technique does not perfectly portray real-world PV panel operation [30].

Solar panels are one of the most widespread renewable energy technologies in the world, valued at over US\$115 billion in 2019 [31] and is expected to continue growing by leaps and bounds in the coming decade. Solar accounts for over 58% of all renewable energy in the US [32], and the World Bank estimates that solar will account for more than half of all renewable energy capacity through the next 5 years [33]. Advances in PV technology coupled with falling costs of raw materials led to continued global market growth even through the turbulence caused by the Covid-19 pandemic [31]. Growing demand for renewable energy technologies is projected to increase mineral extraction needs by nearly 500% by 2050, posing numerous challenges, such as environmentally and labor friendly mineral mining, transportation, and processing [34].

Building Integrated Photovoltaics: Although solar panels are an incredibly useful technology, their performance is adversely affected as temperatures rise. Because of this sensitivity to high temperatures, steps must be taken to manage panel temperatures to improve electrical performance. One method for dissipating or harvesting this excess heat is to integrate PV panels into the façade of the building they power. Building integration or application allows for airflow to dissipate excess heat, and reservoirs (usually of potable water) to collect it for later

use heating the building and providing hot water.

Figure 1.4 shows a simple schematic for a typical BIPV system. In this system, the PV panel is a part of the building façade. An air channel between the panel and wall allows outside air to enter from the bottom, absorb heat from the back of the PV panel to cool it, then exit from the top of the system. In some configurations, this heated air is redirected to heat the interior of the building, even further improving efficiency [35], [36].

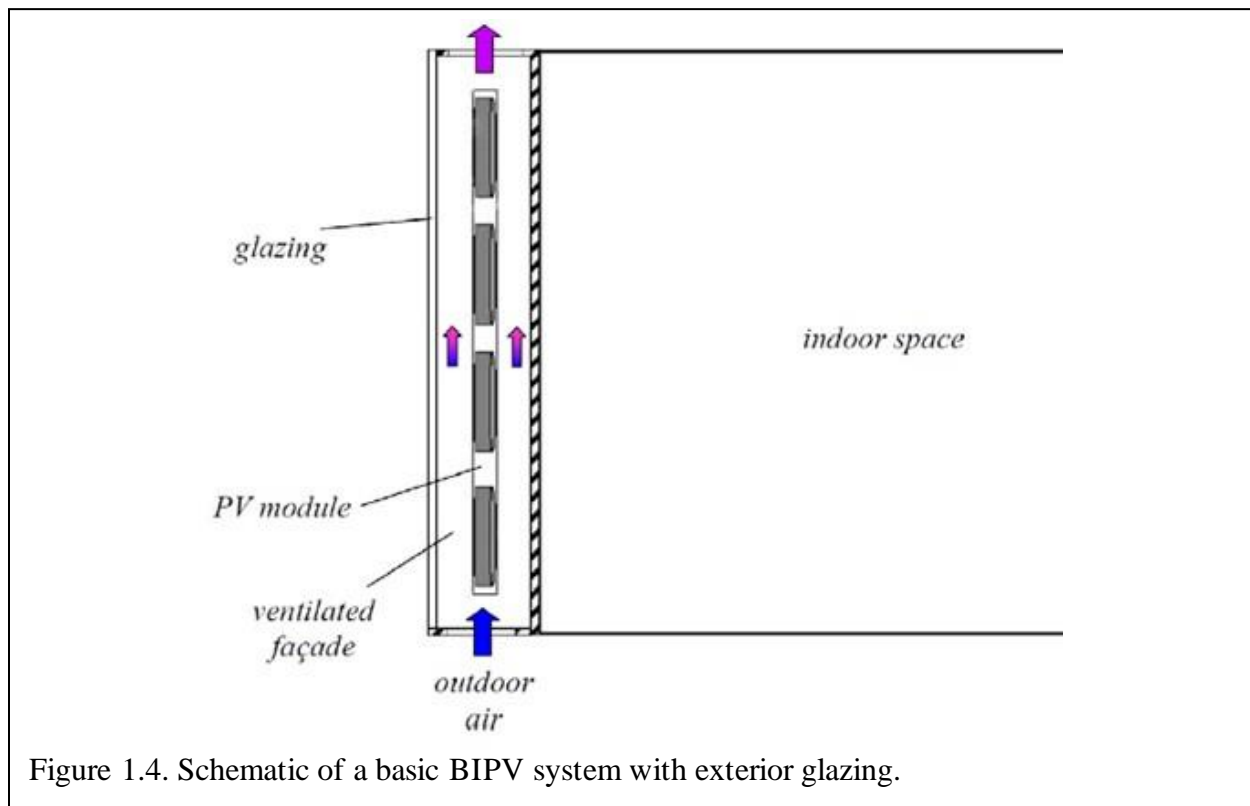


Figure 1.4. Schematic of a basic BIPV system with exterior glazing.

Integration of PV panels into a building envelope offers two key benefits: improved performance and ability to store and utilize wasted heat asynchronously. BIPV systems have consistently shown improvements in the thermal management, electrical performance, and PV panel lifetime because they remove excess heat from the panel's back surface. The BIPV system benefits are maximized when excess thermal energy is used to heat air or water for use in the building. Finally, PV panels may be integrated or retrofit into many types of building envelopes,

making them very widely applicable [35]–[37].

Like any technology BIPV is not without its limitations. The cost to integrate PV into the building envelope is a significant barrier, as the system must first be designed and then installed correctly. Despite the performance and lifetime improvements offered, BIPV systems only account for 1% to 3% of worldwide PV installations [36]. Expertise necessary for BIPV design and installation are limited in many locations, further inhibiting the large-scale adoption of BIPV systems [37].

Phase Change Materials (PCM): There are many means that have been developed and employed to manage the temperature of solar panels under operation. Beyond building integration, PCM are a promising technology that has been gaining increased interest over the past decade.

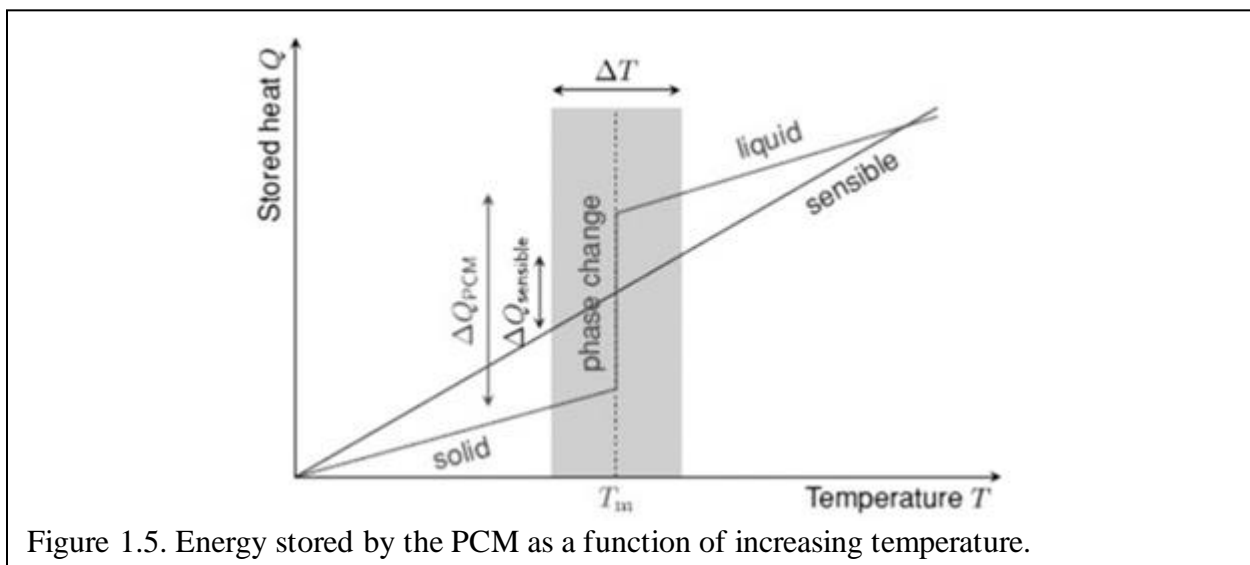
When a material changes phase, its temperature remains approximately constant as it absorbs or releases energy, and PCM leverages this phenomenon to control PV panel temperatures. As a PCM absorbs latent heat from a PV panel, the solid material melts while maintaining a constant temperature. Figure 1.5 shows a plot of the energy stored by the PCM as its temperature increases [38]. Once the PCM has fully melted, its thermal management abilities are seriously reduced because the melted material increases the temperature as more thermal energy is absorbed. The time and temperature range over which this phase change takes place vary according to the thermal conductivity of the material used, its mass, and impurities that enhance (or retard) thermal transport. PCM may also serve as thermal energy storage over a material-specific temperature range, allowing otherwise wasted heat to be used later [38].

Every study performed so far has shown that PCM improves PV performance by keeping panel temperatures lower. PCM is theoretically able to melt and freeze repeatedly and thus

should be able to aid in thermal management for long periods of time. PCM also has the added benefit of being able to store thermal energy for use in other applications [38].

PCM can be classified as organic, inorganic, or eutectic. Organic PCM are further subdivided into paraffin and non-paraffin types such as fatty acids and alcohols. Inorganic PCM are separated into metallics and salt hydrates such as KCl, MgCl_2 , and carbonate salts. Eutectic PCM are some combination of PCM, including organic-organic, inorganic-inorganic, and inorganic-organic [39]. Paraffin PCM have traditionally been very popular as they are inexpensive and easy to obtain. However, plant-based, and other biodegradable and environmentally friendly materials have been gaining popularity. In the long-term, paraffin is not a sustainable PCM as it is manufactured from petroleum byproducts.

For all their benefits, PCM are not free of flaws. For example, PCM materials may have poor thermal conductivity, be flammable, or undergo phase separation after repeated cycling [38]. The phase change of a PCM is also typically nonuniform and features such as different tilt angles have been shown to highly influence PCM melting times [40]. Expansion and contraction may also lead to leakage of PCM materials in some circumstances [41].



Research Scope

Since there are nearly endless ways of assembling a BIPV-PCM system, the scope of this work is necessarily limited in several ways. First, the “building” of the BIPV-PCM system under investigation is limited to a standard 20-foot shipping container because shipping containers are plentiful and inexpensive. Second, the PV panels in this application are also confined to those that are commercially available, with a preference for monocrystalline silicon PV panels manufactured in the US. The PCM are limited to naturally formed materials that are abundant, renewable, and environmentally friendly.

Research Questions: This combination of technologies and the selected PCM types are areas of ongoing research. Investigation into the broad range of effects due to increasingly frequent severe weather is also an area of growing interest. This work focuses on the long-term viability of the BIPV-PCM microfacility in terms of both performance and commercializability in increasingly unfavorable severe weather and temperature conditions. The four key questions asked in this work are:

- Can BIPV-PCM appreciably mitigate PV or building interior temperatures even when subjected to high temperatures and severe weather conditions?
- How do PCM thickness and channel spacing impact the thermal profile?
- Of the selected PCM, if any, performs best and under what circumstances?
- Is there a market for this kind of technology, and if so, what is the most direct path to commercialization?

The first three of these questions are answered through the thermal modeling, simulation, and analysis of Chapters 2, 3, and 4. The last point is addressed by the commercialization plan developed in Chapter 5.

Selected PV: There are amazing new advances in PV technology cropping up all the time, but many of these innovative solar power devices are not yet commercialized. Global supply chain issues, tariffs, and taxes all can also make internationally manufactured PV components difficult to access, which drives up costs. To avoid potential supply chain issues, the PV panels used to represent real-world panels in this work are limited to monocrystalline or amorphous silicon PV panels. Lumos and Mission Solar manufacture Monocrystalline Silicon Panels, while Solar Tech Universal and First Solar produce the thin-film amorphous silicon and CdTe PV panels, respectively. These PV panel types are listed in Table 1.1 along with their respective ideal efficiency ranges and manufacturers.

Table 1.1. PV types, their optimal efficiencies, and US manufacturers.		
PV Type	Optimal Efficiency [%]	US Manufacturer
Monocrystalline Silicon	16.76 – 17.62 17.45 – 18.05 18.4 – 19.3	Lumos Mission Solar Solar Tech Universal
Thin-Film Amorphous Silicon Heterojunction	19.3 – 19.9	Solar Tech Universal
Thin-Film CdTe	17.0 – 18.2	First Solar

Selected PCM: There are a staggering number of potential phase change materials that could be used for thermal management in a PV or BIPV applications, all of which have benefits and drawbacks. Effort is made to source less toxic, more sustainable, easy to maintain or replace PCM for this work. This requires sourcing PCM from international suppliers rather than exclusively US manufacturers, as well as avoiding fossil-fuel based PCM such as paraffin waxes.

Two US-based PCM manufacturing companies, Phase Change Solutions and PureTemp, produce PCM made of proprietary, non-toxic, plant-based materials. Although the specific content of these PCM is proprietary, specifications that include their melting point, specific heat, thermal conductivity, and so on are available. The other sustainable PCM modeled in this work

are beeswax [39], [42], [43], candelilla wax [43], [44], and soy wax [39], [43]. Finally, Table 1.2 lists the melting temperature ranges and thermal conductivities of these substances.

Table 1.2. Phase change material, melting temperatures, and thermal conductivities.

PCM	Melting Temperature Range [°C]	Thermal Conductivity [$\frac{W}{m \cdot K}$]
Beeswax	61 to 65	0.25
Candelilla wax	68 to 72	2.13
Soy wax	43.3 to 79.4	0.324
BioPCM® from Phase Change Solutions	-75 to 175 *	0.15 to 2.5
PureTemp® from PureTemp	-37 to 151 *	0.15 to 0.25

* Melting temperature is tunable within this range and can be adjusted according to application needs.

Thermal Modeling and Simulation: A simplified thermal model is formulated from core mathematical expressions that describe the conduction, convection, and radiation in the BIPV-PCM microfacility.

Weather data is available from a variety of sources, but often does not include extreme weather events which are typically considered anomalous. Climate change projections suggest that extreme weather events are not exactly anomalous, and certain extreme weather events will be intensifying and happening with increased frequency [45], [46]. Some issues will be universal across every state, such as widespread drought and extreme heat. Coastal areas will be more dramatically affected by sea level rise over the next few decades than inland areas farther away from oceans or with higher elevation. The threat of wildfires is intensifying in the southwest and even includes urban centers like Austin. Despite widespread drought, climate change projections indicate that many places will experience more intense precipitation and associated flooding.

Understanding how these types of extreme weather events found in the generated weather data files and investigating the types of effects that they would have on the BIPV-PCM microfacility is straightforward as the thermal effects are primarily dependent on the ambient

temperature, total incident solar radiation, and wind effects.

The software used in this endeavor is limited to Matlab which is not ideal for comprehensive thermal modeling of complex 3D systems with layers of very different dimensions. Thus, Matlab is used to simulate steady-state solutions to partial differential equations that describe the conduction and convection of the system using the finite difference method. Although transient solutions were not obtained due to computational limitations, phase change in the PCM may be modeled by the widely accepted and enthalpy-porosity method [47] which converges rapidly and is highly accurate [48]. The enthalpy-porosity method incorporates a “mushy zone” where phase change is predominantly taking place, and this method has been discovered to yield much more accurate results than other phase change models, including other enthalpy models [47], [48]. The actual melting and freezing processes of the PCM are not directly simulated, and instead the value of the energy absorbed by the PCM is just simulated for comparative purposes.

Novelty and Contributions of this Work

In the following chapters, a mathematical basis for the simplified three-box thermal model is developed and different PCM types, thicknesses, and channel spacings are simulated for the proposed BIPV-PCM microfacility system. The novelty and contributions of this work are summarized into four main areas as follows.

- Both BIPV and PV-PCM systems have been investigated in experimental and modeling environments, but investigations of integrated BIPV-PCM systems are still rare. The public concerns of climate change are driving the need to develop buildings and facilities with smaller carbon footprints by utilizing sustainable materials. Hence systems combining BIPV and PCM turn out to be a promising solution.

- Sustainable PCM types have not been systematically studied in the context of their use for PV thermal management. Thermal management of PV panels using PCM is a relatively new area of study. Existing investigations are limited to petroleum-based paraffin waxes which are inexpensive to source, yet non-sustainable in the long term. Thus, a comparative investigation of sustainable PCM types, such as beeswax, candelilla wax, and soy wax, is highly desirable and necessary.
- Since BIPV designs are often proprietary, building a three-box model to comparatively evaluate PCM types, thicknesses, and channel spacings makes further investigation into this hybrid technology more accessible to independent researchers. This base model also provides a starting point for further optimization of systems like BIPV-PCM integrated facilities while still allowing changing environmental effects to be incorporated.
- The last contribution of this work is the business plan for the BIPV-PCM microfacility developed using the BMC strategic management tool. Since the BIPV-PCM microfacility has hardly been investigated from a technology or performance standpoint, it is unsurprising that this specific hybrid technology has not been widely commercialized. The product development roadmap and the customer segments proposed in this work can be used to promote the mass adoption of this incredible technology in the US and international markets.

Table 1.3. Variables and Constants Used in Chapter 1.

Variable or Constant	Name	Units
η	Efficiency	%
FF	Fill Factor	-
I_0	Dark Saturation Current	A
I_L	Light Generated Current	
I_{mp}	Current at Max Power	
I_{net}	Net Current	
I_{sc}	Short-Circuit Current	
k_B	Boltzmann Constant	$\frac{J}{K}$
n_{id}	Ideality Factor	-
P	Power	$W, \frac{J}{s}$
$P_{in(solar)}$	Solar Power Input	
P_{mp}	Maximum Power	
q	Heat Transfer Rate	W
T	Temperature	K, °C
V	Voltage, Applied Voltage	V
V_{mp}	Voltage at Max Power	
V_{oc}	Open-Circuit Voltage	

II. THERMAL MODELING

The base thermal model is developed from well-known mathematical expressions for conduction, convection, and radiation, as well as recent developments in modeling melting and solidification of PCM. The chapter concludes with a detailed review of the layers of the BIPV-PCM system and base temperature requirements for generalized production facilities in which humans will be working.

Conduction

Conduction occurs when more energetic (hotter) particles transfer energy to less energetic (cooler) particles through physical interactions between the molecules without bulk transport in a stationary medium. Although the particles within a medium are in constant random motion, the net transport of energy due to molecular motion is zero at thermal equilibrium. The random motion of the particles in the hotter areas of a system are more energetic than those in the cooler areas of the system. Even though the random motion of the particles in the medium still takes place in every direction, in the presence of a thermal gradient there is a *net* energy transport toward the cooler areas.

Conduction Basic Concepts: Conduction can thus be modeled as a diffusive process and quantified using Fourier's Law:

$$q_x'' = -k \frac{dT}{dx} \quad \text{Eq. 2.1}$$

Where q_x'' (W/m²) is the heat flux, or heat transfer rate in the x (m) direction per unit area (m²) perpendicular to the direction of energy transport. The heat flux is proportional to the temperature gradient $\frac{dT}{dx} \left(\frac{K}{m} \right)$ via the thermal conductivity $k \left(\frac{W}{m \cdot K} \right)$, which is an inherent property of the material itself. The negative sign on the right-hand-side of equation 2.1 indicates that the direction of the energy flux is from hot (more energetic) to cold (less energetic). The direction of

heat flux is perpendicular to an isothermal surface (a surface with a constant temperature) along the direction of the thermal gradient. This naturally leads to the expression of the thermal flux as a vector, and is also shown here in cartesian coordinates:

$$\vec{q}'' = -k\nabla T = -k\left(\frac{\partial T}{\partial x}\hat{i} + \frac{\partial T}{\partial y}\hat{j} + \frac{\partial T}{\partial z}\hat{k}\right) \quad \text{Eq. 2.2}$$

In the direction \hat{n} , normal to the isotherm, the thermal flux is expressed:

$$q''_n = -k \frac{\partial T}{\partial \hat{n}} \quad \text{Eq. 2.3}$$

This concept is illustrated in 2-dimensions in Figure 2.1 [49].

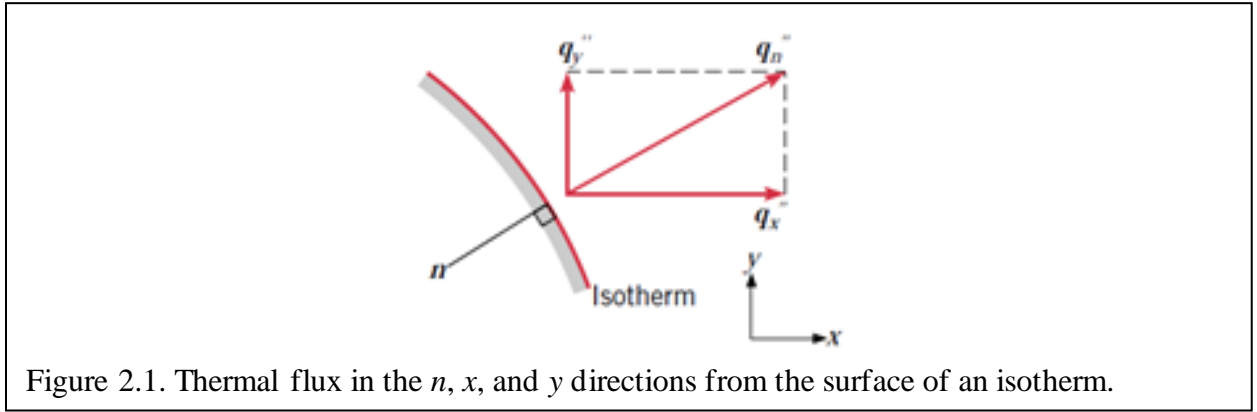


Figure 2.1. Thermal flux in the n , x , and y directions from the surface of an isotherm.

This thermal flux is driven by the temperature gradient along the \hat{n} direction across a surface. If the medium is isotropic, the thermal conductivity, k , is not directionally dependent. The general vector expression for the conduction rate equation in cartesian coordinates is:

$$\vec{q}'' = \vec{q}''_x\hat{i} + \vec{q}''_y\hat{j} + \vec{q}''_z\hat{k} \quad \text{Eq. 2.4}$$

And:

$$q''_x = -k \frac{\partial T}{\partial x}, \quad q''_y = -k \frac{\partial T}{\partial y}, \quad q''_z = -k \frac{\partial T}{\partial z} \quad \text{Eq. 2.5}$$

One of the unique features of Fourier's law is that it is not derived from first principles, but rather from experimental observations. Furthermore, it is an expression that defines thermal conductivity and applies to all matter regardless of its state. While conduction is present in fluids

as well as solids, due to the dramatic differences in molecular spacing a solid may have a thermal conductivity that is four orders of magnitude greater than a gas [49]–[51].

Thermal Conductivity: Solids can be thought of as a periodic arrangement of atoms engulfed in a sea of free electrons that can move somewhat freely. In this arrangement, thermal transport can take place via two means: motion of free electrons and vibrational waves in the lattice structure. Since the atoms in the periodic lattice are bound to one another, they move in concert and form waves that dissipate and interact throughout the volume of the lattice. The thermal conductivity of a solid material is the sum of these two effects:

$$k = k_e + k_l \quad \text{Eq. 2.6}$$

Where k_e refers to the thermal conductivity due exclusively to the motion of free electrons in the solid and k_l refers to the thermal conductivity due to the vibrational motion in the lattice [50].

In pure materials, the thermal conductivity caused by electron motion (k_e) is significantly greater than the thermal conductivity due to lattice vibrations (k_l), and can be quantified using the Wiedemann-Franz-Lorenz law:

$$k_e = \frac{L_0 T}{\rho_e} \quad \text{Eq. 2.7}$$

Here, the Lorenz number, L_0 , is a constant and the electrical resistivity, ρ_e , is defined as the sum of the residual electrical resistivity at absolute zero due to lattice imperfections, ρ_0 , and an intrinsic resistivity term, ρ' , which dominates at temperatures over 100 K.

$$\rho_e = \rho_0 + \rho' T \quad \text{Eq. 2.8}$$

Combining these we can immediately see that, to a first order approximation, k_e is independent of temperature:

$$k_e = \frac{L_0 T}{\rho_0 + \rho' T} \approx \frac{L_0 T}{\rho' T} = \frac{L_0}{\rho'} \quad \text{Eq. 2.9}$$

In non-metallic solids free electrons are less plentiful, so thermal flux is dominated by lattice vibrations. This lattice thermal conductivity depends on the frequency of atomic interactions between atoms in the lattice, and these atomic interactions increase along with the temperature. Additionally, lattice regularity increases the lattice thermal conductivity, meaning well-ordered materials like diamond and quartz have much higher lattice thermal conductivities than amorphous materials like glasses. In this case, the thermal flux is highly temperature dependent.

The mechanisms driving thermal conductivity in liquids, and by extension gases, is not well understood. Generally, the thermal conductivity of a non-metallic liquid decreases with increasing temperature, as well as with increasing molecular weight [49]. Metallic liquids are, however, useful for thermal conduction in systems with very high thermal flux, such as those in nuclear reactors. The thermal conductivity of metallic liquids is typically much higher than that of non-metallic liquids.

The Heat Diffusion Equation: The law of conservation of energy plays a role in determining thermal transport as well. Application of this law requires the definition of some fixed volume through which energy and matter may pass. Thus, the thermal and mechanical energy into and generated in the control volume less the thermal and mechanical energy out of the control volume must be equal to the total energy stored in the control volume. Likewise, the rate of energy into the control volume (\dot{E}_{in}) plus the rate of energy generated (\dot{E}_g) less the rate of energy out of the control volume (\dot{E}_{out}) must be equal to the rate of energy stored (\dot{E}_{st}) in the control volume. This general energy conservation requirement is illustrated in Figure 2.2 [49] and can be expressed as:

$$\dot{E}_{in} + \dot{E}_g - \dot{E}_{out} = \dot{E}_{st} \quad \text{Eq. 2.10}$$

When the inflow and outflow of energy are equal, the volume has reached a steady state. The thermal energy generation term, \dot{E}_g , refers to energy that has been transformed from some other form into thermal energy, such as through some volumetric chemical reactions within the material. Under steady state conditions, the energy generation and energy storage term are zero. At the surfaces of the system, energy storage and generation are not considered, and thus:

$$\dot{E}_{in} - \dot{E}_{out} = 0 \quad \text{Eq. 2.11}$$

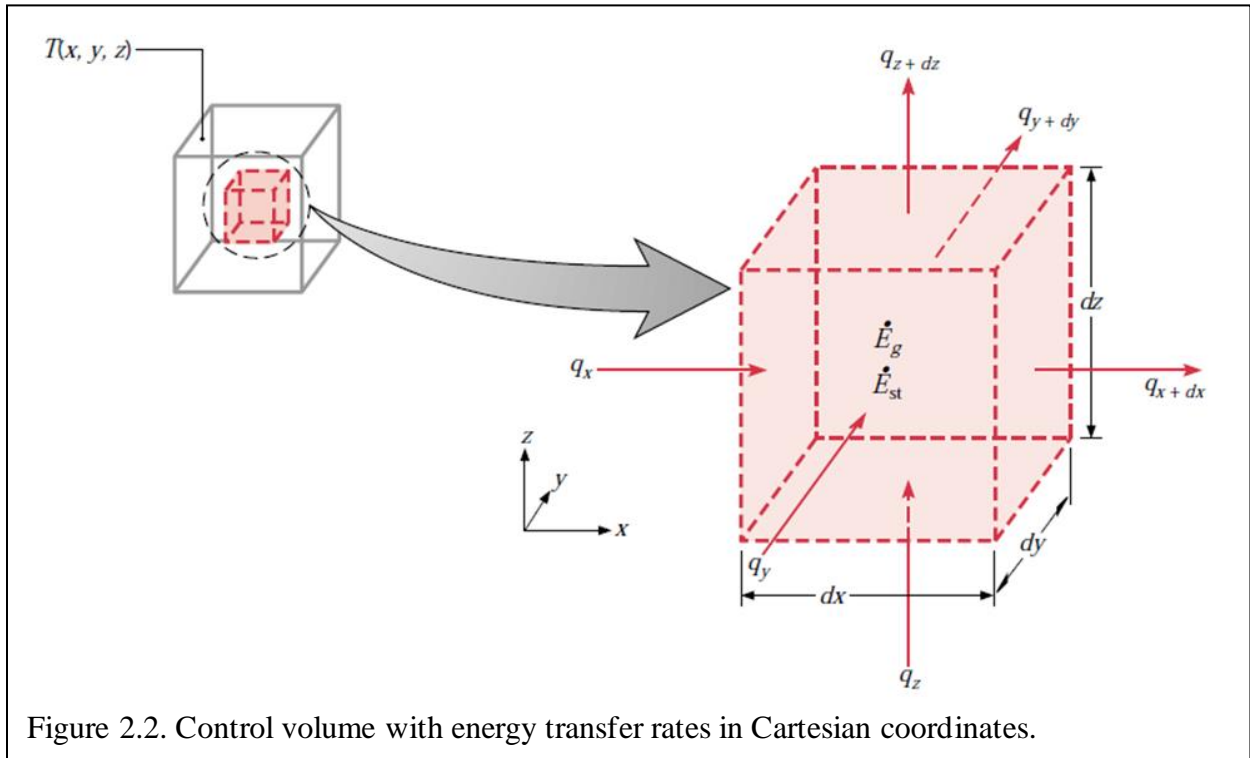


Figure 2.2. Control volume with energy transfer rates in Cartesian coordinates.

Determination of the temperature distribution throughout a medium allows for a slew of other information about a system to be determined, such as optimizing insulation thicknesses or calculating the effects of thermal stresses on structural integrity. To calculate the temperature distribution in a material, first a differential control volume must be defined, then the relevant energy transfer processes within that volume must be clearly identified, and then appropriate rate equations applied. This process results in a partial differential equation (PDE) that provides the temperature distribution throughout the medium once solved.

In cartesian coordinates – which will be the most applicable coordinate system for the modules in this work due to the shape of the production facility, solar panels, and panel spacing – conductive thermal flux can be defined in each of the three dimensions as:

$$q_{x+dx} = q_x + \frac{\partial q_x}{\partial x} dx \quad \text{Eq. 2.12}$$

$$q_{y+dy} = q_y + \frac{\partial q_y}{\partial y} dy \quad \text{Eq. 2.13}$$

$$q_{z+dz} = q_z + \frac{\partial q_z}{\partial z} dz \quad \text{Eq. 2.14}$$

The conductive thermal flux constitutes energy flow, or in other words:

$$\dot{E}_{in} = q_x + q_y + q_z \quad \text{Eq. 2.15}$$

$$\dot{E}_{out} = q_{x+dx} + q_{y+dy} + q_{z+dz} \quad \text{Eq. 2.16}$$

The energy source term, \dot{E}_g , quantifies the amount of energy generated within this differential volume and can be expressed as:

$$\dot{E}_g = \dot{q} dxdydz \quad \text{Eq. 2.17}$$

Where \dot{q} is the rate of energy generated within the differential volume (W/m^3), where the differential volume is $dxdydz$.

Finally, the energy storage term quantifies changes in the amount of thermal energy stored within the control volume, and can be expressed as:

$$\dot{E}_{st} = \rho C_p \frac{\partial T}{\partial t} dxdydz \quad \text{Eq. 2.18}$$

Where ρ is the density of the material, C_p is the specific heat capacity of the material, $\frac{\partial T}{\partial t}$ is the temperature change with respect to time. The $\rho C_p \frac{\partial T}{\partial t}$ term is the time rate-of-change of the internal energy of the medium per volume.

Substituting all these expressions into the conservation of energy equation yields:

$$q_x + q_y + q_z + \dot{q}dxdydz - (q_{x+dx} + q_{y+dy} + q_{z+dz}) = \rho C_p \frac{\partial T}{\partial t} dxdydz \quad \text{Eq. 2.19}$$

Which becomes:

$$-\frac{\partial q_x}{\partial x} dx - \frac{\partial q_y}{\partial y} dy - \frac{\partial q_z}{\partial z} dz + \dot{q}dxdydz = \rho C_p \frac{\partial T}{\partial t} dxdydz \quad \text{Eq. 2.20}$$

Multiplying the flux components by the appropriate differential area of the control surface yields the thermal transfer rate in each direction:

$$q''_x dydz = q_x = -k \frac{\partial T}{\partial x} dydz \quad \text{Eq. 2.21}$$

$$q''_y dxdz = q_y = -k \frac{\partial T}{\partial y} dxdz \quad \text{Eq. 2.22}$$

$$q''_z dxdy = q_z = -k \frac{\partial T}{\partial z} dxdy \quad \text{Eq. 2.23}$$

Also:

$$\frac{\partial q_x}{\partial x} = \frac{\partial}{\partial x} \left(-k \frac{\partial T}{\partial x} dydz \right) = \frac{\partial}{\partial x} \left(-k \frac{\partial T}{\partial x} \right) dydz \quad \text{Eq. 2.24}$$

$$\frac{\partial q_y}{\partial y} = \frac{\partial}{\partial y} \left(-k \frac{\partial T}{\partial y} dxdz \right) = \frac{\partial}{\partial y} \left(-k \frac{\partial T}{\partial y} \right) dxdz \quad \text{Eq. 2.25}$$

$$\frac{\partial q_z}{\partial z} = \frac{\partial}{\partial z} \left(-k \frac{\partial T}{\partial z} dxdy \right) = \frac{\partial}{\partial z} \left(-k \frac{\partial T}{\partial z} \right) dxdy \quad \text{Eq. 2.26}$$

These expressions can then be substituted into the energy conservation expression:

$$\frac{\partial}{\partial x} \left(k \frac{\partial T}{\partial x} \right) dxdydz + \frac{\partial}{\partial y} \left(k \frac{\partial T}{\partial y} \right) dxdydz + \frac{\partial}{\partial z} \left(k \frac{\partial T}{\partial z} \right) dxdydz + \dot{q}dxdydz = \rho C_p \frac{\partial T}{\partial t} dxdydz \quad \text{Eq. 2.27}$$

Dividing by $dxdydz$ on both sides yields the heat diffusion equation, also referred to as the heat equation, and is an expression of the conservation of energy within the medium:

$$\frac{\partial}{\partial x} \left(k \frac{\partial T}{\partial x} \right) + \frac{\partial}{\partial y} \left(k \frac{\partial T}{\partial y} \right) + \frac{\partial}{\partial z} \left(k \frac{\partial T}{\partial z} \right) + \dot{q} = \rho C_p \frac{\partial T}{\partial t} \quad \text{Eq. 2.28}$$

In the event the thermal conductivity of the material is not directionally dependent – that is, the thermal conductivity is the same throughout the medium – then this expression can be simplified as [52], [53]:

$$\frac{\partial^2 T}{\partial x^2} + \frac{\partial^2 T}{\partial y^2} + \frac{\partial^2 T}{\partial z^2} + \frac{\dot{q}}{k} = \frac{1}{\alpha} \frac{\partial T}{\partial t} \quad \text{Eq. 2.29}$$

Here, the thermal diffusivity term, $\alpha = \frac{k}{\rho C_p}$, quantifies the effectiveness of thermal transport in the medium. Higher thermal diffusivity indicates a medium is better at transporting heat, while lower thermal diffusivity indicates less efficient thermal transport through the medium. The heat equation is second order in spatial coordinates and thus requires two boundary conditions for each coordinate. However, as the heat equation is first order in time, only the initial condition must be specified to solve it. Although there are a wide variety of boundary and initial conditions that can be applied to innumerable thermal transport problems, the boundary conditions relevant to the overall system to be modeled in this work and will be outlined in later sections.

Radiation

Radiative thermal transport stems from changes in the electron configuration of the particles in the medium, and transports energy via electromagnetic waves. Unlike conduction and convection, radiative energy transfer does not require the presence of a medium, and in fact, radiative energy is transported most efficiently through a vacuum.

Radiation Basic Concepts: The maximum thermal energy flux from an ideal radiator (also referred to as a blackbody) surface is described by the Stefan-Boltzmann Law [49]:

$$q'' = \sigma T_s^4 \quad \text{Eq. 2.30}$$

Where T_s (K) is the absolute temperature of a perfect blackbody surface of the medium and σ is

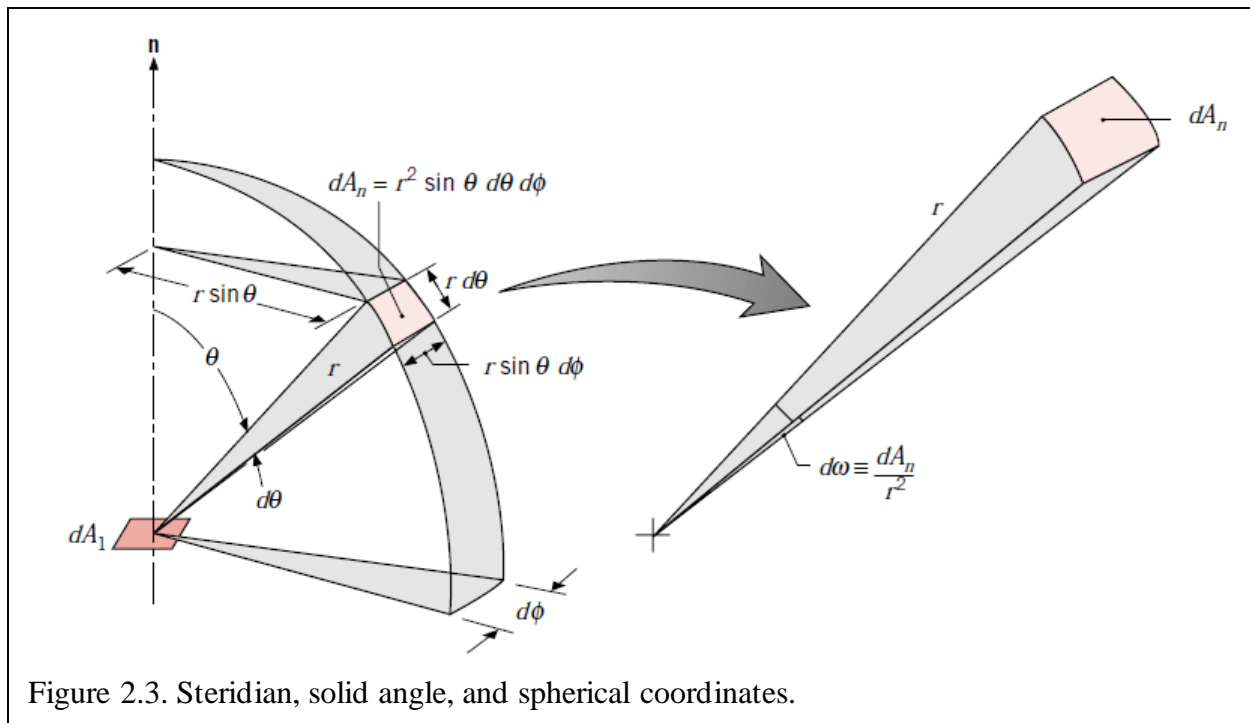
the Stefan-Boltzmann constant ($5.67 \times 10^{-8} \frac{W}{m^2 K^4}$). Non-ideal, real surfaces adjust this energy flux via their material-dependent emissivity, ϵ , yielding:

$$q'' = \epsilon \sigma T_s^4 \quad \text{Eq. 2.31}$$

Thus, the net rate of radiative thermal exchange between a surface and its surroundings can be expressed as:

$$q = \epsilon A \sigma (T_s^4 - T_{surr}^4) \quad \text{Eq. 2.32}$$

Where A is the surface area of the object radiating thermal energy, ϵ is the emissivity of the surface, T_{surr} refers to the temperature of the surroundings, and T_s refers to the temperature of the surface.



Radiation propagating through a medium (like air) has a wavelength (λ) and wave frequency (ν) related by the speed of light through this medium (c_0) as follows:

$$\lambda = \frac{c_0}{\nu} \quad \text{Eq. 2.33}$$

Thermal radiation wavelengths range from $10^{-1} \mu m$ to $10^2 \mu m$, and radiation from a surface is

comprised of a combination of wavelengths within this range. The magnitude of the radiation varies with wavelength throughout this range, which can be thought of as a nonuniform continuous distribution of individual wavelengths. This spectral distribution is influenced by the temperature and makeup of the radiating surface. To further complicate matters, radiation may be emitted in all directions and a surface may radiate in preferential directions generating a directional distribution of the emitted radiation.

Blackbody Radiation: A blackbody is the idealized standard against which real radiating bodies are compared and its radiation intensity is well known [20], [49]:

$$I_{\lambda,b}(\lambda, T) = \frac{2hc_0^2}{\lambda^5 \left[e^{\frac{hc_0}{\lambda k_B T}} - 1 \right]} \quad \text{Eq. 2.34}$$

Where $h = 6.6256 \times 10^{-34} J \cdot s$, $k_B = 1.3805 \times 10^{-23} \frac{J}{K}$, and $c_o = 2.998 \times 10^8 \frac{m}{s}$ are the Planck constant, Boltzmann constant, and speed of light in a vacuum, respectively. Because a blackbody is a diffuse emitter, its spectral emissive power, also known as the Planck Distribution, is:

$$E_{\lambda,b}(\lambda, T) = \pi I_{\lambda,b}(\lambda, T) = \frac{2\pi hc_0^2}{\lambda^5 \left[e^{\frac{hc_0}{\lambda k_B T}} - 1 \right]} \quad \text{Eq. 2.35}$$

Defining the first and second radiation constants, $C_1 = 2\pi hc_0^2 = 3.742 \times 10^8 \frac{W \cdot \mu m^4}{m^2}$ and $C_2 =$

$\frac{hc_0}{k_B} = 1.439 \times 10^4 \mu m \cdot K$, the Planck Distribution becomes:

$$E_{\lambda,b}(\lambda, T) = \frac{C_1}{\lambda^5 \left[e^{\frac{C_2}{\lambda T}} - 1 \right]} \quad \text{Eq. 2.36}$$

Blackbodies emit radiation that varies continuously with wavelength, and the temperature of the blackbody determines the spectral region in which the emitted radiation is concentrated.

The magnitude of emitted radiation and relative amount of short-wavelength radiation increases with increasing temperature. As temperature increases, the maximum spectral emission shifts to shorter wavelengths as temperature increases. The blackbody curve has a peak magnitude at some characteristic temperature and wavelength, and this maximum is found by setting derivative of the spectral energy with respect to wavelength to zero yields Wien's Displacement Law:

$$\lambda_{max}T = C_3 \quad \text{Eq. 2.37}$$

Where the third radiation constant, $C_3 = 2897.6 \mu m \cdot K$. The total emissive power of a blackbody is the sum of emission of every wavelength, or:

$$E_b = \int_0^\infty \frac{C_1}{\lambda^5 [e^{C_2/\lambda T} - 1]} d\lambda = \sigma T^4 \quad \text{Eq. 2.38}$$

Where σ is the Stefan-Boltzmann constant and is equal to $5.670 \times 10^{-8} \frac{W}{m^2 \cdot K^4}$. This solution allows calculation of the total radiation emitted by the blackbody emitted in all directions at a given temperature. Since the emitted radiation is diffuse, the total intensity of the blackbody's radiative emission is [49], [52], [53]:

$$I_b = \frac{E_b}{\pi} \quad \text{Eq. 2.39}$$

Radiation from Real Surfaces: Of course, real surfaces do not emit as much radiation as the idealized, perfect blackbody. Blackbody radiation thus constitutes the maximum possible radiation a real body may emit at the same temperature. The emissivity, ε , is defined as the ratio of radiation emitted by the real surface to the radiation that would be emitted by a blackbody at the same temperature. To complicate matters further, spectral radiation from real surfaces is typically distributed very differently from that of the smooth Planck Distribution and real surfaces are frequently not diffuse, which causes the emitted radiation to have a directional distribution. These phenomena are shown in Figure 2.4.

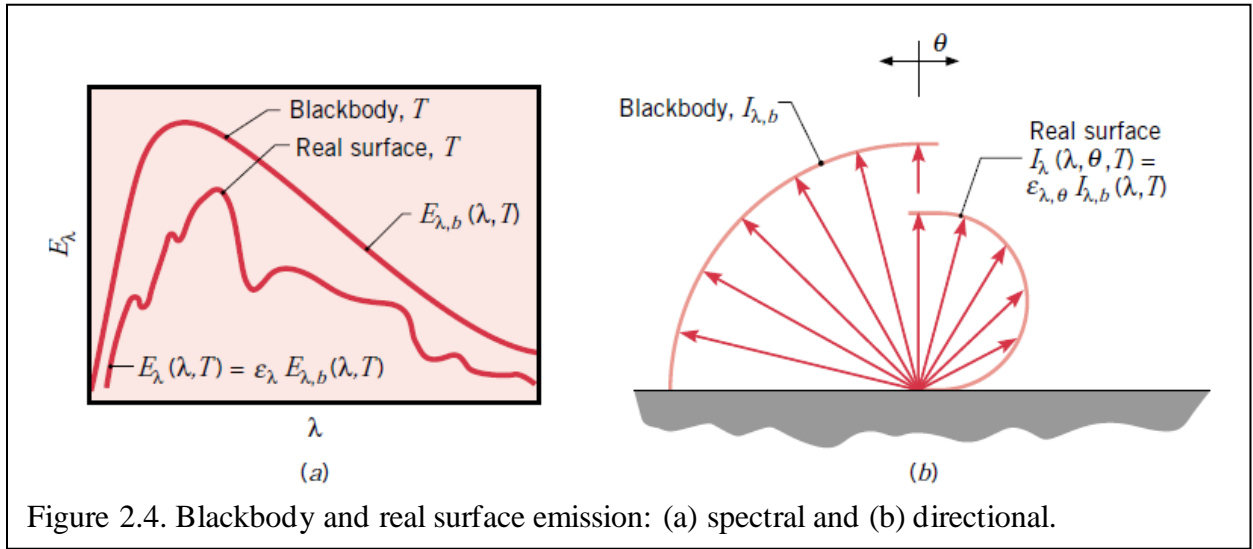
The spectral directional emissivity is a ratio of the intensity of the emitted radiation at a certain wavelength in the (θ, ϕ) direction to the intensity of emitted radiation at this wavelength from a blackbody at this temperature, or:

$$\varepsilon_{\lambda,\theta}(\lambda, \theta, \phi, T) \equiv \frac{I_{\lambda,e}(\lambda, \theta, \phi, T)}{I_{\lambda,b}(\lambda, T)} \quad \text{Eq. 2.40}$$

Likewise, the total emissivity represents an average emissivity over all directions and wavelengths:

$$\varepsilon(T) \equiv \frac{E(T)}{E_b(T)} = \frac{\int_0^\infty E_\lambda(\lambda) d\lambda}{E_b(T)} = \frac{\int_0^\infty \varepsilon_\lambda(\lambda, T) E_{\lambda,b}(\lambda, T) d\lambda}{E_b(T)} \quad \text{Eq. 2.41}$$

The key benefit of this analysis is that if the emissivity of a real surface is known, then its emission characteristics are relatively easy to compute. The emissivity of a significant number of materials and coatings have been experimentally determined.



Absorption, Reflection, and Transmission: When irradiation is incident on a semitransparent medium the radiation is either reflected, transmitted, or absorbed, and this can be expressed mathematically as:

$$G_\lambda = G_{\lambda,refl} + G_{\lambda,trans} + G_{\lambda,abs} \quad \text{Eq. 2.42}$$

Where G_λ is the spectral irradiation, or the rate that radiation with wavelength λ strikes a differential surface area per unit wavelength interval $d\lambda$ about λ . Reflectivity is a measure of the fraction of irradiance that is reflected by a surface and the spectral, directional reflectivity,

$\varrho_{\lambda,\theta}(\lambda, \theta, \phi) \equiv \frac{I_{\lambda,i,refl}(\lambda, \theta, \phi)}{I_{\lambda,i}(\lambda, \theta, \phi)}$, and thus the spectral reflectivity is:

$$\varrho_\lambda(\lambda) \equiv \frac{G_{\lambda,refl}(\lambda)}{G_\lambda(\lambda)} = \frac{\int_0^{2\pi} \int_0^{\pi/2} \varrho_{\lambda,i}(\lambda, \theta, \phi) I_{\lambda,i}(\lambda, \theta, \phi) \cos\theta \sin\theta d\theta d\phi}{\int_0^{2\pi} \int_0^{\pi/2} I_{\lambda,i}(\lambda, \theta, \phi) \cos\theta \sin\theta d\theta d\phi} \quad \text{Eq. 2.43}$$

And then the total reflectivity is:

$$\varrho \equiv \frac{G_{refl}}{G} = \frac{\int_0^\infty \varrho_\lambda(\lambda) G_\lambda(\lambda) d\lambda}{\int_0^\infty G_\lambda(\lambda) d\lambda} \quad \text{Eq. 2.44}$$

Idealized reflection may be diffuse or spectral, that is, the reflected irradiance may not be directionally dependent, or may reflect at an angle equal to the incident angle of irradiance. Real surfaces are neither purely diffuse nor purely spectral, though mirrors and polished objects more closely resemble spectral radiation while rough surfaces more closely resemble diffuse reflection. In a similar fashion, spectral and total transmissivity may be defined as the ratio of transmitted radiation to total irradiation, or:

$$\zeta_\lambda = \frac{G_{\lambda,trans}}{G_\lambda} \quad \text{Eq. 2.45}$$

$$\zeta = \frac{G_{trans}}{G} = \frac{\int_0^\infty \zeta_\lambda(\lambda) G_\lambda(\lambda) d\lambda}{\int_0^\infty G_\lambda(\lambda) d\lambda} \quad \text{Eq. 2.46}$$

Perhaps unsurprisingly, spectral and total absorptivity are then defined as:

$$\alpha'_\lambda = \frac{G_{\lambda,abs}}{G_\lambda} \quad \text{Eq. 2.47}$$

$$\alpha' \equiv \frac{G_{abs}}{G} = \frac{\int_0^\infty \alpha'_\lambda(\lambda) G_\lambda(\lambda) d\lambda}{\int_0^\infty G_\lambda(\lambda) d\lambda} \quad \text{Eq. 2.48}$$

Solar Radiation: Because the sun is so incredibly huge ($1.39 \times 10^9 \text{ m}$ in diameter) and distant (roughly $1.5 \times 10^{11} \text{ m}$ from the earth), its light strikes earth's atmosphere at zenith angle, θ_z , with virtually parallel rays. The angle of this radiation is dependent not only on the position of earth in orbit around the sun, but also on the geographical latitude. Thus, the extraterrestrial solar irradiation, $G_{S,0}$ is defined as:

$$G_{S,0} = S_c \cdot f \cdot \cos\theta_z \quad \text{Eq. 2.49}$$

Where the solar constant, S_c , is a measure of the solar energy flux through a surface normal to the sun's rays when the earth is at its mean distance from the sun, known to be $1353 \frac{\text{W}}{\text{m}^2}$. The value of f ranges from 0.97 to 1.03, and accounts for the eccentricity of earth's orbit, and the $\cos\theta_z$ term projects the surface normal to the sun's rays on the surface of earth's atmosphere.

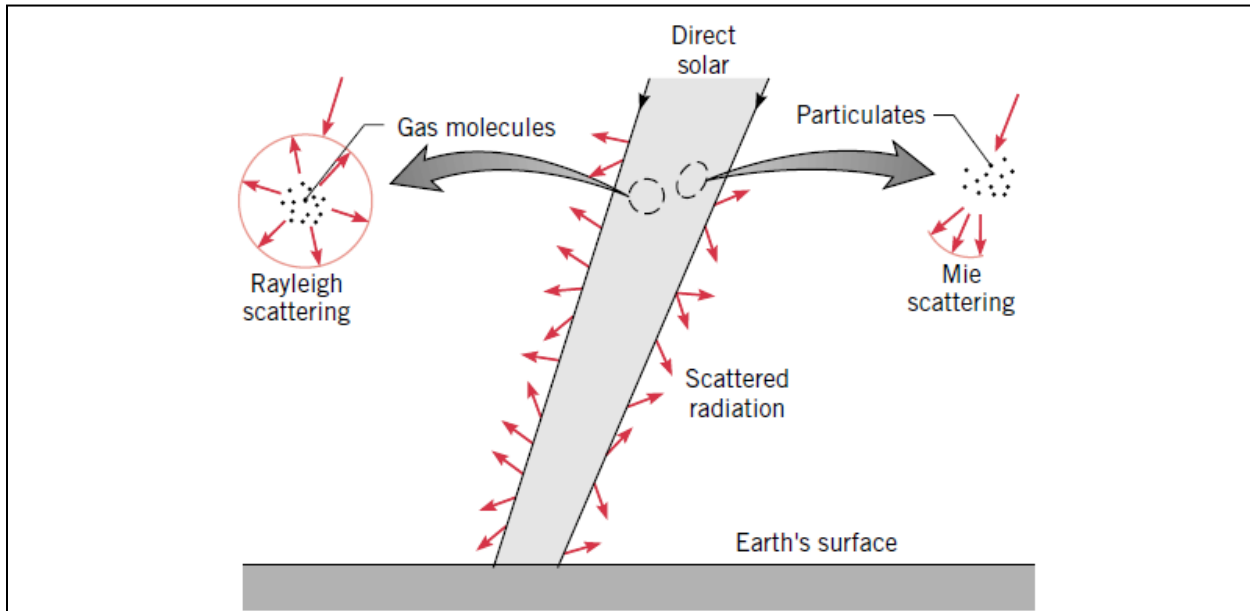


Figure 2.5. Rayleigh and Mie Scattering of the sun's radiation as it passes through the Earth's atmosphere.

As this solar radiation passes through the atmosphere, portions of the radiation are absorbed and scattered by molecules in the atmosphere, changing the spectral distribution of the incoming radiation. Atmospheric scattering changes the direction of the radiation and can be classified as

either Rayleigh or Mie scattering, as shown in Figure 2.5 [20], [49]. Rayleigh scattering redirects incident radiation in all directions, while Mie scattering, while still taking place in all directions, scatters radiation mainly in the same direction as the incident radiation. Thus, roughly half of all radiation scattered by Rayleigh scattering returns to space while the other half strikes the planet, and most of the radiation scattered by Mie scattering reaches the surface. The cumulative effect of these two types of scattering is that most of the radiation that passes through the atmosphere is oriented very closely to the direction of the incident rays. The portion of the total incident radiation which strikes earth's surface parallel to the zenith angle is termed direct radiation, while the rest of the incident radiation is called diffuse radiation. On clear days, the diffuse radiation makes up approximately 10% of the total solar radiation while on overcast days total solar radiation may be made up entirely of diffuse radiation.

Earth's surface emits long-wave radiation which may be calculated as:

$$E' = \varepsilon' \sigma T^4 \quad \text{Eq. 2.50}$$

And likewise, earth's atmosphere emits radiation, which can be expressed as:

$$G_{atm} = \sigma T_{sky}^4 \quad \text{Eq. 2.51}$$

Where T_{sky} is the effective temperature of the sky dependent on atmospheric conditions and ranges from approximately 230K for cold, clear skies and 285K for warm, cloudy skies. It should be noted that spectral properties of surfaces at short-wavelengths may differ from those of long-wavelength behaviors, and thus the solar absorptivity of a surface, α_s , may have a different value than the surface emissivity, ε . The ratio of α_s to ε can be used to determine whether the surface rejects (small $\frac{\alpha_s}{\varepsilon}$) or collects (large $\frac{\alpha_s}{\varepsilon}$) energy [20], [49], [52], [53].

Convection

Convection involves random diffusive particle-particle thermal transport much like the conduction process, as well as energy transfer via the macroscopic motion of aggregates of particles through the medium. The cumulative effect of these two processes is summarily referred to as convection. Once again, in the presence of a thermal gradient, the net energy transport via both random particle-particle and bulk motional processes is from the hotter to the cooler areas of the system.

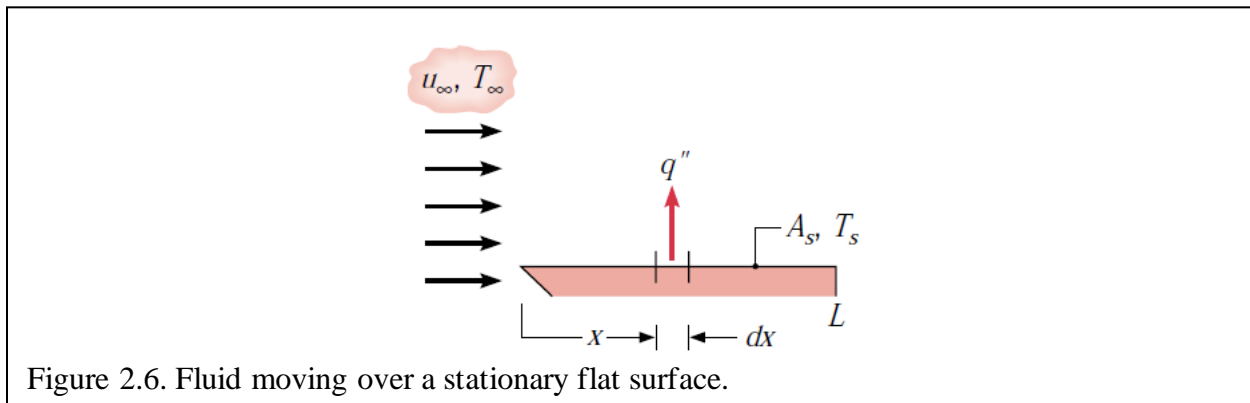


Figure 2.6. Fluid moving over a stationary flat surface.

Convection Basic Concepts: Of particular interest is the interaction between a moving fluid (macroscopic motion of aggregates) at one temperature with a bounding stationary surface at a different temperature as shown in Figure 2.6. At the surface the velocity of the fluid must be zero, which creates a boundary layer wherein the fluid velocity varies from zero at the surface to that of the finite bulk velocity of the fluid. This boundary layer is referred to as the hydrodynamic (or velocity) boundary layer. In much the same fashion a thermal boundary layer is formed when there is a difference in temperature between the surface and the fluid. Furthermore, at the interface between the surface and the fluid, energy is transferred exclusively via diffusive mechanisms. When the fluid speed is low these diffusive effects dominate, and the thicknesses of the hydrodynamic and thermal boundary layers are relatively low. As the fluid speed increases the thickness of these boundary layers also increases, and the effects of these

energy transport mechanisms contribute more significantly to overall thermal transfer through the medium [49].

Convection can be characterized as either free or forced. Free convection occurs due to the buoyancy forces induced by temperature variations within the fluid, while forced convection occurs due to flow driven by external means (fans, pumps, wind, etc.). Additionally, latent heat exchange due to phase change (such as condensation and boiling) significantly influences convection. The local heat flux q'' (W/m²) can be described using Newton's Law of Cooling regardless of the specifics about the mode of convection [49], [52], [53]:

$$q'' = h'(T_s - T_f) \quad \text{Eq. 2.52}$$

Where T_s refers to the temperature at the surface, T_f refers to the temperature of the fluid, and the proportionality constant h' is the local heat transfer coefficient (W/m²K), which aims to describe all the effects that influence convection in a single value. Since the local flow conditions and convection coefficients vary across the surface of the stationary solid or fluid, the total heat transfer rate, q , can be found by integrating the local heat flux over the surface area, A_s :

$$q = \int_{A_s} q'' dA_s = \int_{A_s} h'(T_s - T_f) dA_s \quad \text{Eq. 2.53}$$

If the temperature across the surface doesn't vary, this expression becomes:

$$q = (T_s - T_f) \int_{A_s} h' dA_s \quad \text{Eq. 2.54}$$

Defining the average heat transfer coefficient, \bar{h} , over the surface:

$$\bar{h} = \frac{1}{A_s} \int_{A_s} h' dA_s \quad \text{Eq. 2.55}$$

Allows the heat transfer rate to be expressed as:

$$q = \bar{h} A_s (T_s - T_f) \quad \text{Eq. 2.56}$$

Special cases yield more specific local heat transfer coefficients. For the case of fluid flowing parallel to a flat surface as shown in Figure 2.6, the local heat transfer coefficient becomes [49]:

$$\bar{h} = \frac{1}{L} \int_0^L h' dx \quad \text{Eq. 2.57}$$

And the heat transfer rate for this special case is:

$$q = \bar{h}L(T_s - T_f) \quad \text{Eq. 2.58}$$

Similarly, when a fluid with one molar concentration, $C_{A,f}$ (kmol/m³), flows over a surface with another concentration, $C_{A,s}$, where $C_{A,f} \neq C_{A,s}$, convective mass transfer occurs. The molar flux at the surface, N_A'' (kmol/m²s), can be expressed and handled in much the same way as the thermal transport is via the use of a convection mass transfer coefficient, h_m (m/s), as follows:

$$N_A'' = h_m(C_{A,s} - C_{A,f}) \quad \text{Eq. 2.59}$$

Once again, an average mass transfer coefficient, \bar{h}_m , may be defined:

$$\bar{h}_m = \frac{1}{A_s} \int_{A_s} h_m dA_s \quad \text{Eq. 2.60}$$

And the total molar transfer rate across the entire surface can be expressed:

$$N_A = \bar{h}_m A_s (C_{A,s} - C_{A,f}) \quad \text{Eq. 2.61}$$

Alternatively, species transfer can be modeled as the mass flux, n_A'' (kg/m²s), and mass transfer rate, n_A (kg/s), which can be found by multiplying Equations 2.59 and 2.61 by the molecular weight of the fluid, M_A (kg/kmol), and are expressed below:

$$n_A'' = h_m(\rho_{A,s} - \rho_{A,f}) \quad \text{Eq. 2.62}$$

$$n_A = \bar{h}_m A_s (\rho_{A,s} - \rho_{A,f}) \quad \text{Eq. 2.63}$$

In the special case of mass transfer from the surface of a flat plate, the average mass transfer

coefficient becomes:

$$\bar{h}_m = \frac{1}{L} \int_0^L h_m dx \quad \text{Eq. 2.64}$$

Convection Boundary Layers: As mentioned, three types of boundary layers are formed when a moving fluid passes over a flat surface: velocity, thermal, and concentration. To develop a sound understanding of these concepts, each of these boundary layer types is explored in greater detail in the sections that follow.

The particles of a moving fluid directly in contact with the solid surface must have a zero velocity, or $u_f = 0$. Shear stresses, τ , within the fluid mean that the next “layer” of particles from the surface are slowed, in turn slowing the next layer and so on. Figure 2.7 illustrates the velocity boundary layer formed by a fluid flowing across a flat surface. At a distance, δ (m), from the surface shear stresses become negligible and the velocity component parallel to the surface increases from zero at the surface to the freestream speed of the moving fluid, u_{free} . Formally, the velocity boundary layer thickness, δ , is defined as the thickness where the fluid velocity is equal to 99% of the freestream velocity, or $u_f = 0.99u_{free}$. The surface shear stress, τ_s , can be determined from the velocity gradient through the velocity boundary layer [49]:

$$\tau_s = \mu \left. \frac{\partial u_f}{\partial y} \right|_{y=0} \quad \text{Eq. 2.65}$$

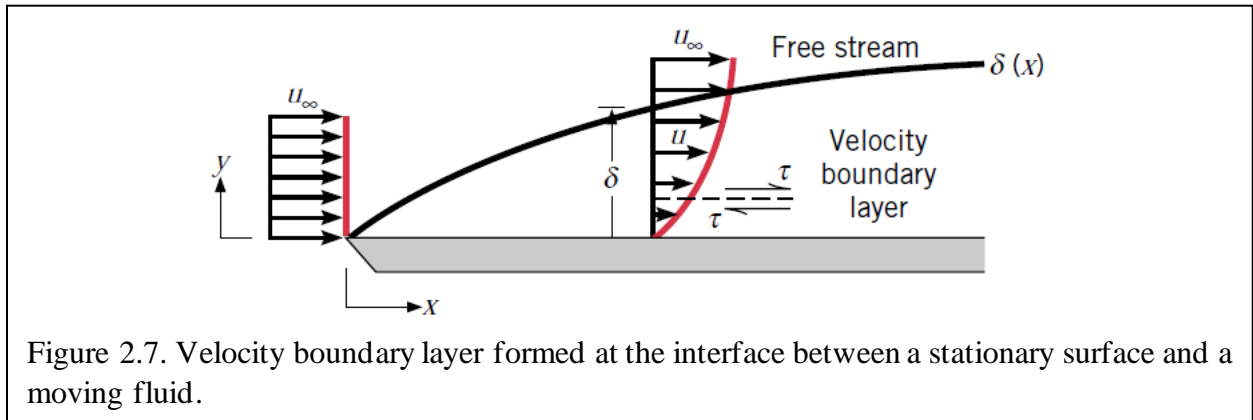
Where μ is the dynamic viscosity (Ns/m²) of the fluid and $\frac{\partial u_f}{\partial y}$ is the velocity gradient through the velocity boundary layer thickness. Frictional drag due to surface friction and shear stress can be determined from the friction coefficient:

$$C_f \equiv \frac{\tau_s}{\frac{\rho u_{free}^2}{2}} \quad \text{Eq. 2.66}$$

When the surface and moving fluid temperatures differ, a thermal boundary layer forms in much the same way that the velocity boundary layer does. At the leading edge, fluid particles in contact with the surface of the plane must necessarily be at the same temperature as the plane. These fluid particles exchange thermal energy with the particles in the next plane further from the surface, which in turn exchange energy with the next layer of fluid particles, causing varying temperature gradients through this thermal layer. The thickness of the thermal boundary layer, δ_T (m), is defined as:

$$(T_s - T) = 0.99(T_s - T_f) \quad \text{Eq. 2.67}$$

Where T_s refers to the temperature of the surface, T_f refers to the temperature of the fluid, and T refers to the varying temperature within this boundary layer. At the leading-edge $T = T_f$ and at the solid surface $T = T_s$. As T increases from T_s to T_f , the ratio $(T_s - T)/(T_s - T_f)$ approaches 0.99.



On the solid surface the molecules are not in motion, so thermal transport can only occur via conduction. The local heat flux, q_s'' , is determined by applying Fourier's Law to the fluid at the surface:

$$q_s'' = -k_f \left. \frac{\partial T}{\partial y} \right|_{y=0} \quad \text{Eq. 2.68}$$

Here k_f refers to the thermal conductivity of the fluid, while $\left. \frac{\partial T}{\partial y} \right|_{y=0}$ refers to the temperature

gradient through the thermal boundary layer. Applying Newton's Law of Cooling and rearranging yields an expression for the local heat transfer coefficient, h' :

$$h' = \frac{-k_f \left. \frac{\partial T}{\partial y} \right|_{y=0}}{(T_s - T_f)} \quad \text{Eq. 2.69}$$

The thermal conductivity of the fluid, k_f , and the temperature of the fluid, T_f , are constant, at least in relation to the thermal boundary layer. Because the fluid thermal conductivity and temperature difference are constant and because the thickness of the thermal boundary layer is increasing with increasing distance from the leading edge, the temperature gradient of the thermal boundary layer must decrease as the boundary layer thickness increases. Thus, thermal effects extend more deeply into the fluid stream with increasing distance from the leading edge of the surface, but the magnitude of the thermal flux and heat transfer coefficient decrease. The thermal boundary layer is illustrated in Figure 2.8.

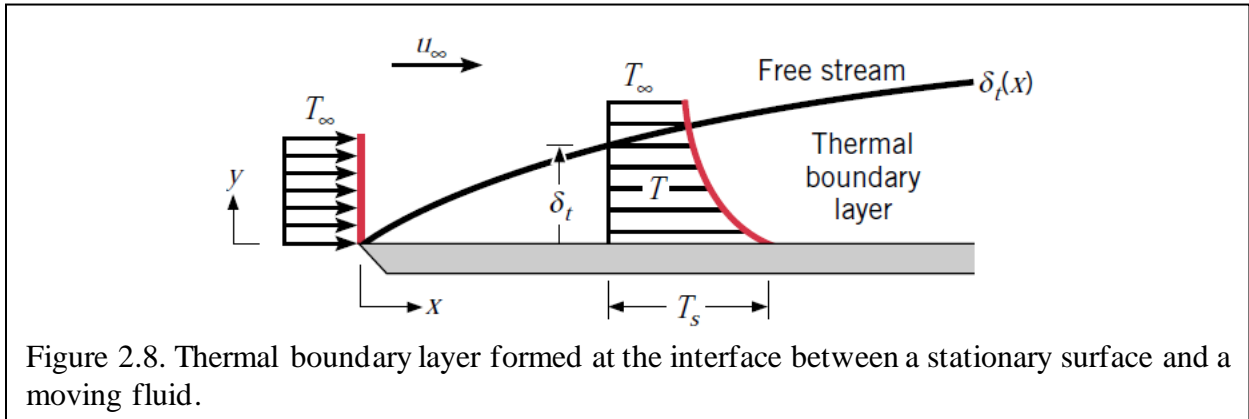


Figure 2.9 shows the mass transfer layer formed at the interface between the moving fluid and the solid surface. This boundary layer forms because at this interface the concentration of a species in the fluid at the surface, $C_{A,s}$, differs from that of the free stream, $C_{A,f}$. The thickness of this layer is determined by ratio of concentration differences as follows:

$$\frac{(C_{A,s} - C_A)}{(C_{A,s} - C_{A,f})} = 0.99 \quad \text{Eq. 2.70}$$

Here $C_{A,r}$ refers to the concentration of species A at a height, y , from the solid surface. An analogue to Fourier's Law, Fick's Law describes the molar flux, N_A'' , as follows [49], [51]:

$$N_A'' = -D_{AB} \frac{\partial C_A}{\partial y} \quad \text{Eq. 2.71}$$

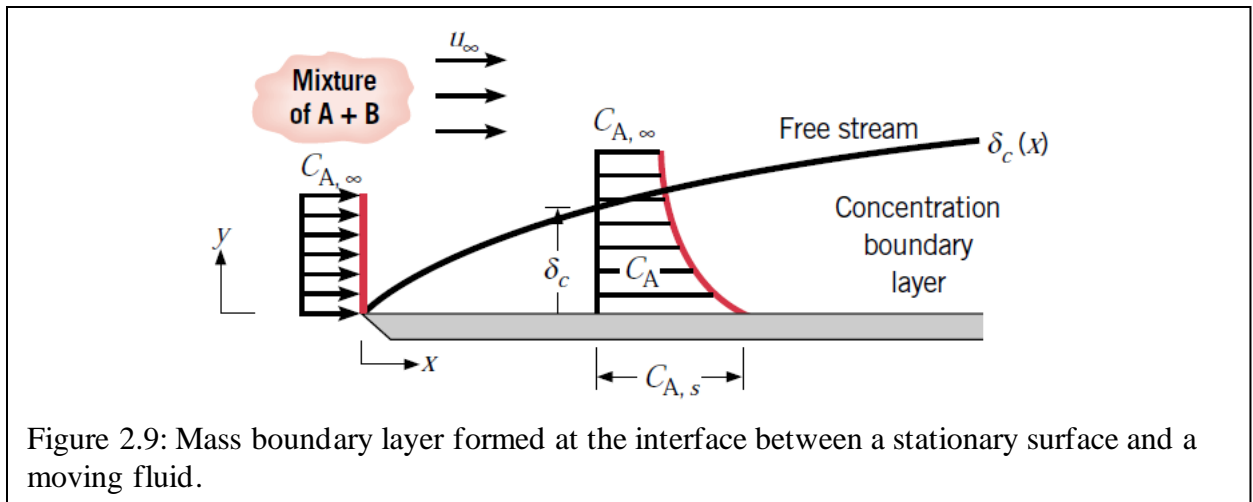
Here, D_{AB} is the binary diffusion coefficient, a property of the material of the species in question, and $\frac{\partial C_A}{\partial y}$ is the concentration flux through the concentration boundary layer. Within this boundary layer, transfer of the species within the fluid takes place via both diffusion and fluid motion, but at the interface between the solid surface and the fluid there is no fluid motion so all species transfer must take place through diffusion. Since there can be no species flux at the interface, the species flux is defined such that:

$$N_A'' = -D_{AB} \left. \frac{\partial C_A}{\partial y} \right|_{y=0} \quad \text{Eq. 2.72}$$

And a convection mass transfer coefficient may be defined as:

$$h_m = \frac{-D_{AB} \left. \frac{\partial C_A}{\partial y} \right|_{y=0}}{C_{A,s} - C_{A,f}} \quad \text{Eq. 2.73}$$

This mass transfer may also be expressed on a mass basis rather than a molar mass basis as:



$$n_A'' = -D_{AB} \frac{\partial \rho_A}{\partial y} \quad \text{Eq. 2.74}$$

$$h_m = \frac{-D_{AB} \frac{\partial \rho_A}{\partial y} \Big|_{y=0}}{\rho_{A,s} - \rho_{A,f}} \quad \text{Eq. 2.75}$$

While a velocity boundary layer and thus surface friction will exist at the interface between a surface and a moving fluid, thermal and concentration boundary layers only exist where there is a thermal or species concentration difference, respectively. All three situations can and do arise simultaneously and although for all three phenomena the boundary layer thickness increases with increasing distance from the leading edge, the thicknesses of these boundary layers do not necessarily increase at the same rate [49].

Laminar and Turbulent Flow: Convective thermal transport at the interface between a moving fluid and a surface is highly dependent on the regularity of the fluid flow at the surface. Highly ordered laminar flow is characterized by clear streamlines in the fluid that can be resolved into parallel and perpendicular components. Although the fluid flow at the leading edge is initially laminar, at some distance from the leading edge this flow begins to transition to

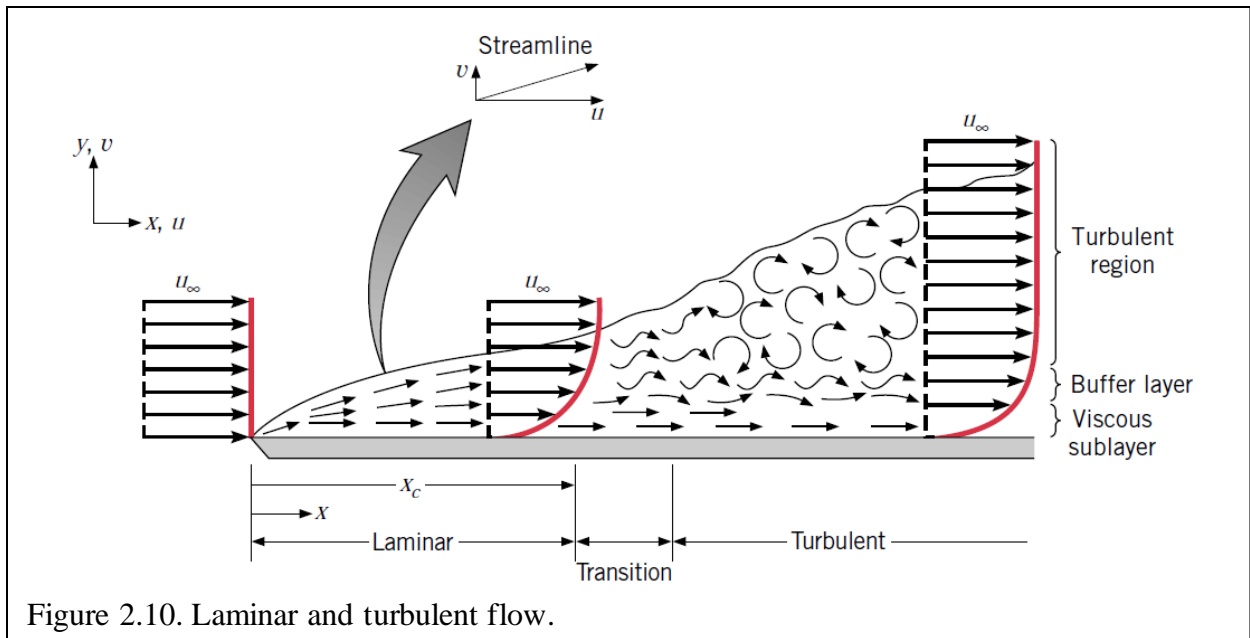


Figure 2.10. Laminar and turbulent flow.

turbulent flow. Fluctuations within the fluid increase throughout this transition region until the entire flow past this point is turbulent. The highly irregular fluid motion of turbulent flow is characterized by significantly greater boundary layer thicknesses, greater wall shear stress, and convective thermal and mass transfer coefficients.

The turbulent boundary layer is comprised of three zones: the laminar sublayer, the buffer layer, and the turbulent zone. Thermal transport in the laminar sublayer is dominated by diffusion, by turbulent mixing in the turbulent zone, and by equal parts diffusion and turbulent mixing within the transition zone. Laminar and turbulent flow in the velocity boundary layer formed by a moving fluid across a stationary flat plate is shown in Figure 2.10.

The dimensionless Reynold's Number relates the dynamic viscosity of the fluid (μ), fluid density (ρ), fluid freestream velocity (u_{free}), to the distance from the leading edge (x). The

Table 2.1. Local coefficients for Laminar Flow Zone Parallel to a Flat Plate.

Variable	Defined as	Locally Equivalent to
C_f	$\frac{\tau_s}{\rho u_{free}^2}$	$0.664 Re_x^{-1/2}$
\bar{C}_f	$\frac{\bar{\tau}_s}{\rho u_{free}^2}$	$1.328 Re_x^{-1/2}$
Nu	$\frac{h'L}{k_f}$	$0.332 Re_x^{1/2} Pr^{1/3}$
\bar{Nu}	$\frac{\bar{h}'x}{k_f}$	$0.664 Re_x^{1/2} Pr^{1/3}$
Sh	$\frac{h_m L}{D_{AB}}$	$0.332 Re_x^{1/2} Sc^{1/3}$
\bar{Sh}	$\frac{\bar{h}_m x}{D_{AB}}$	$0.664 Re_x^{1/2} Sc^{1/3}$
$\frac{\delta_{vel}}{x}$	-	$5 Re_x^{-1/2}$
$\frac{\delta_{conc}}{\delta_{vel}}$	-	$Pr^{-1/3}$
$\frac{\delta_{ther}}{\delta_{vel}}$	-	$Sc^{-1/3}$

Table 2.2. Local Coefficients for Turbulent Flow Zone Parallel to a Flat Plate.

Variable	For Range	Locally Equivalent to
C_f	$5 \times 10^5 < Re_x < 10^7$	$0.0592 Re_x^{-1/5}$
Nu	$0.6 < Pr < 60$	$0.0296 Re_x^{4/5} Pr^{1/3}$
Sh	$0.6 < Sc < 3000$	$0.0296 Re_x^{4/5} Sc^{1/3}$

Reynold's Number ranges from 10^5 to 3×10^6 at the edge of the transition region (x_c), though a representative value of 5×10^5 is typically used to indicate transition from laminar to turbulent flow.

$$Re_{x,c} = \frac{\rho_f u_{free} x_c}{\mu} = 5 \times 10^5 \quad \text{Eq. 2.76}$$

In general, the thermal and hydrodynamic entry lengths for turbulent flow through any duct geometry are shorter than for laminar flows, and the velocity and temperature profiles develop simultaneously. Because of this, the shape of the entrance region strongly influences the hydrodynamic entry length. When $\frac{L}{D_h} > 3$ for $Pr_{air} \approx 0.7$, the correlation of the average local Nusselt number, $\overline{Nu_D}$ is:

$$\frac{\overline{Nu_D}}{Nu_\infty} = 1 + \frac{C'}{\left(\frac{L}{D_h}\right)^{n'}} \quad \text{Eq. 2.77}$$

Table 2.3. Average Coefficient of Friction, Nusselt, and Sherwood Numbers for Turbulent Flow.

Variable	For Range	Locally Equivalent to
$\bar{C}_{f,L}$	$5 \times 10^5 < Re_L \leq 10^8$ $Re_{x,c} = 5 \times 10^5$	$0.074 Re_L^{-1/5}$
\overline{Nu}_L	$0.6 < Pr < 60$ $5 \times 10^5 < Re_L \leq 10^8$ $Re_{x,c} = 5 \times 10^5$	$0.037 Re_L^{4/5} Pr^{1/3}$
\overline{Sh}_L	$0.6 < Sc < 3000$ $5 \times 10^5 < Re_L \leq 10^8$ $Re_{x,c} = 5 \times 10^5$	$0.037 Re_L^{4/5} Sc^{1/3}$

Where C' and n' are constants depending on the geometry of the duct opening, and Nu_∞ is the value of the Nusselt number in the fully developed region. For this study, the opening of the parallel plate ducts will be a straight path, so $C' = 0.9756$ and $n' = 0.760$ [54].

Free Convection: In the absence of moving air, convection takes place via naturally arising buoyant forces. Buoyant forces arise when there is a density gradient and a body force such as gravity acting on a fluid.

For horizontal plates with $T_s < T_{amb}$, the top-side convective thermal transport is inefficient, because the downward moving air is impeded by the plate surface; when $T_s > T_{amb}$, convective thermal transport from the topside of the horizontal surface is much more efficient. The average Nusselt number for the top surface both hot ($T_s > T_{amb}$) and cold ($T_s < T_{amb}$) plates are shown in Table 2.4 below.

Table 2.4. Average Nusselt Numbers for Horizontal Plates.		
Hot/Cold Top-Side Surface	Average Nusselt Number	Ra_L Range
Hot ($T_s > T_{amb}$)	$\overline{Nu}_L = 0.54 Ra_L^{1/4}$	$10^4 \leq Ra_L \leq 10^7$
	$\overline{Nu}_L = 0.15 Ra_L^{1/3}$	$10^7 \leq Ra_L \leq 10^{11}$
Cold ($T_s < T_{amb}$)	$\overline{Nu}_L = 0.27 Ra_L^{1/4}$	$10^5 \leq Ra_L \leq 10^{10}$

In the proposed BIPV-PCM system, the ratio of plate length, L , and plate spacing, b , is large.

For vertical channels with a the average Nusselt number for uniform wall temperatures is:

$$\overline{Nu}_{L,b} = \left[\frac{C'_1}{\left(\frac{Ra_{b,L} b}{L}\right)^2} + \frac{C'_2}{\left(\frac{Ra_{b,L} b}{L}\right)^{1/2}} \right]^{-1/2} \quad \text{Eq. 2.78}$$

And the average Nusselt number for uniform wall flux is:

$$\overline{Nu}_{L,b} = \left[\frac{C'_1}{\frac{Ra_{b,L}^* b}{L}} + \frac{C'_2}{\left(\frac{Ra_{b,L}^* b}{L}\right)^{2/5}} \right]^{-1/2} \quad \text{Eq. 2.79}$$

The constants C'_1 and C'_2 are defined in Table 2.5 for various surface conditions. For $\frac{Ra_{b,L}^* b}{L} \leq 10$ the flow is fully developed within the parallel plate channel, and for $\frac{Ra_{b,L}^* b}{L} \geq 100$ the flow behaves as though each plate is isolated.

The optimal spacing between vertical plates is determined by the balance of upward buoyant forces and opposing viscous forces from the wall surfaces as well as gravitational forces. As the plate spacing decreases, viscous forces increase, which overall decreases the flow rate through the channel and thus decreases the average enthalpy in the channel. For plates with uniform equal temperatures, the optimal heat transfer – and thus the greatest average enthalpy – is found when the spacing of the plates and the plate surface area are balanced. For plates with equal uniform flux, as the spacing, b , decreases, the volumetric heat flux continually increases. Complications arise when the wall temperature is restricted, such that keeping T_w values below set limits also limits how small the b spacing is. The optimal spacing for isoflux plates is defined as the spacing that maximizes the heat dissipation per unit ΔT , where $\Delta T = T_s(L) - T_{amb}$ [49].

Table 2.5. Parallel Plate Natural Convection Constants and Optimal Spacing.

Surface Condition	C'_1	C'_2	b_{opt}
Isothermal plates, equal temperatures	579	2.87	$2.71 \left(\frac{Ra_{b,L}}{b^3 L} \right)^{-1/4}$
Isoflux plates, equal fluxes	48	2.51	$2.12 \left(\frac{Ra_{b,L}^*}{b^4 L} \right)^{-1/5}$

Mixed Free and Forced Convection: In many real-world situations the effects of both natural and forced convection are relevant. Typically, when $\frac{Gr_L}{Re_L^2} \gg 1$ free convection can be neglected, while when $\frac{Gr_L}{Re_L^2} \ll 1$ forced convective effects can be ignored. When $\frac{Gr_L}{Re_L^2} \approx 1$ both free and forced effects are relevant. Three main cases have been identified: assisted (parallel) flow, opposing (antiparallel) flow, and transverse (perpendicular) flow. For opposing flows,

buoyancy effects act to oppose convective motion thereby decreasing the thermal transfer rate. In both assisted and transverse flows, buoyancy effects enhance heat transfer. To a first approximation, the Nusselt number for mixed free and forced convection for assisted and opposing flow on vertical or inclined plates is [49], [54], [55]:

$$Nu_{mix}^3 = Nu_{forced}^3 \pm Nu_{free}^3 \quad \text{Eq. 2.80}$$

Assisted flow is characterized by the sum of the cubed free and forced Nusselt numbers, while opposing flow the difference. Horizontal plates experiencing transverse flows are described with a very similar equation:

$$Nu_{mix}^{7/2} = Nu_{forced}^{7/2} \pm Nu_{free}^{7/2} \quad \text{Eq. 2.81}$$

Although buoyancy effects can appreciably enhance thermal transfer for laminar flows, in turbulent flows the effect is negligible [49].

Phase Change

The PCM in the proposed BIPV-PCM system will cyclically undergo melting and freezing over the course of the days and seasons. The liquid to solid phase change will typically take place during periods of darkness. Additionally, only steady state solutions to the thermal equations were sought, so the act of melting is explored here, but not specifically simulated. When a pure material changes phase it remains at a constant temperature until the entire mass of the material has changed phase. Real-world materials are typically not pure, and the materials selected for use in the proposed system are not pure substances, so the abrupt solid-liquid interface model does not accurately model the melting process in the proposed PCM types.

The Mushy Zone: To better model the real-world behavior of the melting PCM, the abrupt melting temperature solid-liquid transition can be modified to be a “mushy zone” which is further split into high liquid fraction and low liquid fraction zones, as shown in Figure 2.11 [47].

Numerical simulation of this phase change would require tracking the moving zone interfaces as well as coupling of the physical processes and continually modifying the mesh to compensate for the changing zones. The fixed grid method is a means of addressing the shifting zones while reducing computing time. The key benefit of the fixed grid method is that the same governing equations can be employed within both phases, with the moving location of the mushy zone determined by the temperature distribution.

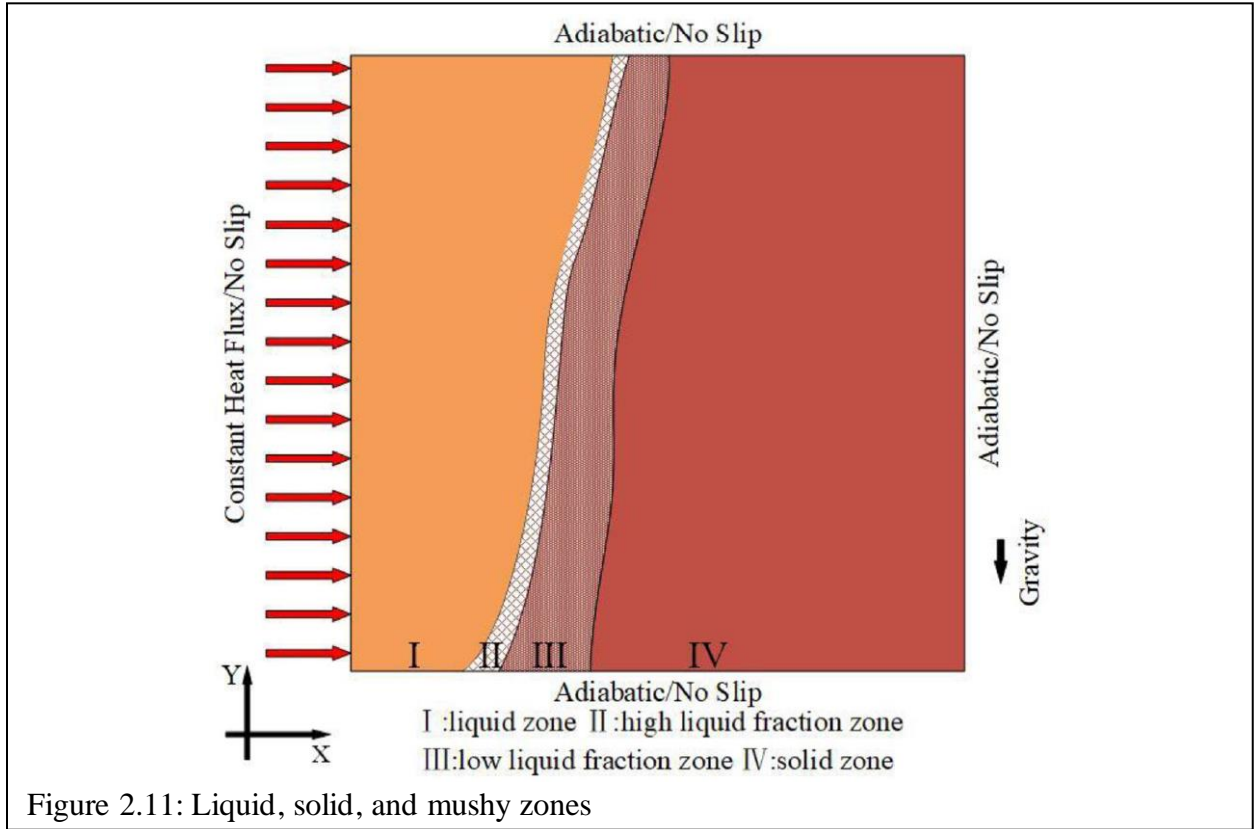


Figure 2.11: Liquid, solid, and mushy zones

The enthalpy-porosity method using the fixed grid method is widely accepted for modeling phase change in non-pure materials. In this method, the mushy zone is modeled as a porous medium. The permeability, K' of the mushy region is expressed as:

$$K' = \frac{l_d^2 \varphi_L^3}{180(1 - \varphi_L)^{m'}} \quad \text{Eq. 2.82}$$

Where φ_L is the temperature dependent liquid fraction, l_d is the length of the dendritic structures in the mushy zone, which for simplicity is assumed to be constant. The constant m' are shared in

Table 2.6 for three possible permeabilities, which deviate significantly in the high liquid fraction zone, but give roughly the same results in the low liquid fraction zone. A mushy zone constant, C_{mush} , is defined as:

$$C_{mush} = \frac{180\mu(1 - \phi_L)^{m'-2}}{l_d^2} \quad \text{Eq. 2.83}$$

Although the width of the mushy zone waxes and wanes, initially conduction through the more solid regions dominates before convective transport takes over as the main vehicle for thermal transport [47].

Table 2.6: Permeability variants and associated constants.

Permeability (K')	Permeability Constant (m')
1	2
2	4/3
3	1

The Improved Enthalpy-Porosity Method: In the improved enthalpy-porosity method, the high liquid fraction is modeled as a mushy fluid in which small portions of the solid separate from the bulk and become suspended in the liquid before dissolving completely. Thus, to eliminate the high degree of variation from the different m' values, the high liquid fraction zone is modeled as a homogeneous mixture. The continuity equation is then:

$$\frac{\partial u_f}{\partial x} + \frac{\partial v_f}{\partial y} = 0 \quad \text{Eq. 2.84}$$

In the low liquid fraction and the solid region, the momentum equations in the x - and y -directions, respectively, may be expressed as:

$$\frac{\partial}{\partial t}(\rho_f u_f) + \nabla \cdot (\rho_f u_f \vec{u}_f) = \nabla \cdot (\mu_L \nabla u_f) - \frac{\partial p_f}{\partial x} - C_{mush} u_f \frac{(1 - \phi_L)^2}{\phi_L^3 + \delta'} \quad \text{Eq. 2.85}$$

$$\frac{\partial}{\partial t}(\rho_f v_f) + \nabla \cdot (\rho_f v_f \vec{u}_f) = \nabla \cdot (\mu_L \nabla v_f) - \frac{\partial p_f}{\partial y} - C_{mush} v_f \frac{(1 - \phi_L)^2}{\phi_L^3 + \delta'} + \frac{\rho_f g \beta (i - i_{ref})}{c_p}$$

Eq.2.86

For the high liquid fraction and liquid regions, the momentum equations in the x - and y -directions are:

$$\frac{\partial}{\partial t}(\rho_f u_f) + \nabla \cdot (\rho_f u_f \vec{u}_f) = \nabla \cdot (\mu_b \nabla u_f) - \frac{\partial p_f}{\partial x} \quad \text{Eq.2.87}$$

$$\frac{\partial}{\partial t}(\rho_f v_f) + \nabla \cdot (\rho_f v_f \vec{u}_f) = \nabla \cdot (\mu_b \nabla v_f) - \frac{\partial p_f}{\partial y} + \frac{\rho_f g \beta (i - i_{ref})}{c_p} \quad \text{Eq.2.88}$$

The modified viscosity, μ_b is defined as:

$$\mu_b = \mu_L (1 - \varphi_s - 1.16 \varphi_s^2)^{-2.5} \quad \text{Eq.2.89}$$

Finally, the energy equation is:

$$\frac{\partial}{\partial t}(\rho_f i) + \nabla \cdot (\rho_f i \vec{u}_f) = \nabla \cdot \left(\frac{k \nabla i}{c_p} \right) - \frac{\partial}{\partial t}(\rho_f \varphi_L i_f) - \nabla \cdot (\rho_f \varphi_L i_f \vec{u}_f) \quad \text{Eq.2.90}$$

Enthalpy is related to temperature via the following expression:

$$C_p = \left. \frac{di}{dT} \right|_p \quad \text{Eq.2.91}$$

Or, for the phase change modeling:

$$i = C_p T \quad \text{Eq.2.92}$$

The liquid fraction can be described as follows:

$$\varphi_L = \begin{cases} 0, & T \leq T_s \\ \frac{T - T_s}{2\Delta T_r}, & T_s < T < T_L \\ 1, & T \geq T_L \end{cases} \quad \text{Eq.2.93}$$

The center of the melting range is $T_{mid} = \frac{T_L + T_s}{2}$, and the effective radius of the temperature is

$$\Delta T_r = \frac{T_L - T_s}{2}.$$

At the beginning of melting, the mushy fraction increases rapidly because the bulk of the thermal transport is carried out via conduction. As the mushy region grows and the liquid

fraction begins to dominate the development of the mushy zone slows as more latent heat is absorbed for phase change. When the liquid fraction is below 20% conductive effects dominate, but as the liquid fraction grows from 20% to 100% of the cavity the natural convective effects grow stronger. As natural convection intensifies, the Rayleigh number increases, thereby accelerating the rate at which thermal energy is transported from the higher temperature liquid side of the PCM channel. Under more intense convective transport the shape of the melting front is deformed and more inclined as the width of the mushy zone begins to vary.

Summary

This chapter has developed the mathematical basics for conduction, radiation, convection, and melting phase change. Because only the steady state solution of the developed model is sought, much of the nuance and detail described in this chapter are not applied. However, the deep understanding developed through this mathematical analysis of thermal transport form the basis for the three-box model developed in later chapters.

Table 2.7. Variables and Constants Used in Chapter 2.

Variable or Constant	Name	Units
A, A_s	Area, Surface Area	m^2
α	Thermal Diffusivity	$\frac{\text{m}^2}{\text{s}}$
α'	Total Absorptivity	-
$\alpha'_\lambda, \alpha'_\lambda(\lambda)$	Spectral Absorptivity	
c_0	Speed of Light	$\frac{\text{m}}{\text{s}}$
C_1	First Radiation Constant	$\frac{\text{W} \cdot \mu\text{m}^4}{\text{m}^2}$
C_2	Second Radiation Constant	$\mu\text{m} \cdot \text{K}$
C_3	Third Radiation Constant	
$C_{A,f}$	Molar Concentration of Fluid	$\frac{\text{kmol}}{\text{m}^3}$
$C_{A,s}$	Molar Concentration of Solid	
C_f	Coefficient of Friction, Fanning Friction Factor, Friction Factor	-
C_p	Specific Heat Capacity	$\frac{\text{J}}{\text{kg} \cdot \text{K}}$

Table 2.7. Variables and Constants Used in Chapter 2 (continued).

Variable or Constant	Name	Units
D_{AB}	Binary Diffusion Coefficient	m^2
\dot{E}_g	Rate of Energy Generated	W
\dot{E}_{in}	Rate of Energy In	
\dot{E}_{out}	Rate of Energy Out	
\dot{E}_{st}	Rate of Energy Stored	
$E_\lambda(\lambda)$	Spectral Emissive Power	
$E_{\lambda,b}(\lambda, T)$	Spectral Emissive Power of Blackbody Emitter	
$E_b, E_b(T)$	Total Emissive Power of Blackbody Radiation	
$E, E(T)$	Total Emissive Power	
E'	Earth's Total Emissive Power	
ε	Emissivity	-
ε'	Earth's Total Emissivity	
$\varepsilon_{\lambda,\theta}, \varepsilon_{\lambda,\theta}(\lambda, \theta, \phi, T)$	Spectral Directional Emissivity	
f	Eccentricity	
$G_\lambda, G_\lambda(\lambda)$	Spectral Irradiation	$\frac{W}{m^2}$
$G_{\lambda,abs}$	Absolute Spectral Irradiation	
$G_{\lambda,refl}, G_{\lambda,refl}(\lambda), G_{refl}$	Reflected Spectral Irradiation	
$G_{\lambda,trans}$	Transmitted Spectral Irradiation	
$G_{S,0}$	Extraterrestrial Solar Irradiation	
G_{atm}	Radiation Emitted by Earth's Atmosphere	$\frac{W}{m^2}$
G_r	Grashof Number	-
h	Planck's Constant	J · s
h'	Local Heat Transfer Coefficient	$\frac{W}{m^2 \cdot K}$
\bar{h}	Average Heat Transfer Coefficient	
h_m	Local Mass Transfer Coefficient	
\bar{h}_m	Average Mass Transfer Coefficient	
i	Enthalpy	$\frac{J}{K}$
I_b	Total Intensity of Blackbody Radiation	$\frac{W}{sr}$
$I_{\lambda,b}(\lambda, T)$	Spectral Intensity of Emitted Radiation by Blackbody	
$I_{\lambda,e+r}(\lambda, \theta, \phi)$	Spectral Intensity of Emitted and Reflected Radiation	
$I_{\lambda,i}, I_{\lambda,i}(\lambda, \theta, \phi), I_{\lambda,i}(\lambda)$	Spectral Intensity of Incident Radiation	

Table 2.7. Variables and Constants Used in Chapter 2 (continued).

Variable or Constant	Name	Units
$I_{\lambda,e}, I_{\lambda,e}(\lambda, \theta, \phi), I_{\lambda,e}(\lambda)$	Spectral Intensity of Emitted Radiation	$\frac{W}{m^2 \cdot sr \cdot \mu m}$
k	Thermal Conductivity	$\frac{W}{m \cdot K}$
k_e	Free Electron Thermal Conductivity	
k_f	Fluid Thermal Conductivity	
k_l	Lattice Thermal Conductivity	
k_B	Boltzmann Constant	$\frac{J}{K}$
K'	Permeability of Mushy Region	-
λ	Wavelength	m
L	Characteristic Surface Length	
L_0	Lorenz Number	$\frac{W \cdot \Omega}{K^2}$
l_d	Length of the Dendritic Structures	m
m'	Permeability Constant	-
μ	Dynamic Viscosity	$\frac{N \cdot s}{m^2}$
μ_b	Modified Fluid Viscosity	
μ_f	Fluid Viscosity	
N_A	Moles of Substance A	mol
N_A''	molar flux at the surface	$\frac{mol}{m^2 s}$
n_A	Mass Transfer Rate	$\frac{kg}{s}$
n_A''	Mass Flux	$\frac{kg}{m^2 s}$
Nu	Nusselt Number	-
\overline{Nu}	Average Nusselt Number	
ν	Wave Frequency	$\frac{1}{s}, Hz$
\vec{q}''	Heat Flux Vector	$\frac{W}{m^2}$
q''	Heat Flux	
\dot{q}	Rate of Energy Generated Within the Differential Volume	$\frac{W}{m^3}$
q	Heat Transfer Rate	W
$Re_{x,c}$	Reynold's Number at the Transition Region	-
ρ	Density	$\frac{kg}{m^3}$
ρ_e	Electrical Resistivity	$\Omega \cdot m$
ρ_0	Resistivity Due to Lattice Imperfections	
ρ'	Intrinsic Resistivity	

Table 2.7. Variables and Constants Used in Chapter 2 (continued).

Variable or Constant	Name	Units
$\rho_{A,f}$	Density of Fluid	$\frac{\text{kg}}{\text{m}^3}$
$\rho_{A,s}$	Density of Surface	
σ	Stefan-Boltzmann Constant	$\frac{\text{W}}{\text{m}^2\text{K}^4}$
ϱ	Total Reflectivity	-
$\varrho_{\lambda}(\lambda)$	Spectral Reflectivity	
$\varrho_{\lambda,i}(\lambda, \theta, \phi)$	Incident Spectral Reflectivity	
$\varrho_{\lambda,\theta}, \varrho_{\lambda,\theta}(\lambda), \varrho_{\lambda,\theta}(\lambda, \theta, \phi)$	Reflectivity	
S_c	Solar Constant	$\frac{\text{W}}{\text{m}^2}$
T	Temperature	K, °C
T_{amb}	Ambient Temperature	
T_f	Fluid Temperature	
T_s	Surface Temperature	
T_{sky}	Sky Temperature	
T_{surr}	Temperature of Surroundings	
ΔT_r	Effective Radius of the Temperature	
τ_s	Surface Shear Stress	$\frac{\text{N}}{\text{m}^2}$
φ_L	Temperature Dependent Liquid Fraction	-
u_f	Fluid Speed in the x-direction	$\frac{\text{m}}{\text{s}}$
u_{free}	Fluid Free Stream Velocity	
v_f	Fluid Speed in the Y-Direction	
x_c	Location of Transition Region Edge	m
ζ	Total Transmissivity	-
ζ_{λ}	Spectral Transmissivity	

III. THE BIPV-PCM MICROFACILITY AND ENVIRONMENT

In this chapter the BIPV-PCM microfacility, as well as severe weather events and high temperature environments are described in more detail. This chapter starts with a discussion of the factors which directly influence PV output, followed by detailing the types of severe weather events that most influence these factors and how they will be modeled in this work, and concludes with a discussion of the relevant variables and constants.

Factors Influencing PV Performance

Although the effects of climate change are far-reaching, in this work the focus is exclusively upon those environmental effects which directly influence PV output. For the purposes of this work, the environmental effects and weather events included are limited to those which most directly influence PV performance and thus the overall performance of the BIPV-PCM facility. The following sections quantify the amount and angle of incident sunlight reaching the PV panel, cloud cover and humidity, wind speed, ambient temperature, and natural degradation of the panel over time and use affect the PV panel output.

Sunlight: The most obvious factor that drives the performance of a PV module is the amount of incident sunlight reaching the panel. However, beyond merely the hourly quantity of sunlight, the intensity and angle of incidence of the light with respect to the PV panel's surface influence the amount of energy generated by the panel. The date, time, latitude, elevation angle, and declination of the sun determine how much sunlight enters Earth's atmosphere, while the PV panel's angle with respect to the incoming light determines how much of the radiation can be absorbed. Cloud coverage and relative humidity also influence the amount of light that reaches the PV panel surface and are discussed in the later sections.

The power emitted by the sun as well as the distance between the earth and sun vary

over the course of a year, causing the radiant power density, G in $\frac{W}{m^2}$, to fluctuate at the surface of Earth's atmosphere. Equation 3.1 describes fluctuation of this radiant power density at the surface of Earth's atmosphere annually as [20]:

$$\frac{G}{G_{const}} = 1 + 0.33 \cos \left(\frac{360^\circ(n_{doty} - 2)}{365 \text{ days}} \right) \quad \text{Eq. 3.1}$$

where G_{const} refers to the solar constant, $1.353 \frac{kW}{m^2}$, and n_{doty} is the day of the year expressed as a number. For example, n_{doty} for the date of August 8th would usually be 220 but would be 221 on leap years. The variation in the incoming solar radiation due to the eccentricity of Earth's orbit is so minor that it's typically ignored, so for this work incoming solar radiation will be taken to be $G = G_{const} = 1.353 \frac{kW}{m^2}$ [20].

The duration of daylight and the path of the sun through the sky are dependent on both the location's latitude as well as the day of year and the time of day. The Local Solar Time (LST) and Local Time (LT) may not always be the same, as local times are influenced by daylight savings time and time zone boundaries. Solar noon is defined as the moment when the sun reaches its highest position in the sky at a given location, date, and time. To correct for the eccentricity of Earth's orbit, an Equation of Time (EoT) is formulated by first defining a Local Solar Time Meridian (LSTM) and linking it to the globally used Universal Coordinated Time (UTC), and the amount the earth rotates in an hour $\left(15^\circ = \frac{360^\circ}{24 \text{ hours}}\right)$ as follows [20]:

$$LSTM = 15^\circ(UTC - LT) \quad \text{Eq. 3.2}$$

The EoT is an empirical equation that is widely accepted in this analysis due to the extremely predictable nature of Earth's orbit [20]:

$$EoT = 9.87 \sin(2B') - 7.53 \cos B' - 1.5 \sin B' \quad \text{Eq. 3.3}$$

Where [20]:

$$B' = \frac{360^\circ}{365 \text{ days}} (n_{doty} - 81) \quad \text{Eq. 3.4}$$

From here a time correction can be determined as [20]:

$$TC = \frac{4 \text{ min}}{1^\circ} (\varphi_{long} - LST) + EoT \quad \text{Eq. 3.5}$$

Next the LST can be found [20]:

$$LST = LT + \frac{TC}{60 \text{ min}} \quad \text{Eq. 3.6}$$

The hour angle (HRA) adjusts this solar time into \pm degree values, which are negative before solar noon (HRA = 0°) and positive afterward. The HRA is expressed as [20]:

$$HRA = 15^\circ (LST - 12) \quad \text{Eq. 3.7}$$

The declination refers to the angle between the celestial plane – the disk in which the planets rotate about the sun – and the equator of the Earth. Because Earth is tilted at an angle of 23.4° relative to the celestial plane, the sun's declination varies from +23.4° to -23.4°, and may be expressed as [20]:

$$\delta_{dec} = -23.4^\circ \cos \left[\frac{360^\circ}{365 \text{ days}} (n_{doty} + 10) \right] \quad \text{Eq. 3.8}$$

The declination reaches its maximum on the summer and winter solstices on June 22 and December 21-22, respectively, and is zero at the equinoxes on March 22 and September 22. This equation does not account for Earth's elliptical orbit or any variation in the output radiation from the sun. The declination angle is also commonly expressed as [20]:

$$\delta_{dec} = 23.4^\circ \sin \left[\frac{360^\circ}{365 \text{ days}} (n_{doty} + 284) \right] \quad \text{Eq. 3.9}$$

Where the reference points used are the equinoxes rather than the solstices. Both Equations 3.8 and 3.9 exhibit less than a 0.3% difference and are considered interchangeable [20].

The elevation angle refers to the height of the sun as measured from the horizontal at a given latitude. In the northern hemisphere, the sun's path through the sky is high during the summer and much lower in the winter, and the further from the equator the more dramatic this effect. At the northern- and southern-most latitudes winters are marked by extremely long nights and days that span hours and summers with the reverse effect. The elevation angle is expressed very simply as a relationship between the declination and the latitude [20]:

$$\alpha_{elev} = 90^\circ + \varphi_{lat} - \delta_{dec} \quad \text{Eq. 3.10}$$

In the northern hemisphere where this study is conducted the latitude is always positive; When Equation 3.10 is greater than 90° the value is subtracted from 180° , or [20]:

$$\alpha_{elev} = 180^\circ - (90^\circ + \varphi_{lat} - \delta_{dec}) = 90^\circ - (\varphi_{lat} - \delta_{dec}) \quad \text{Eq. 3.11}$$

Equation 3.10 is greater than 90° in the northern hemisphere when δ_{dec} ranges from 0 to -23.4° , and the equations can be combined into Equation 3.12 [20]:

$$\alpha_{elev} = 90^\circ \pm (\varphi_{lat} - \delta_{dec}) \quad \text{Eq. 3.12}$$

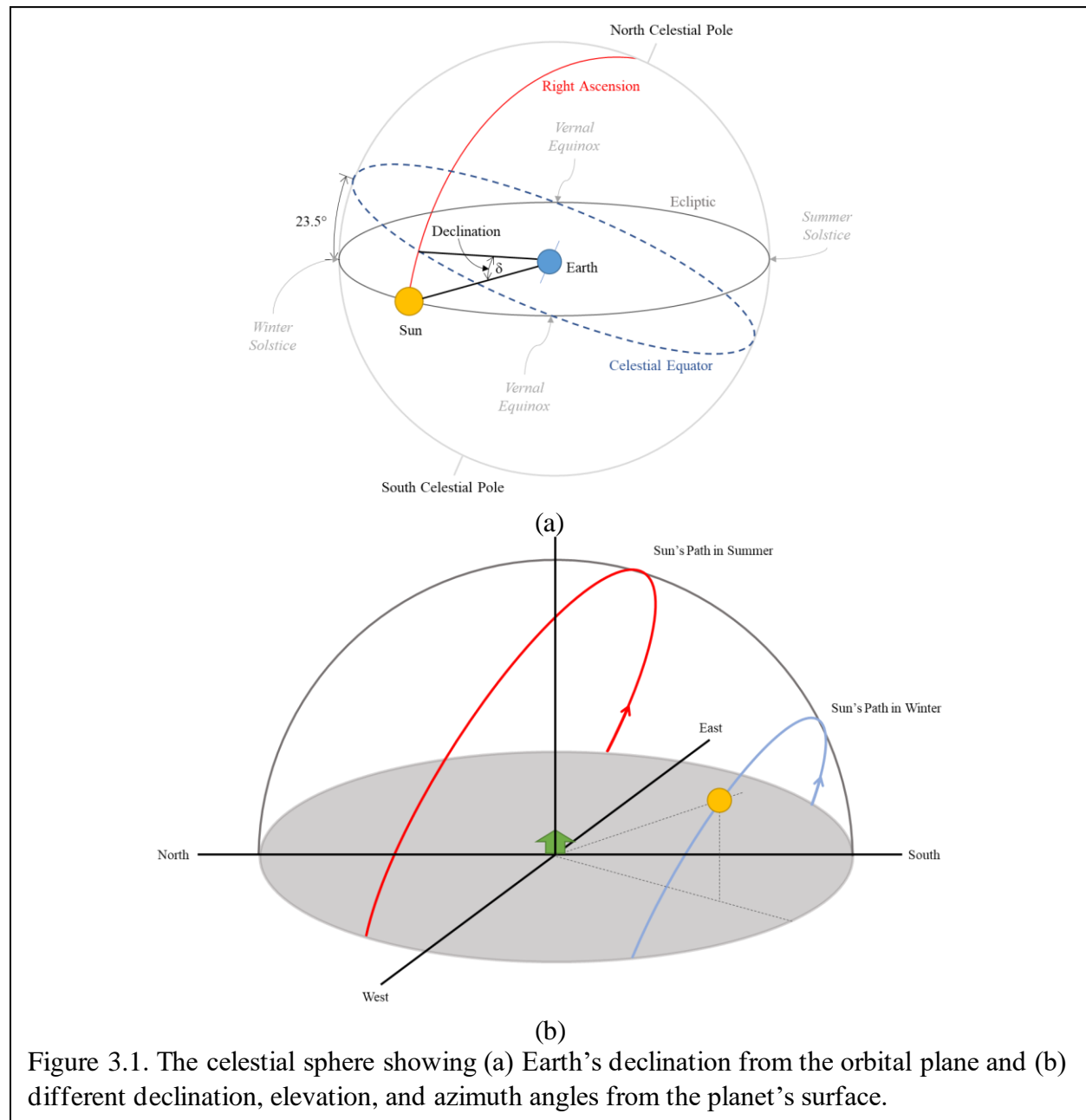
The elevation angle may also be expressed as a function of δ_{dec} , φ_{lat} , and HRA [20]:

$$\alpha_{elev} = \sin^{-1}(\sin \delta_{dec} \sin \varphi_{lat} + \cos \delta_{dec} \cos \varphi_{lat} \cos HRA) \quad \text{Eq. 3.13}$$

The azimuth angle is a measure of the angle from magnetic north to the direction from which the sunlight originates. At the equinoxes the sun rises in exactly due east at 90° from due north and sets exactly due west at 270° from due north. At solar noon on the equinox in the northern hemisphere, the sun is at exactly due south, or 180° from due north. The azimuth angle is calculated as follows [20]:

$$\theta_{Az} = \begin{cases} \text{before solar noon: } \cos^{-1}\left(\frac{\sin \delta_{dec} \cos \varphi_{lat} - \cos \delta_{dec} \sin \varphi_{lat} \cos HRA}{\cos \alpha_{elev}}\right) \\ \text{after solar noon: } 360^\circ - \cos^{-1}\left(\frac{\sin \delta_{dec} \cos \varphi_{lat} - \cos \delta_{dec} \sin \varphi_{lat} \cos HRA}{\cos \alpha_{elev}}\right) \end{cases} \quad \text{Eq. 3.14}$$

The declination, angle of elevation, and azimuth angle determine the total amount of sunlight that strikes the planet and are illustrated in Figure 3.1 [2], [3].



Finally, the amount of sunlight that can be absorbed by the PV panel is dictated by the relative angle between the surface of the PV panel and the angle of the incoming light, as only the perpendicular component of the sunlight can be absorbed by the PV panel. When the incident sunlight and PV panel are exactly perpendicular the maximum amount of radiation can be

absorbed, but as the angle between incident light and the panel surface wanes the radiation absorbed decreases. In this work, panels do not track the passage of the sun and remain fixed in place as part of façade of the facility roof, so the tilt angles of the PV panels on the roof is 0° . Figure 3.2 shows the relationship between the tilt angle, incident sunlight, and the component of this light perpendicular to the panel surface. For the horizontal (0°) roof panels, the component of the solar radiation perpendicular to the PV panel is [20]:

$$G_{roof} = G_{incident} \sin(\alpha_{elev} + 0^\circ) \quad \text{Eq. 3.15}$$

The walls of the BIPV-PCM microfacility are struck by solar radiation as well [20]:

$$G_{Ewall} = G_{incident} \cos(\alpha_{elev} + 90^\circ) = G_{incident} \cos(\alpha_{elev}) \quad \text{Eq. 3.16}$$

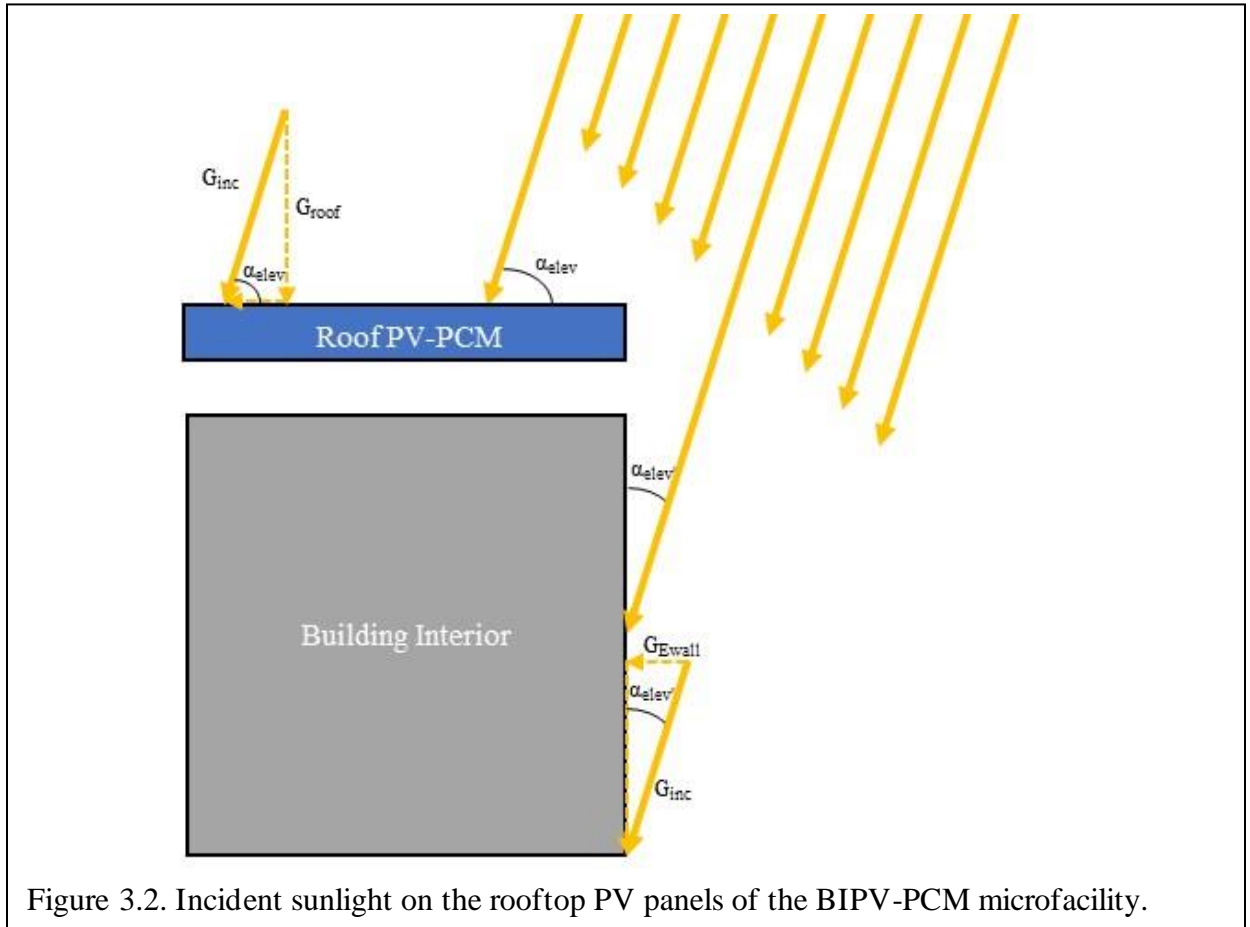


Figure 3.2. Incident sunlight on the rooftop PV panels of the BIPV-PCM microfacility.

The expressions developed in this section determine the total possible amount of sunlight that can reach the rooftop PV panels and the facility walls and represent the maximum possible

solar radiation that may be absorbed by the panels and exterior walls of the BIPV-PCM microfacility. However, environmental factors may reduce the amount of solar radiation that strikes the BIPV-PCM microfacility as well.

Cloud Cover: Once incoming sunlight reaches Earth's atmosphere, portions of this incident sunlight are blocked or scattered away by clouds, smoke particulates, water vapor, and so on before the remaining radiant energy is absorbed by the panel and transformed into heat and electricity. In Chapter 2 the concepts of atmospheric absorption and scattering among other phenomena were discussed at length. Typically, the average throughput of light through the atmosphere, $G_{incident}$, is taken to be 70% of the total radiation, G , at the surface of Earth's atmosphere due to absorption, scattering, and other typical atmospheric effects [20].

Local cloud cover in an area directly impacts the quantity and power of the incoming sunlight. Cloud cover is expressed using oktas, a unit of measurement that describes how many eighths of the sky are covered by clouds at a given location [58]. Cloud coverage ranges from 0 oktas for perfectly clear skies, 1 okta for coverage greater than 0 but less 10% cloud coverage to 8 oktas for 100% overcast skies [58]. The breakdown between oktas is uneven and half-oktas are used in this work to better approximate the effect of cloud coverage on solar radiation to the PV panel. The breakdown of oktas used in this simulation is shown in Table 3.1.

This okta measurement system can be used to generate a proportionality constant that indicates the fraction of incident sunlight that reaches the PV panel. For a partly cloudy sky measured at 3 oktas the cloud coverage is 40%, which means that 60% of incident solar radiation reaches the panel surface. This can be expressed simply as:

$$G_{cc} = (1 - n_{cc})G_{incident} \quad \text{Eq. 3.17}$$

where G_{cc} is the radiation that reaches the panel through the cloud cover and n_{cc} is the decimal

percentage of cloud cover blocking incoming radiation. To account for the okta measurements with and without variation in the percent cloud coverage, the decimal percentage spread of the variation, Δn , the base minimum cloud coverage for that okta value, n_{base} , and a random number between 0 and 1, n_{rand} , make up the n_{cc} expression:

$$n_{cc} = n_{base} + n_{rand}\Delta n \quad \text{Eq. 3.18}$$

For example, at 2 oktas the cloud coverage ranges between 20% and 30% (0.2 – 0.3) so the radiation that reaches the PV panel, G_{cc} , ranges from 70% to 80%. Thus, when NOAA data shows 2 oktas of cloud coverage, the base minimum amount of cloud coverage, $n_{base} = 0.2$, cloud coverage varies between 20% and 30% so $\Delta n = 0.1$, and for this case Eq. 3.17 becomes:

$$G_{cc} = (1 - n_{cc})G_{incident} = (1 - [n_{base} + n_{rand}\Delta n])G_{incident} \quad \text{Eq. 3.19}$$

Although oktas are often measured in more recent data, this specific measure of cloud cover is frequently not included in historical data. Instead, historical data includes a measure of the vertical distance from the surface to atmospheric obstructions which obscure 5/8 (or 5 – 8 oktas for this work) or more of the sky, with a vertical distance of 22,000 meters used to denote clear skies. The expression in Equation 3.19 can be modified to reflect a random variation in cloud cover between 5 and 8 oktas of total sky coverage for any vertical distance measurement of

Table 3.1. Cloud Coverage in Oktas

Number of Oktas	Cloud Coverage Fraction	Decimal Percent Ranges n_{cc}		Δn	n_{base}
0	0/10	0.0		-	0
1	1/10 or less but not 0	0	0.1	0.1	0
2	2/10 to 3/10	0.2	0.3	0.1	0.2
3	4/10	0.4	0.4	0	0.4
4	5/10	0.5	0.5	0	0.5
5	6/10	0.6	0.6	0	0.6
6	7/10 to 8/10	0.7	0.8	0.1	0.7
7	9/10 but less than 10/10	0.9	1	0.1	0.9
8	10/10	1		-	1

less than 22,000 meters. Thus, $n_{cc} = 0$ when the visibility value is 22,000 so $G_{cc} = G_{incident}$, and for any other value, G_{cc} is expressed as:

$$G_{cc} = (1 - [0.6 + 0.4 n_{rand}])G_{incident} \quad \text{Eq. 3.20}$$

Relative Humidity: Relative humidity (RH) is expressed as a percentage value which is the ratio of the water vapor's partial pressure to the equilibrium vapor pressure of water at the same temperature [58]. Relative humidity influences the behavior of a PV panel by both contributing to greater local scattering of incident solar radiation, as well as decreasing the rate by which the panel can shed thermal energy via convection because more water vapor rich air stores thermal energy. Few studies have been performed that specifically investigate the effects of high humidity on PV panels or quantify this effect in a meaningful way, apart from Kazem [59] and Touati et al [60], who studied the effects of relative humidity (RH) on PV panels.

Kazem studied PV panels which were oriented for optimal power generation in Sohar in the Al Batinah North governance of Oman, a region characterized by exceptionally high RH during the months of July through September. In this time period, RH ranges from about 75% to just over 90% RH. Kazem found that as RH increases the incident solar radiation at the panel surface decreases due to local scattering. Furthermore, Kazem found that for Sohar where temperatures rarely exceed 35°C, RH effects tended to dominate over temperature effects. In this study, Kazem successfully verified there is a correlation between RH and PV panel output but did not specifically quantify this effect. Kazem's data indicate that a simple linear fit is reasonable, as shown in Equation 3.21. The linear relationship between RH and PV panel output for mild temperatures (< 35°C) and high RH (> 70%) used in this work is based on Kazem's reported data and is expressed:

$$P_{out} = -2.02RH + 242 \quad \text{Eq. 3.21}$$

To transform this analysis to efficiency, this output power is compared to a constant maximum output power under ideal conditions of 125W, yielding a similar expression for the PV panel efficiency as a function of the RH:

$$Efficiency = -1.62RH + 194 \quad \text{Eq. 3.22}$$

In 2013, Touati et al compared the behavior of monocrystalline and amorphous silicon PV panels oriented for optimal power output in Dota of Qatar. They found that PV efficiency decreased with increasing panel temperature as well as with increasing RH. Touati et al. were able to quantify the decrease in panel efficiency as a function of RH and panel temperature as shown in Table 3.2. Their findings indicate that the effects of both panel temperature and RH are more pronounced with amorphous silicon PV than with monocrystalline silicon PV, and temperature is a more dominant factor than RH for panel efficiency for the measured ranges of temperature and RH. In Touati's study, temperatures lower than 40°C and RH lower than 22% were not measured.

Table 3.2. The effect of relative humidity and ambient temperature changes for silicon PV panels.		
Type of Silicon PV Panel	Change in Efficiency per 1°C Change in Panel Temperature over 25°C	Change in Efficiency per 1% Change in RH
Monocrystalline	-0.15%	-0.06%
Amorphous	-0.43%	-0.18%

Relative humidity decreases the amount of incoming sunlight due to the presence of water vapor molecules which scatter the light in all directions equally. As the amount of water vapor in the air increases, the amount of scattering in all directions increases thus overall decreasing the total amount of light that reaches the panel surface. Temperature effects inhibit the behavior of the charge carriers in the semiconductor materials that make up the PV panel itself and are not a result of decreased incident radiation. Thus, when RH is very high, less light reaches the panel to be converted into electricity, while very high temperatures can decrease PV

performance even in otherwise perfect lighting conditions.

Kazem and Touati's findings support this reasoning, as Kazem found that the effects of RH dominate over those of temperature when the RH is very high ($> 70\%$) but the temperature is not ($< 35^\circ\text{C}$), while Touati found that temperature effects dominate at ambient temperatures over 40°C and lower RH ($< 28\%$). This suggests that very high humidity decreases the amount of useful light available to the panel, while very high temperatures reduce performance due to limitations in the semiconductor regardless of the amount of light scattering. In temperature ranges that will negatively affect PV performance combined with RH ranges that scatter a noticeable quantity of light from the panels, the combined effects of poorly performing semiconductors and reduced light decrease PV performance more than any one effect acting on its' own. For the purposes of this work, Touati's 0.06% decrease in PV panel efficiency change for every percent change of RH will be used at all temperatures when pre-processing real-world data.

In the historical data used to construct real-world data sets, the RH is not explicitly recorded and so is calculated directly from the dew point and the ambient temperature. The relationship between temperature (T , in $^\circ\text{C}$), dew point (T_{dew} , in $^\circ\text{C}$), and relative humidity (RH , expressed as a percentage) is well-known. Numerous calculators are available on the Internet, including from the National Oceanic and Atmospheric Administration (NOAA) [61], and the expression for RH is [62]:

$$RH = 100\% \frac{\exp\left(\frac{17.625T_{dew}}{243.04 + T_{dew}}\right)}{\exp\left(\frac{17.625T}{243.04 + T}\right)} \quad \text{Eq. 3.24}$$

Ambient Temperature: The open circuit voltage, V_{oc} , of a PV cell is highly dependent on temperature, primarily due to the strong temperature dependence of the dark saturation current, I_0 . As the temperature increases, the dark saturation current increases because of the increased carrier concentration. As shown previously, as I_{sc} increases, V_{oc} decreases, so as panel temperature increases the output power decreases [20]. The PV module efficiency is related to the short circuit current, open circuit voltage, and fill factor quantifying the maximum output power via this expression:

$$\eta = \frac{P_{mp}}{P_{in(solar)}} = \frac{I_{sc} V_{oc} FF}{P_{in(solar)}} \quad \text{Eq. 3.25}$$

As the ambient temperature increases, V_{oc} decreases and I_{sc} increases but to a lesser degree than V_{oc} . The FF also decreases as V_{oc} decreases since the maximum possible area under the IV curve must decrease. For every 1°C of temperature increase over 25°C the efficiency of the PV panel decreases by 0.08% and its overall power output decreases by 0.45% [20], [38], and for the purposes of this work these factors will be treated as constants which do not vary under different environmental conditions.

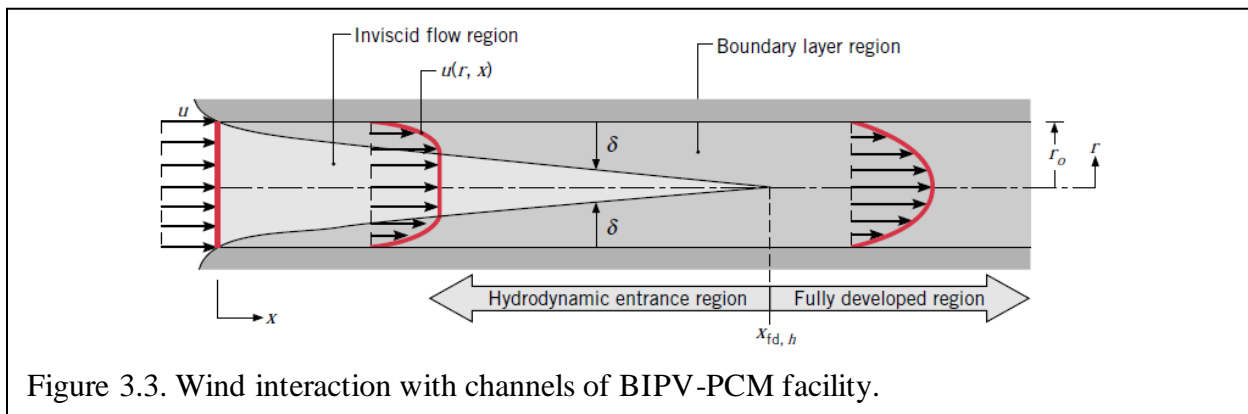
In this work, rising temperature effects are a key motivation behind investigating the BIPV-PCM microfacility. Although the rise of global temperatures and increasingly frequent heat waves are unavoidable, mitigating these effects is necessary to continually draw useful power from the PV panels. PCM aids in thermal management by absorbing thermal energy to change the phase of the PCM, acting as a heat sink. Building integration of the PV-PCM aids thermal management by providing a channel through which warmed air may be expelled from the system or redirected into the facility to maintain interior temperatures during cold seasons. Further specifications on the spacing and orientation of the BIPV facility as well as the PCM are covered in later sections.

Wind: Wind benefits the BIPV-PCM facility by helping remove warmed air and cool the system. Wind may interact with the surfaces of the PV panels on the roof and the exterior walls of the facility, as well as move freely through the channel between the PV-PCM and the building exterior. Convective thermal transport can be natural, forced, or a combination of the two as discussed in Chapter 2, and the overall convection coefficient on the exterior surfaces is typically a combination of the natural and forced convection coefficients. For simplification purposes, the exact means of attaching and integrating the PV panels into the exterior of the facility are neglected, and all air flow within the channel between the PV-PCM and the building is presumed to be turbulent. No fans or other means to create continuous forced convection in the channel are employed, so in the absence of wind only free convection takes place at the surfaces and within the channels.

Wind passing along the roof of the facility will draw thermal energy away from the system regardless of the direction of the wind, so any incident wind will have a net cooling effect on the roof surface. Wind striking the walls of the system more effectively removes thermal energy when the wind direction is parallel to the wall surface, and the maximum amount of thermal energy is removed when the wind direction is exactly parallel to the building wall. Wind direction perpendicular to the wall surface will result in the air passing around and over the facility and will virtually not interact with the opposing wall surface at all. Thus, wind direction has no appreciable effect on convective thermal transport on the roof of the facility, and wind speed is the key factor driving forced convective transport [49].

Similarly, wind coming from any direction will induce thermal transport within the channel between the roof PV panel and the building roof, while the direction of the wind strongly influences how rapidly thermal energy is removed from the system through the East and

West wall channels. Wind direction parallel to the wall channels induces the maximum air flow through the channel while wind passing across (perpendicular to the wall surfaces) does not appreciably influence airflow within the channel. When the incident wind is between perpendicular and parallel to the channel length, some component of the wind is parallel to the channel and this portion of the wind induces forced convection through the channel. Figure 3.3 shows the entry and fully developed regions within the channel between the PV-PCM and the building façade.



Panel Degradation: Panel degradation is influenced by a variety of weathering factors including incident sunlight, dust, high temperatures, and relative humidity. Specifying the degree to which each of these complex and perpetually evolving factors influence PV output and efficiency over time is an area of ongoing research. PV panels exposed to long periods of high temperatures and high relative humidity have been observed to degrade more rapidly than panels not exposed to these environmental conditions. A constant efficiency degradation rate, R_d , of 0.95%/year may be applied, based on the findings of Phinikarides et al for crystalline silicon PV panels [63].

Extreme Weather Analysis

Historical weather patterns from 1970 – 2015 were used to create sets of baseline real-world weather patterns. Annual weather data from different individual years or spans of years

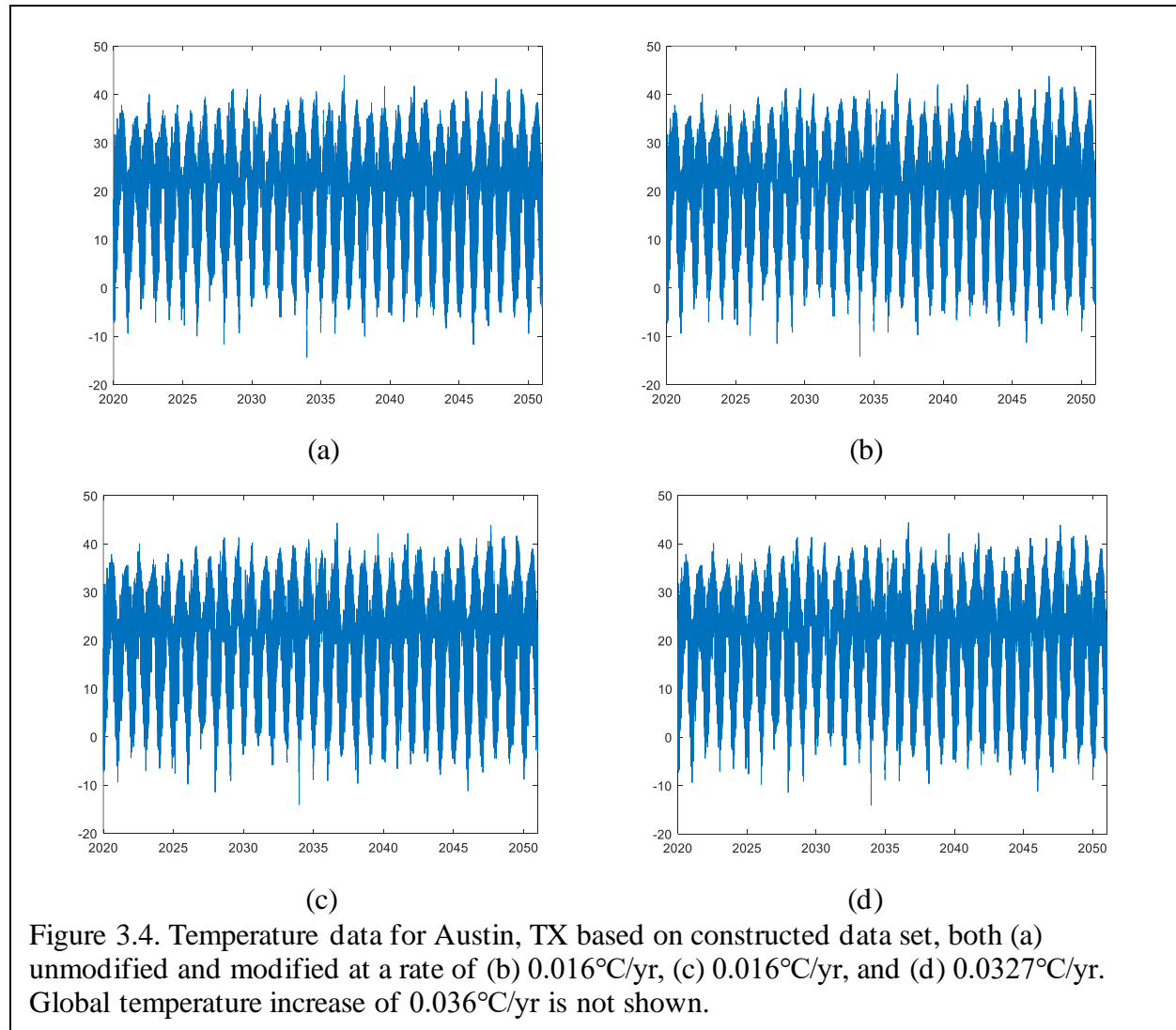
were assembled into 30-year sets in chronological order, taking care to align leap years. Because there are 11 leap years in the 1970 – 2015 period and 8 leap years will be necessary for every 30-year constructed data set leap years may be out of chronological order with respect to the years used to create the weather data sets immediately before and after the leap year, but leap years will be in chronological order with respect to one another throughout the data sets.

As an example, a target 30-year data set could be nominally composed of the years 1970 – 1975, 1980 – 1990, and 2000 – 2012. However, to align leap years the actual data set is: 1972 – 1976, 1981 – 1991, and 2000 – 2014. An added benefit of using historical weather data in this fashion is that the instances of severe weather events will increase with time regardless of which specific historical years are used to make up the data set. These “unmodified” weather data sets are then adjusted to reflect increasing global temperatures. Severe weather events were also investigated and relevant ambient temperatures, wind speeds, and so on selected to simulate the steady-state solution for the three-box model of the BIPV-PCM microfacility.

Overall Increasing Temperatures: Regardless of what actions we take to combat climate change, global temperatures will continue to steadily rise over the next 20 years and beyond. The aggressiveness of the steps we take in the next few years will determine whether global temperatures will rise to 1.5°C or to 2.0°C by 2030 or 2050. As of 2015, global temperatures were already 0.87°C higher than pre-industrial times and were increasing at a rate of from 0.1°C to 0.3°C every 10 years and are unlikely to cause warming greater than 0.5°C in the next 20 to 30 years. More dramatic increases will be experienced over land masses, and thus will be larger than these global averages [46]. In the five years from 2015 to 2020 the global temperature is estimated to have risen by 0.05-0.15°C to between 0.92°C and 1.02°C globally. Thus, to reach a maximum 1.5°C warming by 2050 temperatures may only increase by 0.48-0.58°C over the next

30 years (a rate of 0.016-0.0193°C/yr). To reach a maximum of 2°C, global warming of no more than 0.98-1.08°C over the next 30 years (0.0327-0.036°C/yr) may take place.

In this work, the global temperature increase is modeled as a straight line with a constant slope around which the temperatures will vary. Additionally, for increasing temperature rates will be used: 0.016°C/yr and 0.0193°C/yr for a maximum 1.5°C temperature increase by 2050, and 0.0327°C/yr and 0.036°C/yr for a 2°C maximum global increase over this period. Figure 3.4 shows the temperature in Austin, Texas over a 30-year period made of assembled annual data, first (a) unmodified, and then increasing at a rate of (b) 0.016°C/yr, (c) 0.0193°C/yr, and (d) 0.0327°C/yr.



The increase rate of $0.036^{\circ}\text{C}/\text{yr}$ is not shown for space purpose.

Extreme Weather Events: As global temperatures continue to rise; previously anomalous weather events are becoming more and more frequent. Climate change effects will undoubtedly cause significant property damage, loss of human, animal, and plant life, an increase in waterborne pathogens, and all manner of other forms of negative impacts on life as we know it today. The types of extreme weather events that most directly impact PV performance and lifetime are extreme heat, drought, wildfires, heavy precipitation, flooding, and humidity. However, the important elements of each of these types of weather events relate to the ambient temperature, overall incident solar radiation reaching the rooftop panel, and wind speed.

PV panels operate less efficiently as panel temperatures increase. It is inevitable that annual PV panel efficiency will drop as global temperatures rise. Although it's becoming more difficult to define "normal" temperatures and weather patterns, the Environmental Protection Agency (EPA) defines a heat wave as a period in which the daily minimum temperature adjusted for humidity is greater than the 85th percentile of the July through August historical temperatures from 1981 to 2010 for the area. In other words, a heat wave must be at least as hot as the nine hottest days during a typical summer between 1981 and 2010. During long periods of excessive heat nights are hotter and there is little opportunity for PV panels to cool down overnight, resulting in extended periods of lower output power due to reduced efficiency [64].

The 2021 historic heat wave in the Pacific Northwest (PNW) lasted from June 26th through July 2nd, but still resulted in more than 100 heat-related deaths [65]. A heat wave is specified by its duration of high daily minimum temperatures adjusted for humidity and the temperatures exceeding typical temperatures for that area [66]. The PNW heat wave in 2021 lasted for 7 days and temperatures reached over 40°C , even in areas further north in Canada. One

Canadian town reached a record 49.6°C, then was virtually destroyed in a wildfire shortly after [67]. Heat waves of this magnitude were previously estimated to happen only once in a millennium, but with global warming of 2°C, events of this magnitude are expected to happen every 5 to 10 years, if not more frequently [68].

Heat wave events such as the ones that took place in Seattle over 2021 are expected to occur once every 5-10 years at both 1.5°C and 2°C warming levels, with the 1.5°C warming expected to trend toward the 10-year frequency. Less severe heat waves occur randomly throughout the 30-year data sets naturally, but these heat waves do not accurately reflect the increase in heat wave season, duration, intensity, and frequency due to continued global temperature rise. Heat waves of varying intensity and duration are predicted over increasingly lengthy heat wave seasons and with increasing frequency over the 2020-2050 period. The average heat wave duration, frequency, intensity, and season length are estimated from the EPA's Climate Change Indicators data [66] and shown in Table 3.3.

Table 3.3: Lesser Heat Wave Specifications.				
Decade	Average Length of HW Season (days)	Average Frequency (#HW/year)	Average HW Length (days)	Intensity (°C above threshold temperature)
2020-2030	82.59	7.049	4.098	1.419
2030-2040	101.49	8.614	4.316	1.469
2040-2050	124.707	10.528	4.544	1.519

A changing climate has led to an increase in short-duration, high-intensity precipitation that can cause flooding and other adverse effects. As atmospheric temperatures continue to rise, so does the volume of water that this warmer atmosphere can hold. An atmosphere that can hold a greater quantity of water will release this water in intense precipitation events or via hurricanes and tropical cyclones [69]. As global temperatures rise the atmosphere holds greater volumes of water while higher temperatures cause increased rates of evaporation over land masses, causing a decrease in average relative humidity [70].

While generally overcast skies and an absence of direct sunlight are typical for periods of active and severe precipitation, subsequent RH effects also reduce PV performance. Despite an overall drop in total RH over time due to rising global temperatures, local RH increases temporarily immediately after extreme precipitation events (downpours, hurricanes, etc.) that are followed by warm temperatures. However, the interplay between RH, ambient and atmospheric temperatures, cloud cover, solar irradiation, and so on, is highly complex and not completely understood. Higher temperatures mean greater rates of water evaporation (and lower temperatures mean slower rates of evaporation), so the rate of increase in RH after precipitation is dependent on the ambient temperature. As temperatures increase, the rate of evaporation also increases, because at higher temperatures the amount of energy necessary for a water molecule to shift from the liquid to gaseous state is lessened. At high humidities closer to saturation, evaporation slows. Evaporation of water after precipitation is driven by the energy of solar irradiation; less sunlight yields lower rates of humidity increase. Wind also influences evaporation rates, as more saturated air can be replaced with less saturated air in areas where evaporation is taking place.

For the purposes of this work, predicting the exact rise and fall of RH after precipitation is not necessary. Instead, the RH is calculated as a function of the ambient temperature and the dewpoint temperature recorded in the weather data and these extremes are used to guide the case studies for the limited steady state simulation of different BIPV-PCM microfacility geometries.

BIPV-PCM Microfacility Specifications

There is a plethora of ways to integrate PV panels and PCM into a building, and numerous sizes of shipping containers on the market. In this work the facility was limited to a 20-foot shipping container facility, and the PV panels were assumed to cover the entire rooftop

of the building. In the following sections, the specifications on this building as well as select PV and PCM are detailed.

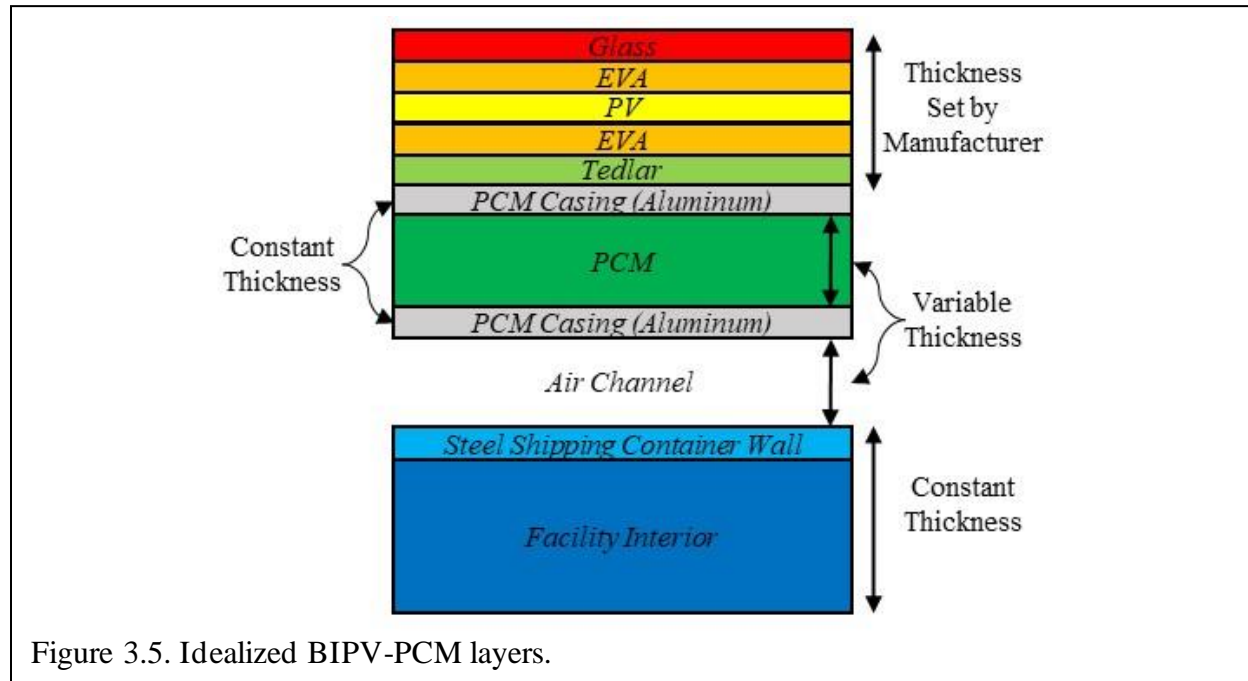


Figure 3.5. Idealized BIPV-PCM layers.

Building: The base facility dimensions are modeled on a standard shipping container. The standard dimensions of these containers are 20- or 40-feet (6.096 – 12.192 meter), 8-foot (2.4384 meter) width, 8.5-foot (2.5908 meter) height, and a wall thickness of 0.075 inches (0.001905 meter). Typically shipping containers are made of Corten weathering steel with a corrugated surface with a depth of about 1 inch (0.0254 meter) [71], [72]. For simplification, the corrugated walls are not modeled in favor of a flat 0.075-inch (0.001905 meter) thick Corten steel wall.

The orientation of the long-axis of the shipping container facility is North-South such that the long sides of the container facility are oriented East-West. The spacing between the PV-PCM and the building exterior varies between 5cm and 50cm as does the overall thickness of the PCM. Although in practice railing and other equipment is present in a BIPV-PCM facility, for simplicity the means for attaching the PV-PCM is not considered. Convection within the channel between the PV-PCM and the building exterior is presumed to behave as turbulent flow.

The temperature of the building interior may range between 17°C and 25°C (62.6°F and 77°F) with a $\pm 2^\circ\text{C}$ tolerance (total range of 59°F to 80.6°F). If the microfacility is used for vertical farming, then growing conditions must be considered. Growing plants indoors requires interior temperatures ranging from 60 - 75°F (15.56 - 23.89°C) with cooler temperatures during dark times [73], [74].

PV Panels: The type of PV panel simulated is limited to monocrystalline silicon from three US-based manufacturers: Lumos, Mission Solar, and Solar Tech Universal. These companies source and manufacture their panels within North and South America as much as possible to reduce dependence on more distant manufacturing centers. Monocrystalline silicon PV panels are used in this study in part because silicon-based PV is very well-studied, and a large amount of detailed information is available for them. Additionally, silicon-based PV are comparatively the simplest types of PV to manufacture as compared to CdTe, CIGS, or Perovskite PV.

Apart from their overall surface area and dimensions, the emissivity and conductivity of the front glass material and EVA (ethylene vinyl acetate) or other encapsulant materials and the PV-backing material are key to modeling the thermal behavior of the PV panels in the BIPV-PCM facilities. Much of this information is proprietary and unavailable. However, since the PV panels are exceedingly thin as compared to the other dimensions of the facility, exact modeling of the thermal behavior within the very thin layers of the PV panel is not necessary.

In general, every PV panel will be composed of surface glass (typically a low-iron glass made for PV applications), an encapsulant (typically EVA), the energy-generating monocrystalline silicon, another layer of encapsulant, and the back sheet. Specifications of each

manufacturer's monocrystalline silicon PV panels are shared in Table 3.4.

Table 3.4: Monocrystalline Silicon PV Panel Specifications.				
Company	Lumos	Mission Solar		Solar Tech Universal
Name	LSX305	MSE330SR8K	MSE425SX6W	PERC315
Dimensions [in (m)]	65.51 (1.664) × 40.94 (1.04)	65.98 (1.676) × 39.69 (1.008)	82.1 (2.086) × 41.5 (1.054)	65.4 (1.663) × 39.25 (.997)
Nominal Operating Cell Temperature (NOCT) [°C]	43.6	46.43	44.69	45.02
Rated Power at STC [W]	305	330	425	315
V _{mp} [V]	32.73	34.53	40.27	34.4
I _{mp} [A]	9.32	9.556	10.55	9.2
V _{oc} [V]	40.79	41.06	49.28	41.1
I _{sc} [A]	10.06	10.045	11.09	9.7
Efficiency [%]	17.62	19.53	19.3	19.3
Temperature Coefficient of P _{max} [$\frac{\%}{^{\circ}\text{C}}$]	-0.453	-0.375	-0.359	-0.366
Temperature Coefficient of V _{oc} [$\frac{\%}{^{\circ}\text{C}}$]	-0.337	-0.28	-0.261	-0.28
Temperature Coefficient of I _{sc} [$\frac{\%}{^{\circ}\text{C}}$]	+0.054	+0.045	+0.044	+0.043
Front Glass – Thickness [in (mm)]	0.24 (6)	0.126 (3.2)	0.126 (3.2)	0.125 (3.2)
Front Glass – Type	FT Low-Iron PV Glass	Tempered, Low Iron, Anti- Reflective Coating	Tempered, Low Iron, Anti- Reflective Coating	Anti-Reflective, Tempered Solar Glass (>94% transmittance)
Encapsulant	(unknown)	EVA	EVA	TPO (hydrophobic)

PCM: As detailed in Chapter 1, the types of PCM used in this study are beeswax, candelilla wax, and soy wax, which were selected because of their applicable melting ranges and the long-term sustainability of their production. For modeling and simulation, the most relevant details of the PCM themselves are shown in Table 3.5 [39], [42]–[44], [75]–[77].

Typically, the PCM chamber is made of aluminum with a thickness of 4mm. The interior chamber volume is 5% larger than the solid PCM volume. In this work, the PCM surface areas match those of the PV panels on the rooftop of the microfacility and their thicknesses range from

5cm to 50cm. A cross-section of the idealized BIPV-PCM layers is shown in Figure 3.5, but the actual thickness of all PV layers is extremely small as compared to the PCM, channel and building interior.

Table 3.5. PCM Specifications.				
Feature	Beeswax	Candelilla Wax	Soy Wax	Aluminum
Thermal Conductivity $\left[\frac{W}{m \cdot K}\right]$	0.25	2.13	0.324	210
Specific Heat Capacity $\left[\frac{J}{g \cdot ^\circ C}\right]$	0.476	0.75471	0.496	0.900
Melting Temperature Range $[^\circ C]$	61-66	68.5-72.5	43.3-79.4	n/a (660.37)
Density (at 15°C) $\left[\frac{g}{cm^3}\right]$	0.958-0.970	0.950-0.990	0.9	2.6989

Summary

In this chapter, all the key elements can be combined into a cohesive model, starting with the maximum amount of incoming solar radiation for the date and time of day for the given location. This total possible solar radiation is reduced by cloud/smoke coverage, then further dissipated by local temperature and humidity effects. The radiation that reaches the panel surface is reflected or transmitted into the panel, and a portion of the absorbed energy is transformed to usable electricity while the rest is dissipated as waste heat.

Some of this “leftover” thermal energy escapes through the front surface of the PV panel via radiation and convection, and some of it is conducted through the back of the PV panel into the PCM chamber. When the PCM is in solid form, thermal energy is conducted through the PCM chamber and escapes via radiation and convection in the channel between the PV-PCM and the building exterior. Melted PCM transports thermal energy at a reduced rate because the thermal energy is transported primarily via thermal convection in the enclosed liquid. When the PCM is in the process of melting, thermal energy is absorbed from the PV-side while the PCM

absorbs energy without changing temperature as the PCM changes phase from solid to liquid. Throughout these processes, the wind speed and direction influence the rate of thermal loss through both the channel between the PV-PCM and the building, as well as at the surface of the PV module.

The interior of the BIPV-PCM facility has a set range of acceptable interior temperatures. When thermal dissipation through the surfaces and channels is not sufficient to manage the interior temperature of the facility, other forms of thermal management within the building interior, such as air-conditioning units, must be utilized.

Real-world weather data sets are constructed from archived data recorded between 1970 and 2015. These data sets are first modified by increasing temperatures linearly to reflect reaching only 1.5°C or 2°C warming by 2050. The key variables that influence the behavior of any specific geometry of the BIPV-PCM system are the wind speed and temperature, so extreme weather events are translated as extremes in the wind speeds and ambient temperatures the BIPV-PCM microfacility are exposed to. The extremes in the real-world data sets are used to guide the case studies of the BIPV-PCM microfacility using the three-box model developed in the next chapter.

Table 3.6. Variables and Constants Used in Chapter 3.

Variable or Constant	Name	Units
α_{elev}	Elevation Angle	°
δ_{dec}	Declination Angle	
FF	Form Factor	-
G_{const}	Solar Constant, $1.353 \frac{kW}{m^2}$	$\frac{W}{m^2}$
G_{cc}	Incident Solar Radiation, Less Cloud Cover	
$G_{incident}$	Incident Solar Radiation	
G_{Ewall}	Incident Solar Radiation, Wall	
G_{roof}	Incident Solar Radiation, Roof	$\frac{W}{m^2}$

Table 3.6. Variables and Constants Used in Chapter 3 (Continued).

Variable or Constant	Name	Units
I_0	Dark Saturation Current	A
I_{sc}	Saturation Current	
n_{base}	Base Minimum Cloud Coverage for an Okta Value	-
n_{cc}	Cloud Cover Decimal Percentage	
n_{doty}	Numerical Day of the Year	
n_{rand}	Random Number Between 0 and 1	
$P_{in(solar)}$	Solar Power into Panel	W
P_{mp}	Maximum PV Panel Power	
P_{out}	Power Output	
TC	Time Correction	-
T_{dew}	Dew Point Temperature	K
V_{oc}	Open Circuit Voltage	V
ϕ_{lat}	Latitude	°
θ_{Az}	Azimuth Angle	

IV. THE THREE-BOX MODEL

A three-box model is developed from the thermal and environmental modeling described in Chapters 2 and 3. The three-box model simplifies the BIPV-PCM microfacility into three key components: the PV-PCM layer, the air channel layers, and the shipping container building layer.

Mathematical Modeling and Simulation Basic Concepts

A mathematical model describes a physical system in mathematical terms and when this model is simulated, it can be used to predict behavior and examine the effects of using different components in the system. Modeling the thermal behavior of physical systems is quite common in science and engineering, and there are a variety of forms of thermal models may take.

Types of Models: Mathematical models take a variety of different forms to describe the behavior and interaction of the components of the system. Static models describe the steady state of a system that has reached an equilibrium state, while dynamic models describe the transient nature of the system under study. Both types of models involve solving a set of partial differential equations.

The weather data points used to model environmental effects are individual data points, however, these data points describe continuous environmental phenomena such as ambient temperature, wind speed, and relative humidity. Thus, the most accurate way to describe the thermal behavior of the BIPV-PCM is to use a continuous model. Additionally, the thermal behavior of the BIPV-PCM system modeled in this work is drawn from established thermal equations and physical theory rather than empirical findings, thus a deductive rather than inductive model is employed in this work.

In general, mathematical models may be linear or non-linear. It should be noted that linear models may have non-linear expressions within them, and that non-linear models may be

linearized. Thermal models tend to have numerous non-linear conditions and can usually be assumed to be non-linear unless significant simplifications are made to the system. One of the most common types of nonlinearity in thermal models is the temperature dependence of the material properties of the system components, such as when the thermal conductivity or specific heat of a material in the system varies with temperature. Thermal transfer due to surface radiation is proportional to the non-linear fourth-order temperature difference between the surface and the ambient temperature. Finally, boundary conditions such as thermal flux that change with ambient temperature are also a key source of nonlinearity in thermal models. Many of these drivers of non-linearity are under study in this work, so even with simplifications the mathematical model in use with the three-box model is non-linear.

Both implicit and explicit models may be used to describe time-dependent systems. Explicit models can use the state of the system at an initial time to predict the state of the system later but requires a very short time-step to calculate accurate results. Implicit models on the other hand allow for any time-step size to be used but also use the current and future state of a system in the solving process which can be computationally expensive. Furthermore, implicit models best describe systems that reach dynamic equilibrium and change gradually over time.

Differential equations describing physical laws such as those that govern thermal behavior are typically deterministic in that there is not an element of randomness that influences the output of the model, whereas probabilistic models involve an element of randomness that's best describes with a probability distribution. Although there is some use of a random weighting variable in this model to describe unknown cloud coverage, the overall modeling used to describe the BIPV-PCM system is deterministic.

General Simulation Abilities and Limitations: All mathematical modeling and simulation options have strengths and weaknesses. Perhaps the greatest advantage of simulation over experimentation is that numerous long-term simulated experiments can be analyzed in a comparatively short period of time. Furthermore, simulation allows for components and other characteristics of the system to be modified to examine their effect on the overall behavior of the system. In this work, these advantages allow for investigation of different PCM types and combinations of PCM thickness and channel spacing under various weather conditions.

Disadvantages with mathematical modeling and simulation stem primarily from the fact that every model is necessarily simplified from the real-world problem and thus does not fully include all elements of the physical system or boundary and initial conditions. What information to include and how to include it influences the accuracy and predictive capabilities of a mathematical model. The inclusion of too much information can cause simulation times to be excessively long, so that the model is not feasible for simulating meaningful results. Likewise, excluding too much information may result in an over-simplified model, yielding unrealistic results that do not accurately reflect the real-world system.

The approximations and simplifications made in this work most certainly do not yield an exact prediction of system behavior and status in thirty years. Rather, the model in this work was created with the intent of functioning as an approximation of the real-world behavior with different PCM types, thicknesses, and channel spacing, and is intended to be used purely for comparative purposes. The weather and ambient temperatures used as inputs for this model will not be the exact representations of the future climate. However, this model does allow for a one-to-one comparison of different BIPV-PCM systems.

Finite Element Analysis: There are a variety of different ways to simulate physical systems, and choice of tools is dependent on what information is being sought by the simulation. Finite element analysis (FEA) is used to predict how a system will react to environmental effects. A continuous real-world object can be divided into many smaller elements, then the appropriate PDE is solved over each small element to describe how the overall system behaves.

In FEA, the system is covered in nodes which describe a single point, then lines between the nodes are drawn which create a mesh that encloses the smaller elements. More nodes mean a finer mesh, but also mean a more computationally costly calculation. Fewer nodes can lead to inaccurate results that fail to accurately describe the system. Appropriately meshing the system is critical for ensuring a balance between computational stringency and computation time. Parts of the system that undergo large or rapid changes, or areas in the geometry with sharp angles or smaller components are best described with finer meshing, while large uniform areas undergoing more gradual changes can be accurately modeled using fewer nodes and a coarser mesh. When outside influences act on the system, each element adjusts to minimize the total energy of the system. The equations describing the physical behavior of each element are solved and then assembled into a system of equations that describes the entire system.

Matlab Software: Matlab is a matrix-based software that may be used for analyzing data, developing unique algorithms, and creating computational models. Matlab also comes equipped with a PDE toolbox that makes the process for solving structural mechanics, heat transfer, and other PDEs relatively straightforward.

First the geometry is created or imported, followed by generating an appropriate mesh for the geometry, defining the physical, boundary, and initial conditions for the system, then solving and post-processing the results for visualization and analysis. This workflow is illustrated as a

simple flowchart in Figure 4.1 below.

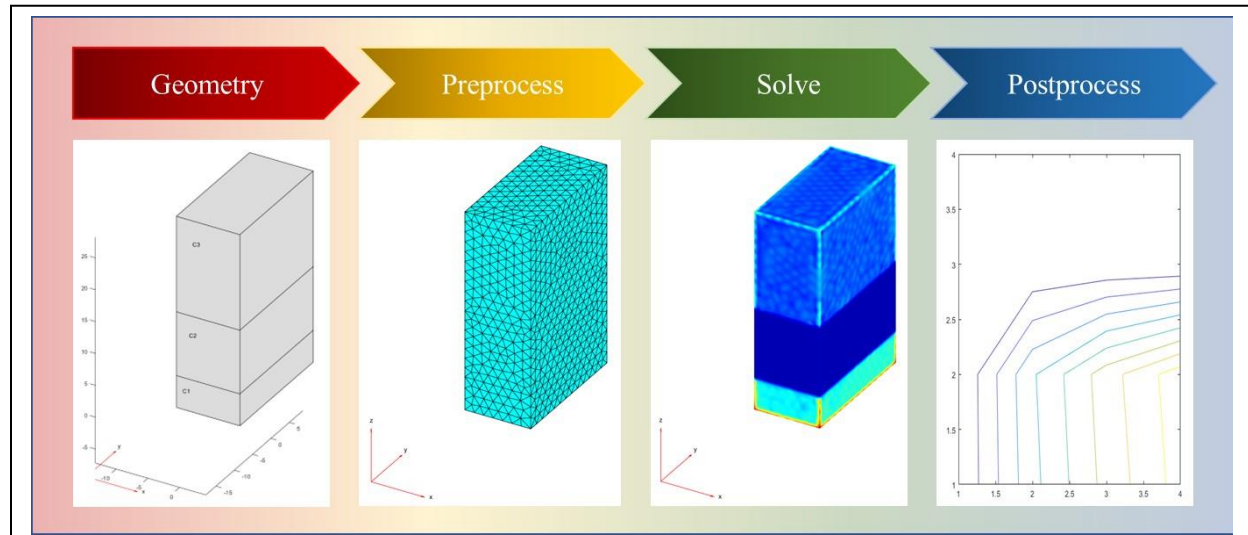


Figure 4.1. Basic workflow for modeling and simulation in Matlab.

Three-dimensional geometries may be generated using computer-aided design (CAD) software such as AutoCAD or Solidworks and then imported into Matlab. In the absence of CAD software, geometries with some limitations may be created in Matlab. For this work, the BIPV-PCM microfacility is represented only in 2 dimensions to simplify simulation and ensure it can be calculated in a reasonable amount of time.

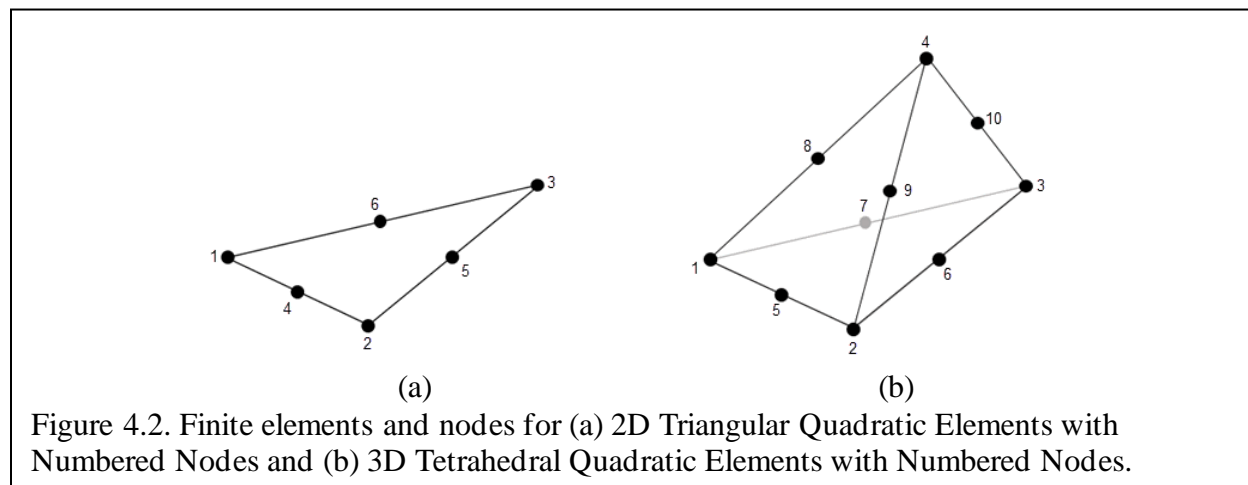


Figure 4.2. Finite elements and nodes for (a) 2D Triangular Quadratic Elements with Numbered Nodes and (b) 3D Tetrahedral Quadratic Elements with Numbered Nodes.

The mesh is then generated using the generateMesh function in Matlab's PDE Toolbox. This mesh generation function creates triangular elements for 2D geometries and tetrahedral elements for 3D geometries. Triangular and tetrahedral elements by default have nodes at each corner and

at the centers of each edge, as shown in Figure 4.2. This quadratic geometric order tends to yield the most accurate results and is the default means of meshing used by Matlab. Notably, PDE solvers in Matlab work with the meshes rather than the geometry directly. Material properties are contained within the defined geometry and the solver applies these parameters to the nodes and elements defined of the mesh.

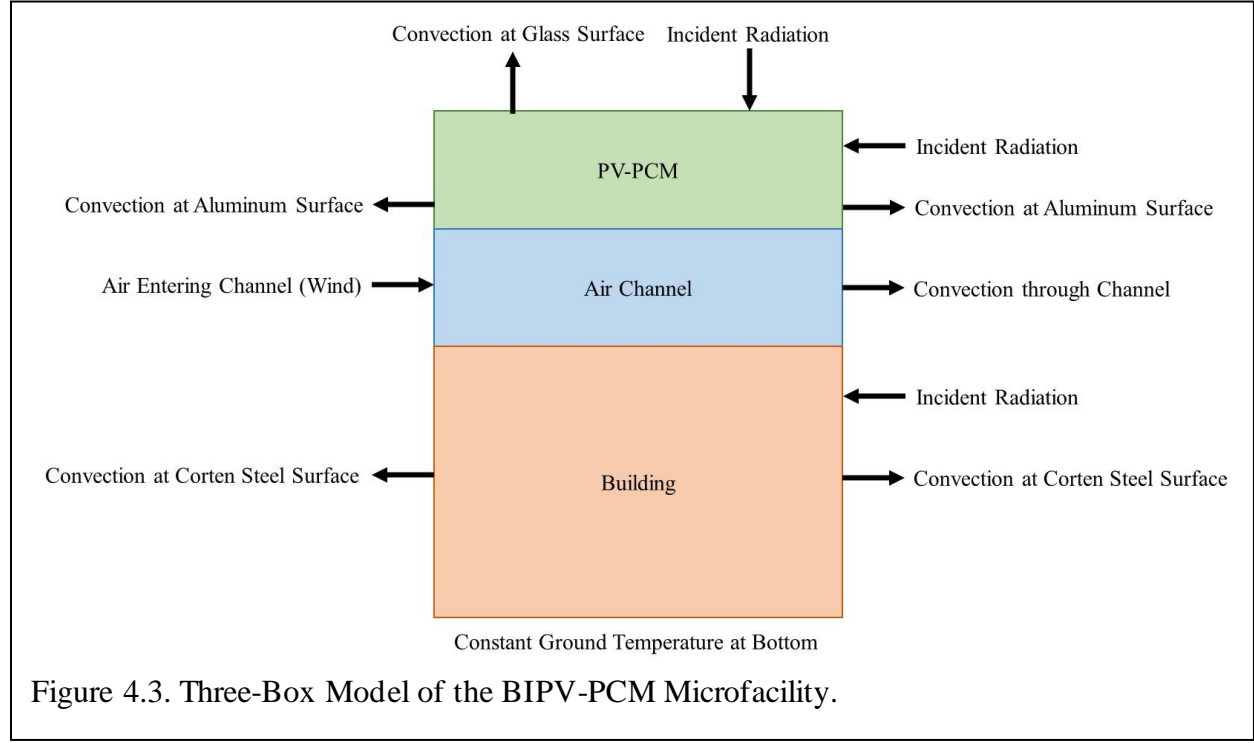
Specifying the Model

Limitations and Approximations: The combination of programmatic limitations with 2D and 3D geometry formation in Matlab, internal meshing and boundary condition limitations, as well as the 30-year timespan of the collected weather data require numerous simplifications and approximations to the model.

First, Matlab's geometry creation capabilities are extremely rudimentary and are unable to model the exact geometry of the BIPV-PCM microfacility. Although more sophisticated 3D geometries built in a 3D computer aided drafting program such as AutoCAD or Solidworks can be imported into Matlab for solving, these CAD programs were not available for this work. Additionally, the air channel cannot be accurately modeled because Matlab's geometry applications do not permit separate objects to be meshed and simulated as a single geometry. Since the PV layers, the aluminum PCM chamber walls, and the Corten steel walls of the shipping container facility are all very thin especially as compared to the other dimensions of the facility, they are all simulated as boundary conditions and not explicitly modeled in the geometry.

To further simplify the simulation, thermal storage is also neglected except at temperatures greater than the PCM melting temperature where this stored thermal energy is modeled as a lump-sum of stored thermal energy according to the latent heat and overall mass of

the PCM. The ground temperature under the facility is modeled as a constant temperature value at the bottom face as well. Finally, it was not computationally efficient to draw ambient temperatures from the weather data sets for the PDE solver. Thus, these data sets were used to determine extremes in the environment which were used to examine specific extreme weather



cases. The three-block model for the BIPV-PCM system is shown in Figure 4.3.

Governing Equations: Equations describing energy conservation as well as conductive, convective, and radiative thermal behavior were reviewed at length in Chapter 2. The general energy equation is:

$$\dot{E}_{in} + \dot{E}_{gen} - \dot{E}_{out} = \dot{E}_{st} \quad \text{Eq. 4.1}$$

The rate of energy into the overall system is the incident solar energy less the solar energy converted to electricity by the rooftop panel, no energy is generated inside the system, and energy leaves the system via convective and radiative thermal flux from the surfaces. It was not possible to include radiative energy losses as they made the computation time for even this

simplified model exceedingly long. Additionally, the incident solar energy is split between the amount normal to the walls of the building and the amount normal to the roof of the building. Solar energy perpendicular to the roof surface is decreased by the panel efficiency and the rest is estimated to be transformed to heat. The remaining component of the incoming solar energy striking the vertical walls is presumed to fully transform into thermal energy and is split between the PV-PCM and building layers according to their relative surface areas. The component of the incident solar radiation perpendicular to the walls of the microfacility is presumed to be entirely transformed to heat.

For each of the faces of the 2D three-box model with solid PCM, the governing energy expression is:

$$(1 - \eta_{eff})G_{inc_{roof}}A_{roof} + G_{inc_{wall}}A_{wall} + k_{PCM}A_{roof}\frac{\partial^2 T}{\partial x^2} + k_{PCM}A_{wall}\frac{\partial^2 T}{\partial y^2} - (Q_{conv_{roof}} + 2Q_{conv_{wall}} + Q_{rad_{roof}} + 2Q_{rad_{wall}}) = \rho_{PCM}C_{p_{PCM}}V_{PCM}\frac{\partial T}{\partial t}$$

Eq. 4.2

Here η_{eff} is the panel efficiency, $G_{inc_{roof}}$ and $G_{inc_{wall}}$ are the components of incident energy from the sun, A_{roof} and A_{wall} are the exterior surface areas of the roof and wall, and ρ_{PCM} , $C_{p_{PCM}}$, and V_{PCM} are, respectively, the mass density, specific heat, and overall layer volume of the PV-PCM layer of the three-box model.

The expression for $Q_{conv_{wall}}$ is multiplied by 2 as there are 2 walls in the 2D model that experience conductive thermal transport. The expressions for $Q_{conv_{roof}}$ and $Q_{conv_{wall}}$ are:

$$Q_{conv_{roof}} = A_{roof}h_{tot}(T - T_{amb})$$

Eq. 4.3

$$Q_{conv_{wall}} = A_{wall}h_{tot}(T - T_{amb})$$

Eq. 4.4

Though ignored in this model, the expressions for $Q_{rad_{roof}}$ and $Q_{rad_{wall}}$ are:

$$Q_{rad_{roof}} = \sigma \varepsilon_{glass} A_{roof} (T^4 - T_{amb}^4) \quad \text{Eq. 4.5}$$

$$Q_{rad_{wall}} = \sigma \varepsilon_{Al} A_{wall} (T^4 - T_{amb}^4) \quad \text{Eq. 4.6}$$

Upon melting, the PCM stores an additional quantity of energy equivalent to:

$$q_{melt_{PCM}} = m_{PCM} L_{f_{PCM}} = \rho_{PCM} V_{PCM} L_{f_{PCM}} \quad \text{Eq. 4.7}$$

Thus, for ambient temperatures greater than the melting point of the PCM, an additional

$q_{melt_{PCM}}$ term is included, and the PDE for the PCM layer is:

$$\begin{aligned} (1 - \eta_{eff}) G_{inc_{roof}} A_{roof} + G_{inc_{wall}} A_{wall} + k_{PCM_{Liq}} A_{roof} \frac{\partial^2 T}{\partial x^2} + k_{PCM_{Liq}} A_{wall} \frac{\partial^2 T}{\partial y^2} \\ - (Q_{conv_{roof}} + 2Q_{conv_{wall}}) = \rho_{PCM} C_{p_{PCM}} V_{PCM} \frac{\partial T}{\partial t} + \rho_{PCM} V_{PCM} L_{f_{PCM}} \end{aligned} \quad \text{Eq. 4.8}$$

Where $k_{PCM_{Liq}}$ is the thermal conductivity of liquid PCM and $L_{f_{PCM}}$ is the latent heat of fusion of the PCM. Here, radiative terms have been removed as they are not simulated with this model.

Between the PV-PCM and the building, the coefficients and boundaries must also describe the thermal energy entering and leaving the channel. The mean temperature of the air in the channel changes through the length of the channel due to thermal convection at the channel surfaces. The convective thermal flux through the channel must be equivalent to the rate at which air's thermal energy increases, plus the rate of work done to move the air through the control volume. In this work, air is modeled as a perfect gas with a constant specific heat, and convection through the channel may be expressed:

$$q_{chan_{conv}} = \dot{m} C_{p_{air}} (T_{m,exit} - T_{m,enter}) \quad \text{Eq. 4.9}$$

Where \dot{m} is the mass flowrate, C_p , is the specific heat of air, and $T_{m,enter}$ and $T_{m,exit}$ are the mean temperature in the channel at the entrance and exit, respectively. For consistency, the entrance

edge is taken to be the left edge of the channel layer in the three-box model, and this edge is kept at ambient temperature. The mass flow rate is dependent on the wind speed, width of the channel, and overall depth of the microfacility and mass density of air, and the above expression changes to:

$$q_{chan_conv} = \rho_{air} A_{wall} v_{wind} C_{p_{air}} (T - T_{amb}) \quad \text{Eq. 4.10}$$

Thus, for the air channel layer, the PDE expression is:

$$k_{air} A_{roof} \frac{\partial^2 T}{\partial x^2} + k_{air} A_{wall} \frac{\partial^2 T}{\partial y^2} - \rho_{air} A_{wall} v_{wind} C_{p_{air}} (T - T_{amb}) = \rho_{air} C_{p_{air}} V_{chan_{air}} \frac{\partial T}{\partial t} \quad \text{Eq. 4.11}$$

Where v_{wind} and $V_{chan_{air}}$ are the wind speed and the overall volume of the air channel layer in the three-box model.

Finally, the building layer is modeled similarly to the solid PCM layer with convective thermal transport on the exterior Corten steel walls of the building only:

$$G_{inc_{wall}} A_{wall_{bldg}} + k_{air} A_{roof} \frac{\partial^2 T}{\partial x^2} + k_{air} A_{wall} \frac{\partial^2 T}{\partial y^2} - 2Q_{conv_{wall}} = \rho_{air} C_{p_{air}} V_{air_{bldg}} \frac{\partial T}{\partial t} \quad \text{Eq. 4.12}$$

Matlab's partial differential equation toolbox requires this expression to be rearranged into the following format:

$$m \frac{\partial^2 u}{\partial t^2} + d \frac{\partial u}{\partial t} - \nabla \cdot (c \nabla u) + au = f \quad \text{Eq. 4.13}$$

After rearranging these equations into the format of Equation 4.13, the following set of energy equations describing the three layers (PV, channel, and building) of the BIPV-PCM microfacility are shown in Table 4.1 and the relevant coefficients are shown in Table 4.2. For completeness, the terms that model radiation have been left in these expressions. However, for the simulation

performed, radiative effects were removed.

Table 4.1. Governing Equations for Three-Box BIPV-PCM Microfacility Model.

PCM Face	
	$\rho_{PCM} C_{pPCM} V_{PCM} \frac{\partial T}{\partial t} - k_{PCM} A_{wallPCM} \frac{\partial^2 T}{\partial x^2} - k_{PCM} A_{roofPCM} \frac{\partial^2 T}{\partial y^2}$ $+ (A_{roof} h_{tot} + 2A_{wall} h_{tot} + \sigma \varepsilon_{glass} A_{roof} T^3 + 2\sigma \varepsilon_{Al} A_{wall} T^3) T$ $= (1 - \eta_{eff}) G_{incroof} A_{roof} + G_{incwall} A_{wall} - A_{roof} h_{tot} T_{amb} - 2A_{wall} h_{tot} T_{amb}$ $- \sigma \varepsilon_{glass} A_{roof} T_{amb}^4 - 2\sigma \varepsilon_{Al} A_{wall} T_{amb}^4 - \rho_{PCM} V_{PCM} L_{fPCM}$
Air Channel	
	$\rho_{air} C_{pair} V_{chanair} \frac{\partial T}{\partial t} - k_{air} A_{wallchan} \frac{\partial^2 T}{\partial x^2} - k_{air} A_{roofchan} \frac{\partial^2 T}{\partial y^2} + \rho_{air} A_{wallchan} v_{wind} C_{pair} T$ $= \rho_{air} A_{wallchan} v_{wind} C_{pair} T_{amb}$
Building	
	$\rho_{air} C_{pair} V_{airbldg} \frac{\partial T}{\partial t} - k_{air} A_{wallbldg} \frac{\partial^2 T}{\partial x^2} - k_{air} A_{roofbldg} \frac{\partial^2 T}{\partial y^2} + (2A_{wallbldg} h_{tot} + 2\sigma \varepsilon_{cort} A_{wallbldg} T^3) T$ $= G_{incwall} A_{wallbldg} - 2A_{wallbldg} h_{tot} T_{amb} - 2\sigma \varepsilon_{cort} A_{wallbldg} T_{amb}^4$

Table 4.2. PDE Coefficients for the Three-Box BIPV-PCM Microfacility Model.

PCM Face	
d	$\rho_{PCM} C_{pPCM} V_{PCM}$
c	$k_{PCM} A_{wallPCM} + k_{PCM} A_{roofPCM}$
a	$A_{roof} h_{tot} + 2A_{wall} h_{tot} + \sigma \varepsilon_{glass} A_{roof} T^3 + 2\sigma \varepsilon_{Al} A_{wall} T^3$
f	$(1 - \eta_{eff}) G_{incroof} A_{roof} + G_{incwall} A_{wall} - A_{roof} h_{tot} T_{amb} - 2A_{wall} h_{tot} T_{amb} - \sigma \varepsilon_{glass} A_{roof} T_{amb}^4$ $- 2\sigma \varepsilon_{Al} A_{wall} T_{amb}^4 - \rho_{PCM} V_{PCM} L_{fPCM}$
Air Channel	
d	$\rho_{air} C_{pair} V_{chanair}$
c	$k_{air} A_{wallchan} + k_{air} A_{roofchan}$
a	$\rho_{air} A_{wallchan} v_{wind} C_{pair}$
f	$\rho_{air} A_{wallchan} v_{wind} C_{pair} T_{amb}$
Building	
d	$\rho_{air} C_{pair} V_{airbldg}$
c	$k_{air} A_{wallbldg} + k_{air} A_{roofbldg}$
a	$2A_{wallbldg} h_{tot} + 2\sigma \varepsilon_{cort} A_{wallbldg} T^3$
f	$G_{incwall} A_{wallbldg} - 2A_{wallbldg} h_{tot} T_{amb} - 2\sigma \varepsilon_{cort} A_{wallbldg} T_{amb}^4$

Physical and Thermal Properties: The PCM elements are typically modeled as a layer of PCM sandwiched between layers of aluminum of the same thickness. The thickness of the PCM layer varies between 5 cm and 50 cm as does the width of the channel between the PV-PCM and the building exterior. The thermal properties of air were estimated as linear function of the ambient temperature for relevant temperature ranges and at constant atmospheric pressure. The

air channel between the aluminum PCM chamber backing and the Corten steel exterior of the shipping container facility is modeled as turbulent convective flow between plates using adjusted thermal values and coefficients, while the faces of this air channel layer will be modeled as purely convective. For both the air channel and the “faces” of the air channel convection will be influenced directly by the windspeed extremes as found in the weather data. For simplicity, the temperature of the bottom face of the facility is modeled as a constant temperature throughout the year.

Table 4.3. Three-Box Model Geometric Dimensions.			
Layer	Height (m)	Width (m)	Depth (m)
PCM	0.05 to 0.5	2.4384	6.096
Air Channel	0.05 to 0.5		or
Building Interior	2.5908		12.192

Determining what PCM type and what combination of PCM thickness and channel spacing impact the interior temperature of the facility the most is the key output of these simulations. The building interior for the generalized production facility may range between 17°C and 25°C (62.6°F and 77°F) with a $\pm 2^\circ\text{C}$ tolerance (total range of 59°F to 80.6°F). Growing plants indoors requires interior temperatures ranging from 60 - 75°F (15.56 - 23.89°C) with cooler temperatures during dark times, though the exact temperature ranges vary according to the type of plants being grown [73], [74]. Additionally, there are numerous applications for the BIPV-PCM microfacility in which higher interior temperatures may be acceptable, so interior temperatures up to 35°C in the interior of the facility are considered feasible. Tables 4.4 and 4.5 detail the relevant geometric dimensions and thermal properties assigned to the different layers in the BIPV-PCM system.

Boundary Conditions: Defining the boundary conditions of the system is a critical initial step in the simulation process. Matlab’s PDE Solver can apply Dirichlet, Neumann, and mixed boundary conditions to individual exterior edges of 2D geometries. Dirichlet boundary

conditions specify the temperature on the exterior surface of the geometry at this edge and must satisfy the form:

$$hu = r \quad \text{Eq. 4.14}$$

Since the temperature along the bottom edge of the building layer is modeled as a constant 20C, the boundary condition for this edge is:

$$1 \times T = 20 \quad \text{Eq. 4.15}$$

When the PDE is scalar, that is, when only one PDE is needed to describe the system, the generalized Neumann boundary conditions specify the thermal flux at the exterior surface, and must satisfy the form:

$$\hat{n} \cdot (c\nabla u) + qu = g \quad \text{Eq. 4.16}$$

Here, the c value is the same as that which is used to define the PDE coefficients, and because of the scalar nature of the PDE and the format the PDE coefficients were put into, q and g are essentially the same as the a and f values used but specified to each exterior edge of the geometry. To further simplify the model and improve computational efficiency, the radiative thermal losses were ignored in the calculation. Figure 4.4 shows the three-box model with faces labeled, as well as the geometry meshed with 2 different element sizes. Boundary conditions for each exterior edge are shown in Table 4.5.

Table 4.4. Three-Box Model Thermal Properties.

Layer	Density [$\frac{kg}{m^3}$]	Thermal Conductivity [$\frac{W}{m \cdot K}$]	Specific Heat [$\frac{J}{kg \cdot K}$]	Latent Heat [$\frac{J}{K}$]
Glass	2.2	0.76	0.83	n/a
Aluminum	2.6989	210	0.9	n/a
Beeswax	0.958	0.25	0.476	1.378×10^5
Candelilla Wax	0.95	2.13	0.75471	1.52×10^5
Soy Wax	0.9	0.324	0.496	8.46×10^4
Air Channel	1.266	0.242	1	n/a
Corten Steel	7.865	56.0656	0.105	n/a
Interior	1.266	0.242	1	n/a

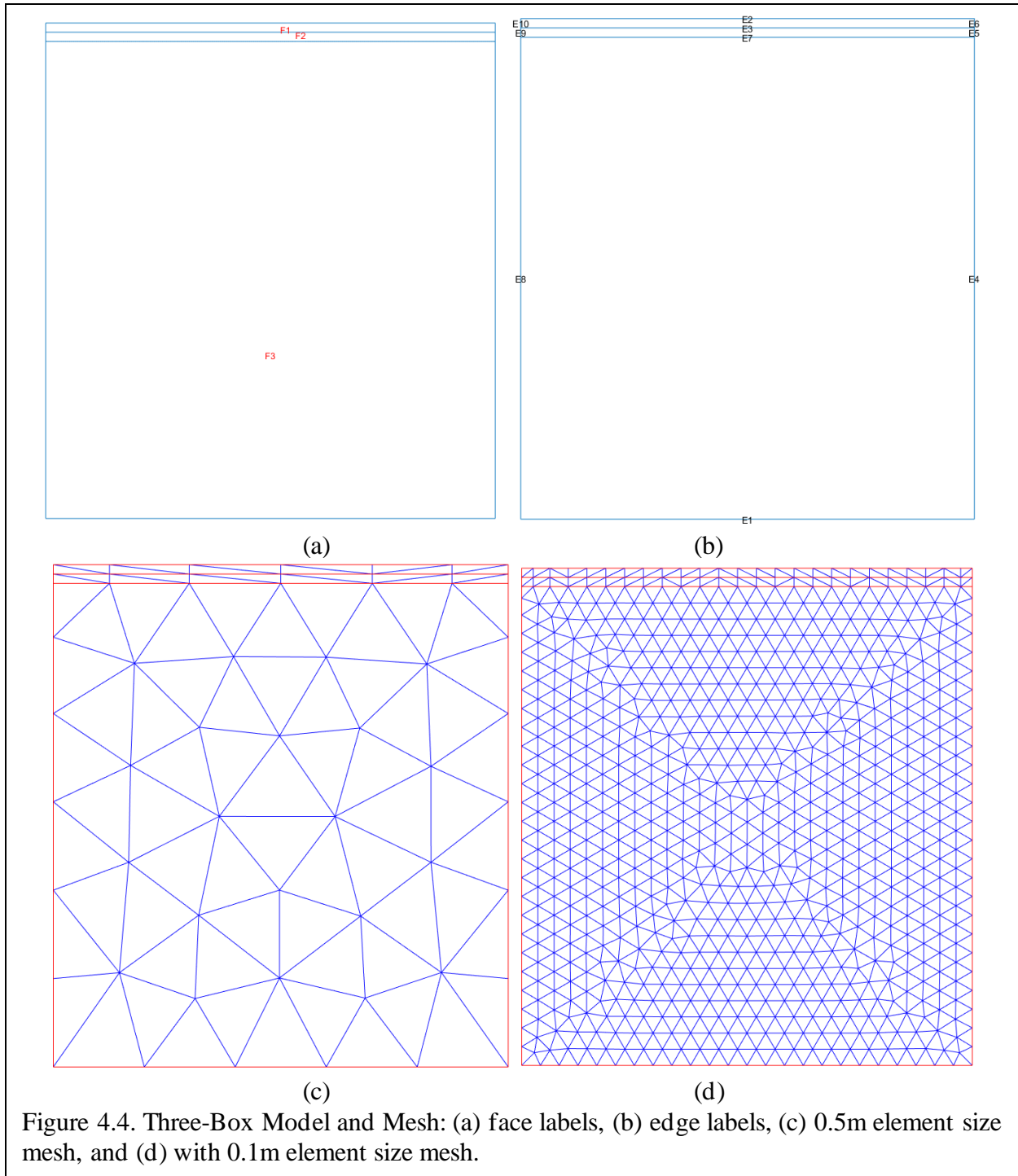


Figure 4.4. Three-Box Model and Mesh: (a) face labels, (b) edge labels, (c) 0.5m element size mesh, and (d) with 0.1m element size mesh.

Mesh and Initial Conditions: The maximum mesh element size was set to 0.1m and the minimum element was 0.05m, with 3112 total number nodes. The dimensions of the mesh must reflect the dimensions of the system itself. The depth of the BIPV-PCM range is kept constant at 6.096 meters (20 feet) and the building height is fixed at 2.5908m (8.5 feet). The channel spacing

and PV-PCM height both range from 0.05m to 0.5m. The geometry of the system and mesh are two separate entities in Matlab, and because the PDE solves at the nodes of the mesh, care must be taken to ensure that the mesh accurately reflects the layers of the system. Figure 4.4 (c) and (d) shows the three-box model with varying mesh sizes, including the mesh size of 0.1m used in these simulations. For simplicity, all three domains in the three-box model for the BIPV-PCM microfacility are set to an initial temperature of 20°C.

Table 4.5. Boundary Conditions for the Three-Box Model.

Edge	Boundary Condition Expression		Type
PV-PCM – Top	q	$A_{roof} h_{tot} + \sigma \epsilon_{glass} A_{roof} T^3$	Neumann $\hat{n} \cdot (c \nabla u) + qu = g$
	g	$(1 - \eta_{eff}) G_{in} c_{roof} A_{roof} - A_{roof} h_{tot} T_{amb} - \sigma \epsilon_{glass} A_{roof} T_{amb}^4$	
PV-PCM – Left & Right	q	$A_{wall} h_{tot} + \sigma \epsilon_{Al} A_{wall} T^3$	
	g	$\frac{1}{2} G_{in} c_{wall} A_{wall} - A_{wall} h_{tot} T_{amb} - \sigma \epsilon_{Al} A_{wall} T_{amb}^4$	
Channel – Right	q	$\rho_{air} A_{wall,chan} v_{wind} C_{p,air}$	Dirichlet $hu = r$
	g	$\rho_{air} A_{wall,chan} v_{wind} C_{p,air} T_{amb}$	
Channel – Left	h	1	
	r	T_{amb}	
Building – Bottom	h	1	Neumann $\hat{n} \cdot (c \nabla u) + qu = g$
	r	293.15	
Building – Left/Right	q	$A_{wall,bldg} h_{tot} + \sigma \epsilon_{cort} A_{wall,bldg} T^3$	
	g	$\frac{1}{2} G_{in} c_{wall} A_{wall,bldg} - A_{wall,bldg} h_{tot} T_{amb} - \sigma \epsilon_{cort} A_{wall,bldg} T_{amb}^4$	

Simulation Results and Analysis

To support the simulation of these conditions, large weather data sets spanning 30 years were assembled and preprocessed to obtain real-world extremes and medians of wind speeds, cloud coverage, relative humidity, ambient temperatures, and so on [58]. Representative values for extreme weather and higher ambient temperatures were drawn from this real-world data and these values were used in the simulation for consistency and comparability between facilities.

Real-world and representative environmental data is shown in Table 4.6.

Table 4.6. Real-world environmental data used to determine relevant values for simulation.					
	Min	Mid		Max	
Temperature Ramp Rates due to Climate Change [K/yr]	0.48	0.579		0.981	
Ambient Temperature [K]	258.85	273.43	288	302.58	317.15
Ambient Temperature w/ 0.48 K/yr Climate Change Increase	259.33	273.91	288.48	303.06	317.63
Ambient Temperature w/ 0.579 K/yr Climate Change Increase	259.43	274	288.58	303.15	317.73
Ambient Temperature w/ 0.981 K/yr Climate Change Increase	259.83	274.41	288.98	303.56	318.13
Ambient Temperature w/ 1.08 K/yr Climate Change Increase	259.93	274.51	289.08	303.66	318.23
Wind Speed [m/s]	0	5.53	11.05	16.58	22.1

Despite the simplifications inherent in this model, each simplification is universal across all simulated facilities. PCM types, thicknesses, and channel spacings may be compared to one another even if the model does not represent the real-world temperature profile of the facility with absolute accuracy. Although numerous simulations of the BIPV-PCM microfacility were completed, only the most relevant and interesting results are shared in this work. In the interest of space, images have been put together at the end of the chapter.

Table 4.7. Representative environmental data used in simulation.			
	Ambient Temperatures	Wind Speeds	Convection coefficient
	273.15	0	5
	293.15	10	10
	303.15	20	25
	313.15	30	50
	323.15	40	100
	333.15	50	250

PCM of 5cm Thickness with Channel Spacing of 5cm: Figure 4.5 shows the BIPV-PCM facility with 5cm thickness of PCM and a 5cm channel spacing for beeswax, candelilla wax, and soy wax PCM at an ambient exterior temperature of 323K (about 50°C) with zero wind speed. Figure 4.6 shows the geometry of the BIPV-PCM microfacility at 323K with a wind speed of 30 m/s. For very thin PCM layers and building spacings of 5cm there is no appreciable difference in the temperature profile of the building interior between different PCM types at any temperature

or with any variation of wind speed.

Although there is no meaningful difference in the performance of the various PCM used in each case, the presence of high winds does lower the temperature of the facility. However, the interior facility temperatures still match the exterior temperature at steady state, hence BIPV - PCM facilities that have a PCM of 0.5m thickness and a 0.5m channel spacing are only feasible in areas with continuous high winds, and for applications that either permit higher building interior temperatures or employ additional cooling methods. This thickness of PCM and channel spacing are not an ideal option for a microfacility in which human workers will work. Furthermore, as this combination does not significantly mitigate high temperatures within the facility, this combination of PCM thickness and spacing are not ideal for vertical farm applications.

PCM of 50cm Thickness with Channel Spacing of 5cm: Figure 4.7 shows the steady state thermal results for a microfacility with 50cm thickness PCM and a channel spacing of 5cm for each PCM type at 323K, a wind speed of 30 m/s. In all wind speed cases and all PCM types for this PCM thickness and channel spacing, the steady state interior temperature matches that of the ambient environment.

Figure 4.8 shows the temperature profile of the facility for melted PCM with a 30 m/s wind speed at 333K. For these cases the interior building temperature for the candelilla wax PCM is slightly lower than that of the other two PCM types. The melted PCM is modeled as a heat sink due to the thermal energy stored through the melting process. Despite the slightly better performance with candelilla wax, at high temperatures this PCM thickness and channel spacing do not sufficiently mitigate building interior temperatures enough to be a comfortable working environment for humans.

PCM of 5cm Thickness with Channel Spacing of 50cm: Figures 4.9 and 4.10 show the steady state thermal results for a microfacility with 5cm thickness PCM and a channel spacing of 50cm for each PCM type at 323K and with 0 m/s and 30 m/s wind speeds, respectively. As with the other BIPV-PCM microfacility geometries, this spacing and PCM thickness do little to mitigate the interior building temperature in high temperatures even with high wind speeds. This orientation also does not yield optimal temperature ranges for human usage or vertical farms.

PCM of 50cm Thickness with Channel Spacing of 50cm: On the opposite end of the spectrum, the BIPV-PCM microfacility with PCM of thickness 0.5m and with a channel spacing of 0.5m indicate that this orientation does somewhat mitigate the interior temperature. Overall, there is not significant variation in the performance between different types of PCM for this channel spacing and PCM thickness, but this orientation does aid in lowering the interior temperature appreciably. Figures 4.11 and 4.12 show this thicker PCM and channel spacing for temperatures under the PCM melting point with different high wind speeds. Minor variations in the temperature profile for the different PCM types does not appreciably impact the overall steady-state performance of the different types of solid PCM, but does indicate that of the three, candelilla wax impacts the temperature of the top PV-PCM layer the most at high temperatures below the melting temperature.

At ambient temperatures over the melting point of the PCM, energy is stored in the PCM layer according to the latent heat of the material. Figure 4.13 shows that the candelilla wax more appreciably decreases the interior building temperature as compared to the beeswax or soy wax. The temperature in the melted PCM layer for all PCM types is lower than ambient temperature for this combination of PCM thickness and channel spacing. This BIPV-PCM orientation yields a lower interior temperature despite very high exterior temperatures than the other BIPV-PCM

orientations, but still fails to keep the interior building temperature within a reasonable range for human operation.

Summary

Out of all the various PCM thicknesses and channel spacings studied, the clear frontrunners are the thickest PCM and the largest channel spacing. This outcome indicates that the larger the channel spacing, the more thermal energy is convected through the channel, even in the absence of strong winds forcing the convection. Furthermore, at temperatures above the PCM melting point, the thicker layer of PCM absorbs a greater quantity of thermal energy, which helps decrease the temperature within the facility.

Further investigation should include more detailed modeling that includes radiative effects and more accurate characterization of the wind in the environment, as well as the convective processes in the channel and within the building. However, given the limitations of Matlab regarding geometric modeling, utilizing a program such as Solidworks or AutoCAD to better model the facility geometry would likely improve results. Finally, other programs such as COMSOL might be considered, as Matlab software is not currently capable of accurately modeling subdomains or defining boundary conditions between subdomains.

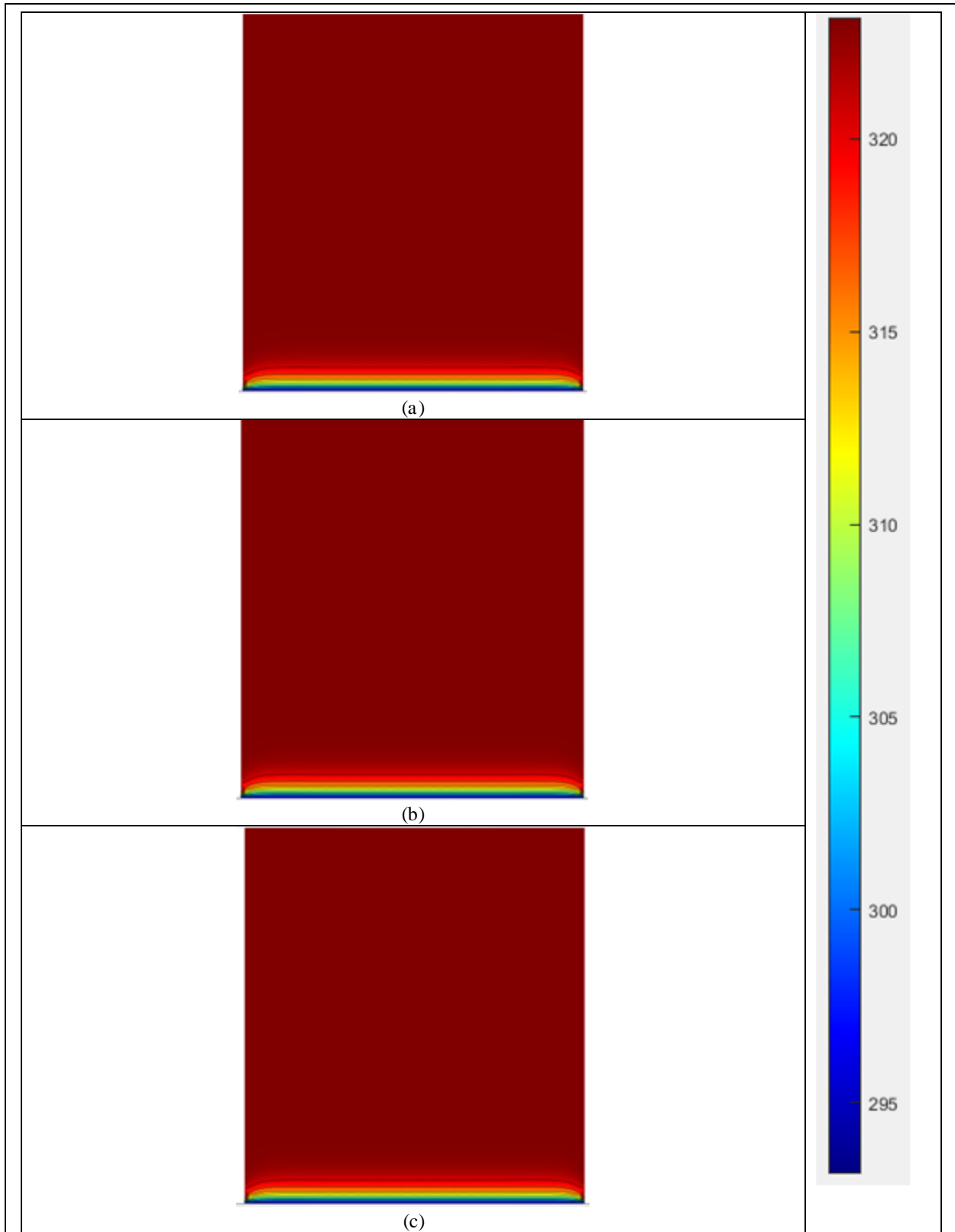


Figure 4.5. Solid 5cm Thick PCM, 5cm Channel Spacing, No Wind, $T_{amb} = 323K$ (a) Beeswax (b) Candelilla Wax (c) Soy Wax.

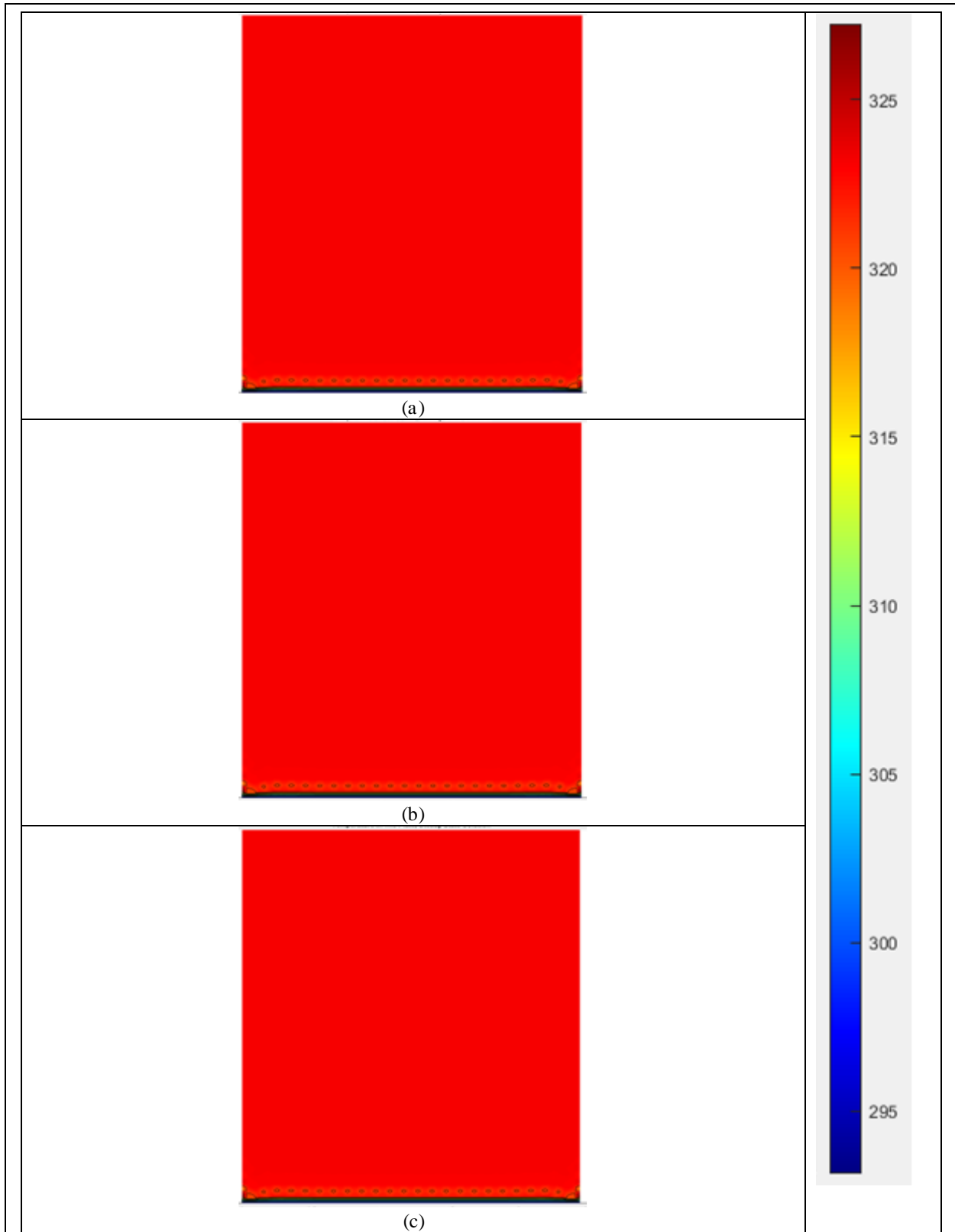


Figure 4.6. Solid 5cm Thick PCM, 5cm Channel Spacing, 30 m/s Wind Speed, $T_{amb} = 323K$
(a) Beeswax (b) Candelilla Wax (c) Soy Wax.

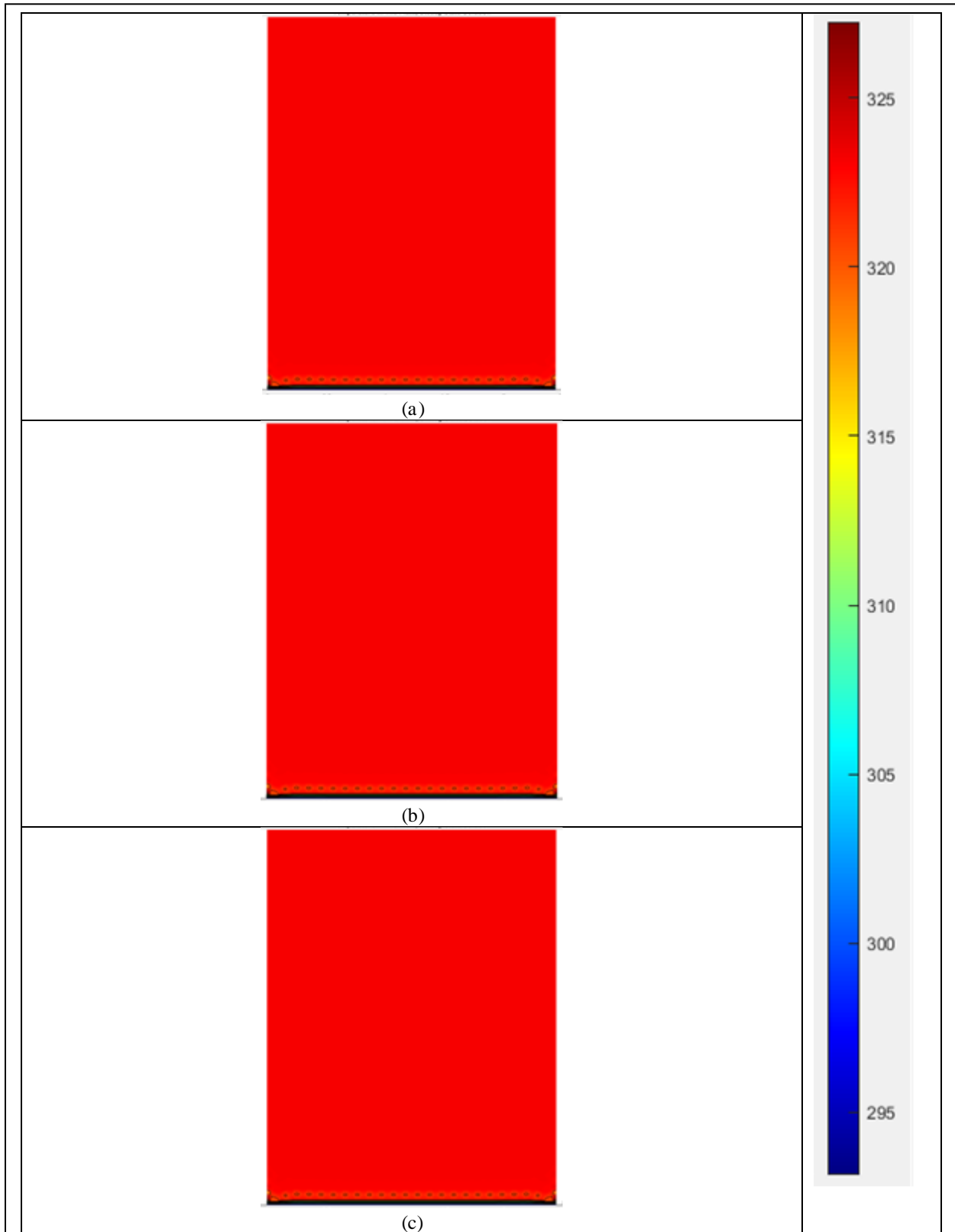


Figure 4.7. Solid 50cm Thick PCM, 5cm Channel Spacing, 30 m/s Wind Speed, $T_{amb} = 323K$
(a) Beeswax (b) Candelilla Wax (c) Soy Wax.

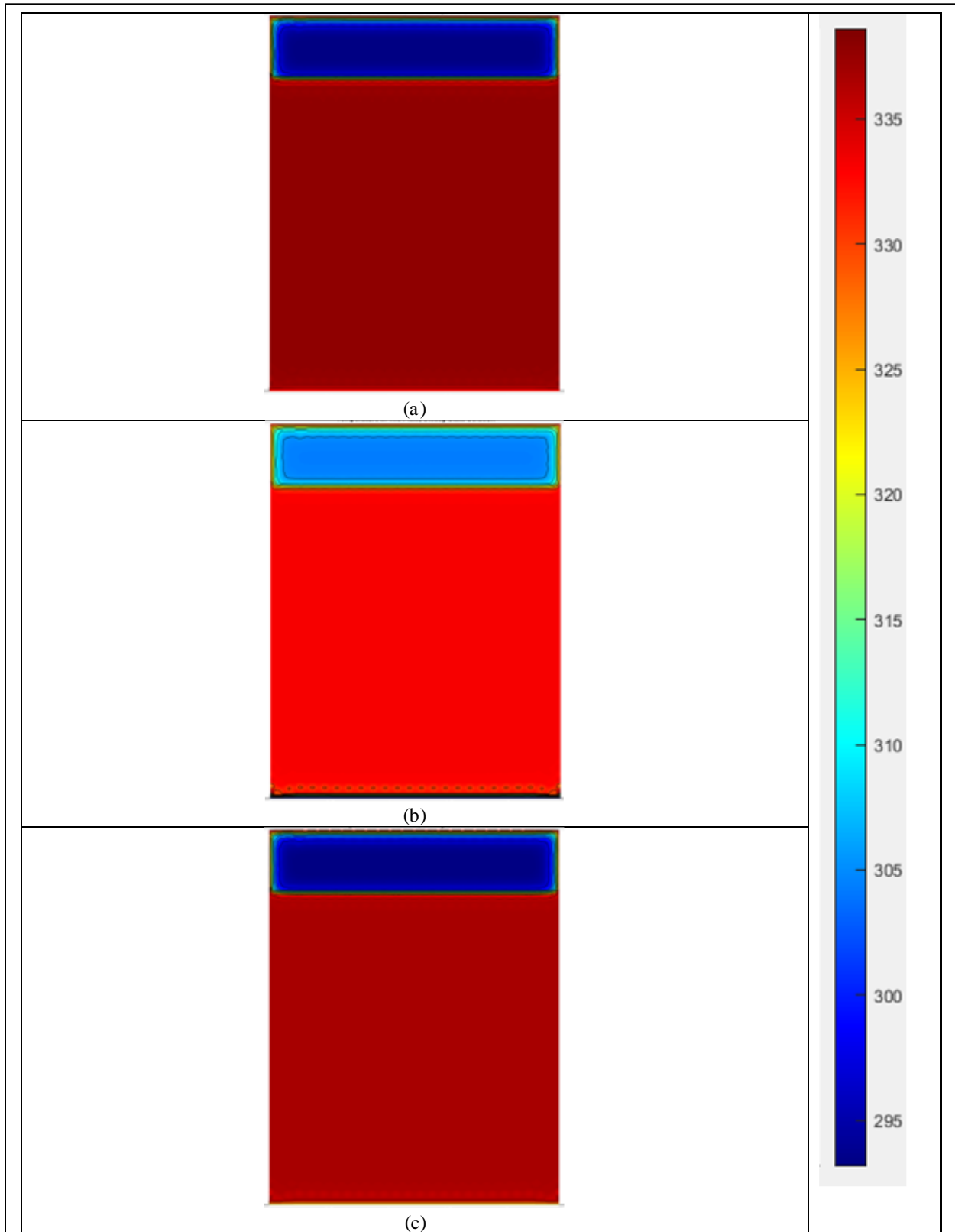


Figure 4.8. Melted 50cm Thick PCM, 5cm Channel Spacing, 30 m/s Wind Speed, $T_{amb} = 333K$ (a) Beeswax (b) Candelilla Wax (c) Soy Wax.

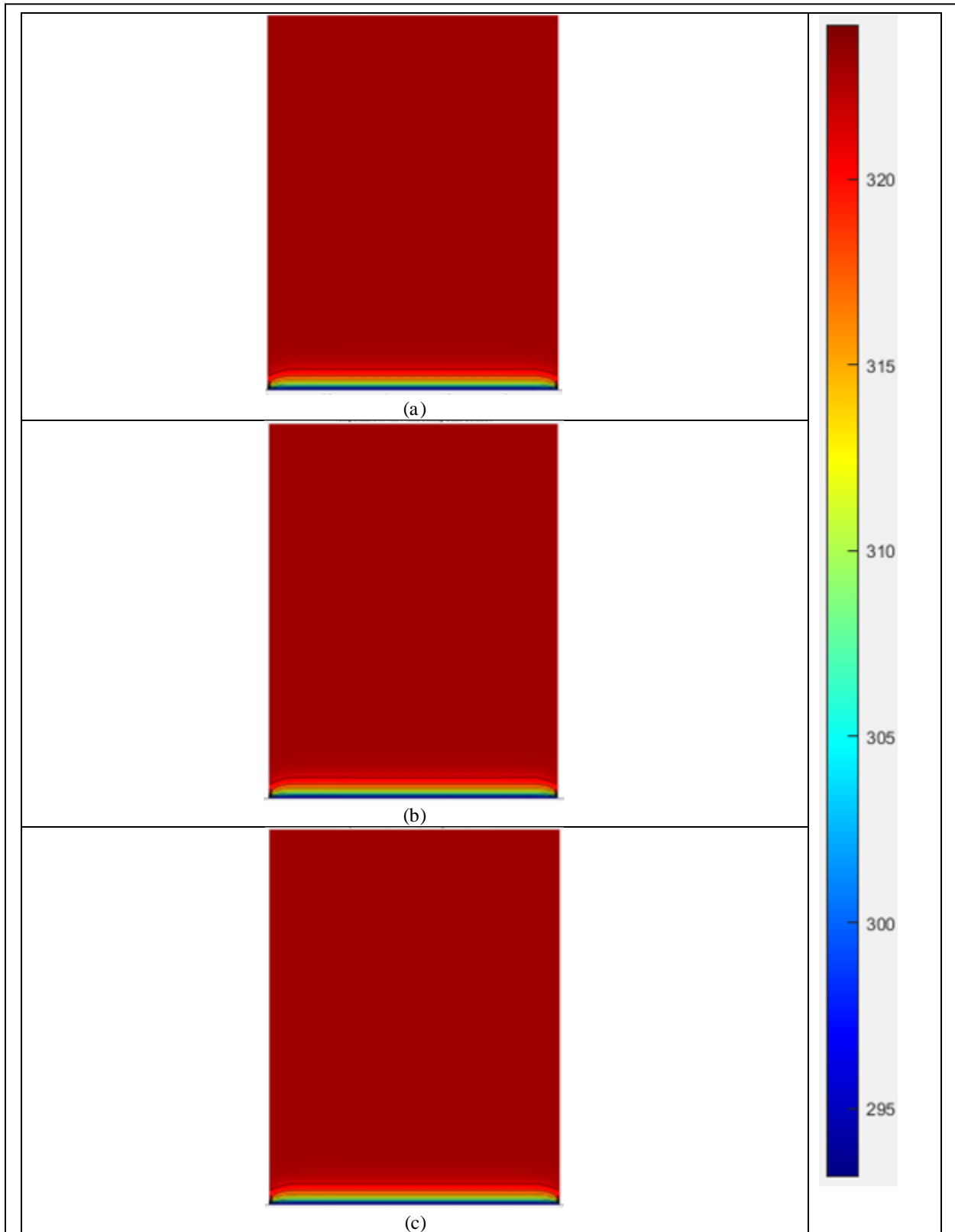


Figure 4.9. Solid 5cm Thick PCM, 50cm Channel Spacing, 0 m/s Wind Speed, $T_{amb} = 323K$
(a) Beeswax (b) Candelilla Wax (c) Soy Wax.

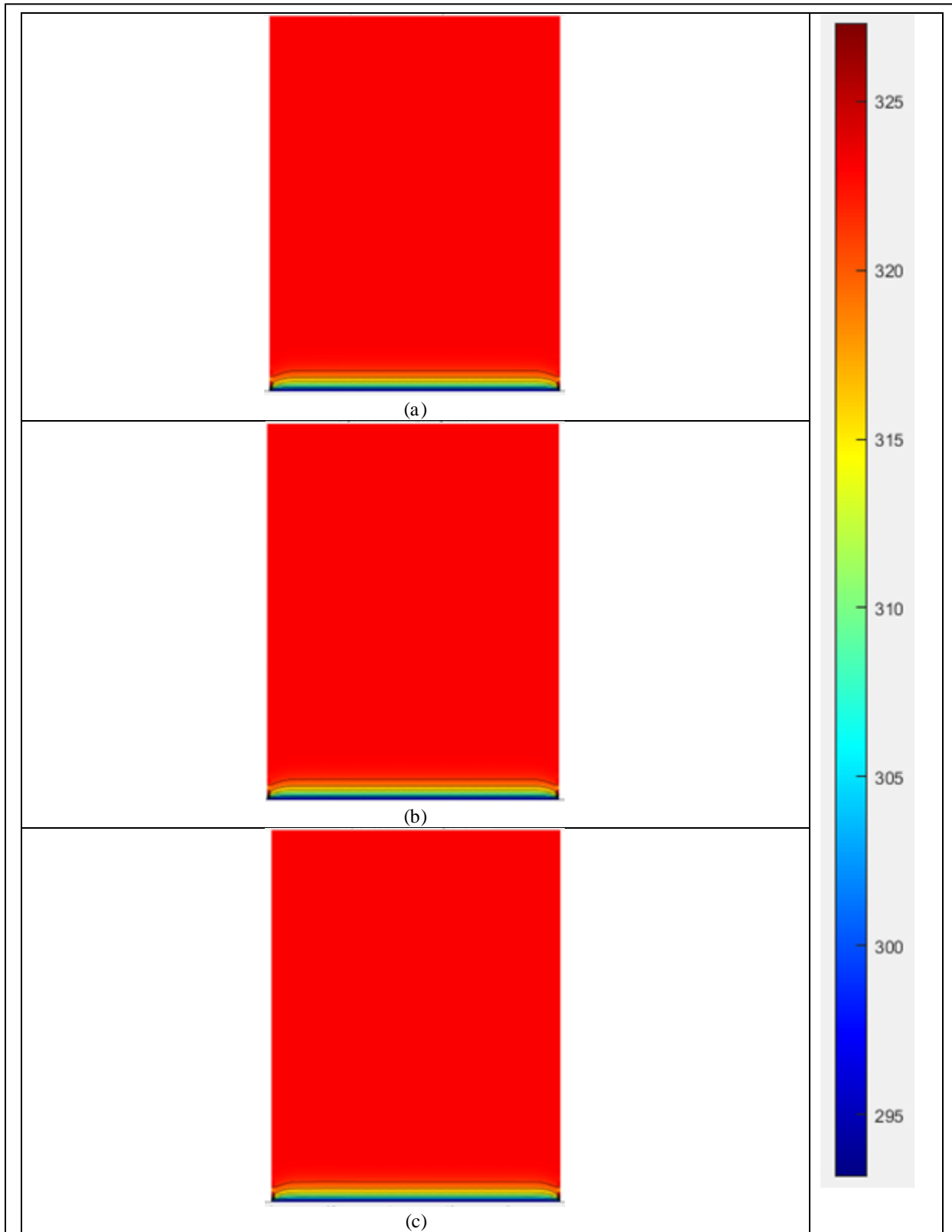


Figure 4.10. Solid 5cm Thick PCM, 50cm Channel Spacing, 30 m/s Wind Speed, $T_{amb} = 323K$ (a) Beeswax (b) Candelilla Wax (c) Soy Wax.

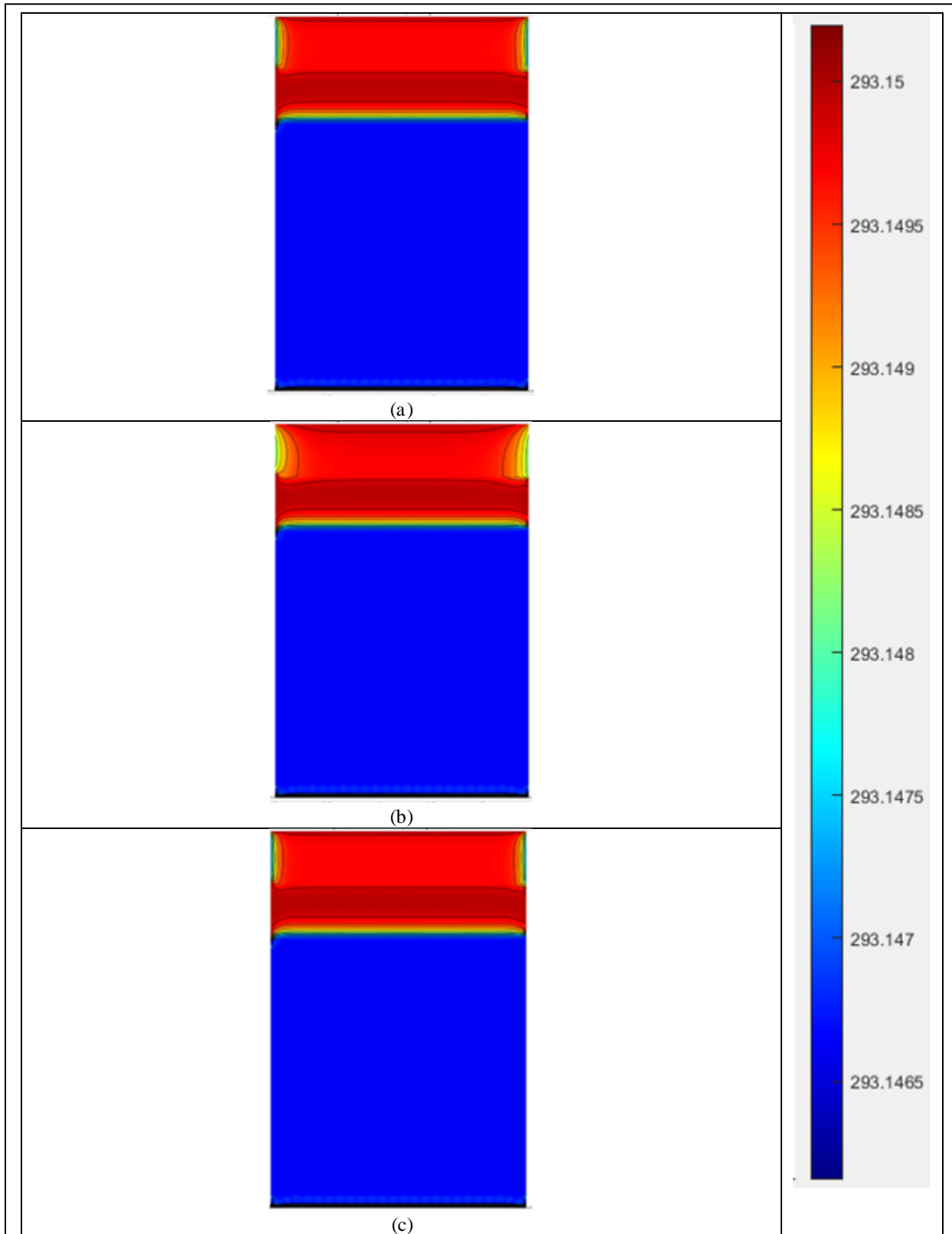


Figure 4.11. Solid 50cm Thick PCM, 50cm Channel Spacing, 30 m/s Wind Speed, $T_{amb} = 323K$ (a) Beeswax (b) Candelilla Wax (c) Soy Wax.

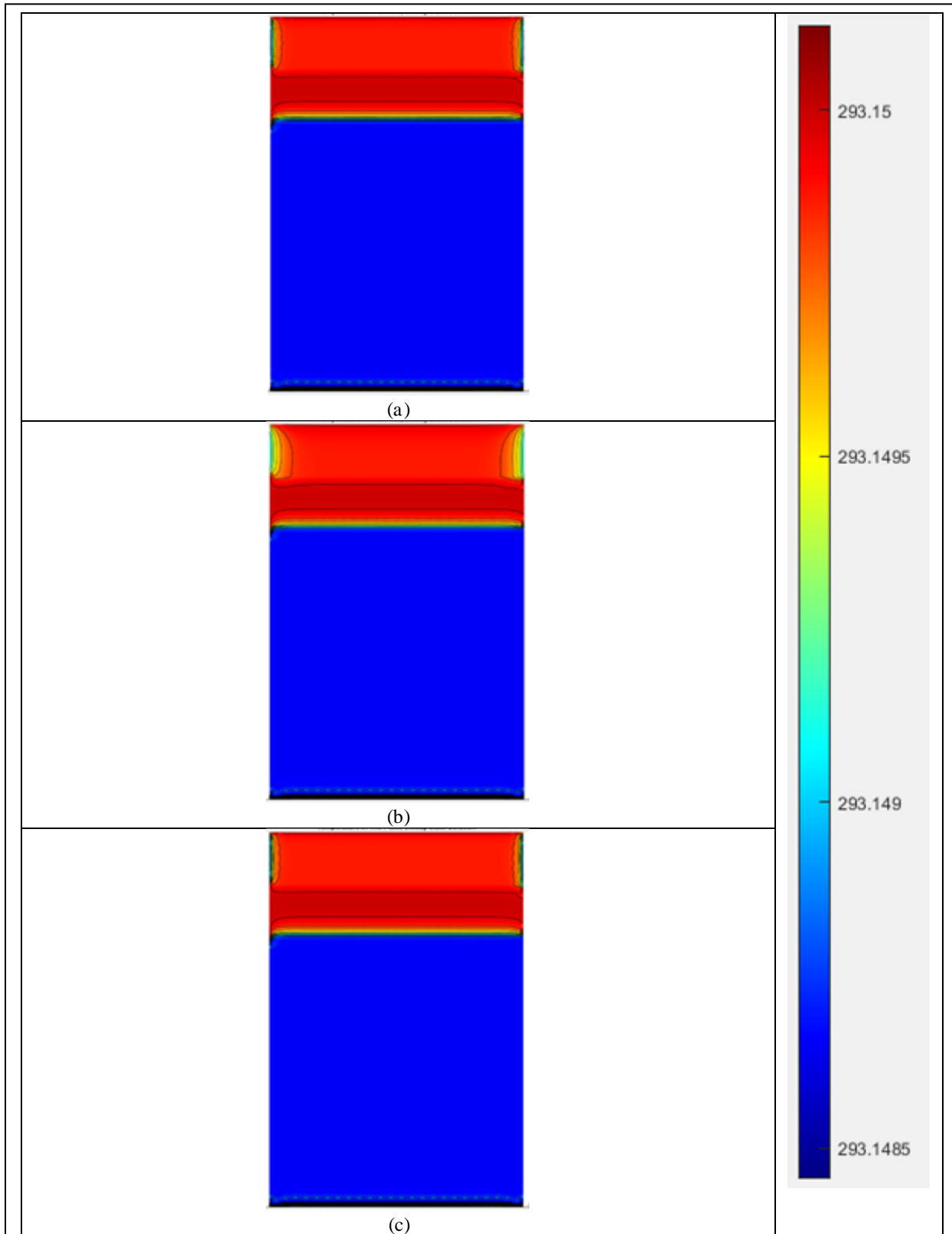


Figure 4.12. Solid 50cm Thick PCM, 50cm Channel Spacing, 50 m/s Wind Speed, $T_{amb} = 323K$ (a) Beeswax (b) Candelilla Wax (c) Soy Wax.

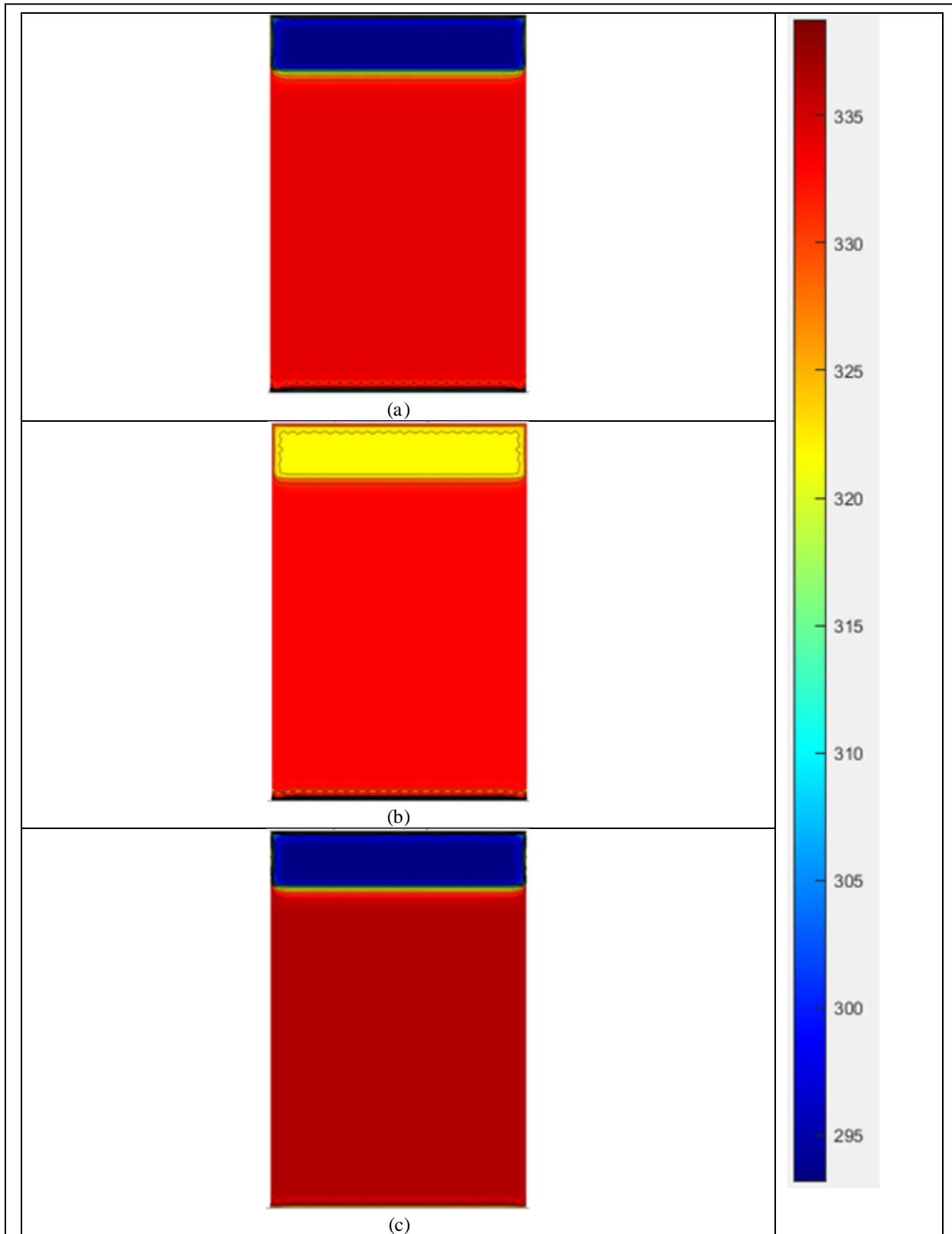


Figure 4.13. Melted 50cm Thick PCM, 50cm Channel Spacing, 50 m/s Wind Speed, $T_{amb} = 333K$ (a) Beeswax (b) Candelilla Wax (c) Soy Wax.

V. THE BIPV-PCM MICROFACILITY BUSINESS MODEL

In the previous chapters the physical viability of the BIPV-PCM facility was examined under high temperature and wind profiles simulating severe weather conditions. In this chapter a business model is proposed for the commercialization of the BIPV-PCM microfacility using the business model canvas (BMC), a popular strategic management technique. The BIPV-PCM microfacility is an application of green technologies that is still relatively novel and will continue undergoing significant improvements as it is optimized. Furthermore, as high temperatures and severe weather events become more pronounced, the problems and needs of potential customer segments will change. Because of its breadth of inquiry, flexibility, and versatility, the BMC is an ideal tool for mapping out a commercialization plan for new and enabling technologies, as well as products and services being offered in a fluctuating market.

Introduction

Although a deep investigation into the thermal performance of the BIPV-PCM microfacility is surely vital to optimizing its design, the importance of understanding how to commercialize this technology cannot be understated. Excellent product concepts often fail because no clear path to commercialization was mapped out to take them from the lab-bench to market. Hence developing a business plan for the proposed BIPV-PCM microfacility product is a critical element for its commercial success. In fact, the number one reason that new businesses fail is the lack of a business plan, and the number two reason is the failure to clearly define their customer segments [78].

There are numerous ways to develop and communicate a business plan, but perhaps one of the simplest and most popular is the BMC. This strategic management tool provides a simple framework for segmenting potential customers according to their needs and problems, then

guides the development of the most efficient value offering and means of utilizing resources and partnerships. One of the other great benefits to the BMC is its versatility. The BMC can be used to develop a concise business plan for any product or service and is easy for virtually any audience to understand. A straightforward business plan is key to driving support and buy-in from investors and other important stakeholders [79]–[82].

Additionally, the BMC is incredibly flexible and can be adjusted to suit fluctuating customer needs or quickly pivot to serve new markets as they arise. In the earliest commercialization stages for a new product or technology like the BIPV-PCM microfacility, being able to rapidly adjust to meet customer needs or compensate for changing market conditions is important at any time but are of heightened importance in the earliest stages of commercialization. The BMC's simple layout and categorization of different components of the plans also helps to illuminate growth opportunities and potential challenges and allows a business to clearly evaluate their strengths and weaknesses. In all, the BMC is a perfect tool to summarize the commercialization path for the BIPV-PCM microfacility.

The Business Model Canvas

The BMC is a popular tool for gathering the most pertinent information and analyzing how these key drivers for the business fit together. There are nine components to the BMC: customer segments, value proposition, channels, customer relationships, revenue streams, key resources, key activities, key partnerships, and cost structures. In addition to collecting and curating a variety of key information into an easy-to-understand format, the BMC illuminates the relationships between different elements visually in a way which other business plan formats typically do not. The flexibility and customer focus of the BMC allows for rapid adjustment to reflect evolving market needs and preferences [79]–[81], [83]–[85].

Customer Segments: Since the primary purpose of a business is to serve the customer, it is of the utmost importance to start by clearly defining who customer segments are for the product. What are the customers' pain points? What are their needs and aspirations? How are they addressing these challenges currently? What problems do the customer want to be solved? Developing a persona for each type of customer and identifying each customer type's goals and pain points is critical in identifying exactly what the value proposition of the product is. Customers do not exist to support a business, but rather the opposite – a business or product can only continue to exist if it is serving the needs of the customer. Customer segments are not limited only to users who will directly generate revenue, they include any product users who are necessary for the business model to be successful.

A company defines, categorizes, and organizes different types of customers into segments to identify the wants and needs of each type of segment. For example, customer segments may have similar pain points and needs, or be separated according to assets, regions, or other slight nuances between the problems the product solves. Conversely, diversified customer segments have radically different customers with unrelated needs and problems. Multi-sided platforms have diversified customer segments that are inter-dependent, such as a newspaper which needs both advertisers and readers to make the business model work. A niche market is one that has highly specialized needs and problems which the product or service caters to, while mass market customer segmentation focuses on a massive group of customers with broadly similar needs [80], [82], [84], [86].

There are a variety of different types of customers, such as end users, decision makers, payers, influencers, recommenders, and saboteurs. End users are the customers who will be using the product or service. However, in many cases the end user does not have decision-making

power over purchases. Although end users may or may not be able to provide any insight into the decision-making process, this customer segment can provide feedback regarding how to improve the usability of the product. The decision maker's role is to make the final decision regarding whether to purchase the product or service, and decision makers are typically highly influenced by the wants and needs of the other customer types – except for the end user. The payer and decision maker may not be the same entity in the customer ecosystem. The payer is usually most influenced by cost and return-on-investment (ROI) and less interested in the wants and needs of other customer types. Influencers take all sorts of forms, but all of them are thought leaders who weigh in on purchases and typically do not hold purchasing power in the customer ecosystem. A recommender on the other hand is an expert that is consulted explicitly to recommend a solution to a problem, who knows the specifications and other factual details about existing solutions and has developed a set of criteria to rank key needs. Finally, the saboteur is a member of the customer ecosystem that does not benefit from the proposed solution and is actively working against its adoption. These are the most common customer types encountered in the sales process of any product or service, though other potential customer types can exist in the customer ecosystem [87].

Value Proposition: The value proposition specifies how the product addresses the needs and desires of each customer segment and creates value. The value provided by a product or service may be qualitative or quantitative, but whatever form the value proposition takes, it delivers a unique mix of elements that satisfy the customer segments' needs and solves their problems. The value proposition is a customized array of benefits the company offers each customer segment. There are a wide variety of forms the value proposition can take, and the value proposition is specific to each customer segment; the same product may have radically

different value propositions for each customer segment.

Value propositions take on a variety of combinations. Some value propositions are directly money-related, such as offering a comparable product at a lower price or offering a product that decreases operating costs for customers. Providing products or services to customers who otherwise lack access to them, or providing customized products and services are also ways to deliver value to different customer segments. Improved performance is a very common way of providing value to customers as well. For example, a product's value proposition for a customer segment may include delivering cost savings to a group that previously was unable to access this type of product while also providing the product at a lower price and with a lifetime service guarantee [79], [81]–[83], [85].

Channels: The methods by which the business connects to the customer through customer touch points influence the overall customer experience and serve to not only deliver the value proposition to customers, but also to help them evaluate the value proposition, purchase products and services, provide customer support and raise awareness of the company's other relevant products and services. Determining the optimal mix of channels to reach specific customer segments is vital for the success of the business model, and be achieved through owned channels, partner channels, or a mix of the two. Owned direct channels such as websites or brick and mortar stores have higher overhead but higher profit margins, while partner indirect channels are less costly to utilize but also lead to lower margins.

Customer Relationships: Customer relationships are established through the channels used to connect with the customer. The type of relationship a company establishes with a customer segment influences the overall customer experience, and numerous relationship types can co-exist between the company and the customer.

Transactional customer relationships are limited interactions between the company and customer for short transactions. A transactional relationship is the shallowest and most temporary form of customer relationship and precludes the development of any kind of deep relationship with the customer. On the other hand, in a long-term relationship the company and customer interact on a recurring basis over a long period of time. This type of long-term customer relationship necessitates the development of a deep relationship between the customer and the company. Self-service and automated customer relationships virtually eliminate the person-to-person interaction between the company and the customer. In a self-service relationship, the supplies are provided to the customer to meet their own needs. Automated services take the self-service customer relationship a step further and simulate a personalized relationship by automating and customizing self-service elements. At the other extreme, customer relationships may be based on providing human interaction in which the customer can communicate with a person or even a dedicated customer representative.

With the ubiquity of social media and general community connectivity in the age of the internet, community building is a contemporary form of customer relationship in which companies tap into or facilitate connections between users to form user communities. This type of customer relationship has the added benefit of providing companies with additional insight into the needs and problems of their customer segments [79], [82]–[84].

Revenue Streams: One of the key success factors for any company is its ability to generate sufficient revenue to meet business needs and potentially expand the business. Revenue streams specify the value that each customer segment is willing to pay for, how customers want to pay, and how much each revenue stream contributes to the overall company bottom line. Each customer segment may generate one or more revenue streams, and each revenue stream may

have its own pricing mechanism.

Perhaps the most popular and well-known revenue stream is the sale of assets – ownership rights to a physical product is sold by the company to the customer. A second common revenue stream is the subscription model, in which continuous access to a service is sold for a recurring fee, such as a monthly magazine subscription. Like the subscription fee revenue model, leasing grants temporary exclusive rights for a customer to use a product for a limited period in exchange for a fee. Intellectual property may be licensed to customers for a fee much like physical property may be leased. There are numerous other forms of revenue streams including brokerage fees, advertising, and usage fees to name just a few [79], [80], [83], [84].

Key Resources: Every business requires resources and assets to function. These resources include all the key needs to deliver on the value proposition to the different customer segments, maintaining positive relationships with customers, reaching different markets via different channels, and so on. The type of business model and value proposition drive the kinds of key resources the company needs to deliver value and continue to grow.

Different value propositions require different types of key resources which fall into 4 main categories. Physical resources include all the physical assets necessary to deliver the product or service. Retail shops, company vehicles, warehouses, manufacturing equipment, distribution facilities, and computer systems are all types of physical resources. Human resources are also key resources for every business model, but for some the human element is especially important to delivering on the value proposition. Brands, patents, proprietary information and knowledge, specialized software, and databases of customer information are all intellectual property resources, and many business models rely on their intellectual property to meet their business and customer needs. Financial resources are a key component for some business models

and may take the form of stock options offered to employees and other stakeholders, financing, or lines of credit for customers, the ability to take out loans, or simply cash. Whatever form they take, specifying the key resources relevant to the customer segment and value proposition is an important element of mapping out the business model [81]–[83].

Key Activities: Every business must take action to deliver on their value propositions and these key activities are necessary for the business to successfully operate. Although key activities include such things as software development, supply chain management, complex problem-solving, or any of a plethora of other possible actions in support of reaching markets, maintaining customer relationships, and ultimately generating revenue, they can be split into three main categories: production, problem-solving, and platform/networking. Production generally covers key activities centered around the design, manufacture, and distribution of typically mass-produced physical products. Problem-solving involves developing innovative solutions to customer problems, such as with design firms and consultants. Many businesses' value proposition is the platform and network they provide their customers, so their key activities revolve around building and improving the platform software and network, branding, customer support, and promoting the platform itself [80], [81], [83].

Key Partnerships: All businesses require partners outside the business to function, and the network of partners and suppliers make up the key partnerships in a business model. Beyond simply listing suppliers and other partners, key partnerships specify the types of key resources and key activities associated with these partners. A company might partner with a manufacturing facility for exclusive production of a product with the understanding that their intellectual property will also be kept secure or cooperate with a company offering a complimentary product to deliver greater value to a shared customer segment. These strategic alliances typically take the

form of a buyer-supplier relationship to ensure the consistent availability of key resources, joint ventures to develop innovative products or businesses, and strategic partnerships.

Although there are numerous reasons two businesses may partner with one another, three key motivations drive most key partnerships: acquisition of resources, risk reduction, or optimization of resources. Most companies rely on other firms to accomplish some of the key activities necessary to deliver on their value propositions, and these strategic partnerships allow a company to extend their capabilities by acquiring knowledge, customers, or simply additional time to deliver on other aspects of the value proposition by licensing software or utilizing independent brokers as a sales force. Other key partnerships take the form of strategic alliances that reduce risk in the competitive environment and allow innovative products to be developed between firms that are otherwise in competition. Perhaps the most familiar form of key business partnership is the buyer-supplier relationship, in which firms share infrastructure or outsource certain activities to optimize their economies of scale [81], [82], [84].

Cost Structures: Creating and delivering value to customers, maintaining customer relationships, acquiring resources, manufacturing and distribution, and all other activities in support of generating revenue and operating under a particular business model incur costs. The cost structure of the business model details the costs of the key resources and activities and determines what costs are most important and required for the business model. Typically, a company's cost structure falls somewhere on the spectrum between a cost-driven or value-driven model. Cost-driven models are oriented around reduction of costs everywhere possible, offering low priced value propositions, extensive outsourcing and automation, self-service, and bare-bones “no frills” services. Value-driven models on the other hand are highly focused on value creation for customers, offering premium and personalized products and services.

Cost structures are characterized by four main attributes: fixed costs, variable costs, economies of scale, and economies of scope. Fixed costs remain constant regardless of the volume of products or services sold and include building rent and annual employee salaries. Variable costs change along with the volume of products or services sold, such as the cost of raw materials used in manufacturing. As a company grows it is more able to purchase materials or services at bulk rates, and these economies of scale decrease overall costs to deliver on the value propositions of the various customer segments. As the company expands its scope of operations, company assets such as branding or company activities such as marketing and advertising support a variety of value and product offerings [80], [81], [83], [84].

The BIPV-PCM Microfacility BMC

Although a deep investigation into the thermal performance of the BIPV-PCM microfacility is surely vital to optimizing its design, the importance of understanding how to commercialize this technology cannot be understated. New technologies can gain market momentum largely due to the clear definition of a business plan and customer segments. Thus, a critical element of the BIPV-PCM microfacility analysis is the development of a BMC for the microfacility [78].

Customer Segments: The BIPV-PCM microfacility is a small, somewhat mobile building that employs unique energy-generating features and sustainable materials. In the most general sense, customers could feasibly include anyone who utilizes small modular buildings for virtually any purpose. Currently, customers that use modular small-footprint buildings are using shipping containers and other small buildings that require various outfitting to be used for their intended function. Examples of potential uses of the BIPV-PCM microfacility include vertical farms, modular storage units, “portable” rooms, small walk-up businesses, or temporary shelters.

The key differentiating features of the BIPV-PCM microfacility are the incorporation of onsite renewable energy sources and sustainable materials. The potential market can be separated into customer segments that value environmentally friendly products or whose branding relies on eco-friendliness. Secondary customer segments include environmentally conscious consumers who seek out “eco-friendly” and “green” products. The customer segments focused on in this BMC are Hannah, the environmentally conscious business owner, and Eddie, the green-branded business owner. Although Sharon and Alex, the green products consumers, are considered in this analysis, they are not customer segments specifically targeted.

Hannah is an environmentally conscious small business owner who has a genuine desire to reduce their carbon footprint because they are deeply concerned about climate change and its adverse effects on the weather, ecosystems, and the planet at large. Hannah has disposable income from their career which they have used to “green” their own home with solar panels, water-saving plumbing, rainwater collection, etc. The small businesses Hannah owns tend to utilize environmentally practices and incorporate green technologies whenever possible. This customer segment finds value in green technologies like the BIPV-PCM microfacility specifically because it reduces carbon footprint and energy used by the building, and because the types of materials used in the PCM are sustainable and in most cases plant-based. Hannah represents a key customer segment because their goal is to make the greatest positive impact on the environment and are actively seeking ways to do so.

On the other end of this customer segment spectrum is Eddie, whose business relies on green marketing and making sales to environmentally conscious end users. Eddie’s company brand and marketing angle are revolving around attracting end customers who appear to be environmentally conscious. For Eddie, the environmental impact of their business is secondary to

being able to point out visible solar panels or a “plant-based, vegan, organic” certification to their customers. Green-branded business owners like Eddie are less concerned about environmental impact and more interested in being outwardly “green.” Thus, using visible PV panels and being able to boast about their use of sustainable, or even “vegan and organic” PCM in the building is an important value-add for this customer segment. Eddie also represents a key customer segment because even though the actual performance of the BIPV-PCM microfacility may be of lesser importance to them, they are still actively seeking out ways at the very least be environmentally friendly.

These two customer segments represent opposite ends of a spectrum, and customers within the “environmentally conscious business owners” may fall anywhere on this spectrum. both these customer segments are likely to seek out sustainable materials and renewable energy sources to incorporate into their buildings, but their motivations and personal reasons for “going green” are very different.

An additional customer segment would include customers who make purchases at the BIPV-PCM microfacility, which may include a diverse customer base depending on the application of the microfacility. As global temperatures and the frequency of severe weather events increase, more and more people are expressing increasing concern about the state of the environment and taking steps to “green” their homes and lifestyles. The demographics and background of these climate concerned people varies radically and includes people of all ages, races, religions, financial status, etc. Market research conducted for this work indicates that although people of all economic backgrounds have genuine climate change concerns, financial barriers often prevent their transition from climate concerned person to climate concerned

consumer. Since financial barriers are likely to persist, this end-user customer segment can be split into two main groups.

Sharon represents the first group of green consumers. Sharon is a financially privileged consumer who can purchase high-end luxury items and afford to be selective about which stores and businesses they support. Sharon actively seeks out businesses that visibly utilize green technology, but the depth of their research into the actual environment impact of the business is typically shallow. Alex represents the other end-user customers, who are highly enthusiastic about supporting environmentally friendly businesses and products whenever possible but find these types of products inaccessible due to exceedingly high costs. Alex jumps at the chance to support green initiatives wherever possible when affordable but is limited by available funds.

Both Sharon and Alex represent niche markets that highly value green technologies, products, and services of virtually any variety. However, Alex will be more cost-driven than the financially privileged Sharon segment. Since Alex does not traditionally have access to green technologies, purchasing from businesses that do utilize these types of environmentally friendly measures is a fair alternative and helps meet the need to reduce their cumulative carbon footprint. For products such as the BIPV-PCM microfacility, both Alex and Sharon support and purchase from “green” businesses but neither of them are not directly affected by the cost of the microfacility itself. Instead, this niche customer segment finds value in the sustainable PCM used with the energy generating solar panels and the innovative environmentally friendly design and is more inclined to make purchases at this type of facility based on their shared desire to support environmentally conscious businesses.

Value Proposition: The key differentiator between the BIPV-PCM microfacility and other shipping container-type facilities is the energy efficiency offered by the incorporation of

the PV-PCM system, sustainable materials for PCM, and a very limited amount of cooling to the interior of the building. This design can be optimized for specific uses as well; for example, although vertical farms in shipping container style facilities already exist on the market, few of them include solar panels and none incorporate sustainable PCM specifically to improve PV performance. Although there is considerable overlap between these customer segments, Eddie's emphasis on the visibility versus Hannah's focus on their cumulative environmental impact means these customer segments do not have the same value proposition.

For Eddie, green branding is a key part of their marketing strategy, and supporting this need must be a key part of the value proposition for this customer segment. Two key elements of the value proposition are key for Eddie. First, designing the BIPV-PCM microfacility so that the PV panels and PCM chamber are very visible to anyone walking up to the facility. Next, using sustainable plant-based materials which meet vegan and organic standards in a certifiable way should be included in the value proposition of the BIPV-PCM microfacility. The overall high-tech, sleek design of the microfacility and the technical novelty of the use of PCM may also deliver value to Eddie's more high-end or tech-savvy customers. Ultimately, Eddie is less concerned about the magnitude or quality of the environmental impact they are making by utilizing green technologies in their business and more concerned with drawing in customers like Sharon and Alex. The value proposition for this customer segment should focus on the lower energy overhead costs, high visibility of the PV panels, and PCM that is vegan, organic, plant based, and sustainable. Hannah is more interested in making the most positive environmental impact. The use of PV panels coupled with sustainable materials that further improve performance are also strong value propositions for this customer segment because they deliver a lower carbon footprint using sustainable materials as well as green energy generation. The value

proposition for both these customer segments should also include up-front costs that are competitive with other small footprint facilities without PV options.

Business owners have three general options for small-footprint buildings: spend upwards of \$40,000 on a modular building, spend time and funds updating a \$5,000 shipping container to be usable and aesthetically pleasing to customers, or invest in a BIPV-PCM microfacility that meets small-footprint building needs and is ready to use. More than 75% of customer segments represented by either Hannah or Eddie are likely to choose the BIPV-PCM microfacility for the next facility they purchase. However, less than 25% of customer segments represented by Eddie and less than 40% of customer segments represented by Hannah are likely to switch from their existing facility to the BIPV-PCM microfacility, primarily due to high switching and sunk costs.

Additionally, ensuring that the BIPV-PCM microfacility technology is convenient to use is a key element of a strong value proposition for both customer segments represented by Hannah and Eddie. When asked what reasons they might avoid using innovative green technologies, it is expected that a 50% or more of the segment represented by Eddie and 40% or more of the segment represented by Hannah will cite lack of confidence in the long-term performance of the PV panels or other green technology.

Channels: Shipping and delivery of the BIPV-PCM microfacility itself will be a shared channel between these two unique customer segments. The transport of small-footprint buildings and shipping containers is common, and there is extensive infrastructure in support of this type of delivery and installation. Typically, the microfacility unit will be transported via shipping partners that handle both truck and rail freight.

After-sales customer support must be available to both segments to ensure that the facility is continuously running smoothly and to build customer rapport through personalized

maintenance service. Customer support will take place through traditional phone/call center service as well as through a company-owned website that includes live-chat during limited business hours and e-mail support. Finally, a limited maintenance and service warranty should be in place to reduce the overall risk customers are taking with the BIPV-PCM investment and to build customer confidence in the product.

Customer Relationships: The customer relationships with Sharon and Alex are limited. In the event there are some consumers, upon the purchases of a BIPV-PCM microfacility, who are interested in the functionality of the product or have questions about the sustainable PCM used, the company's webpage will have a FAQ section that shares relevant information, and this information may also be accessed through customer support channels. The bulk of this customer relationship is expected to be purely for informational exchange, providing support for and fostering an online community. This community may be developed either through existing social media platforms or potentially through the company webpage. The green end-user community formed from queries by Alex and Sharon is a significant value-add for both Eddie and Hannah customer segments. The relationship with this customer segment is limited to assisting with questions and information. However, this generally low-cost investment may help Sharon and Alex transition into green business owners at some point in the future. Luckily, user communities are not novel, and it is relatively easy and virtually free to host one on social media platforms such as Facebook, Discord, and Twitter. For instance, in the earliest stages, a dedicated Discord server and a Facebook group and company Twitter account can be utilized to directly reach users and answer questions, along with e-mail responses and queries through the company website. A simple FAQ page can be included on the website to collect and summarize questions from social media and other channels into a centralized online location. This simple FAQ page may

eventually turn into a wiki or other large informational database. Additionally, communities built to educate consumers like Sharon and Alex about the BIPV-PCM microfacility are an added asset to both business owners Hannah and Eddie because they can provide insight into the needs of green business supporters and trends within this community.

For both customer segments represented by Hannah and Eddie, minimizing switching costs and developing personalized long-term relationships are key. Developing long-term relationships requires a dedicated customer success team that makes regular contact with Hannah and Eddie or their employees to check on the performance and satisfaction with the BIPV-PCM microfacility. Since Hannah and Eddie have invested in a higher cost microfacility, building a long-term relationship will require a high level of customer service to compensate for the switching costs they have incurred. This “human element” coupled with consistent monitoring of the quality delivered and proactively seeking to understand evolving customer needs will foster positive relationships and long-term loyalty. Lowering switching costs for these customer segments is also crucial, whether the business owner is utilizing the BIPV-PCM microfacility to reduce their carbon footprint or strengthen their green branding.

Many of the current small-footprint buildings on the market do not utilize PV panels or any other extraneous features; perhaps the closest existing product is the “tiny house” which has become increasingly popular in the past few years. Many of these residential homes are installed with PV panels and built in shipping containers of various sizes and orientations. A shipping container facility typically costs less on average than other standard brick and mortar buildings. Shipping containers themselves are low cost (approximately \$5,000 for 20’ container), but they have exceptionally thin walls and require additional outfitting such as insulation and paneling to manage thermal effects and to make the interior more aesthetically pleasing. A very simple “tiny

home” style 20’ shipping container home with solar panels costs \$21,000 or more, depending on what other amenities are included. The proposed BIPV-PCM microfacility has minimal interior amenities and does not include features such as composting toilets or interior rooms, both to reduce manufacturing costs and to allow maximum versatility to end users that will use the microfacility for a wide variety of applications [88], [89]. Modular buildings tend to have a slightly larger square footage and are overall higher cost than the approximately 160 square foot shipping container microfacility. For example, Boxx Modular quoted a 10’ by 36’ modular building at \$45,000 [90]. To make the BIPV-PCM microfacility an attractive option to these customer segments, providing a microfacility that addresses their unique needs at a cost range of \$21,000 to \$45,000 is imperative.

Revenue Streams: Revenues will stem primarily from the sale or rental of the physical BIPV-PCM microfacility. The customer segment represented by Hannah is likely willing to purchase at a higher price because of their dedication to reducing their carbon footprint coupled with the added benefits in the value proposition (strong personalized customer and user support, limited-service warranty, and market insight through the user community). This customer segment is also more likely to switch existing buildings for the BIPV-PCM microfacility if the switching costs are within their budget and will request retrofit designs more readily. Eddie, the green business owner focusing on green branding, is more likely to choose facility features which are the lowest cost but the most immediately visually obvious to their customers. However, Eddie-type customers will be less likely to seek out retrofit designs or switch existing buildings to the BIPV-PCM microfacility unless the switching costs are exceptionally low.

Additional revenue streams may develop from licensing the designs for and retrofitting of the PV-PCM to existing small-footprint buildings. Hannah-type customer segments will certainly

express an interest in this application, and new, as-yet unexplored customer segments may also be drawn in by the possible versatility of the retrofit option. However, retrofitting existing buildings with BIPV-PCM will require designer's expertise and a fully functional thermal model, which is not deeply explored in this work.

Key Resources: The partnerships formed to produce and distribute the BIPV-PCM microfaciltiy are very important resources for realizing this business model. It is unlikely that the firm itself will be mass-producing the microfacilities or transporting them from the factories to their destination. Hence the importance of these key manufacturing and distribution relationships cannot be understated.

Human resources are also a key part of the revenue stream for this business model. Offering microfacility buyers and users a personalized customer service is vital for building strong long-term customer relationships, as well as fostering a thriving community of people interested in supporting green technologies. Additionally, the intellectual property surrounding the design and optimization of the PV-PCM system as well as retrofitting existing small-footprint facilities with these features are key resources vital to the success of this business model.

Key Activities: For this business model, manufacturing and distribution are outsourced to other companies with more expertise in these areas. Thus, the key activities for this business involve developing unique designs of the BIPV-PCM microfacility that solve the customers' problems and meet their needs as well as providing customer support post sale.

Optimizing the performance and eye-catching design of the PV-PCM elements as well as emphasizing the benefits and sustainability of PCM are the most important actions for successfully realizing this model in the short term. To optimize the BIPV-PCM microfacility's

power and thermal performance, a more precise mathematical model is needed. This updated model should be able to simulate PCM thicknesses and channel spacings under varying ambient temperatures, shifting wind speeds, and over the course of days or through seasonal cycles. Thermal performance is considered optimized when the facility design allows for the system to be kept at temperatures between 16 and 25°C as discussed in Chapter 4.

After thermal and power performance optimization, design adjustments to improve the visibility of the green technology and increase the aesthetic appeal of the microfacility while still maintaining thermal and power performance can begin. First the optimized BIPV-PCM microfacility is shown to focus groups of the different customer segments to get their feedback on the appearance of the facility. This feedback is used to adjust the aesthetic of the BIPV-PCM microfacility based on this used feedback, then the performance of this updated design is checked against the optimized thermal and power performance baseline. The aesthetic design of the BIPV-PCM microfacility is considered optimized once at least 60% of the focus group either describes the microfacility design as “green,” “high tech,” “sleek,” or “solar powered”, or if they make further inquiry about system performance or cost.

Aiming to solve retrofitting design problems for customers to expand the licensure of this IP as well as expanding the company website to include community building capabilities are key activities in the longer term. Expansion of the company website to include more community building capabilities is a relatively low-cost investment, but its success is driven by the engagement and health of the community. The Matlab “Mathworks” forum is one such healthy online community formed for informational purposes that requires very little funding to maintain but a large amount of consistent community buy-in. However, every online community develops its own culture over time. Shifting users from social media platforms to the company website

forums may be a challenge. Further market research into the sociological habits of online forums and customer segments represented by Sharon and Alex should be performed to determine whether an informational user forum on the company website should be offered concurrently with mainstream social media platforms, or if the initial community touchpoint should exclusively be done through free social media platforms.

Retrofitting design issues would need to be solved by in-house designers, and a very flexible and well-defined mathematical model for generating accurate simulation needs to be developed in support of these efforts. The retrofit would still be a niche service offering but would expand the potential customer base substantially. However, due to the skill necessary to optimize unique retrofitted designs, the salaries for BIPV-PCM retrofit designs would cause relatively high overhead costs. Additionally, the customer segments for the BIPV-PCM retrofit would be different from those discussed in this work, and they warrant future investigation.

Key Partnerships: Some of the most important partnerships include manufacturing partners who provide the shipping container building shell and build the PV-PCM that is incorporated into the building. Shipping container manufacturers use raw materials to create the container itself, while shipping container suppliers source containers from manufacturers. Most shipping container manufacturers (and thus suppliers) are in China and India. To save transportation costs, containers will be sourced from US domestic manufacturers such as W&K Containers, Inc. and American President Lines, both headquartered in California [91] and USA Containers in Utah [92], [93]. One of the key reasons to partner with shipping container manufacturers is to include them in the design of the PCM chamber and take advantage of bulk raw material purchasing where possible.

Suppliers of the PV panels and mass quantities of the sustainable PCM are also key

partners. The PV panels and PCM partners will be US-based. Although there are numerous US solar manufacturers, many of them source a significant amount of their PV materials from overseas. Lumos, Mission Solar, and Solar Tech Universal are all US-based companies that manufacture the most or all of the silicon-based PV panels in the US, and are based in Colorado, Texas, and Florida, respectively [94]–[96]. PCM manufacturers for the selected PCM types that manufacture beeswax, candelilla wax, and soy wax are ideal partners as well, so that all PCM can be purchased in bulk from one supplier. Jedwards International, Inc. in Massachusetts and Hase Petroleum Wax Co. in Illinois both manufacture all these PCM wax types [97]. Additionally, there are a few plant based PCM manufacturers in the US, such as Advanced Cooling Technologies in Pennsylvania and Phase Change Solutions, Inc. in North Carolina, who are developing “tunable” PCM for a plethora of applications [98], [99].

Additionally, the distributors capable of transporting shipping containers and small buildings are vital partners necessary to make this business model work. Partnering with other firms like Boxx Modular based in Texas who mass produce specialized small-footprint facilities such as modular buildings [90]. Existing modular vertical farm manufacturers like Grow Pod Solutions, Inc., Freight Farms, Inc., and FarmBox Foods in California, Massachusetts, and Colorado, respectively, are also potential future partners [100]–[102].

Cost Structures: This business model is primarily value-driven even though the customer segments are likely to be cost-driven. This business model positions the company as a designer and broker of the PV-PCM technology. The value provided to all customer segments is the BIPV-PCM microfacility itself followed by personalized customer support and a user community that provides a repository of useful information about the product and insight into the customer base. The fixed costs in support of this business model are limited and include salaries

for designers, salespeople, and customer support specialists. Variable costs are high, with the manufacturing, distribution, and customer care costs increasing with the sales volume.

As the company expands, economies of scale in the purchase of raw PV panels and large volumes of PCM will decrease variable operating costs related to manufacturing. The user community, information repository, and broader education of potential end users on climate change and the benefits of sustainable building materials will be served by economies of scope as the company continues to grow.

The costs associated with the manufacturing of the BIPV-PCM microfacility include the raw materials and labor costs, as well as any tool upkeep negotiated by the manufacturing company. Any injection or other molds needed for any portions of the BIPV-PCM facility typically must be purchased in advance of large-scale manufacturing. Costs associated with the distribution of the microfacility may include both truck and train freight. If any of the materials are manufactured outside of the US, taxes, tariffs, and other import and customs fees must also be considered.

PV panels designed to work with the 20' shipping container facility will require some specialized mounting frames or brackets, and incorporating this number of panels will likely benefit from some design optimization of the panels themselves by the panel manufacturer. Beyond manufacturing and shipping costs, customer service and designer salaries are significant expenses associated with the BIPV-PCM microfacility purchasing and rental revenue streams. Additional costs of maintenance and repair are incurred with microfacility rentals, and licensure requires careful IP protection, and the financial ability exert this IP protection when necessary.

The Overall BMC for the BIPV-PCM Microfacility

The business model canvas that was developed in this chapter for the BIPV-PCM microfacility is shown in Figure 5.1. The BMC diagram combines the elements discussed in this chapter into a quick visual reference. The business model created in this chapter for the BIPV-PCM microfacility examines the desirability, viability, and feasibility of the microfacility as a product, and develops a strategy for delivering value and generating revenue. In all, the BIPV-PCM microfacility concept is attractive to certain niche markets, but the design is still immature and requires further development before it can be realistically commercialized.

Although the three-box model developed in Chapter 4 was primarily run in the steady state, transient solutions were used to make a more definitive comparison between channel spacing, PCM type, and PCM thickness. These results are shown in Table 5.1 and confirm that candelilla wax delivers the lowest interior building temperatures as compared to the other PCM types under the same ambient temperature (323K) and wind speed (30 m/s). Transient comparison also confirmed that thicker PCM delivers better performance, however, under the same wind speed the channel thickness did not appear to have an appreciable effect.

Table 5.1. Interior Building Temperature for Transient Solution at 0.005s.

PCM Thickness and Channel Spacing	Beeswax	Candelilla Wax	Soy Wax
50cm PCM, 50cm Channel	315K	312K	319K
5cm PCM, 50cm Channel	312K	312K	316K
50cm PCM, 5cm Channel	313K	312K	316K
5cm PCM, 5cm Channel	317K	312K	318K

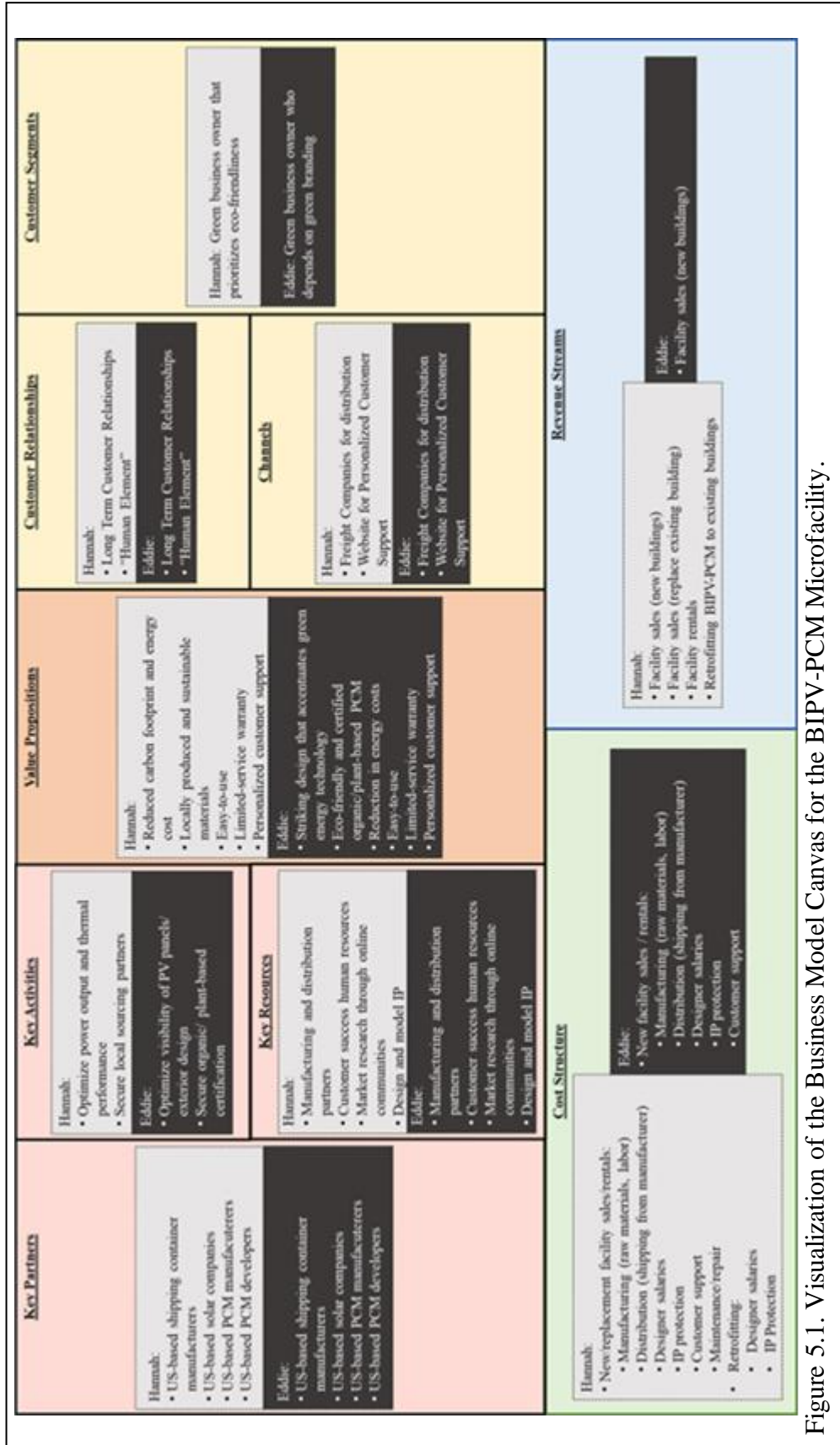


Figure 5.1. Visualization of the Business Model Canvas for the BIPV-PCM Microfacility.

VI. CONCLUSION AND FUTURE WORK

Conclusions

Photovoltaics are perhaps one of the most well-developed and widely used green energy technologies on today's market. However, incorporating PV panels into buildings or coupling them with phase change materials to mitigate negative thermal effects and improve generation performance are still a relatively new area. In this work, a simplified BIPV-PCM facility was investigated starting from an in-depth look at the mathematical basis for thermal modeling of such systems and concluding with the development of a commercialization plan. This work was motivated by alarming concerns about increasing global temperatures and the severe weather that these growing temperatures will cause.

Chapter 2 explored the mathematical foundations for modeling conduction, radiation, convection, and phase change in extensive detail. The depth of understanding developed in this chapter was invaluable in forming a computationally efficient but useful thermal model in Chapter 4.

Chapter 3 investigated global temperature rise and severe weather events, as well as the ways these environmental factors affect the BIPV-PCM microfacility. This chapter started with the incident solar radiation followed by an in-depth look at numerous environmental factors that influence the performance and thermal behavior of the BIPV-PCM microfacility system. Environmental features such as cloud cover, relative humidity, and heat waves were carefully reviewed to determine the ways they would affect the thermal performance of the BIPV-PCM system, and then transformed into mathematical expressions that approximately simulated these environments. This chapter also described how real-world historical weather data from 1970 through 2015 was randomized into data sets that were pre-processed to simulate increasing

global temperatures and more frequent severe weather events caused by the rising temperature over a 30-year period.

In Chapter 3, key variables influencing the thermal behavior of the BIPV-PCM microfacility were investigated. The most relevant variables for the model developed in later chapter are the amount of solar radiation reaching the panel, the wind speed, and the ambient temperature. That is, extreme weather events were translated into wind speeds and ambient temperatures the microfacility was exposed to. Maxima and minima of the real-world data sets were also used to guide the values for wind speed, convection coefficient, solar radiation, and ambient temperatures for the case studies of the BIPV-PCM microfacility used in the three-box model developed in the next chapter.

Chapter 4 developed the three-box model of the BIPV-PCM microfacility based on the first principles discussed in Chapter 2 and the detailed analysis of the environmental effects on the - microfacility in Chapter 3. This model simplified the BIPV-PCM microfacility system into three key layers: the PV-PCM, the air channel between the PV-PCM and the building, and the building itself. The Matlab software was limited regarding generating complex geometries and lacked the ability to define boundary conditions between subdomains.

The three-box model developed and simulated in Chapter 4 is simplified to suit the limitations of the software while still providing useful information. Despite the model's simplicity, its result still allowed for comparison between different PCM types and, to a limited degree, the effects of high winds and temperatures on the facility. Four geometries of the BIPV-PCM microfacility were simulated under various temperature and wind conditions, and the performance is compared. The results indicate that thicker PCM and wider channel spacing lower interior temperatures within the facility and for the PV panel surface more than thinner

PCM or narrower channel spacing. Furthermore, these results indicate that BIPV-PCM microfacility will still require additional forms of cooling to maintain comfortable interior operating temperatures.

In Chapter 5 the business model canvas was applied to the BIPV-PCM microfacility technology. The main reason new businesses fail is a failure to map out a business plan, followed closely by not having well-defined customer segments. Since a business exists to provide value for the customer, the BMC begins with clearly defining different customer segments as well as their problems and needs, and these customer segments guide the rest of the thinking through customer touch points, partnerships, activities, and cost and revenue structures. Despite the immaturity of the BIPV-PCM microfacility and the limitations in the three-box model, this technology shows incredible promise. The design of the BIPV-PCM microfacility may be improved by developing a more complex thermal model and using more sophisticated simulation tools. However, even in the absence of further optimization, this green technology shows great promise and marketability.

Future Research Opportunities

There are numerous ways that the BIPV-PCM microfacility may be further improved to deliver even greater value to customers:

- Developing a better model than the rough three-box model developed in this work.
- Incorporating other green technologies such as geothermal or wind energy technology into the design.
- Designing building geometries that optimize power generation and thermal control in specific types of environments.
- Developing key partnerships with other technology manufacturers and designers.

- Exploring other types of sustainable PCM.
- Partnering with PCM developers to “tune” PCM performance to specific environments and customer needs.
- Expanding into unique applications for the microfacility, potentially by partnering with the military or global nonprofit organizations.

APPENDIX

Appendix A: Vertical Farming

Vertical farming (VF) is gaining increased popularity despite its high initial costs. It addresses a number of these issues simultaneously by producing a greater quantity of food in a smaller amount of space using less water and virtually no pesticides. Likewise, PV and other “green energy” technologies are becoming more widespread in part because they are becoming more efficient, cost effective, and commercially available. Techniques such as building integration, the inclusion of technologies such as PCM, and complimentary combinations of green energy generation also serve to make PV an increasingly viable option, especially in VF applications.

The concept of vertical farming is not novel. In 1966 Othmar Ruthner patented an apparatus for year-round farming in a 3-dimensional setting, and in 1970 a 4-year trial of this type of multi-layer farming was conducted [103]. However, vertical farming as it is known today – with artificial lighting for large-scale farming in warehouses and skyscrapers – was not presented to the public until the late 2000s by Dr. Dickson Despommier. A parasitologist by trade, Dr. Despommier began seriously investigating vertical farming in 2001 for a number of reasons: first because of the lackluster results of a rooftop garden project, next as a means of preventing the spread of parasitic infections, and finally because of growing concerns about food insecurity and, specifically, vulnerability within food supply chains [103], [104].

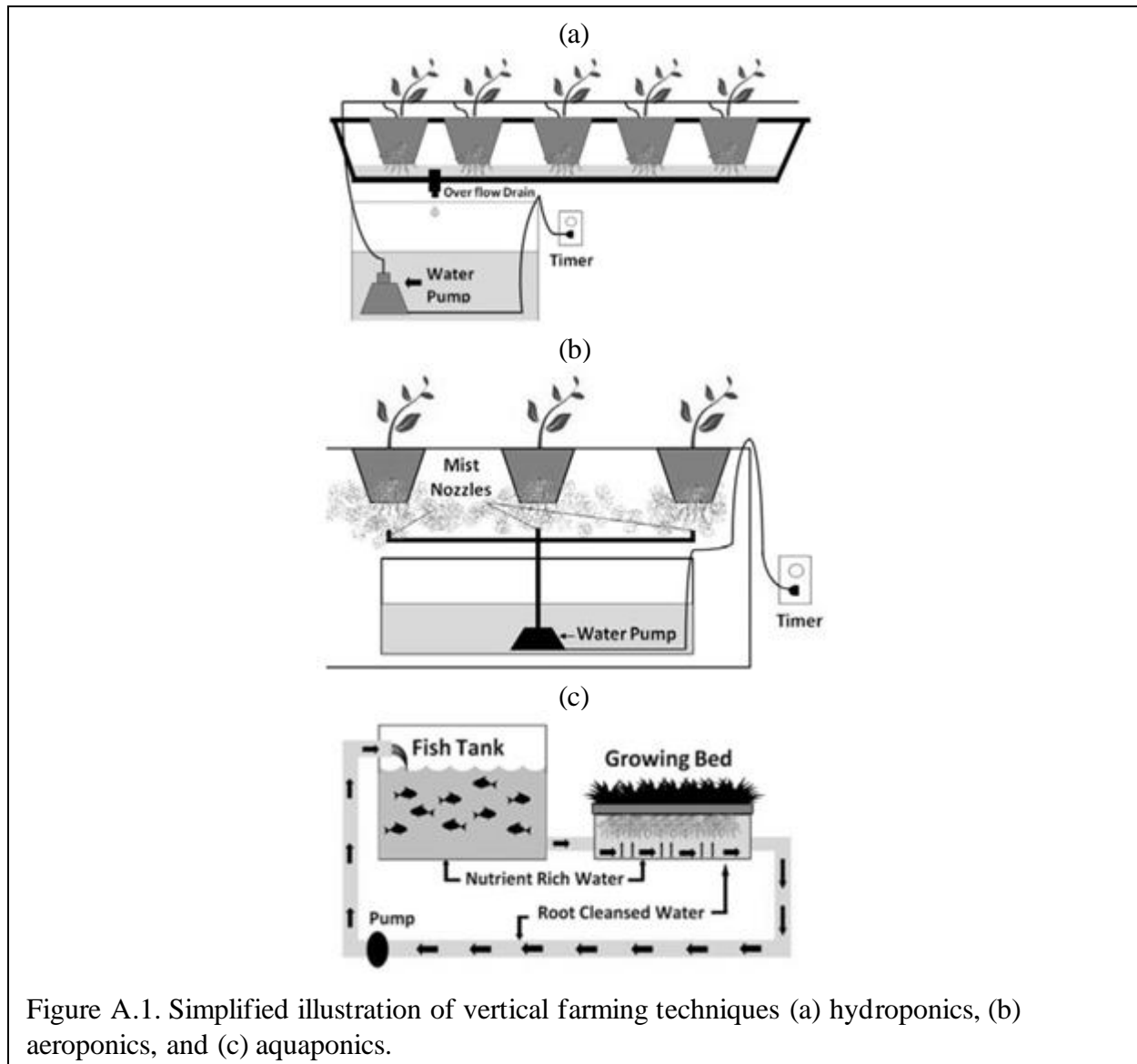
Vertical farming is a relatively straightforward concept: stack layers of food plants on top of one another so a greater amount of food can be produced in a smaller amount of horizontal space. The five essential things a plant needs to grow are appropriate temperatures, light, water, air, and nutrients. Growing food plants indoors is by no means simple and despite decades of

investigation the mechanisms by which plants interact with nutrients and their environment are not well understood. Significant work has been performed in pursuit of achieving optimal crop yields and nutritional quality, ranging from genetic engineering [105] to employing root-associated bacteria and fungus [106] to selectively breeding more nutrient efficient plants [107] and beyond. As light-emitting diodes (LEDs) have become more efficient and cost effective, they have become increasingly attractive for vertical farming applications [108]. In fact, determining optimal wavelengths of light to promote plant growth is a subject of intense research [109]–[111]. Providing the right mix of macro-nutrients (e.g., nitrogen and others found in traditional fertilizers) and micro-nutrients (e.g., the trace minerals drawn from fertile soil) presents unique challenges as well [112]. Despite these obstacles, vertical farming is gaining popularity globally to address growing concerns about food insecurity and climate change [103].

Methods by which food plants may be grown vertically include hydroponics, aeroponics, and aquaponics. Each of these methods involves providing a controlled environment free of pests and seasonal temperature changes, sufficient light, and appropriate water and nutrients to the plant roots. These growing methods are differentiated primarily by the way that the nutrient solution is delivered to the roots and where the nutrients themselves originate. Perhaps the most well-known method is hydroponics, wherein plants are grown in an inert substrate such that roots can access water with dissolved micro and macro nutrients. Aeroponics on the other hand forego the inert growing medium in favor of regularly spraying root systems with a mist of nutrient-enriched water vapor. Finally, aquaponics incorporates fish farming for nutrient production as a part of a closed-loop hydroponic growing system. Each of these methods uses less water than traditional horizontal and greenhouse farming systems. Hydroponics is by far the most widespread methodology used in the commercial realm, while aeroponics uses the smallest

amount of water and has been shown to enhance nutrient uptake, and aquaponics offers a closed-system that does not require external nutrients to be added to the system [113]. Each of these methodologies is illustrated in its most basic form in Figure A.1.

The benefits of vertical farming are monumental, especially in the face of the many



problems such as climate change and food supply insecurity that humanity faces over the next several decades. Chiefly among the benefits of vertical farming is the ability to form closed loop systems which can conserve 70% of the water used in the system [14]. Aeroponics, specifically, conserves up to 95% of the water utilized in the system. Furthermore, vertical farming provides a

controlled environment throughout the year, protecting crops from adverse weather conditions which are estimated to account for roughly 90% of crop losses according to the US Department of Agriculture [14], [103]. Vertical farming allows crops to be grown regardless of the season so that food can be produced year-round, while virtually eliminating the need for pesticides and herbicides [103], [113]. Cities and urban centers are also rapidly increasing in size and by 2050 roughly 70% of the human population is projected to live in cities [114]. Vertical farming allows food to be grown in urban centers, reducing transport distances and food spoilage [113].

Hydroponics uses significantly less water than traditional farming and is the most widely commercialized growth technique with a variety of prefabricated systems available on the market. Furthermore, hydroponically grown plants have been shown to grow faster, ripen earlier, and have higher yields than traditionally grown plants. Aeroponics was developed by NASA and can conserve up to 95% of the water used in the system. Plants grown using aeroponic techniques have been shown to absorb minerals more efficiently and may potentially yield crops with higher nutritional content. Aquaponics eliminates the requirement for nutrient solution to be replenished and includes the production of farmed fish in addition to food crops [14], [103], [113].

Of course, vertical farming is not free of flaws. Foremost are the exorbitant initial costs, which can be on the order of millions or hundreds of millions of dollars depending on the square footage utilized [14]. Interior controlled environments require lighting, which increases electricity needs significantly, driving up initial and operating costs and increasing the carbon footprint [14], [113]. Fast-growing crops like basil and lettuce are the most frequently grown crops in vertical farms because they are the most profitable, but other (slower growing crops like grains) can certainly be grown using vertical farming techniques [113].

Hydroponics requires that the nutrient solution be adjusted to suit the needs of the different types of plants being grown, and that this solution be periodically replenished [112]. Like hydroponics, the aeroponics technique requires specialized nutrient solutions to feed the crops, but also that the droplets of the nutrient solution used and the frequency with which the plant roots are misted are carefully monitored [115]. Finally, aquaponics also requires careful management of the nutrient solution delivered to the plants as well as careful management of the fish farming component of the system [116].

Interest in vertical farming has increased internationally over the past few decades as climate change has started adversely affecting crops and weather while water becomes scarcer and the global population's food needs continue to climb [14]. In 2020, the global vertical farming market was estimated at US\$3 billion but is projected to grow to an estimated US\$10.4 billion by 2027, with the greatest growth in China, Japan, Canada, and Germany [117]. This growth is truly cutting edge; in March 2021 the Germany-based Infarm received another US\$100 million in investment funding, bringing their overall funding to over US\$400 million [118], but this level of funding is not uncommon [119] and growing increasingly frequent, especially in the wake of the Covid-19 pandemic [120].

Interest in renewable energy sources has grown as technology has improved and become more cost effective. Renewable energies such as wind turbines and PV panels have found their way into all sorts of applications including residential neighborhoods, manufacturing plants such as semiconductor wafer fabs [121], [122], and in isolated areas beyond the reach of existing electrical grids [123]–[125]. A quick Google search reveals that renewable energy has been applied successfully to modular vertical farm facilities available on the commercial market, though the design incorporating PV and other energy generation technologies into these facilities

is typically proprietary. To date it does not appear that any commercial VF manufacturers have incorporated PCM into the design of their facilities, most likely because PV panels enhanced with PCM for thermal management is still a relatively new area of research. Furthermore, while the existing PV-equipped VF modules on the market have building applied (BA) panels, none of the panels are incorporated into the building envelope of the module itself. Finally, while there have been studies on how temperature and weather may affect the power, efficiency, and lifetime of solar panels, it appears that no studies have explicitly investigated how increasingly frequent extreme weather events influence these factors.

Appendix B: Microgrids

Microgrids are a part of the US Department of Energy's initiatives to improve power quality and reliability, increase energy efficiency, and provide independence from the main grid [126]. However, this technology is by no means new or unfamiliar; the earliest microgrid was built in 1882 by Thomas Edison, and universities have utilized microgrids to handle their electrical needs for many years now [127].

A microgrid is a self-controlled power distribution system designed to balance electrical flows to meet power needs. Microgrids are localized power distribution systems that may operate independently of the main electrical grid and can be designed to meet specific system needs. Balancing and management of the voltage, current, power, loads, and storage devices are an integral part of microgrid operations [121]. Microgrids have been gaining interest in the US and internationally because of their ability to serve very remote regions that do not have access to large-scale power distribution systems [123], [124], and because they offer redundancy (a "backup") to the main grid [128]. Connected microgrids can exchange electricity with the main grid, and island microgrids operate fully in an independent mode with no electrical connection to the main grid.

The loads of a generalized production facility can differ substantially from those of the residential sector which has relatively constant power needs. A given production facility is assumed to operate 24 hours a day, 7 days a week, and its varying loads are dominated by seasonal patterns.

For the purposes of this work, the power needs of a general production facility are assumed to follow a seasonal pattern but otherwise be randomized [121]. A VF is something of a hybrid between the residential and the manufacturing facility case in that the power needs for

lighting (and pumps, etc.) for the growing chamber will be relatively stable through the year, but the power needs for environmental control and the input power from the BIPV will vary with the seasons and other environmental conditions. To determine seasonal loads for the VF case, electrical information will be collected from a local shipping contained VF (Hemphill Farms in Maxwell, Texas). These figures will be used as an initial guideline for power needs in the VF case and will include anomalous results from the historic freeze in the area over February 2021. Both distribution-based and worst-case design methodologies are employed to address with seasonal variations with the knowledge that worst-case scenario-based designs are often over-engineered and more costly [121].

The aim in microgrid design is to properly size the generator and capacity to meet a set of design objectives, such as minimizing cost or maximizing PV power output. Typically, microgrid design methods are classified into two main areas: deterministic and probabilistic models. In probabilistic models, the power input, the electrical load, or both these variables behave randomly. In deterministic models the power and electrical load are presumed to be constant. Between the two methodologies for microgrid design, probabilistic models have been shown to more accurately reflect the real-world behavior of distributed generation systems that incorporate intermittent energy sources such as PV [121].

Among the benefits microgrids offer is the ability to deliver electricity independent of the main utility grid. When a microgrid is used with renewable energy sources such as wind turbines and PV panels, the risk of blackouts is dramatically reduced [122]. Generally the electrical power used in a microgrid is generated nearby, virtually eliminating voltage drop and power loss issues common when transmitting electricity over long distances [121]. Additionally, microgrids are designed for specific applications and may be optimized to suit these specific needs, thus

reducing investment costs.

Microgrids are however not a “silver bullet” that can solve all the issues surrounding power needs. First, microgrids coupled with intermittent power sources require energy storage devices which take up space, generate heat under operation, can be costly, and are often made of materials that are not environmentally friendly [128]. Estimation of load needs are also based on historical data which may or may not accurately reflect power needs in the future [121]. Additionally, microgrid design requires a certain level of expertise that may not always be available in a given location, such as in isolated areas far from the main grid [129]. The site and size of the distributed generation system must be carefully designed in order to reduce power losses and improve reliability of the microgrid [123]. Finally, the main barriers to widespread adoption of renewables-based microgrids are the high cost of upfront investment and the intermittency of the power that is supplied [122].

As of the end of 2020, it was estimated that 1.3 billion people – more than 15% of the total global population – do not have access to electricity. Despite this gap in electricity access, global energy demand is expected to increase by 28% between 2020 and 2040 [130]. Microgrids have been employed in isolated and rural areas that are distant from established electric grid infrastructure or are in areas that make building a larger grid exceedingly difficult [123]. Microgrids are also gaining popularity as renewable energy technologies and climate change concerns become more ubiquitous, as microgrids can provide some redundancy and protection against severe environmental events and can adjust to compensate for the variable input energy from renewable energy sources like solar panels and wind turbines.

Furthermore, the inner workings of each of the vertical farming types have slightly different requirements and there are biological factors that must be considered when finalizing a

VF design which are beyond the scope of this work. Thus, the power needs for the special case of the VF are limited to maintaining a temperature control within the container in response to the external environment and providing sufficient power to meet the constant lighting needs of a shipping container VF.

Microgrid design for facilities powered by renewable energy technologies like PV and wind turbines can be challenging because of their nonconstant input power. Although power networks for generalized production facilities and residential buildings have some similarities, they have a few key differences [121]. First, voltage drops for production facilities are not an issue because the power is produced in proximity to the facility. Next, distributed generation planning for production facilities is usually a one-time event as power needs tend to remain essentially stable over time. Finally, production facilities are presumed to own the power generation units (in this case PV panels) and can adjust the load as desired.

A microgrid is designed for each of the thermally optimized production facilities determined via thermal modeling and simulation. To ensure this work is most broadly applicable in future research, the island microgrid will be designed for a generalized production facility with randomized power needs. Microgrids will be tested and optimized under the ramping-up, randomized extreme weather event conditions with the goal of ensuring functionality in coming decades as climate change effects intensify further.

PV-powered vertical farms have specialized needs that can differ from a generalized facility, which are centered around providing constant lighting and constant temperature ranges within the facility throughout the year. Although the lighting requirements are constant year-round, controlling the temperature in the growing environment is highly coupled to the temperature and weather conditions of the external environment. Thus, the VF case serves as an

interesting problem in microgrid design because of its dependence on local weather and temperature changes that take place much more rapidly than day-night or seasonal cycles.

The software used for the microgrid design will be limited to MatLab as, again, this is a popular and widely accessible software package. Microgrid design requires mixed-integer nonlinear programming (MINLP), and a variety of solvers have been designed. Table B.1 provides a list of open-source solvers that are currently available, each of which uses the LP-BB (LP-based branch-and-bound) algorithm.

Table B.1: Open Source MINLP Solvers

Solver Name	Interface	Language
COCONUT	AMPL, GAMS	C
COUENNE	AMPL, C++, GAMS	C++
SCIP	AMPL, C, GAMS, MATLAB, OSiL, ZIMPL	C

Appendix C: Radiation

Radiation Intensity: Since radiation may be emitted in all directions, it is generally most sensible to use spherical coordinates to describe the behavior of surface radiation. When a differential surface area, dA_I thermally emits in some direction and subtends a differentially small solid angle, $d\omega$ (in steradian, sr) as defined from dA_I . The differential area, dA_n , a distance r from the emitting area, dA_I , is found by multiplying the solid angle $d\omega$ by the radius, similarly to the way an arclength may be found in two dimensions. This differential area may also be related to the spherical coordinates as [20], [49]:

$$dA_n = r^2 \sin\theta d\theta d\phi = r^2 d\omega \quad \text{Eq. C. 1}$$

The spectral intensity, $I_{\lambda,e}$, is the rate at which radiant energy emitted of wavelength λ emitted in the (θ, ϕ) direction per unit area of the emitting surface normal to this direction ($dA_I \cos\theta$), per unit solid angle ($d\omega$), per the unit wavelength interval ($d\lambda$) centered around λ , and has units of $\frac{W}{m^2 \cdot sr \cdot \mu m}$:

$$I_{\lambda,e}(\lambda, \theta, \phi) \equiv \frac{dq}{dA_I \cos\theta \cdot d\omega \cdot d\lambda} = \frac{dq_\lambda}{dA_I \cos\theta \cdot d\omega} \quad \text{Eq. C. 2}$$

Here, $dq_\lambda \equiv \frac{dq}{d\lambda}$ has units of $\frac{W}{\mu m}$ and expresses the rate that energy of wavelength λ leaves dA_I and passes through dA_n . Rearranging yields:

$$dq_\lambda = I_{\lambda,e}(\lambda, \theta, \phi) dA_I \cos\theta d\omega \quad \text{Eq. C. 3}$$

If the spectral intensity, $I_{\lambda,e}$ is known, the foregoing expression allows calculation of the rate that the radiation emitted by the surface is propagated into the area subtended by solid angle $d\omega$ in the (θ, ϕ) direction. Further substitution allows the spectral radiation flux associated with dA_I to be expressed as:

$$dq''_\lambda = I_{\lambda,e}(\lambda, \theta, \phi) \cos\theta \sin\theta d\theta d\phi \quad \text{Eq. C. 4}$$

The heat flux due to radiative emission into any solid angle or over any (finite) wavelength interval may be found if $I_{\lambda,e}(\lambda, \theta, \phi)$ is known.

Emission: Emissive Power quantifies the amount of radiative energy emitted per unit of surface area, and Spectral Emissive Power, E_λ , expresses the rate that radiation with wavelength λ is emitted from a surface in all directions, per unit wavelength $d\lambda$ about λ :

$$E_\lambda(\lambda) = \int_0^{2\pi} \int_0^{\pi/2} I_{\lambda,e}(\lambda, \theta, \phi) \cos\theta \sin\theta d\theta d\phi \quad \text{Eq. C. 5}$$

The Total Emissive Power, E , is rate of radiative emission of all wavelengths in all directions:

$$E = \int_0^\infty E_\lambda(\lambda) d\lambda = \int_0^\infty \int_0^{2\pi} \int_0^{\pi/2} I_{\lambda,e}(\lambda, \theta, \phi) \cos\theta \sin\theta d\theta d\phi d\lambda \quad \text{Eq. C. 6}$$

The intensity of radiative emission or, $I_{\lambda,e}(\lambda)$, for a diffuse emitter is entirely independent of direction, and thus the spectral and total emissive power for a diffuse emitter are, respectively:

$$E_\lambda(\lambda) = I_{\lambda,e}(\lambda) \int_0^{2\pi} \int_0^{\pi/2} \cos\theta \sin\theta d\theta d\phi = \pi I_{\lambda,e}(\lambda) \quad \text{Eq. C. 7}$$

$$E = \pi \int_0^\infty I_{\lambda,e}(\lambda) d\lambda = \pi I_e \quad \text{Eq. C. 8}$$

Where I_e is the total intensity of the emitted radiation.

Irradiation: The spectral intensity of incident radiation, $I_{\lambda,i}$, is the rate at which radiant energy of wavelength λ is incident on a surface from the (θ, ϕ) direction per unit area of the surface normal to this direction, per unit solid angle about the (θ, ϕ) direction, per unit wavelength interval $d\lambda$ about λ – just like with the spectral emission for emission [49]:

$$I_{\lambda,i}(\lambda, \theta, \phi) \equiv \frac{dq}{dA_1 \cos\theta \cdot d\omega \cdot d\lambda} \quad \text{Eq. C. 9}$$

Irradiation quantifies the incident radiation flux from all directions, and spectral irradiation, G_λ , refers, perhaps unsurprisingly, to the rate of irradiation of wavelength λ per unit wavelength

$d\lambda$ about λ , incident of a surface per unit area of the surface, or:

$$G_{\lambda}(\lambda) = \int_0^{2\pi} \int_0^{\pi/2} I_{\lambda,i}(\lambda, \theta, \phi) \cos\theta \sin\theta d\theta d\phi \quad \text{Eq.C. 10}$$

And the Total Irradiation is:

$$G = \int_0^{\infty} G_{\lambda}(\lambda) d\lambda = \int_0^{\infty} \int_0^{2\pi} \int_0^{\pi/2} I_{\lambda,i}(\lambda, \theta, \phi) \cos\theta \sin\theta d\theta d\phi d\lambda \quad \text{Eq.C. 11}$$

Again, irradiation of diffuse surfaces offers some simplifications, and the spectral and total irradiation can then be expressed as, respectively [20], [49]:

$$G_{\lambda}(\lambda) = \pi I_{\lambda,i}(\lambda) \quad \text{Eq.C. 12}$$

$$G = \pi I_i \quad \text{Eq.C. 13}$$

Radiosity: Finally, radiant energy leaving the surface must be accounted for, and is termed radiosity. Radiosity includes the reflected portions of the irradiation as well as emitted radiant energy. Spectral radiosity, J_{λ} , quantifies the rate at which radiant energy leaves a unit area of the surface at wavelength λ , per unit wavelength $d\lambda$ about λ , and includes radiant energy associated with emission and reflection leaving in all directions, or:

$$J_{\lambda}(\lambda) = \int_0^{2\pi} \int_0^{\pi/2} I_{\lambda,e+r}(\lambda, \theta, \phi) \cos\theta \sin\theta d\theta d\phi \quad \text{Eq.C. 14}$$

And the total radiosity is then:

$$J = \int_0^{\infty} J_{\lambda}(\lambda) d\lambda = \int_0^{\infty} \int_0^{2\pi} \int_0^{\pi/2} I_{\lambda,e+r}(\lambda, \theta, \phi) \cos\theta \sin\theta d\theta d\phi d\lambda \quad \text{Eq.C. 15}$$

Once again, for diffuse surfaces, $I_{\lambda,e+r}$ is independent of direction and the expressions for spectral and total radiosity become, respectively:

$$J_{\lambda}(\lambda) = \pi I_{\lambda,e+r} \quad \text{Eq.C. 16}$$

$$J = \pi I_{e+r} \quad \text{Eq.C. 17}$$

Appendix D: Further Notes on Modeling Convection

To utilize convective thermal transport effects in a way that improves system performance, a deep understanding of the development and modeling of velocity, thermal, and concentration boundary layers is beneficial.

Velocity Boundary Layer and Conservation of Mass: Conservation of mass dictates that matter can neither be created nor destroyed, but only transformed from one type to another. In terms of convective fluid flow, this means that the difference between the rate of matter flowing into a differential volume and the rate of matter flowing out is equal to the rate of matter increasing within the differential volume element. Presuming a homogenous fluid density, ρ_f , the mass stored within the differential volume, \dot{M}_{st} may be expressed as:

$$\dot{M}_{st} = \frac{\partial}{\partial t} (\rho_f dx dy) = \frac{\partial \rho_f}{\partial t} dx dy \quad \text{Eq. D.1}$$

The rate at which mass enters the x -face of the differential volume is $\rho_f u dy$, and the rate at which mass leaves the $(x + dx)$ -face of the differential volume is $\left[\rho_f u_f + \frac{\partial}{\partial x} (\rho_f u_f dx) \right] dy$.

Likewise, in the perpendicular direction these rates can be expressed as $\rho_f v_f dx$ and

$\left[\rho_f v_f + \frac{\partial}{\partial y} (\rho_f v_f dy) \right] dx$, respectively. Combined these express the conservation of mass

through the differential volume:

$$\rho_f u_f dy - \left[\rho_f u_f + \frac{\partial (\rho_f u_f)}{\partial x} dx \right] dy + \rho_f v_f dx - \left[\rho_f v_f + \frac{\partial (\rho_f v_f)}{\partial y} dy \right] dx = \frac{\partial \rho_f}{\partial t} dx dy \quad \text{Eq. D.2}$$

With some rearranging this becomes the Continuity Equation, which must be satisfied at every location within the velocity boundary layer:

$$\frac{\partial \rho_f}{\partial t} + \frac{\partial (\rho_f u_f)}{\partial x} + \frac{\partial (\rho_f v_f)}{\partial y} = 0 \quad \text{Eq. D.3}$$

Newton's Second Law states that the net force acting on a differential mass element must equal the time rate of change in momentum of the fluid, or in simplest terms $\vec{F}_{net} = \frac{\partial \vec{p}}{\partial t}$.

Although a wide variety of forces may act on the differential volume, they take the form of either body forces proportional to the volume, or surface forces proportional to the surface area of the differential volume. Body forces may be resolved into x and y components and components of these forces per unit volume may be expressed as X and Y , respectively. Surface forces include fluid static pressure, p , and viscous stresses which can be separated into normal (σ_{ii}) and shear (τ_{ij}) components. The fluid static pressure is equivalent to the force applied normal to a face of the differential volume divided by the surface area of this face and exists within the fluid even when it is not in motion. Normal and shear stresses arise only when the fluid is in motion, and the subscripts on these variables refer first to the direction normal to the differential surface and then to the direction of the applied force. It should be noted that normal stresses lead to a linear deformation of the volume element, while shear stresses cause an angular deformation of the differential volume, but both types of stress are tensile rather than compressive. It has also been shown that [49]:

$$\sigma_{xx} = 2\mu \frac{\partial u_f}{\partial x} - \frac{2}{3}\mu \left(\frac{\partial u_f}{\partial x} + \frac{\partial v_f}{\partial y} \right) = 2\mu \frac{\partial u_f}{\partial x} - \frac{2}{3}\mu (\vec{\nabla} \cdot \vec{v}) \quad \text{Eq. D.4}$$

$$\sigma_{yy} = 2\mu \frac{\partial v_f}{\partial y} - \frac{2}{3}\mu \left(\frac{\partial u_f}{\partial x} + \frac{\partial v_f}{\partial y} \right) = 2\mu \frac{\partial v_f}{\partial y} - \frac{2}{3}\mu (\vec{\nabla} \cdot \vec{v}) \quad \text{Eq. D.5}$$

$$\tau_{xy} = \tau_{yx} = \mu \left(\frac{\partial u_f}{\partial y} + \frac{\partial v_f}{\partial x} \right) \quad \text{Eq. D.6}$$

$$\vec{\nabla} \cdot \vec{v} = \frac{\partial u_f}{\partial x} + \frac{\partial v_f}{\partial y} \quad \text{Eq. D.7}$$

The net surface forces may be expressed in the x and y dimensions as:

$$F_{s,x} = \left(\frac{\partial \sigma_{xx}}{\partial x} + \frac{\partial \tau_{xy}}{\partial y} - \frac{\partial p}{\partial x} \right) dx dy \quad \text{Eq. D.8}$$

$$F_{s,y} = \left(\frac{\partial \sigma_{yy}}{\partial y} + \frac{\partial \tau_{xy}}{\partial x} - \frac{\partial p}{\partial y} \right) dx dy \quad \text{Eq. D.9}$$

Mass flow from both the x - and y -directions contribute to the total x -momentum. As found previously, the mass flux into the x -face of the control volume is $(\rho_f u_f)$ and so the momentum flux in the x -direction from the x -face is $(\rho_f u_f)u_f$. Likewise, the mass flux from the y -face is $(\rho_f v_f)$, and thus the contribution to momentum from this mass transfer is $(\rho_f v_f)u_f$. Thus, the net rate of x -momentum into the control volume is $(\rho_f u_f)u_f + (\rho_f v_f)u_f$ and the net rate of x -momentum out of the control volume is:

$$\frac{\partial [(\rho_f u_f)u_f]}{\partial x} dx dy + \frac{\partial [(\rho_f v_f)u_f]}{\partial y} dy dx \quad \text{Eq. D.10}$$

Furthermore, the x -momentum of the fluid within this control volume may be changing with respect to time, and may be expressed as:

$$\frac{\partial}{\partial t} (\rho_f u_f) dx dy \quad \text{Eq. D.11}$$

These may all be combined to express Newton's Second Law in the x -direction as follows:

$$X + \frac{\partial \sigma_{xx}}{\partial x} + \frac{\partial \tau_{xy}}{\partial y} - \frac{\partial p}{\partial x} = \frac{\partial}{\partial t} (\rho_f u_f) dx dy + \frac{\partial [(\rho_f u_f)u_f]}{\partial x} dx dy + \frac{\partial [(\rho_f v_f)u_f]}{\partial y} dy dx \quad \text{Eq. D.12}$$

Rearranging and making some substitutions this expression is simplified to:

$$X + \frac{\partial \tau_{xy}}{\partial y} + \frac{\partial}{\partial x} (\sigma_{xx} - p) = \rho_f \left(\frac{\partial u_f}{\partial t} + u_f \frac{\partial u_f}{\partial x} + v_f \frac{\partial u_f}{\partial y} \right) \quad \text{Eq. D.13}$$

Similarly, Newton's Second Law in the y -direction may be expressed as:

$$Y + \frac{\partial \tau_{xy}}{\partial x} + \frac{\partial}{\partial y}(\sigma_{yy} - p) = \rho_f \left(\frac{\partial v_f}{\partial t} + u_f \frac{\partial v_f}{\partial x} + v_f \frac{\partial v_f}{\partial y} \right) \quad \text{Eq.D.14}$$

The Continuity Equation, Newton's Second Law, and viscous stresses comprise the complete representation of 2-dimensional fluid flow within the velocity boundary layer. Solving these equations yields a velocity field within this boundary layer, and this field allows the wall shear stress, τ_s , to be determined [49].

Thermal Boundary Layer and Conservation of Energy: Outside of potential energy effects (from chemical or gravitational potential energy), the energy per unit of mass within the differential control volume includes both kinetic energy of the molecules within the fluid, $\frac{V'^2}{2}$ (where $V'^2 \equiv u_f^2 + v_f^2$), as well as the internal thermal energy, e . The rate at which energy is stored in the differential volume, \dot{E}_{st} , is:

$$\dot{E}_{st} = \frac{\partial}{\partial t} \left[\rho_f \left(e + \frac{V'^2}{2} \right) \right] dx dy \quad \text{Eq.D.15}$$

In addition to the energy storage rate, the rate at which thermal and kinetic energy passes in and out of the control volume surfaces can be expressed as:

$$\dot{E}_{conv,x} - \dot{E}_{conv,x+dx} = - \frac{\partial}{\partial x} \left[\rho_f u_f \left(e + \frac{V'^2}{2} \right) \right] dx dy \quad \text{Eq.D.16}$$

$$\dot{E}_{conv,y} - \dot{E}_{conv,y+dy} = - \frac{\partial}{\partial y} \left[\rho_f v_f \left(e + \frac{V'^2}{2} \right) \right] dy dx \quad \text{Eq.D.17}$$

Energy is also transferred in and out of the differential volume due to species diffusion and conduction, both molecular processes. Species diffusion has a negligible effect unless a chemical reaction is taking place and thus is ignored in this analysis. The energy passing in and out of the differential control volume due to conductive processes is expressed as:

$$\dot{E}_{cond,x} - \dot{E}_{cond,x+dx} = \frac{\partial}{\partial x} \left(k \frac{\partial T}{\partial x} \right) dx dy \quad \text{Eq.D.18}$$

$$\dot{E}_{cond,y} - \dot{E}_{cond,y+dy} = \frac{\partial}{\partial y} \left(k \frac{\partial T}{\partial y} \right) dy dx \quad \text{Eq.D.19}$$

Finally, energy may flow in and out of the differential volume due to work on or by the volume. The rate at which work is done *on* the volume by surface and body forces may be expressed as:

$$\dot{W}_{net,x} = (Xu_f) dx dy + \frac{\partial}{\partial x} [(\sigma_{xx} - p)u_f] dx dy + \frac{\partial}{\partial y} (\tau_{yx}u_f) dx dy \quad \text{Eq.D.20}$$

$$\dot{W}_{net,y} = (Yv_f) dy dx + \frac{\partial}{\partial y} [(\sigma_{yy} - p)v_f] dy dx + \frac{\partial}{\partial x} (\tau_{xy}v_f) dy dx \quad \text{Eq.D.21}$$

Energy conservation is expressed by equating the energy stored to the energy transferred into and out of the differential volume by these other means, and with some rearranging becomes:

$$\begin{aligned} & \frac{\partial}{\partial t} \left[\rho_f \left(e + \frac{V'^2}{2} \right) \right] = \dots \\ & - \frac{\partial}{\partial x} \left[\rho_f u_f \left(e + \frac{V'^2}{2} \right) \right] - \frac{\partial}{\partial y} \left[\rho_f v_f \left(e + \frac{V'^2}{2} \right) \right] + \frac{\partial}{\partial x} \left(k \frac{\partial T}{\partial x} \right) + \frac{\partial}{\partial y} \left(k \frac{\partial T}{\partial y} \right) + (Xu_f + Yv_f) \dots \\ & - \frac{\partial}{\partial x} (pu_f) - \frac{\partial}{\partial y} (pv_f) + \frac{\partial}{\partial x} (\sigma_{xx}u_f + \tau_{xy}v_f) + \frac{\partial}{\partial y} (\sigma_{yy}v_f + \tau_{yx}u_f) + \dot{q} \end{aligned} \quad \text{Eq. D.22}$$

Where \dot{q} refers to the energy generated per unit volume. This cumbersome equation is a general expression of energy conservation within the thermal boundary layer. By defining the enthalpy per mass, i , and the viscous dissipation, $\mu\Phi$, as:

$$i = e + \frac{p}{\rho_f} \quad \text{Eq.D.23}$$

$$\mu\Phi \equiv \mu \left\{ \left(\frac{\partial u_f}{\partial y} + \frac{\partial v_f}{\partial x} \right)^2 + 2 \left[\left(\frac{\partial u_f}{\partial x} \right)^2 + \left(\frac{\partial v_f}{\partial y} \right)^2 \right] - \frac{2}{3} \left(\frac{\partial u_f}{\partial x} + \frac{\partial v_f}{\partial y} \right)^2 \right\} \quad \text{Eq.D.24}$$

Viscous dissipation measures the rate that viscous effects in the fluid convert mechanical to

thermal energy. Thus, conservation of energy in the thermal layer is ultimately expressed as:

$$\rho_f \frac{\partial i}{\partial t} + \rho_f u_f \frac{\partial i}{\partial x} + \rho_f v_f \frac{\partial i}{\partial y} = \frac{\partial}{\partial x} \left(k \frac{\partial T}{\partial x} \right) + \frac{\partial}{\partial y} \left(k \frac{\partial T}{\partial y} \right) + \left(\frac{\partial p}{\partial t} + u_f \frac{\partial p}{\partial x} + v_f \frac{\partial p}{\partial y} \right) + \mu \Phi + \dot{q}$$

Eq. D.25

Concentration Boundary Layer and Conservation of Species: Finally, the relative transport of various species within the concentration boundary layer are bound by species conservation which must be satisfied throughout this boundary layer. Chemical reactions may generate a species within the control volume with a rate $\dot{M}_{A,gen} = \dot{n}_A$, and the rate that the species is stored within the differential volume is $\dot{M}_{A,st}$, which can be expressed:

$$\dot{M}_{A,st} = \left(\frac{\partial \rho_{A,f}}{\partial t} \right) dx dy \quad \text{Eq. D.26}$$

The species may also be transported through the differential control volume either by convection or by diffusion. The net rate at which the species enters the control volume via convection is:

$$\dot{M}_{A,conv,x} - \dot{M}_{A,conv,x+dx} = (\rho_{A,f} u_f) dy - \left[(\rho_{A,f} u_f) + \frac{\partial (\rho_{A,f} u_f)}{\partial x} dx \right] dy = - \frac{\partial (\rho_{A,f} u_f)}{\partial x} dx dy \quad \text{Eq. D.27}$$

$$\dot{M}_{A,conv,y} - \dot{M}_{A,conv,y+dy} = (\rho_{A,f} v_f) dx - \left[(\rho_{A,f} v_f) + \frac{\partial (\rho_{A,f} v_f)}{\partial y} dy \right] dx = - \frac{\partial (\rho_{A,f} v_f)}{\partial y} dx dy \quad \text{Eq. D.28}$$

The net rate at which the species enters the differential volume by diffusion is dictated by Fick's law:

$$\dot{M}_{A,diff,x} - \dot{M}_{A,diff,x+dx} = \left(-D_{AB} \frac{\partial \rho_{A,f}}{\partial x} \right) dy - \left[\left(-D_{AB} \frac{\partial \rho_{A,f}}{\partial x} \right) + \frac{\partial}{\partial x} \left(-D_{AB} \frac{\partial \rho_{A,f}}{\partial x} \right) dx \right] dy \dots$$

$$\dots = \frac{\partial}{\partial x} \left(D_{AB} \frac{\partial \rho_{fA}}{\partial x} \right) dx dy \quad \text{Eq.D.29}$$

$$\dot{M}_{A,diff,y} - \dot{M}_{A,diff,y+dy} = \frac{\partial}{\partial y} \left(D_{AB} \frac{\partial \rho_{A,f}}{\partial y} \right) dx dy \quad \text{Eq.D.30}$$

Finally, the species conservation may be expressed as:

$$\begin{aligned} \dot{M}_{A,st} &= \dots \\ \dots &= \dot{M}_{A,conv,x} - \dot{M}_{A,conv,x+dx} + \dot{M}_{A,conv,y} - \dot{M}_{A,conv,y+dy} + \dot{M}_{A,diff,x} - \dot{M}_{A,diff,x+dx} + \dots \\ &\quad \dots + \dot{M}_{A,diff,y} - \dot{M}_{A,diff,y+dy} + \dot{M}_{A,gen} \end{aligned} \quad \text{Eq.D.31}$$

Which becomes:

$$\left(\frac{\partial \rho_{A,f}}{\partial t} \right) + \frac{\partial(\rho_{A,f} u_f)}{\partial x} + \frac{\partial(\rho_{A,f} v_f)}{\partial y} = \frac{\partial}{\partial x} \left(D_{AB} \frac{\partial \rho_{A,f}}{\partial x} \right) + \frac{\partial}{\partial y} \left(D_{AB} \frac{\partial \rho_{A,f}}{\partial y} \right) + \dot{n}_A \quad \text{Eq.D.32}$$

This expression can be further simplified by presuming a constant mass density and applying the Continuity Equation:

$$\frac{\partial \rho_{A,f}}{\partial t} + u_f \frac{\partial \rho_{A,f}}{\partial x} + v_f \frac{\partial \rho_{A,f}}{\partial y} = \frac{\partial}{\partial x} \left(D_{AB} \frac{\partial \rho_{A,f}}{\partial x} \right) + \frac{\partial}{\partial y} \left(D_{AB} \frac{\partial \rho_{A,f}}{\partial y} \right) + \dot{n}_A \quad \text{Eq.D.33}$$

For molar concentrations this becomes:

$$\frac{\partial C_A}{\partial t} + u_f \frac{\partial C_A}{\partial x} + v_f \frac{\partial C_A}{\partial y} = \frac{\partial}{\partial x} \left(D_{AB} \frac{\partial C_A}{\partial x} \right) + \frac{\partial}{\partial y} \left(D_{AB} \frac{\partial C_A}{\partial y} \right) + \dot{N}_A \quad \text{Eq.D.34}$$

Convection Simplifications and Approximations: These equations describe the physical processes influencing the velocity, thermal, and concentration boundary layers. Beyond this, some simplifications may be made due to the very small thicknesses of these boundary layers.

The following simplifications apply to the velocity boundary layer:

$$u_f \gg v_f \quad \text{Eq.D.35}$$

$$\frac{\partial u_f}{\partial y} \gg \frac{\partial u_f}{\partial x}, \frac{\partial v_f}{\partial x}, \text{ and } \frac{\partial v_f}{\partial y} \quad \text{Eq.D.36}$$

Here it is clear that the fluid velocity parallel to the surface is much greater than the fluid velocity perpendicular to the surface, and that the gradients normal to the surface are much greater than the gradients parallel to the surface. Simplifications of the thermal boundary layer are expressed as:

$$\frac{\partial T}{\partial y} \gg \frac{\partial T}{\partial x} \quad \text{Eq.D.37}$$

Where it is clear the temperature gradient perpendicular to the surface is much greater than the temperature gradient parallel to the surface. Finally, simplifications of the concentration boundary layer can be expressed as:

$$\frac{\partial C_A}{\partial y} \gg \frac{\partial C_A}{\partial x} \quad \text{Eq.D.38}$$

The concentration gradient perpendicular to the surface is much greater than the concentration gradient parallel to the surface. These simplifications indicate that the normal stresses are negligible and may be excluded so that the only surviving stress term is shear stress:

$$\tau_{xy} = \tau_{yx} = \mu \left(\frac{\partial u_f}{\partial y} \right) \quad \text{Eq.D.39}$$

These equations coupled with a series of simplifications allows for the continuity, momentum, and energy equations to be simplified to a significant degree. If the fluid is Newtonian and non-compressible, and if the density is uniform and does not vary with time, the overall continuity equation for the velocity boundary layer becomes:

$$\frac{\partial u_f}{\partial x} + \frac{\partial v_f}{\partial y} = 0 \quad \text{Eq.D.40}$$

Then, presuming that body forces and normal stresses are negligible, the velocity of the fluid remains constant with respect to time, and substituting the expression for the normal stress, the x-momentum equation becomes:

$$\frac{\mu}{\rho_f} \frac{\partial^2 u_f}{\partial y^2} - \frac{1}{\rho_f} \frac{\partial p}{\partial x} = u_f \frac{\partial u_f}{\partial x} + v_f \frac{\partial u_f}{\partial y} \quad \text{Eq.D.41}$$

In the y-direction, further simplification can be made, presuming y-component of the fluid velocity doesn't change with respect to time, and the gradient of the shear stress with respect to the x-direction, as well as the gradient of the y-velocity with respect to either the x- or y-directions are all negligible, then:

$$\frac{1}{p} \frac{\partial p}{\partial y} = 0 \quad \text{Eq.D.42}$$

The temperature gradient in the x-direction is negligible, and the pressure is constant in time and space. Presuming that no thermal energy is being generated, and that the thermal conductivity and density of the fluid are constant, the energy conservation requirement for the thermal boundary layer reduces to:

$$u_f \frac{\partial i}{\partial x} + v_f \frac{\partial i}{\partial y} = + \frac{k}{\rho_f} \left(\frac{\partial^2 T}{\partial y^2} \right) + \frac{\mu}{\rho_f} \left(\frac{\partial u_f}{\partial y} \right)^2 \quad \text{Eq.D.43}$$

The enthalpy, i , is related to temperature via the heat capacity as follows:

$$C_p = \frac{di}{dT} \Big|_p \quad \text{Eq.D.44}$$

Since constant pressure is presumed, this expression can be rearranged and substituted into the energy conservation equation:

$$C_p u_f \frac{\partial T}{\partial x} + C_p v_f \frac{\partial T}{\partial y} = \frac{k}{\rho_f} \left(\frac{\partial^2 T}{\partial y^2} \right) + \frac{\mu}{\rho_f} \left(\frac{\partial u_f}{\partial y} \right)^2 \quad \text{Eq.D.45}$$

Then with some rearranging and noticing that $\frac{k}{\rho_f C_p} = \gamma$, and $\frac{\mu}{\rho_f} = \vartheta$ this is finally simplified to:

$$u_f \frac{\partial T}{\partial x} + v_f \frac{\partial T}{\partial y} = \gamma \left(\frac{\partial^2 T}{\partial y^2} \right) + \vartheta \left(\frac{\partial u_f}{\partial y} \right)^2 \quad \text{Eq.D.46}$$

Simplification of the species continuity equation can be accomplished by first presuming

that the concentration of the molecular species within the fluid is not changing with time, no chemical reactions are taking place, and the diffusivity constant, D_{AB} does not vary with position. If the concentration gradient parallel to the surface is negligible, then the species continuity equation simplifies to:

$$u_f \frac{\partial C_A}{\partial x} + v_f \frac{\partial C_A}{\partial y} = D_{AB} \frac{\partial^2 C_A}{\partial y^2} \quad \text{Eq.D.47}$$

Normalization of Convective Transport Equations: Boundary layer analysis yields insight into the velocity, temperature, and concentration profiles, but also leads to the development of key boundary layer similarity parameters. Equations 2.134, 2.139, and 2.140, show diffusion terms on the right and convection terms on the left side of the equation, which represents low speed, forced convection. To normalize the boundary layer equations, first dimensionless independent variables are defined as follows:

$$x^* \equiv \frac{x}{L} \quad \text{Eq.D.48}$$

$$y^* \equiv \frac{y}{L} \quad \text{Eq.D.49}$$

Where L is a characteristic length relevant to the analysis. Next dimensionless dependent variables may be defined in a similar fashion:

$$u^* \equiv \frac{u_f}{u_{free}} \quad \text{Eq.D.50}$$

$$v^* \equiv \frac{v_f}{u_{free}} \quad \text{Eq.D.51}$$

$$T^* \equiv \frac{T - T_s}{T_f - T_s} \quad \text{Eq.D.52}$$

$$C_A^* \equiv \frac{C_A - C_{A,s}}{C_{A,f} - C_{A,s}} \quad \text{Eq.D.53}$$

$$p^* \equiv \frac{p}{\rho_f u_{free}^2} \quad \text{Eq.D.54}$$

Thus, the dimensionless conservation equations for velocity, temperature, and concentration along with their wall and freestream boundary conditions are shown in Table D.1 [49].

One of the key results of this normalization analysis of the conservation equations is that a set of dimensionless similarity parameters may be defined. Similarity parameters allow for the solutions obtained for one surface to be applied to other geometrically similar surfaces under other environmental conditions. The first of these similarity parameters is the Reynolds Number, which is a ratio of the inertia to viscous forces [49]:

$$Re_L \equiv \frac{u_f L}{\vartheta'} \quad \text{Eq.D.55}$$

Where $\vartheta' \equiv \frac{\mu}{\rho_f x^*}$ and refers to the molecular viscosity. Small values of Re_L indicate that viscous

forces dominate, keeping the flow laminar and preventing turbulent effects from dominating.

Large values of Re_L indicate that inertial forces dominate and the flow is turbulent.

Table D.1: Non-dimensional convective transfer equations and boundary conditions.

Boundary Layer	Conservation Equation	Boundary Conditions	
		Wall	Freestream
Velocity	$u^* \frac{\partial u^*}{\partial x^*} + v^* \frac{\partial v^*}{\partial y^*} = -\frac{\partial p^*}{\partial x^*} + \frac{\vartheta'}{u_{free} L} \frac{\partial^2 u^*}{\partial y^{*2}}$	$u^*(x^*, 0) = 0$ $v^*(x^*, 0) = 0$	$u^*(x^*, \infty) = 1$
Thermal	$u^* \frac{\partial T^*}{\partial x^*} + v^* \frac{\partial T^*}{\partial y^*} = \frac{\gamma}{u_{free} L} \frac{\partial^2 T^*}{\partial y^{*2}}$	$T^*(x^*, 0) = 0$	$T^*(x^*, \infty) = 1$
Concentration	$u^* \frac{\partial C_A^*}{\partial x^*} + v^* \frac{\partial C_A^*}{\partial y^*} = \frac{D_{AB}}{u_{free} L} \frac{\partial^2 C_A^*}{\partial y^{*2}}$	$C_A^*(x^*, 0) = 0$	$C_A^*(x^*, \infty) = 1$

Next is the Prandtl number, a ratio of the molecular momentum diffusivity to thermal diffusivity:

$$Pr \equiv \frac{\vartheta'}{\gamma} = \frac{c_p \mu}{k} \quad \text{Eq.D.56}$$

The Prandtl number compares the energy diffusion rate to the momentum diffusion rate, so for $Pr \approx 1$, the energy and momentum diffusion rates are roughly equal. When $Pr \gg 1$ the momentum diffusion rate exceeds the energy. For laminar flow, the velocity and thermal boundary layer thicknesses are related to the Prandtl number by:

$$\frac{\delta_{vel}}{\delta_{ther}} \approx Pr^n \quad \text{Eq.D.57}$$

Here, δ_{vel} and δ_{ther} refer to the velocity and thermal boundary layer thicknesses, respectively, and n is some positive exponent.

Finally, the Schmidt Number is a ratio of the molecular momentum and the mass diffusivity:

$$Sc \equiv \frac{\vartheta'}{D_{AB}} \quad \text{Eq.D.58}$$

Just as the Prandtl number compares the energy and momentum diffusion rates, the Schmidt number compares the momentum diffusion rate to the mass diffusion rate. Large values of Sc indicate that momentum diffusion dominates, while small values of Sc indicate mass transfer dominates. Like the Prandtl number analysis, for laminar flows the thicknesses of the velocity and concentration boundary layers is related to the Schmidt number via:

$$\frac{\delta_{vel}}{\delta_{conc}} \approx Sc^n \quad \text{Eq.D.59}$$

Applying these similarity parameters to the conservation equations, the set of boundary layer equations and conditions is shown in Table D.2. The non-dimensional continuity equation is, perhaps obviously:

$$\frac{\partial u^*}{\partial x^*} + \frac{\partial v^*}{\partial y^*} = 0 \quad \text{Eq.D.60}$$

Functional Form: Similarity parameters allow for these equations and their solutions to be significantly generalized and simplified and suggest the forms that solutions may take. For example, the solution of the velocity conservation equation should be a function with dependent variables x^*, y^*, Re_L , and $\frac{\partial p^*}{\partial x^*}$, expressed as:

$$u^* = f_1 \left(x^*, y^*, Re_L, \frac{\partial p^*}{\partial x^*} \right) \quad \text{Eq.D.61}$$

From here a variety of other parameters may be expressed in more convenient functional forms, such as the shear stress at the surface, the coefficient of friction, and the velocity gradient normal to the surface, expressed as, respectively:

$$\tau_s = \mu \frac{\partial u_f}{\partial y} \Big|_{y=0} = \frac{\mu u_{free}}{L} \frac{\partial u^*}{\partial y^*} \Big|_{y=0} \quad \text{Eq.D.62}$$

$$C_f = \frac{\tau_s}{\frac{\rho_f u_{free}^2}{2}} = \frac{2}{Re_L} \frac{\partial u^*}{\partial y^*} \Big|_{y=0} \quad \text{Eq.D.63}$$

$$\frac{\partial u^*}{\partial y^*} \Big|_{y=0} = f_2 \left(x^*, Re_L, \frac{\partial p^*}{\partial x^*} \right) \quad \text{Eq.D.64}$$

For a specific geometry, the friction coefficient may be expressed as:

$$C_f = \frac{2}{Re_L} f_2(x^*, Re_L) \quad \text{Eq.D.65}$$

The $\frac{\partial p^*}{\partial x^*}$ variable is not necessary for a prescribed geometry, that is, for all similar geometries the normalized pressure gradient will be the same and thus need not be included in the expression of the friction coefficient. Thus, the frictional coefficient for convection across a specific geometry may be expressed with a dimensionless space variable, x^* , and the (also dimensionless) Reynolds Number. The eloquence of this outcome is that the function, f_2 , relating C_f to x^* and Re_L is universally applicable to all other geometrically similar surfaces, regardless of fluid velocity, surface size, fluid composition, and so on.

Table D.2: Convective transfer with associated similarity parameters.

Boundary Layer	Conservation Equation	Boundary Conditions	
		Wall	Freestream
Velocity	$u^* \frac{\partial u^*}{\partial x^*} + v^* \frac{\partial v^*}{\partial y^*} = -\frac{\partial p^*}{\partial x^*} + \frac{1}{Re_L L} \frac{\partial^2 u^*}{\partial y^{*2}}$	$u^*(x^*, 0) = 0$ $v^*(x^*, 0) = 0$	$u^*(x^*, \infty) = 1$
Thermal	$u^* \frac{\partial T^*}{\partial x^*} + v^* \frac{\partial T^*}{\partial y^*} = \frac{1}{Re_L Pr} \frac{\partial^2 T^*}{\partial y^{*2}}$	$T^*(x^*, 0) = 0$	$T^*(x^*, \infty) = 1$
Concentration	$u^* \frac{\partial C_A^*}{\partial x^*} + v^* \frac{\partial C_A^*}{\partial y^*} = \frac{1}{Re_L Sc} \frac{\partial^2 C_A^*}{\partial y^{*2}}$	$C_A^*(x^*, 0) = 0$	$C_A^*(x^*, \infty) = 1$

Similar results may be found for other relevant coefficients related to thermal and mass transfer in the thermal and concentration boundary layers. The normalized temperature has the functional form:

$$T^* = f_3 \left(x^*, y^*, Re_L, Pr, \frac{\partial p^*}{\partial x^*} \right) \quad \text{Eq.D.66}$$

The convection heat transfer coefficient, h' , can be expressed with these dimensionless variables as:

$$h' = \frac{k_f}{L} \frac{\partial T^*}{\partial y^*} \bigg|_{y=0} \quad \text{Eq.D.67}$$

Rearranging this yields another dimensionless similarity parameter called the Nusselt Number:

$$Nu \equiv \frac{h' L}{k_f} = \frac{\partial T^*}{\partial y^*} \bigg|_{y=0} \quad \text{Eq.D.68}$$

The Nusselt Number quantifies the thermal transfer via convection at the surface, and may be thought of as a sort of thermal friction coefficient much like the motional friction coefficient, C_f . For a prescribed geometry, the Nusselt Number takes the functional form:

$$Nu = f_4(x^*, Re_L, Pr) \quad \text{Eq.D.69}$$

Once again, this means that, for a specific geometric surface, the Nusselt number can be determined exclusively by the dimensionless parameters x^* , Re_L , and Pr . Beyond this, determination of the Nusselt number allows the thermal convection coefficient h to be calculated and local thermal transfer computed. Additionally, the average thermal transfer coefficient is determined by integrating over the entire surface, so an average Nusselt number may also be determined, which takes the functional form:

$$\overline{Nu} = \frac{\bar{h}L}{k_f} = f_5(Re_L, Pr) \quad \text{Eq.D.70}$$

Finally, the same basic process may be applied to the concentration boundary layer, and the solution of the conservation equation for this layer will take the functional form:

$$C_A^* = f_6\left(x^*, y^*, Re_L, Sc, \frac{\partial p^*}{\partial x^*}\right) \quad \text{Eq.D.71}$$

Once again, applying the dimensionless variables and similarity parameters, the mass convection coefficient may be transformed to:

$$h_m = -\frac{D_{AB}}{L} \frac{(C_{A,f} - C_{A,s})}{(C_{A,s} - C_{A,f})} \frac{\partial C_A^*}{\partial y^*} \Big|_{y=0} = \frac{D_{AB}}{L} \frac{\partial C_A^*}{\partial y^*} \Big|_{y=0} \quad \text{Eq.D.72}$$

Thus, another dimensionless similarity parameter, the Sherwood Number, Sh , may be defined:

$$Sh \equiv \frac{h_m L}{D_{AB}} = \frac{\partial C_A^*}{\partial y^*} \Big|_{y=0} \quad \text{Eq.D.73}$$

The Sherwood number is a measure of convective mass transfer at the surface much like the Nusselt number is a measure of convective heat transfer. It's unsurprising that, for a specific

geometric surface, the Sherwood number takes the functional form:

$$Sh = f_7(x^*, Re_L, Sc) \quad \text{Eq.D.74}$$

Once again, this is a universal function for all geometrically similar surfaces and only requires the dimensionless parameters of x^* , Re_L , and Sc for calculation. Like the average Nusselt number, the average Sherwood number has the form:

$$\overline{Sh} = \frac{\bar{h}_m L}{D_{AB}} = f_8(Re_L, Sc) \quad \text{Eq.D.75}$$

The benefit of the foregoing analysis cannot be understated, as it shows that thermal and mass transfer results may be expressed using just three dimensionless groups rather than an array of individual parameters, and that solutions whether theoretical or experimental are universally applicable and apply for a variety of different material types, fluid speeds, and surface sizes [49].

Turbulence: Random fluctuations of some arbitrary property, P_{rand} , of the fluid (a velocity component, temperature, or concentration) in the moving fluid give rise to turbulence. The random fluctuations of P_{rand} at any moment may be expressed as the sum of time-mean value of the property, \bar{P}_{rand} , and the fluctuating component of this property, P'_{rand} . Turbulent flow increases thermal and mass transport but is exceedingly difficult to theoretically model. The time variation in the instantaneous values of the dependent variables (u_f, v_f, T, C_A) is impossible to predict with certainty, however, it is generally the time-independent \bar{P} that are relevant in application. Thus, each of the dependent flow variables may be replaced by a relevant equation of the form $P_{rand} = \bar{P}_{rand} + P'_{rand}$, and thus, for incompressible steady flows with constant-properties the x-momentum, energy, and species conservation equations become, respectively:

$$\rho_f \left(\bar{u}_f \frac{\partial \bar{u}_f}{\partial x} + \bar{v}_f \frac{\partial \bar{v}_f}{\partial y} \right) = -\frac{dp}{dx} + \frac{\partial}{\partial y} \left(\mu \frac{\partial \bar{u}_f}{\partial y} - \rho_f \overline{u'_f v'_f} \right) \quad \text{Eq.D.76}$$

$$\rho_f c_p \left(\bar{u}_f \frac{\partial \bar{T}}{\partial x} + \bar{v}_f \frac{\partial \bar{T}}{\partial y} \right) = \frac{\partial}{\partial y} \left(k \frac{\partial \bar{T}}{\partial y} - \rho_f c_p \overline{v'_f T'} \right) \quad \text{Eq.D.77}$$

$$\left(\bar{u}_f \frac{\partial \bar{C}_A}{\partial x} + \bar{v}_f \frac{\partial \bar{C}_A}{\partial y} \right) = \frac{\partial}{\partial y} \left(D_{AB} \frac{\partial \bar{C}_A}{\partial y} - \overline{v'_f C'_A} \right) \quad \text{Eq.D.78}$$

The terms $\overline{u'_f v'_f}$, $\overline{v'_f T'}$, and $\overline{v'_f C'_A}$ represent the effect from fluctuations in the momentum, energy, and species transport, respectively. The terms \bar{u}_f , \bar{v}_f , and so on represent time-mean averages of these variables. Thus, total shear stresses and fluxes may be respectively expressed as:

$$\tau_{tot} = \left(\mu \frac{\partial \bar{u}_f}{\partial y} - \rho_f \overline{u'_f v'_f} \right) \quad \text{Eq.D.79}$$

$$q''_{tot} = - \left(k \frac{\partial \bar{T}}{\partial y} - \rho_f c_p \overline{v'_f T'} \right) \quad \text{Eq.D.80}$$

$$N''_{A,tot} = - \left(D_{AB} \frac{\partial \bar{C}_A}{\partial y} - \overline{v'_f C'_A} \right) \quad \text{Eq.D.81}$$

Thus, the x-momentum, energy, and species conservation become:

$$\rho_f \left(\bar{u}_f \frac{\partial \bar{u}_f}{\partial x} + \bar{v}_f \frac{\partial \bar{u}_f}{\partial y} \right) = - \frac{dp}{dx} + \frac{\partial \tau_{tot}}{\partial y} \quad \text{Eq.D.82}$$

$$\rho_f c_p \left(\bar{u}_f \frac{\partial \bar{T}}{\partial x} + \bar{v}_f \frac{\partial \bar{T}}{\partial y} \right) = \frac{\partial q''_{tot}}{\partial y} \quad \text{Eq.D.83}$$

$$\left(\bar{u}_f \frac{\partial \bar{C}_A}{\partial x} + \bar{v}_f \frac{\partial \bar{C}_A}{\partial y} \right) = \frac{\partial N''_{A,tot}}{\partial y} \quad \text{Eq.D.84}$$

Eddies are small groupings of fluid that briefly move in concert and greatly enhance momentum, energy, and species transport before their collective identity is lost. To describe momentum, heat, and mass transport via eddies the following eddy diffusivities are defined, each termed the eddy diffusivity for momentum, heat, or mass transfer [49]:

$$\epsilon_M \frac{\partial \bar{u}_f}{\partial y} \equiv -\overline{u'_f v'_f} \quad \text{Eq.D.85}$$

$$\epsilon_H \frac{\partial \bar{T}}{\partial y} \equiv -\overline{v'_f T'} \quad \text{Eq.D.86}$$

$$\epsilon_S \frac{\partial \bar{C}_A}{\partial y} \equiv -\overline{v'_f C'_A} \quad \text{Eq.D.87}$$

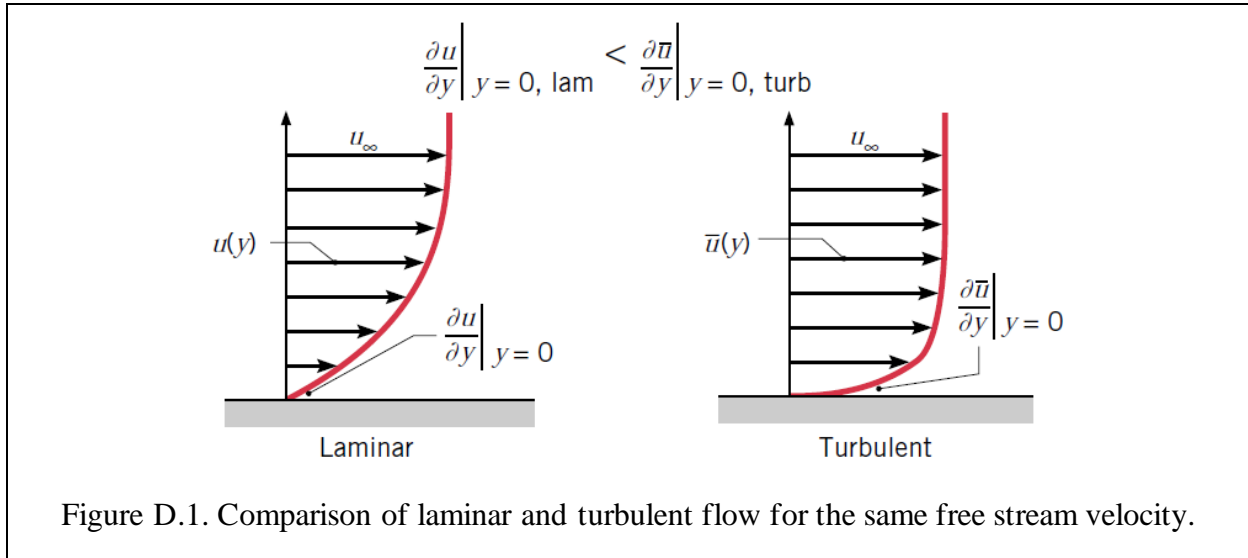
Thus, the total shear stress and fluxes may be expressed as the sum of molecular and eddy elements:

$$\tau_{tot} = \rho_f (\vartheta' + \epsilon_M) \frac{\partial \bar{u}_f}{\partial y} \quad \text{Eq.D.88}$$

$$q''_{tot} = \rho_f c_p (\gamma + \epsilon_H) \frac{\partial \bar{u}_f}{\partial y} \quad \text{Eq.D.89}$$

$$N''_{A,tot} = -(D_{AB} + \epsilon_S) \frac{\partial \bar{C}_A}{\partial y} \quad \text{Eq.D.90}$$

Laminar flow has a smaller velocity gradient, meaning that the velocity profile has a gentler transition from surface to freestream velocities. Turbulent flow, on the other hand, is characterized by a larger velocity gradient. The sharper gradients in turbulent flow enhance thermal and mass transfer but increase wall shear stress. While turbulent flow is often desirable in application, it is difficult to model theoretically due to the inherent difficulty in modeling eddy behavior [49].



Flat Plate External Flow: Fluid moving across the surface of a flat plate can be laminar, turbulent, or a mix of both laminar and turbulent. The following sections examine each of these scenarios and the development of boundary layers that can freely develop on the surface without restriction.

For laminar flow parallel to a flat surface, features such as the frictional coefficient (C_f , Eq. 2.83), Nusselt Number (Nu , Eq. 2.161), and Sherwood Number (Sh , Eq. 2.166) are well-known both theoretically and from experimentation. These results for laminar flow between $x = 0$ and $x = x_c$ are shown in Table 2.3.

The nature of turbulent flow makes it difficult to model, so generally variables like the frictional coefficient and so on are found experimentally and shown in Table 2.4 below. The rapid mixing within the turbulent zone means that boundary layer thickness growth is no longer dictated by Pr or Sc , and thus all boundary layers have roughly the same thickness, $\delta_{vel} = 0.37xRe_x^{-1/5} \approx \delta_{therm} \approx \delta_{conc}$.

For mixed boundary layer conditions, that is, when both laminar and turbulent regions may be found in relatively equal parts across a surface, the average convective thermal transport

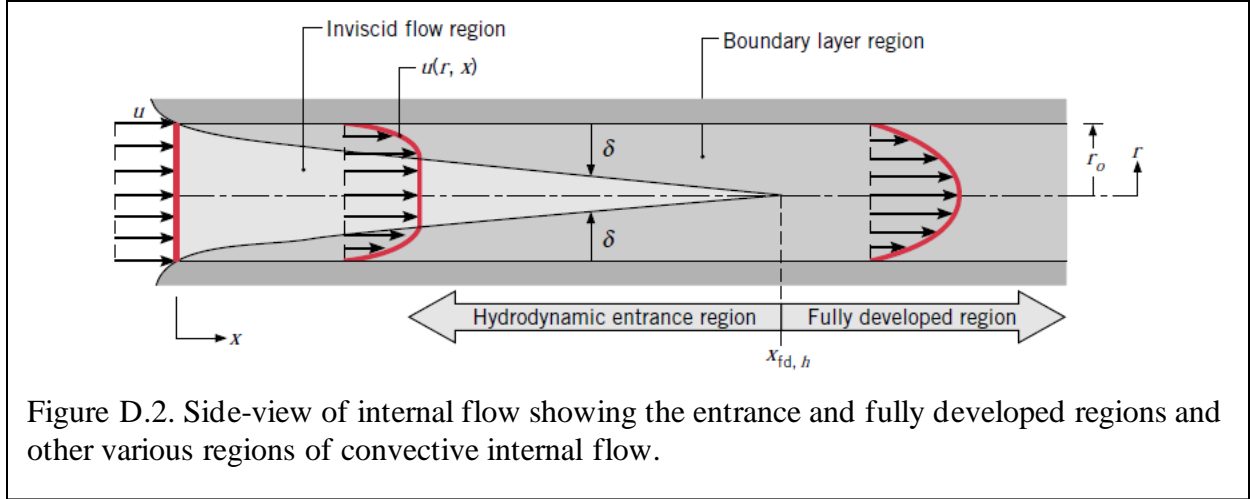
coefficient, \bar{h}_{mix} , is expressed as:

$$\bar{h}_{mix} = \frac{1}{L} \left(\int_0^{x_c} h_{lam} dx + \int_{x_c}^L h_{turb} dx \right) \quad \text{Eq.D.91}$$

Here the transition between laminar and turbulent flow is presumed to be immediate at x_c .

Because of the fastening elements presumed to be located along the edges of the building as well as periodically throughout the regions in which internal flow would be taking place, turbulent flow is expected to take place in the enclosed channels. Thus, for the system in question where $L \gg x_c$, the average coefficient of friction, average Nusselt number, and average Sherwood number are shown in Table 2.3 [49].

Interior Flow in Ducts: When fluid flow is restricted – such as when air is passing through a channel between a PV panel and the building the panel is integrated with – boundary layers form at both surfaces and ultimately meet in the middle of the channel by steadily decreasing the inviscid flow region. The analysis of internal flow requires defining the entrance and fully developed regions. The hydrodynamic entry length, x_e , defines the point at which the boundary layers from the opposing surfaces meet and marks the boundary between the entrance region and the fully developed region. Similarly, the thermal entry length, x_{er} , defined the location where the thermal boundary layers meet. The length of the entry region is dependent on whether the fluid flow is laminar or turbulent.



Effective Hydraulic Diameter for Non-Circular Ducts: For non-circular tubes with sharp corners, the convection coefficients vary at the edges and ultimately dropping to zero in enclosed corners and may be approximated using an effective hydraulic diameter, D_h , when calculating the Reynolds number, friction factor, and Nusselt number:

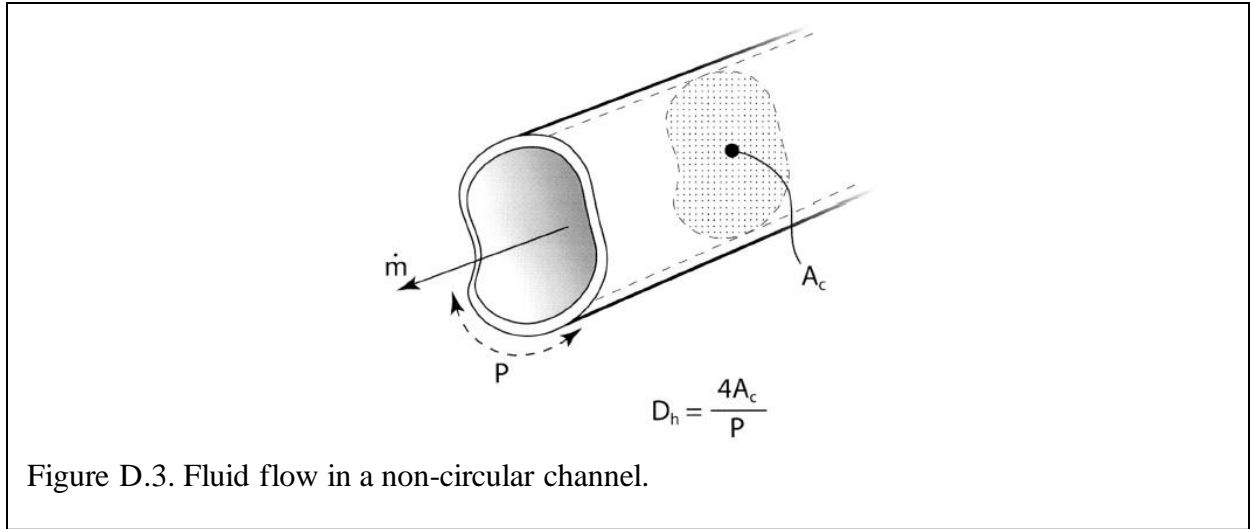
$$D_h \equiv \frac{4A_c}{P'} \quad \text{Eq.D.92}$$

Here, P' refers to the wetted perimeter of the cross section of the passage, and A_c refers to the flow cross-sectional area [49], [54]. In many cases, the D_h expressed in Equation 2.185 may be substituted for the circular tube diameter, D_{cir} , in the same calculations used for circular ducts for Re , Nu , and C_f , but the actual cross-sectional area of the duct must be used to calculate the bulk velocity and mass flow rates.

For example, the Reynolds number for *laminar* fluid flow in a rectangular tube is:

$$Re_D \equiv \frac{\rho u_{av} D_h}{\mu} \quad \text{Eq.D.93}$$

Here, u_{avg} refers to the mean velocity of the fluid over the entire cross-section of the opening, D_h is the hydraulic diameter for the rectangular tube approximation, and ρ and μ are the fluid density and viscosity, respectively. The critical Reynold's number, $Re_{D,c}$, is typically taken to be between 2,100 and 2,300, and the ratio of entry length to channel effective diameter for turbulent flow is typically expected to be $10 \leq \frac{x_e}{D_h} \leq 60$ [49], [54], [55].



The substitution of D_h to determine thermal transfer coefficients is relatively good for turbulent flows and yields results within $\pm 20\%$ of measured results, often even within $\pm 10\%$. However, it does not sufficiently model laminar flows, and is less accurate for ducts with sharp corners. Specialized effective hydraulic diameter expressions for common cases such as the parallel plate duct allow for accuracies to reach up to $\pm 5\%$. The effective hydraulic diameter for the parallel plate duct is:

$$D_h = 2b \quad \text{Eq.D.94}$$

Here, b is the distance between the parallel plates (ranging from 5 cm to 50 cm in this work) and the plates are located at $y = +b/2$ and $y = -b/2$ [54], [55].

Development of Laminar Velocity Profile: The mass flow rate through the channel is:

$$\dot{m} = \rho u_{av} A_c 2b \quad \text{Eq.D.95}$$

and defines the average velocity over the cross-sectional area of the tube. If the passage has a uniform cross-sectional area and is incompressible, then \dot{m} and u_{av} are constant. The mass flow rate may also be expressed in integral form as follows:

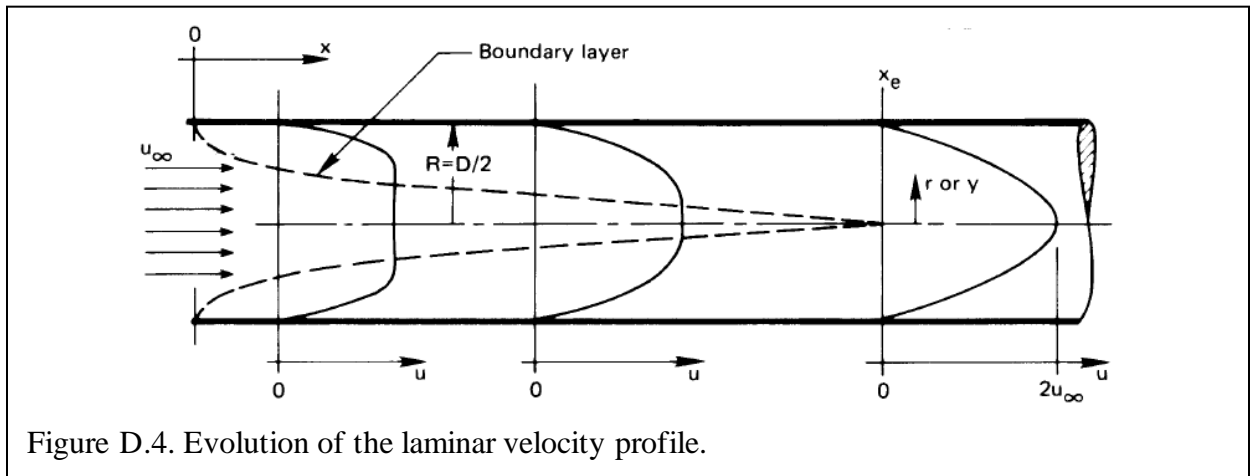
$$\dot{m} = \int_{A_c} \rho u_f(r, x) dA_c \quad \text{Eq.D.96}$$

where $u_f(r, x)$ refers to the fluid velocity at a position x meters from the leading edge and r meters from the center plane of the channel [49].

The velocity profile changes dramatically at the entranceway where a velocity boundary layer is initially formed. This boundary layer grows at the solid surfaces until meeting in the center of the channel and changing very little thereafter in this “fully developed” region. The evolution of the velocity profile shape is shown in Figure D.4. Within the fully developed region the streamlines are parallel, indicating the following [49], [54], [55]:

$$\frac{\partial u_f}{\partial x} = 0 \quad \text{Eq.D.97}$$

$$v_f = 0 \quad \text{Eq.D.98}$$



The hydrodynamic entry length, x_e , is dependent on a handful of variables (D_h , u_{av} , ρ , and μ) and is expressed as:

$$\frac{x_e}{D_h} = f(Re_D) \quad \text{Eq.D.99}$$

Where:

$$Re_D = \frac{\rho u_{av} D_h}{\mu} \quad \text{Eq.D.100}$$

A commonly accepted expression for the entry length is:

$$\frac{x_e}{D_h} \cong 0.03 Re_D \quad \text{Eq.D.101}$$

These values ensure that the drag on the wall of the channel and the drag in the fully developed flow region are within 5% of one another. Typically, the hydrodynamic entry length for flows with Reynolds numbers over 2,100 to 2,300 are well beyond the effective diameter of the opening.

During laminar flow, the velocity profiles within non-circular ducts develop in the same manner as those within circular ducts and take on a generally paraboloidal shape. In the case of fully developed laminar flow between parallel plates the ratio of the average inlet velocity, u_f to the bulk velocity between the plates, u_{av} , has been found to be:

$$\frac{u_f}{u_{av}} = \frac{3}{2} \left[1 - 4 \left(\frac{y}{b} \right)^2 \right] \quad \text{Eq.D.102}$$

Thermal Profile, Bulk Temperature, and Bulk Enthalpy: To model both laminar and turbulent fully developed flows from a thermal standpoint, the bulk temperature, T_b and the bulk enthalpy, i_b , must be understood. The bulk enthalpy can be understood as the average enthalpy of the fluid flowing through a cross section of the duct:

$$\dot{m} i_b \equiv \int_{A_c} \rho u_f i \, dA_c \quad \text{Eq.D.103}$$

Since $i = c_p(T - T_{ref})$, the bulk enthalpy follows: $i_b = c_p(T_b - T_{ref})$, and thus the bulk temperature in the channel can be determined:

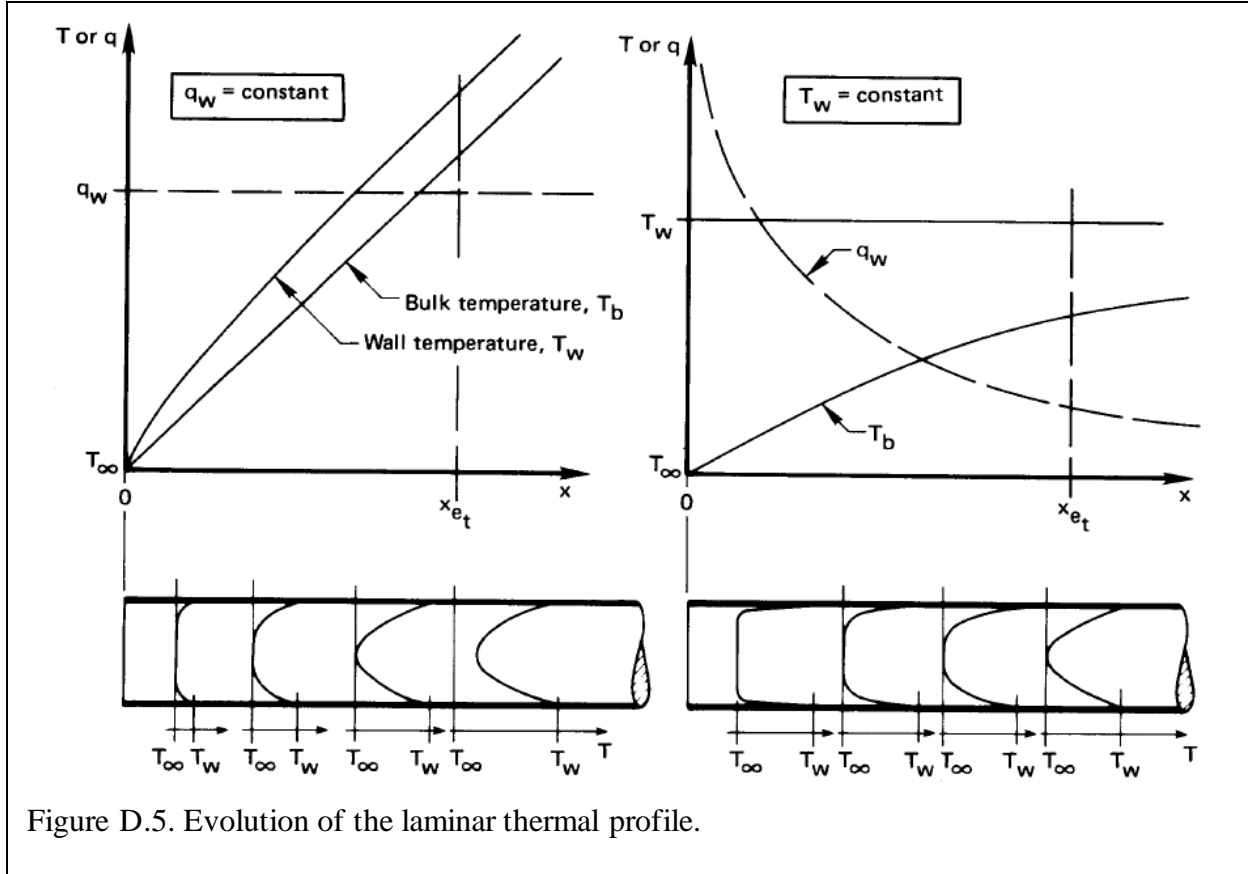


Figure D.5. Evolution of the laminar thermal profile.

$$T_b = \frac{\int_{A_c} \rho c_p u_f T dA_c}{\dot{m} c_p} \quad \text{Eq.D.104}$$

In other words, the bulk temperature is the rate of enthalpy flow through the cross-section of the duct per rate of heat capacity flow through the same cross-section. For either laminar or turbulent flow through a duct, if the fluid were collected into a cup at any x location, it would have a temperature equal to T_b and a total enthalpy equivalent to the average enthalpy of the fluid passing through the cross-section at that location. In fully developed flow, the thermal profile does not change, or:

$$\frac{\partial}{\partial x} \left(\frac{T_w - T}{T_w - T_b} \right) = 0 \quad \text{Eq.D.105}$$

Where T_w refers to the temperature of the channel wall and T is dependent on the x - and y -positions. Unsurprisingly, to have a steady thermal profile through the channel, a steady velocity profile must first evolve. Once the flow is fully developed, the wall conditions influence how the thermal profile evolves. Walls with a constant thermal flux shift the thermal profile but do not change its shape, while walls with a constant temperature do not shift the thermal profile but instead decrease its amplitude [54].

Consider a small, dx section of a duct with perimeter P' such that the surface area is $P'dx$. Application of the conservation of energy leads to the following expression:

$$dQ = q_w P' dx = \dot{m} di_b = \dot{m} c_p dT_b \quad \text{Eq.D.106}$$

Which can be rearranged to yield:

$$\frac{dT}{dx} = \frac{dT_b}{dx} = \frac{q_w P'}{\dot{m} c_p} \quad \text{Eq.D.107}$$

In fully developed flow the boundary layers are no longer changing, thus $(T_w - T_b)$ and i are constant, which means that:

$$\frac{dT}{dx} = \frac{dT_b}{dx} = \frac{q_w P'}{\dot{m} c_p} = \text{constant} \quad \text{Eq.D.108}$$

The Nusselt number for laminar flow between parallel plates has been found for uniform, equal temperatures ($T_{w_1} = T_{w_2}$) at both plates ($Nu_{D_h} = 7.541$) as well as for fixed, equal fluxes ($q_{w_1} = q_{w_2}$) at both plates ($Nu_{D_h} = 8.235$), uniform but different temperatures ($T_{w_1} \neq T_{w_2}$) on each plate ($Nu_1 = Nu_2 = 4$), and uniform but different fluxes ($q_{w_1} \neq q_{w_2}$) on each plate

$$(Nu_1 = \frac{140}{26-9\left(\frac{q_{w_2}}{q_{w_1}}\right)} \text{ and } Nu_2 = \frac{140}{26-9\left(\frac{q_{w_1}}{q_{w_2}}\right)}) \quad [54], [55].$$

The thermal entry length, x_{e_T} , varies for fluids with different Prandtl numbers, and for

very viscous or cold fluids the thermal entry length often exceeds the length of the duct and fully developed flow is never reached. For the purposes of this work Prandtl numbers will be ≤ 10 to ensure fully developed flow can be achieved.

Vertical Plate: In the case of a vertical plate, when $T_s > T_{amb}$, the fluid further from the plate is less dense than the fluid nearer to the surface of the plate, inducing a free convection boundary layer with the fluid moving in the vertical or x -direction. The velocity profile of the rising fluid takes on a different shape than that of the velocity profile for forced convection, as the fluid velocity u_f is equal to 0 at $y = 0$ and $y \rightarrow \infty$. When $T_s < T_{amb}$ the direction of the fluid motion is downward. Luckily, buoyancy effects only influence how conservation of momentum is expressed, so the conservation of energy and conservation of mass expressions are unchanged from their forms in Equations 2.118 and 2.133, respectively. The x -momentum for this geometry with the gravitational body force per unit volume of $X_g = -\rho_f g$ is [49], [54]:

$$u_f \frac{\partial u_f}{\partial x} + v_f \frac{\partial u_f}{\partial y} = -\frac{1}{\rho_f} \frac{dp_{amb}}{dx} - g + v_f \frac{\partial^2 u_f}{\partial x^2} \quad \text{Eq.D.109}$$

Here, $\frac{dp_{amb}}{dx}$ refers to the freestream pressure gradient outside of the boundary layer where $u_f = 0$

so:

$$\frac{dp_{amb}}{dx} = -\rho_{amb} g \quad \text{Eq.D.110}$$

Which yields:

$$u_f \frac{\partial u_f}{\partial x} + v_f \frac{\partial u_f}{\partial y} = g \left(\frac{\rho_{amb} - \rho_f}{\rho_f} \right) + v_f \frac{\partial^2 u_f}{\partial x^2} = g \left(\frac{\Delta \rho}{\rho_f} \right) + v_f \frac{\partial^2 u_f}{\partial x^2} \quad \text{Eq.D.111}$$

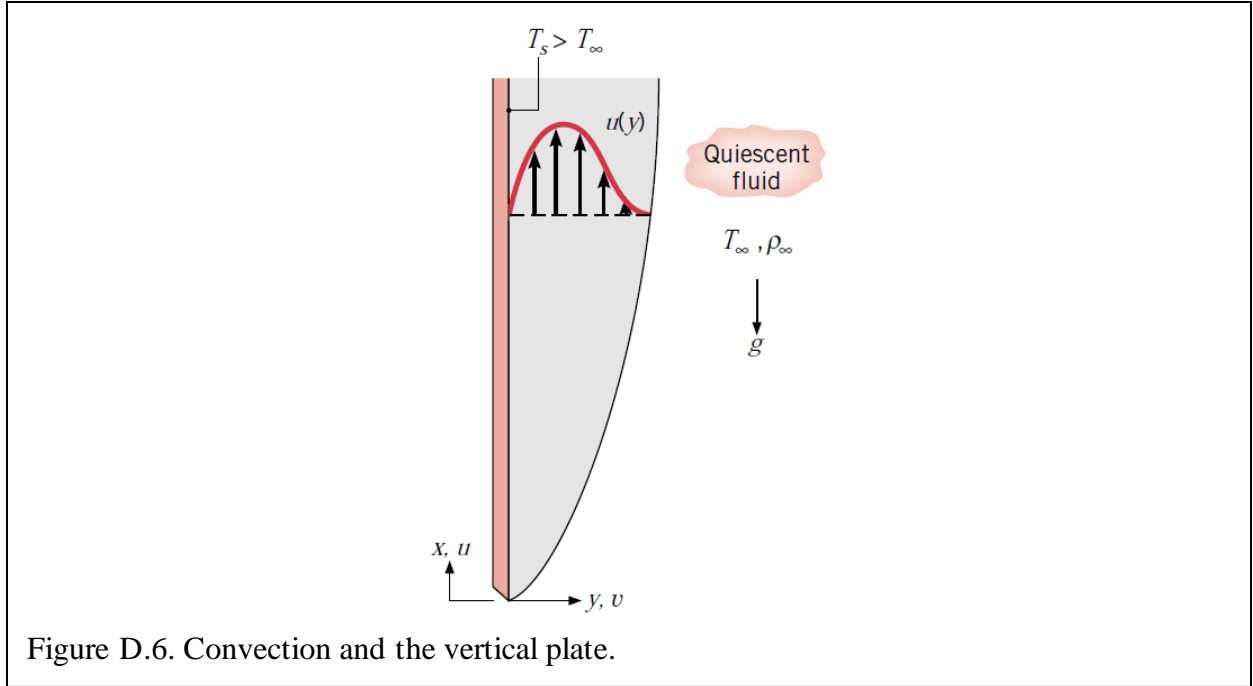


Figure D.6. Convection and the vertical plate.

The term $g \left(\frac{\Delta \rho}{\rho_f} \right)$ is the Buoyant Force that arises due to density variation. The volumetric thermal expansion coefficient, β , is a fluid property that quantifies the density change with changing temperature. The thermal expansion coefficient at constant pressure is expressed as:

$$\beta = -\frac{1}{\rho_f} \left(\frac{\partial \rho_f}{\partial T} \right)_p \quad \text{Eq.D.112}$$

This can be approximated as:

$$\beta \approx -\frac{1}{\rho_f} \frac{\Delta \rho}{\Delta T} = -\frac{1}{\rho_f} \frac{\Delta \rho}{(T_{amb} - T)} \quad \text{Eq.D.113}$$

And so, the momentum equation may be expressed as [49], [54]:

$$u_f \frac{\partial u_f}{\partial x} + v_f \frac{\partial u_f}{\partial y} = g\beta(T - T_{amb}) + \nu_f \frac{\partial^2 u_f}{\partial x^2} \quad \text{Eq.D.114}$$

Application of the normalized x^* , y^* , and the other non-dimensional variables allow the x-momentum equation to be expressed as:

$$u_f^* \frac{\partial u_f^*}{\partial x^*} + v_f^* \frac{\partial u_f^*}{\partial y^*} = \frac{g\beta(T - T_{amb})L}{u_0^2} T^* + \frac{1}{Re_L} \frac{\partial^2 u_f^*}{\partial y^{*2}} \quad \text{Eq.D.115}$$

Choosing $u_0^2 = g\beta(T - T_{amb})L$, this becomes:

$$u_f^* \frac{\partial u_f^*}{\partial x^*} + v_f^* \frac{\partial u_f^*}{\partial y} = T^* + \frac{1}{Re_L} \frac{\partial^2 u_f^*}{\partial y^{*2}} \quad \text{Eq.D.116}$$

In the absence of drag forces slowing, when a particle accelerates under a constant force it reaches a particular speed:

$$u_f = \sqrt{2g\beta\Delta TL} \quad \text{Eq.D.117}$$

And the Grashof number can thus be defined as:

$$Gr_L \equiv \frac{g\beta\Delta TL^3}{v_f^2} \quad \text{Eq.D.118}$$

From here, the Rayleigh number may be defined as:

$$Ra_L \equiv Gr_L Pr \quad \text{Eq.D.119}$$

The Rayleigh number characterizes the type of flow: laminar, turbulent, or mixed. Empirical data shows that natural convective flow from a vertical plate becomes turbulent when:

$$\frac{Ra_L}{\left[1 + \frac{0.492}{Pr^{9/16}}\right]^{16/9}} \cong 10^8 \quad \text{Eq.D.120}$$

Furthermore, empirical data suggests that the most accurate expression for the Nusselt number for laminar natural convection from a vertical plate ($Ra_L \leq 10^9$) is:

$$\overline{Nu}_L = 0.68 + 0.670 Ra_L^{1/4} \left[1 + \left(\frac{0.492}{Pr}\right)^{9/16}\right]^{-4/9} \quad \text{Eq.D.121}$$

For turbulent flow ($Ra_L \geq 10^9$) the best mathematical expression for the Nusselt number is:

$$\overline{Nu}_L = \left\{ 0.825 + 0.387 \left[\frac{Ra_L}{\left[1 + \left(\frac{0.492}{Pr}\right)^{9/16}\right]^{8/27}} \right]^{1/6} \right\}^2 \quad \text{Eq.D.122}$$

Aside from the evaluation of β (which should be evaluated at T_{amb}), properties should be evaluated at the average film temperature [54]:

$$T_{avf} = \frac{T_{amb} + T_s}{2} \quad \text{Eq.D.123}$$

Appendix E: Other Factors Influencing PV Performance

Shade and Debris: Other factors such as shading as well as dust and snow accumulation adversely affect PV performance but are not incorporated into this simulation. Shade may be eliminated as a factor in this simulation by presuming the facility is in an area without tree cover or buildings that could shade part of the facility. Dust and snow accumulation on the surface of the PV panels are also known to decrease PV panel performance. Accumulation of debris on PV panel surfaces is highly variable and can be eliminated via regular cleaning, so for the purposes of this work no surface accumulation is considered.

Drought and Wildfires: Long periods of excessively high temperatures frequently lead to or exacerbate drought conditions, which primarily impact agriculture and water supplies. Roughly 50% of the continental United States is experiencing drought conditions [131], [132] and have been since the spring of 2021. While drought conditions alone do not impact PV performance, they do increase the probability of widespread wildfires. During the 2020 wildfires across California average solar power generation dropped due to the sunlight blocking effects of the ash and soot in the wildfire smoke. According to the California Independent System Operator (CAISO) which oversees all electricity production throughout the state, in the first two weeks of September 2020 solar power generation dropped by 30% from the July average due to wildfire smoke [133].

The ash and soot particles within wildfire smoke are $2.5\mu\text{m}$ or smaller, and this size of particulate matter has been shown to scatter and absorb radiation [134]. Effects from wildfire smoke extend beyond the local areas in which fires are burning, having traveled thousands of miles to affect air quality and visibility on the east coast in both 2020 and 2021 [135]. As drought conditions become more severe, frequent, and widespread, a greater quantity of wildfires

is inevitable. With wildfires growing increasingly more frequent and widespread, the sheer volume of smoke present in the air will be capable of decreasing visibility across larger areas and greater distances.

Forecasting wildfire smoke has been a significant challenge in the past because of the chaotic and unpredictable behavior of smoke plumes and high interdependency on atmospheric conditions. The High-Resolution Rapid Refresh Smoke (HRRR-Smoke) model building on the NOAA's existing weather HRRR model for rain, wind, and thunderstorms. The HRRR-Smoke model is especially accurate at predicting smoke behavior because it combines key metrics including fire radiative power (FRP), which quantifies the thermal energy release of a wildfire in MW, vegetation maps that quantify the burning power of different types of vegetation, as well as wind speed and direction, rain, and atmospheric temperature observations. The HRRR-smoke model forecasts smoke behavior in a 3D grid reaching approximately 16 miles into Earth's atmosphere to an astounding degree of accuracy as compared to earlier models. Application of the HRRR-Smoke model to simulate wildfire smoke behavior would be an excellent way to enhance the accuracy of this work when developing "future" weather models [136]–[138].

Because the purpose of modeling wildfire smoke is to assess the impact on PV panel output, describing the spread of wildfires and wildfire smoke to other geographic areas is not necessary. From the perspective of the PV panel, smoke and heavy cloud cover have the same impact, so wildfire smoke is modeled as cloud coverage with a high okta value to indicate the thickness of the smoke.

The load for the generalized facility is randomized throughout the years simulated, while the load for the VF is highly dependent on both predictable lighting needs and temperature control needs that are coupled to exterior environmental conditions. VF lighting may be on for

anywhere between 8 and 16 hours per day depending on the needs of the plants being grown, so these two extremes along with a 12-hour mid-point lighting range are used to determine load from lighting in the simulation.

Other BIPV-PCM Components: Batteries, air conditioning, heating, and all other accessories are modeled as ideal and essentially ignored in this work. Any heated air expelled by the air conditioner will be neglected in thermal calculations, and no limitations on the capacity or lifetime of energy storage are considered. Future research would benefit from incorporating these features into the model via to better reflect the real-world functionality of the system.

PanelOrient

184

SolarTech_B = 1.663;

%%
%%
%%

%%% Lumos: Max PV Panels

%%
%%
%%

A1_Lumos = fix(Bldg_X/Lumos_A);
A2_Lumos_20 = fix(Bldg_Y_20/Lumos_B);
A2_Lumos_40 = fix(Bldg_Y_40/Lumos_B);

B1_Lumos = fix(Bldg_X/Lumos_B);
B2_Lumos_20 = fix(Bldg_Y_20/Lumos_A);
B2_Lumos_40 = fix(Bldg_Y_40/Lumos_A);

Alpha_Lumos_20 = A1_Lumos*A2_Lumos_20;
Alpha_Lumos_40 = A1_Lumos*A2_Lumos_40;
Beta_Lumos_20 = B1_Lumos*B2_Lumos_20;
Beta_Lumos_40 = B1_Lumos*B2_Lumos_40;

if Alpha_Lumos_20 > Beta_Lumos_20
 TX_Lumos_20 = A1_Lumos*Lumos_A;
 TY_Lumos_20 = A2_Lumos_20*Lumos_B;
else
 TX_Lumos_20 = B1_Lumos*Lumos_B;
 TY_Lumos_20 = B2_Lumos20*Lumos_A;
end

if Alpha_Lumos_40 > Beta_Lumos_40
 TX_Lumos_40 = A1_Lumos*Lumos_A;
 TY_Lumos_40 = A2_Lumos_40*Lumos_B;
else
 TX_Lumos_40 = B1_Lumos*Lumos_B;
 TY_Lumos_40 = B2_Lumos40*Lumos_A;
end

%%
%%
%%

%%% MSE425SX6W: Max PV Panels

%%
%%
%%

```

A1_MSE425SX6W = fix(Bldg_X/MSE425SX6W_A);
A2_MSE425SX6W_20 = fix(Bldg_Y_20/MSE425SX6W_B);
A2_MSE425SX6W_40 = fix(Bldg_Y_40/MSE425SX6W_B);

B1_MSE425SX6W = fix(Bldg_X/MSE425SX6W_B);
B2_MSE425SX6W_20 = fix(Bldg_Y_20/MSE425SX6W_A);
B2_MSE425SX6W_40 = fix(Bldg_Y_40/MSE425SX6W_A);

Alpha_MSE425SX6W_20 = A1_MSE425SX6W*A2_MSE425SX6W_20;
Alpha_MSE425SX6W_40 = A1_MSE425SX6W*A2_MSE425SX6W_40;
Beta_MSE425SX6W_20 = B1_MSE425SX6W*B2_MSE425SX6W_20;
Beta_MSE425SX6W_40 = B1_MSE425SX6W*B2_MSE425SX6W_40;

```

```

if Alpha_MSE425SX6W_20 > Beta_MSE425SX6W_20
    TX_MSE425SX6W_20 = A1_MSE425SX6W*MSE425SX6W_A;
    TY_MSE425SX6W_20 = A2_MSE425SX6W_20*MSE425SX6W_B;
else
    TX_MSE425SX6W_20 = B1_MSE425SX6W*MSE425SX6W_B;
    TY_MSE425SX6W_20 = B2_MSE425SX6W_20*MSE425SX6W_A;
end

```

```

if Alpha_MSE425SX6W_40 > Beta_MSE425SX6W_40
    TX_MSE425SX6W_40 = A1_MSE425SX6W*MSE425SX6W_A;
    TY_MSE425SX6W_40 = A2_MSE425SX6W_40*MSE425SX6W_B;
else
    TX_MSE425SX6W_40 = B1_MSE425SX6W*MSE425SX6W_B;
    TY_MSE425SX6W_40 = B2_MSE425SX6W_40*MSE425SX6W_A;
end

```

```

%%%%%%%%%%
%%%%%%%%%%
%%

```

%% MSE330SR8K: Max PV Panels

```

%%%%%%%%%%
%%%%%%%%%%
%%

```

```

A1_MSE330SR8K = fix(Bldg_X/MSE330SR8K_A);
A2_MSE330SR8K_20 = fix(Bldg_Y_20/MSE330SR8K_B);
A2_MSE330SR8K_40 = fix(Bldg_Y_40/MSE330SR8K_B);

```

```

B1_MSE330SR8K = fix(Bldg_X/MSE330SR8K_B);
B2_MSE330SR8K_20 = fix(Bldg_Y_20/MSE330SR8K_A);
B2_MSE330SR8K_40 = fix(Bldg_Y_40/MSE330SR8K_A);

```



```

Alpha_MSE330SR8K_20 = A1_MSE330SR8K*A2_MSE330SR8K_20;
Alpha_MSE330SR8K_40 = A1_MSE330SR8K*A2_MSE330SR8K_40;
Beta_MSE330SR8K_20 = B1_MSE330SR8K*B2_MSE330SR8K_20;
Beta_MSE330SR8K_40 = B1_MSE330SR8K*B2_MSE330SR8K_40;

```

```

if Alpha_MSE330SR8K_20 > Beta_MSE330SR8K_20
    TX_MSE330SR8K_20 = A1_MSE330SR8K*MSE330SR8K_A;
    TY_MSE330SR8K_20 = A2_MSE330SR8K_20*MSE330SR8K_B;
else
    TX_MSE330SR8K_20 = B1_MSE330SR8K*MSE330SR8K_B;
    TY_MSE330SR8K_20 = B2_MSE330SR8K_20*MSE330SR8K_A;
end

```

```

if Alpha_MSE330SR8K_40 > Beta_MSE330SR8K_40
    TX_MSE330SR8K_40 = A1_MSE330SR8K*MSE330SR8K_A;
    TY_MSE330SR8K_40 = A2_MSE330SR8K_40*MSE330SR8K_B;
else
    TX_MSE330SR8K_40 = B1_MSE330SR8K*MSE330SR8K_B;
    TY_MSE330SR8K_40 = B2_MSE330SR8K_40*MSE330SR8K_A;
end

```

```

%%%%%%%%%%
%%%%%%%%%%
%%

```

%% MSE390SR9S: Max PV Panels

```

%%%%%%%%%%
%%%%%%%%%%
%%

```

```

A1_MSE390SR9S = fix(Bldg_X/MSE390SR9S_A);
A2_MSE390SR9S_20 = fix(Bldg_Y_20/MSE390SR9S_B);
A2_MSE390SR9S_40 = fix(Bldg_Y_40/MSE390SR9S_B);

```

```

B1_MSE390SR9S = fix(Bldg_X/MSE390SR9S_B);
B2_MSE390SR9S_20 = fix(Bldg_Y_20/MSE390SR9S_A);
B2_MSE390SR9S_40 = fix(Bldg_Y_40/MSE390SR9S_A);

```

```

Alpha_MSE390SR9S_20 = A1_MSE390SR9S*A2_MSE390SR9S_20;
Alpha_MSE390SR9S_40 = A1_MSE390SR9S*A2_MSE390SR9S_40;
Beta_MSE390SR9S_20 = B1_MSE390SR9S*B2_MSE390SR9S_20;
Beta_MSE390SR9S_40 = B1_MSE390SR9S*B2_MSE390SR9S_40;

```

```

if Alpha_MSE390SR9S_20 > Beta_MSE390SR9S_20
    TX_MSE390SR9S_20 = A1_MSE390SR9S*MSE390SR9S_A;
    TY_MSE390SR9S_20 = A2_MSE390SR9S_20*MSE390SR9S_B;
else

```

```

TX_MSE390SR9S_20 = B1_MSE390SR9S*MSE390SR9S_B;
TY_MSE390SR9S_20 = B2_MSE390SR9S_20*MSE390SR9S_A;
end

```

```

if Alpha_MSE390SR9S_40 > Beta_MSE390SR9S_40
    TX_MSE390SR9S_40 = A1_MSE390SR9S*MSE390SR9S_A;
    TY_MSE390SR9S_40 = A2_MSE390SR9S_40*MSE390SR9S_B;
else
    TX_MSE390SR9S_40 = B1_MSE390SR9S*MSE390SR9S_B;
    TY_MSE390SR9S_40 = B2_MSE390SR9S_40*MSE390SR9S_A;
end

```

```

%%%%%%%%%%%%%%%%%%%%%%%%%%%%%%%%%%%%%%%%%%%%%%%%%%%%%%%%%%%%%%%%%%%%%%%%
%%%%%%%%%%%%%%%%%%%%%%%%%%%%%%%%%%%%%%%%%%%%%%%%%%%%%%%%%%%%%%%%%%%%%%%%
%%
%%% SolarTech: Max PV Panels
%%%%%%%%%%%%%%%%%%%%%%%%%%%%%%%%%%%%%%%%%%%%%%%%%%%%%%%%%%%%%%%%%%%%%%%%
%%%%%%%%%%%%%%%%%%%%%%%%%%%%%%%%%%%%%%%%%%%%%%%%%%%%%%%%%%%%%%%%%%%%%%%%
%%

```

```

A1_SolarTech = fix(Bldg_X/SolarTech_A);
A2_SolarTech_20 = fix(Bldg_Y_20/SolarTech_B);
A2_SolarTech_40 = fix(Bldg_Y_40/SolarTech_B);

```

```

B1_SolarTech = fix(Bldg_X/SolarTech_B);
B2_SolarTech_20 = fix(Bldg_Y_20/SolarTech_A);
B2_SolarTech_40 = fix(Bldg_Y_40/SolarTech_A);

```

```

Alpha_SolarTech_20 = A1_SolarTech*A2_SolarTech_20;
Alpha_SolarTech_40 = A1_SolarTech*A2_SolarTech_40;
Beta_SolarTech_20 = B1_SolarTech*B2_SolarTech_20;
Beta_SolarTech_40 = B1_SolarTech*B2_SolarTech_40;

```

```

if Alpha_SolarTech_20 > Beta_SolarTech_20
    TX_SolarTech_20 = A1_SolarTech*SolarTech_A;
    TY_SolarTech_20 = A2_SolarTech_20*SolarTech_B;
else
    TX_SolarTech_20 = B1_SolarTech*SolarTech_B;
    TY_SolarTech_20 = B2_SolarTech_20*SolarTech_A;
end

```

```

if Alpha_SolarTech_40 > Beta_SolarTech_40
    TX_SolarTech_40 = A1_SolarTech*SolarTech_A;
    TY_SolarTech_40 = A2_SolarTech_40*SolarTech_B;
else
    TX_SolarTech_40 = B1_SolarTech*SolarTech_B;

```

```
TY_SolarTech_40 = B2_SolarTech_40*SolarTech_A;  
end
```

Import Raw Data (Austin):

```
%%%%%%%%%%%%%%%%%%%%%%%%%%%%%%%%%%%%%%%%%%%%%%%%%%%%%%%%%%%%%%%%%%%%%%%%  
%%%%%%%%%%%%%%%%%%%%%%%%%%%%%%%%%%%%%%%%%%%%%%%%%%%%%%%%%%%%%%%%%%%%%%%%  
%%
```

```
%%% Upload and select base data for processing into data sets
```

```
%%%%%%%%%%%%%%%%%%%%%%%%%%%%%%%%%%%%%%%%%%%%%%%%%%%%%%%%%%%%%%%%%%%%%%%%  
%%%%%%%%%%%%%%%%%%%%%%%%%%%%%%%%%%%%%%%%%%%%%%%%%%%%%%%%%%%%%%%%%%%%%%%%  
%%
```

```
AUS1970 = readtable('C:\Users\amand\Desktop\Dissertation\NOAA Weather Data  
Files\Cities1970-2015\Austin-TX\Austin-1970.csv');
```

```
AUS1970 = AUS1970(:,[2 4 5 6 11 12 14 15]);
```

```
AUS1971 = readtable('C:\Users\amand\Desktop\Dissertation\NOAA Weather Data  
Files\Cities1970-2015\Austin-TX\Austin-1971.csv');
```

```
AUS1971 = AUS1971(:,[2 4 5 6 11 12 14 15]);
```

```
AUS1972 = readtable('C:\Users\amand\Desktop\Dissertation\NOAA Weather Data  
Files\Cities1970-2015\Austin-TX\Austin-1972.csv');
```

```
AUS1972 = AUS1972(:,[2 4 5 6 11 12 14 15]); %% LEAP
```

```
AUS1973 = readtable('C:\Users\amand\Desktop\Dissertation\NOAA Weather Data  
Files\Cities1970-2015\Austin-TX\Austin-1973.csv');
```

```
AUS1973 = AUS1973(:,[2 4 5 6 11 12 14 15]);
```

```
AUS1974 = readtable('C:\Users\amand\Desktop\Dissertation\NOAA Weather Data  
Files\Cities1970-2015\Austin-TX\Austin-1974.csv');
```

```
AUS1974 = AUS1974(:,[2 4 5 6 11 12 14 15]);
```

```
AUS1975 = readtable('C:\Users\amand\Desktop\Dissertation\NOAA Weather Data  
Files\Cities1970-2015\Austin-TX\Austin-1975.csv');
```

```
AUS1975 = AUS1975(:,[2 4 5 6 11 12 14 15]);
```

```
AUS1976 = readtable('C:\Users\amand\Desktop\Dissertation\NOAA Weather Data  
Files\Cities1970-2015\Austin-TX\Austin-1976.csv');
```

```
AUS1976 = AUS1976(:,[2 4 5 6 11 12 14 15]); %% LEAP
```

```
AUS1977 = readtable('C:\Users\amand\Desktop\Dissertation\NOAA Weather Data  
Files\Cities1970-2015\Austin-TX\Austin-1977.csv');
```

```
AUS1977 = AUS1977(:,[2 4 5 6 11 12 14 15]);
```

```
AUS1978 = readtable('C:\Users\amand\Desktop\Dissertation\NOAA Weather Data  
Files\Cities1970-2015\Austin-TX\Austin-1978.csv');
```

```
AUS1978 = AUS1978(:,[2 4 5 6 11 12 14 15]);
```

```
AUS1979 = readtable('C:\Users\amand\Desktop\Dissertation\NOAA Weather Data  
Files\Cities1970-2015\Austin-TX\Austin-1979.csv');
```

```
AUS1979 = AUS1979(:,[2 4 5 6 11 12 14 15]);
```

```
AUS1980 = readtable('C:\Users\amand\Desktop\Dissertation\NOAA Weather Data  
Files\Cities1970-2015\Austin-TX\Austin-1980.csv');
```

```

AUS1980 = AUS1980(:,[2 4 5 6 11 12 14 15]); %% LEAP
AUS1981 = readtable('C:\Users\amand\Desktop\Dissertation\NOAA Weather Data
Files\Cities1970-2015\Austin-TX\Austin-1981.csv');
AUS1981 = AUS1981(:,[2 4 5 6 11 12 14 15]);
AUS1982 = readtable('C:\Users\amand\Desktop\Dissertation\NOAA Weather Data
Files\Cities1970-2015\Austin-TX\Austin-1982.csv');
AUS1982 = AUS1982(:,[2 4 5 6 11 12 14 15]);
AUS1983 = readtable('C:\Users\amand\Desktop\Dissertation\NOAA Weather Data
Files\Cities1970-2015\Austin-TX\Austin-1983.csv');
AUS1983 = AUS1983(:,[2 4 5 6 11 12 14 15]);
AUS1984 = readtable('C:\Users\amand\Desktop\Dissertation\NOAA Weather Data
Files\Cities1970-2015\Austin-TX\Austin-1984.csv');
AUS1984 = AUS1984(:,[2 4 5 6 11 12 14 15]); %% LEAP
AUS1985 = readtable('C:\Users\amand\Desktop\Dissertation\NOAA Weather Data
Files\Cities1970-2015\Austin-TX\Austin-1985.csv');
AUS1985 = AUS1985(:,[2 4 5 6 11 12 14 15]);
AUS1986 = readtable('C:\Users\amand\Desktop\Dissertation\NOAA Weather Data
Files\Cities1970-2015\Austin-TX\Austin-1986.csv');
AUS1986 = AUS1986(:,[2 4 5 6 11 12 14 15]);
AUS1987 = readtable('C:\Users\amand\Desktop\Dissertation\NOAA Weather Data
Files\Cities1970-2015\Austin-TX\Austin-1987.csv');
AUS1987 = AUS1987(:,[2 4 5 6 11 12 14 15]);
AUS1988 = readtable('C:\Users\amand\Desktop\Dissertation\NOAA Weather Data
Files\Cities1970-2015\Austin-TX\Austin-1988.csv');
AUS1988 = AUS1988(:,[2 4 5 6 11 12 14 15]); %%LEAP
AUS1989 = readtable('C:\Users\amand\Desktop\Dissertation\NOAA Weather Data
Files\Cities1970-2015\Austin-TX\Austin-1989.csv');
AUS1989 = AUS1989(:,[2 4 5 6 11 12 14 15]);
AUS1990 = readtable('C:\Users\amand\Desktop\Dissertation\NOAA Weather Data
Files\Cities1970-2015\Austin-TX\Austin-1990.csv');
AUS1990 = AUS1990(:,[2 4 5 6 11 12 14 15]);
AUS1991 = readtable('C:\Users\amand\Desktop\Dissertation\NOAA Weather Data
Files\Cities1970-2015\Austin-TX\Austin-1991.csv');
AUS1991 = AUS1991(:,[2 4 5 6 11 12 14 15]);
AUS1992 = readtable('C:\Users\amand\Desktop\Dissertation\NOAA Weather Data
Files\Cities1970-2015\Austin-TX\Austin-1992.csv');
AUS1992 = AUS1992(:,[2 4 5 6 11 12 14 15]); %%LEAP
AUS1993 = readtable('C:\Users\amand\Desktop\Dissertation\NOAA Weather Data
Files\Cities1970-2015\Austin-TX\Austin-1993.csv');
AUS1993 = AUS1993(:,[2 4 5 6 11 12 14 15]);
AUS1994 = readtable('C:\Users\amand\Desktop\Dissertation\NOAA Weather Data
Files\Cities1970-2015\Austin-TX\Austin-1994.csv');
AUS1994 = AUS1994(:,[2 4 5 6 11 12 14 15]);
AUS1995 = readtable('C:\Users\amand\Desktop\Dissertation\NOAA Weather Data
Files\Cities1970-2015\Austin-TX\Austin-1995.csv');
AUS1995 = AUS1995(:,[2 4 5 6 11 12 14 15]);

```

```

AUS1996 = readtable('C:\Users\amand\Desktop\Dissertation\NOAA Weather Data
Files\Cities1970-2015\Austin-TX\Austin-1996.csv');
    AUS1996 = AUS1996(:,[2 4 5 6 11 12 14 15]); %%LEAP
AUS1997 = readtable('C:\Users\amand\Desktop\Dissertation\NOAA Weather Data
Files\Cities1970-2015\Austin-TX\Austin-1997.csv');
    AUS1997 = AUS1997(:,[2 4 5 6 11 12 14 15]);
AUS1998 = readtable('C:\Users\amand\Desktop\Dissertation\NOAA Weather Data
Files\Cities1970-2015\Austin-TX\Austin-1998.csv');
    AUS1998 = AUS1998(:,[2 4 5 6 11 12 14 15]);
AUS1999a = readtable('C:\Users\amand\Desktop\Dissertation\NOAA Weather Data
Files\Cities1970-2015\Austin-TX\Austin-1999a.csv');
    AUS1999a = AUS1999a(:,[2 4 5 6 11 12 14 15]);
AUS1999b = readtable('C:\Users\amand\Desktop\Dissertation\NOAA Weather Data
Files\Cities1970-2015\Austin-TX\Austin-1999b.csv');
    AUS1999b = AUS1999b(:,[2 4 5 6 11 12 14 15]);
    AUS1999 = [AUS1999a ;AUS1999b];
AUS2000 = readtable('C:\Users\amand\Desktop\Dissertation\NOAA Weather Data
Files\Cities1970-2015\Austin-TX\Austin-2000.csv');
    AUS2000 = AUS2000(:,[2 4 5 6 11 12 14 15]); %%LEAP
AUS2001 = readtable('C:\Users\amand\Desktop\Dissertation\NOAA Weather Data
Files\Cities1970-2015\Austin-TX\Austin-2001.csv');
    AUS2001 = AUS2001(:,[2 4 5 6 11 12 14 15]);
AUS2002 = readtable('C:\Users\amand\Desktop\Dissertation\NOAA Weather Data
Files\Cities1970-2015\Austin-TX\Austin-2002.csv');
    AUS2002 = AUS2002(:,[2 4 5 6 11 12 14 15]);
AUS2003 = readtable('C:\Users\amand\Desktop\Dissertation\NOAA Weather Data
Files\Cities1970-2015\Austin-TX\Austin-2003.csv');
    AUS2003 = AUS2003(:,[2 4 5 6 11 12 14 15]);
AUS2004 = readtable('C:\Users\amand\Desktop\Dissertation\NOAA Weather Data
Files\Cities1970-2015\Austin-TX\Austin-2004.csv');
    AUS2004 = AUS2004(:,[2 4 5 6 11 12 14 15]); %%LEAP
AUS2005 = readtable('C:\Users\amand\Desktop\Dissertation\NOAA Weather Data
Files\Cities1970-2015\Austin-TX\Austin-2005.csv');
    AUS2005 = AUS2005(:,[2 4 5 6 11 12 14 15]);
AUS2006 = readtable('C:\Users\amand\Desktop\Dissertation\NOAA Weather Data
Files\Cities1970-2015\Austin-TX\Austin-2006.csv');
    AUS2006 = AUS2006(:,[2 4 5 6 11 12 14 15]);
AUS2007 = readtable('C:\Users\amand\Desktop\Dissertation\NOAA Weather Data
Files\Cities1970-2015\Austin-TX\Austin-2007.csv');
    AUS2007 = AUS2007(:,[2 4 5 6 11 12 14 15]);
AUS2008 = readtable('C:\Users\amand\Desktop\Dissertation\NOAA Weather Data
Files\Cities1970-2015\Austin-TX\Austin-2008.csv');
    AUS2008 = AUS2008(:,[2 4 5 6 11 12 14 15]); %%LEAP
AUS2009 = readtable('C:\Users\amand\Desktop\Dissertation\NOAA Weather Data
Files\Cities1970-2015\Austin-TX\Austin-2009.csv');
    AUS2009 = AUS2009(:,[2 4 5 6 11 12 14 15]);

```

```

AUS2010 = readtable('C:\Users\amand\Desktop\Dissertation\NOAA Weather Data
Files\Cities1970-2015\Austin-TX\Austin-2010.csv');
AUS2010 = AUS2010(:,[2 4 5 6 11 12 14 15]);
AUS2011 = readtable('C:\Users\amand\Desktop\Dissertation\NOAA Weather Data
Files\Cities1970-2015\Austin-TX\Austin-2011.csv');
AUS2011 = AUS2011(:,[2 4 5 6 11 12 14 15]);
AUS2012 = readtable('C:\Users\amand\Desktop\Dissertation\NOAA Weather Data
Files\Cities1970-2015\Austin-TX\Austin-2012.csv');
AUS2012 = AUS2012(:,[2 4 5 6 11 12 14 15]); %%LEAP
AUS2013 = readtable('C:\Users\amand\Desktop\Dissertation\NOAA Weather Data
Files\Cities1970-2015\Austin-TX\Austin-2013.csv');
AUS2013 = AUS2013(:,[2 4 5 6 11 12 14 15]);
AUS2014 = readtable('C:\Users\amand\Desktop\Dissertation\NOAA Weather Data
Files\Cities1970-2015\Austin-TX\Austin-2014.csv');
AUS2014 = AUS2014(:,[2 4 5 6 11 12 14 15]);
AUS2015 = readtable('C:\Users\amand\Desktop\Dissertation\NOAA Weather Data
Files\Cities1970-2015\Austin-TX\Austin-2015.csv');
AUS2015 = AUS2015(:,[2 4 5 6 11 12 14 15]);

```

Assemble Austin Sets:

```

%%%%%%%%%%
%%%%%%%%%%
%%
%%
%% LEAP YEARS NOTES:
%%
%% Leap Years in future data:
%%      2020 / 2024 / 2028 / 2032 / 2036 / 2040 / 2044 / 2048
%% Leap Years in original data:
%%      1972 / 1976 / 1980 / 1984 / 1988 / 1992 / 1996 / 2000 /
%%      2004 / 2008 / 2012
%%%%%%%%%%
%%%%%%%%%%
%%
%%
%%%%%%%%%%
%%%%%%%%%%
%%
%% Process DATES For Data Set AusSet01: Austin Set 01: 72-76, 80-90, 2000-2013
%%%%%%%%%%
%%%%%%%%%%
%%
%% 1972 >> 2020

```

```

NewYear = AUS1972(:,1);          %%% Pull date and time data from raw data
NewYear = table2array(NewYear);  %%% Change format to array
NewYear = string(NewYear);       %%% Change format to string
NewYear = erase(NewYear, "1972"); %%% Delete real year data pulled from
NewYear = string(NewYear);       %%% Turn to string
Y01 = nan(height(NewYear),1);    %%% Build empty array height of data for this year
Y01 = fillmissing(Y01, 'constant', 2020); %%% Fill empty array with "new" year
Y01 = string(Y01);               %%% Convert to string
NewYear = strcat(Y01,NewYear);    %%% Concatenate into date/time data w/o year
NewYear = datetime(NewYear,'InputFormat','yyyy-MM-dd"T"HH:mm:ss');
NewYear = datetime(NewYear,'Format','yyyy-MM-dd"T"HH:mm:ss Z',
'TimeZone','America/Chicago'); %%% Convert to datetime
DOTY = day(NewYear,'dayofyear');  %%% Day of the year
DOTY = table(DOTY);
NewYear = table(NewYear);         %%% Convert to table
AUS2020 = [NewYear(:,:), DOTY, AUS1972(:,:)]; %%% Combine into new CTYyyyy table

```

%% 1973 >> 2021 %

```

NewYear = AUS1973(:,1);          %%% Pull date and time data from raw data
NewYear = table2array(NewYear);  %%% Change format to array
NewYear = string(NewYear);       %%% Change format to string
NewYear = erase(NewYear, "1973"); %%% Delete real year data pulled from
NewYear = string(NewYear);       %%% Turn to string
Y01 = nan(height(NewYear),1);    %%% Build empty array height of data for this year
Y01 = fillmissing(Y01, 'constant', 2021); %%% Fill empty array with "new" year
Y01 = string(Y01);               %%% Convert to string
NewYear = strcat(Y01,NewYear);    %%% Concatenate into date/time data w/o year
NewYear = datetime(NewYear,'InputFormat','yyyy-MM-dd"T"HH:mm:ss');
NewYear = datetime(NewYear,'Format','yyyy-MM-dd"T"HH:mm:ss Z',
'TimeZone','America/Chicago'); %%% Convert to datetime
DOTY = day(NewYear,'dayofyear');  %%% Day of the year
DOTY = table(DOTY);
NewYear = table(NewYear);         %%% Convert to table
AUS2021 = [NewYear(:,:), DOTY, AUS1973(:,:)]; %%% Combine into new CTYyyyy
tabletwi

```

%% 1974 >> 2022 %

```

NewYear = AUS1974(:,1);          %%% Pull date and time data from raw data
NewYear = table2array(NewYear);  %%% Change format to array
NewYear = string(NewYear);       %%% Change format to string
NewYear = erase(NewYear, "1974"); %%% Delete real year data pulled from
NewYear = string(NewYear);       %%% Turn to string
Y01 = nan(height(NewYear),1);    %%% Build empty array height of data for this year
Y01 = fillmissing(Y01, 'constant', 2022); %%% Fill empty array with "new" year

```

```

Y01 = string(Y01);                %%% Convert to string
NewYear = strcat(Y01,NewYear);    %%% Concatenate into date/time data w/o year
NewYear = datetime(NewYear,'InputFormat','yyyy-MM-dd"T"HH:mm:ss');
NewYear = datetime(NewYear,'Format','yyyy-MM-dd"T"HH:mm:ss Z',
'TimeZone','America/Chicago'); %%% Convert to datetime
DOTY = day(NewYear,'dayofyear');   %%% Day of the year
DOTY = table(DOTY);
NewYear = table(NewYear);          %%% Convert to table
AUS2022 = [NewYear(:,:), DOTY, AUS1974(:,:)]; %%% Combine into new CTYyyyy table

```

%% 1975 >> 2023 %

```

NewYear = AUS1975(:,1);           %%% Pull date and time data from raw data
NewYear = table2array(NewYear);   %%% Change format to array
NewYear = string(NewYear);        %%% Change format to string
NewYear = erase(NewYear, "1975"); %%% Delete real year data pulled from
NewYear = string(NewYear);        %%% Turn to string
Y01 = nan(height(NewYear),1);     %%% Build empty array height of data for this year
Y01 = fillmissing(Y01, 'constant', 2023); %%% Fill empty array with "new" year
Y01 = string(Y01);                %%% Convert to string
NewYear = strcat(Y01,NewYear);    %%% Concatenate into date/time data w/o year
NewYear = datetime(NewYear,'InputFormat','yyyy-MM-dd"T"HH:mm:ss');
NewYear = datetime(NewYear,'Format','yyyy-MM-dd"T"HH:mm:ss Z',
'TimeZone','America/Chicago'); %%% Convert to datetime
DOTY = day(NewYear,'dayofyear');   %%% Day of the year
DOTY = table(DOTY);
NewYear = table(NewYear);          %%% Convert to table
AUS2023 = [NewYear(:,:), DOTY, AUS1975(:,:)]; %%% Combine into new CTYyyyy table

```

%% 1976 >> 2024 %

```

NewYear = AUS1976(:,1);           %%% Pull date and time data from raw data
NewYear = table2array(NewYear);   %%% Change format to array
NewYear = string(NewYear);        %%% Change format to string
NewYear = erase(NewYear, "1976"); %%% Delete real year data pulled from
NewYear = string(NewYear);        %%% Turn to string
Y01 = nan(height(NewYear),1);     %%% Build empty array height of data for this year
Y01 = fillmissing(Y01, 'constant', 2024); %%% Fill empty array with "new" year
Y01 = string(Y01);                %%% Convert to string
NewYear = strcat(Y01,NewYear);    %%% Concatenate into date/time data w/o year
NewYear = datetime(NewYear,'InputFormat','yyyy-MM-dd"T"HH:mm:ss');
NewYear = datetime(NewYear,'Format','yyyy-MM-dd"T"HH:mm:ss Z',
'TimeZone','America/Chicago'); %%% Convert to datetime
DOTY = day(NewYear,'dayofyear');   %%% Day of the year
DOTY = table(DOTY);
NewYear = table(NewYear);          %%% Convert to table

```



```
AUS2024 = [NewYear(:,:), DOTY, AUS1976(:,:)];   %%% Combine into new CTYyyyyy table
```

```
%%% 1981 >> 2025 %%%
```

```
NewYear = AUS1981(:,1);      %%% Pull date and time data from raw data
NewYear = table2array(NewYear); %%% Change format to array
NewYear = string(NewYear);    %%% Change format to string
NewYear = erase(NewYear, "1981"); %%% Delete real year data pulled from
NewYear = string(NewYear);    %%% Turn to string
Y01 = nan(height(NewYear),1); %%% Build empty array height of data for this year
Y01 = fillmissing(Y01, 'constant', 2025); %%% Fill empty array with "new" year
Y01 = string(Y01);           %%% Convert to string
NewYear = strcat(Y01,NewYear); %%% Concatenate into date/time data w/o year
NewYear = datetime(NewYear,'InputFormat','yyyy-MM-dd"T"HH:mm:ss');
NewYear = datetime(NewYear,'Format','yyyy-MM-dd"T"HH:mm:ss Z',
'TimeZone','America/Chicago'); %%% Convert to datetime
DOTY = day(NewYear,'dayofyear'); %%% Day of the year
DOTY = table(DOTY);
NewYear = table(NewYear); %%% Convert to table
AUS2025 = [NewYear(:,:), DOTY, AUS1981(:,:)]; %%% Combine into new CTYyyyyy table
```

```
%%% 1982 >> 2026 %%%
```

```
NewYear = AUS1982(:,1);      %%% Pull date and time data from raw data
NewYear = table2array(NewYear); %%% Change format to array
NewYear = string(NewYear);    %%% Change format to string
NewYear = erase(NewYear, "1982"); %%% Delete real year data pulled from
NewYear = string(NewYear);    %%% Turn to string
Y01 = nan(height(NewYear),1); %%% Build empty array height of data for this year
Y01 = fillmissing(Y01, 'constant', 2026); %%% Fill empty array with "new" year
Y01 = string(Y01);           %%% Convert to string
NewYear = strcat(Y01,NewYear); %%% Concatenate into date/time data w/o year
NewYear = datetime(NewYear,'InputFormat','yyyy-MM-dd"T"HH:mm:ss');
NewYear = datetime(NewYear,'Format','yyyy-MM-dd"T"HH:mm:ss Z',
'TimeZone','America/Chicago'); %%% Convert to datetime
DOTY = day(NewYear,'dayofyear'); %%% Day of the year
DOTY = table(DOTY);
NewYear = table(NewYear); %%% Convert to table
AUS2026 = [NewYear(:,:), DOTY, AUS1982(:,:)]; %%% Combine into new CTYyyyyy table
```

```
%%% 1983 >> 2027 %%%
```

```
NewYear = AUS1983(:,1);      %%% Pull date and time data from raw data
NewYear = table2array(NewYear); %%% Change format to array
NewYear = string(NewYear);    %%% Change format to string
NewYear = erase(NewYear, "1983"); %%% Delete real year data pulled from
```

```

NewYear = string(NewYear);          %%% Turn to string
Y01 = nan(height(NewYear),1);      %%% Build empty array height of data for this year
Y01 = fillmissing(Y01, 'constant', 2027); %%% Fill empty array with "new" year
Y01 = string(Y01);                  %%% Convert to string
NewYear = strcat(Y01,NewYear);      %%% Concatenate into date/time data w/o year
NewYear = datetime(NewYear,'InputFormat','yyyy-MM-dd"T"HH:mm:ss');
NewYear = datetime(NewYear,'Format','yyyy-MM-dd"T"HH:mm:ss Z',
'TimeZone','America/Chicago'); %%% Convert to datetime
DOTY = day(NewYear,'dayofyear');     %%% Day of the year
DOTY = table(DOTY);
NewYear = table(NewYear);           %%% Convert to table
AUS2027 = [NewYear(:,,:), DOTY, AUS1983(:,,:)]; %%% Combine into new CTYyyyy table

%% 1984 >> 2028 %

```

```

NewYear = AUS1984(:,1);             %%% Pull date and time data from raw data
NewYear = table2array(NewYear);     %%% Change format to array
NewYear = string(NewYear);          %%% Change format to string
NewYear = erase(NewYear, "1984");   %%% Delete real year data pulled from
NewYear = string(NewYear);          %%% Turn to string
Y01 = nan(height(NewYear),1);      %%% Build empty array height of data for this year
Y01 = fillmissing(Y01, 'constant', 2028); %%% Fill empty array with "new" year
Y01 = string(Y01);                  %%% Convert to string
NewYear = strcat(Y01,NewYear);      %%% Concatenate into date/time data w/o year
NewYear = datetime(NewYear,'InputFormat','yyyy-MM-dd"T"HH:mm:ss');
NewYear = datetime(NewYear,'Format','yyyy-MM-dd"T"HH:mm:ss Z',
'TimeZone','America/Chicago'); %%% Convert to datetime
DOTY = day(NewYear,'dayofyear');     %%% Day of the year
DOTY = table(DOTY);
NewYear = table(NewYear);           %%% Convert to table
AUS2028 = [NewYear(:,,:), DOTY, AUS1984(:,,:)]; %%% Combine into new CTYyyyy table

%% 1985 >> 2029 %

```

```

NewYear = AUS1985(:,1);             %%% Pull date and time data from raw data
NewYear = table2array(NewYear);     %%% Change format to array
NewYear = string(NewYear);          %%% Change format to string
NewYear = erase(NewYear, "1985");   %%% Delete real year data pulled from
NewYear = string(NewYear);          %%% Turn to string
Y01 = nan(height(NewYear),1);      %%% Build empty array height of data for this year
Y01 = fillmissing(Y01, 'constant', 2029); %%% Fill empty array with "new" year
Y01 = string(Y01);                  %%% Convert to string
NewYear = strcat(Y01,NewYear);      %%% Concatenate into date/time data w/o year
NewYear = datetime(NewYear,'InputFormat','yyyy-MM-dd"T"HH:mm:ss');
NewYear = datetime(NewYear,'Format','yyyy-MM-dd"T"HH:mm:ss Z',
'TimeZone','America/Chicago'); %%% Convert to datetime

```

```

DOTY = day(NewYear,'dayofyear');          %%% Day of the year
DOTY = table(DOTY);
NewYear = table(NewYear);                %%% Convert to table
AUS2029 = [NewYear(:,), DOTY, AUS1985(:,)]; %%% Combine into new CTYyyyy table

```

```

%% 1986 >> 2030 %

```

```

NewYear = AUS1986(:,1);                  %%% Pull date and time data from raw data
NewYear = table2array(NewYear);          %%% Change format to array
NewYear = string(NewYear);               %%% Change format to string
NewYear = erase(NewYear, "1986");        %%% Delete real year data pulled from
NewYear = string(NewYear);               %%% Turn to string
Y01 = nan(height(NewYear),1);            %%% Build empty array height of data for this year
Y01 = fillmissing(Y01, 'constant', 2030); %%% Fill empty array with "new" year
Y01 = string(Y01);                       %%% Convert to string
NewYear = strcat(Y01,NewYear);            %%% Concatenate into date/time data w/o year
NewYear = datetime(NewYear,'InputFormat','yyyy-MM-dd"T"HH:mm:ss');
NewYear = datetime(NewYear,'Format','yyyy-MM-dd"T"HH:mm:ss Z',
'TimeZone','America/Chicago'); %%% Convert to datetime
DOTY = day(NewYear,'dayofyear');          %%% Day of the year
DOTY = table(DOTY);
NewYear = table(NewYear);                %%% Convert to table
AUS2030 = [NewYear(:,), DOTY, AUS1986(:,)]; %%% Combine into new CTYyyyy table

```

```

%% 1987 >> 2031 %

```

```

NewYear = AUS1987(:,1);                  %%% Pull date and time data from raw data
NewYear = table2array(NewYear);          %%% Change format to array
NewYear = string(NewYear);               %%% Change format to string
NewYear = erase(NewYear, "1987");        %%% Delete real year data pulled from
NewYear = string(NewYear);               %%% Turn to string
Y01 = nan(height(NewYear),1);            %%% Build empty array height of data for this year
Y01 = fillmissing(Y01, 'constant', 2031); %%% Fill empty array with "new" year
Y01 = string(Y01);                       %%% Convert to string
NewYear = strcat(Y01,NewYear);            %%% Concatenate into date/time data w/o year
NewYear = datetime(NewYear,'InputFormat','yyyy-MM-dd"T"HH:mm:ss');
NewYear = datetime(NewYear,'Format','yyyy-MM-dd"T"HH:mm:ss Z',
'TimeZone','America/Chicago'); %%% Convert to datetime
DOTY = day(NewYear,'dayofyear');          %%% Day of the year
DOTY = table(DOTY);
NewYear = table(NewYear);                %%% Convert to table
AUS2031 = [NewYear(:,), DOTY, AUS1987(:,)]; %%% Combine into new CTYyyyy table

```

```

%% 1988 >> 2032 %

```

```

NewYear = AUS1988(:,1);                  %%% Pull date and time data from raw data

```

```

NewYear = table2array(NewYear);    %%% Change format to array
NewYear = string(NewYear);        %%% Change format to string
NewYear = erase(NewYear, "1988");  %%% Delete real year data pulled from
NewYear = string(NewYear);        %%% Turn to string
Y01 = nan(height(NewYear),1);     %%% Build empty array height of data for this year
Y01 = fillmissing(Y01, 'constant', 2032); %%% Fill empty array with "new" year
Y01 = string(Y01);                %%% Convert to string
NewYear = strcat(Y01,NewYear);     %%% Concatenate into date/time data w/o year
NewYear = datetime(NewYear,'InputFormat','yyyy-MM-dd"T"HH:mm:ss');
NewYear = datetime(NewYear,'Format','yyyy-MM-dd"T"HH:mm:ss Z',
'TimeZone','America/Chicago'); %%% Convert to datetime
DOTY = day(NewYear,'dayofyear');    %%% Day of the year
DOTY = table(DOTY);
NewYear = table(NewYear);          %%% Convert to table
AUS2032 = [NewYear(:,.), DOTY, AUS1988(:,.)]; %%% Combine into new CTYyyyy table

```

%%% 1989 >> 2033 %%%

```

NewYear = AUS1989(:,1);           %%% Pull date and time data from raw data
NewYear = table2array(NewYear);   %%% Change format to array
NewYear = string(NewYear);        %%% Change format to string
NewYear = erase(NewYear, "1989");  %%% Delete real year data pulled from
NewYear = string(NewYear);        %%% Turn to string
Y01 = nan(height(NewYear),1);     %%% Build empty array height of data for this year
Y01 = fillmissing(Y01, 'constant', 2033); %%% Fill empty array with "new" year
Y01 = string(Y01);                %%% Convert to string
NewYear = strcat(Y01,NewYear);     %%% Concatenate into date/time data w/o year
NewYear = datetime(NewYear,'InputFormat','yyyy-MM-dd"T"HH:mm:ss');
NewYear = datetime(NewYear,'Format','yyyy-MM-dd"T"HH:mm:ss Z',
'TimeZone','America/Chicago'); %%% Convert to datetime
DOTY = day(NewYear,'dayofyear');    %%% Day of the year
DOTY = table(DOTY);
NewYear = table(NewYear);          %%% Convert to table
AUS2033 = [NewYear(:,.), DOTY, AUS1989(:,.)]; %%% Combine into new CTYyyyy table

```

%%% 1990 >> 2034 %%%

```

NewYear = AUS1990(:,1);           %%% Pull date and time data from raw data
NewYear = table2array(NewYear);   %%% Change format to array
NewYear = string(NewYear);        %%% Change format to string
NewYear = erase(NewYear, "1990");  %%% Delete real year data pulled from
NewYear = string(NewYear);        %%% Turn to string
Y01 = nan(height(NewYear),1);     %%% Build empty array height of data for this year
Y01 = fillmissing(Y01, 'constant', 2034); %%% Fill empty array with "new" year
Y01 = string(Y01);                %%% Convert to string
NewYear = strcat(Y01,NewYear);     %%% Concatenate into date/time data w/o year

```

```

NewYear = datetime(NewYear,'InputFormat','yyyy-MM-dd"T"HH:mm:ss');
NewYear = datetime(NewYear,'Format','yyyy-MM-dd"T"HH:mm:ss Z',
'TimeZone','America/Chicago'); %%% Convert to datetime
DOTY = day(NewYear,'dayofyear'); %%% Day of the year
DOTY = table(DOTY);
NewYear = table(NewYear); %%% Convert to table
AUS2034 = [NewYear(:,.), DOTY, AUS1990(:,.)]; %%% Combine into new CTYyyyy table

```

```

%% 1991 >> 2035 %

```

```

NewYear = AUS1991(:,1); %%% Pull date and time data from raw data
NewYear = table2array(NewYear); %%% Change format to array
NewYear = string(NewYear); %%% Change format to string
NewYear = erase(NewYear, "1991"); %%% Delete real year data pulled from
NewYear = string(NewYear); %%% Turn to string
Y01 = nan(height(NewYear),1); %%% Build empty array height of data for this year
Y01 = fillmissing(Y01, 'constant', 2035); %%% Fill empty array with "new" year
Y01 = string(Y01); %%% Convert to string
NewYear = strcat(Y01,NewYear); %%% Concatenate into date/time data w/o year
NewYear = datetime(NewYear,'InputFormat','yyyy-MM-dd"T"HH:mm:ss');
NewYear = datetime(NewYear,'Format','yyyy-MM-dd"T"HH:mm:ss Z',
'TimeZone','America/Chicago'); %%% Convert to datetime
DOTY = day(NewYear,'dayofyear'); %%% Day of the year
DOTY = table(DOTY);
NewYear = table(NewYear); %%% Convert to table
AUS2035 = [NewYear(:,.), DOTY, AUS1991(:,.)]; %%% Combine into new CTYyyyy table

```

```

%% 2000 >> 2036 %

```

```

NewYear = AUS2000(:,1); %%% Pull date and time data from raw data
NewYear = table2array(NewYear); %%% Change format to array
NewYear = string(NewYear); %%% Change format to string
NewYear = erase(NewYear, "2000"); %%% Delete real year data pulled from
NewYear = string(NewYear); %%% Turn to string
Y01 = nan(height(NewYear),1); %%% Build empty array height of data for this year
Y01 = fillmissing(Y01, 'constant', 2036); %%% Fill empty array with "new" year
Y01 = string(Y01); %%% Convert to string
NewYear = strcat(Y01,NewYear); %%% Concatenate into date/time data w/o year
NewYear = datetime(NewYear,'InputFormat','yyyy-MM-dd"T"HH:mm:ss');
NewYear = datetime(NewYear,'Format','yyyy-MM-dd"T"HH:mm:ss Z',
'TimeZone','America/Chicago'); %%% Convert to datetime
DOTY = day(NewYear,'dayofyear'); %%% Day of the year
DOTY = table(DOTY);
NewYear = table(NewYear); %%% Convert to table
AUS2036 = [NewYear(:,.), DOTY, AUS2000(:,.)]; %%% Combine into new CTYyyyy table

```

%%% 2001 >> 2037 %%%

```
NewYear = AUS2001(:,1);      %%% Pull date and time data from raw data
NewYear = table2array(NewYear); %%% Change format to array
NewYear = string(NewYear);   %%% Change format to string
NewYear = erase(NewYear, "2001"); %%% Delete real year data pulled from
NewYear = string(NewYear);   %%% Turn to string
Y01 = nan(height(NewYear),1); %%% Build empty array height of data for this year
Y01 = fillmissing(Y01, 'constant', 2037); %%% Fill empty array with "new" year
Y01 = string(Y01);          %%% Convert to string
NewYear = strcat(Y01,NewYear); %%% Concatenate into date/time data w/o year
NewYear = datetime(NewYear,'InputFormat','yyyy-MM-dd"T"HH:mm:ss');
NewYear = datetime(NewYear,'Format','yyyy-MM-dd"T"HH:mm:ss Z',
'TimeZone','America/Chicago'); %%% Convert to datetime
DOTY = day(NewYear,'dayofyear'); %%% Day of the year
DOTY = table(DOTY);
NewYear = table(NewYear); %%% Convert to table
AUS2037 = [NewYear(:,,:), DOTY, AUS2001(:,,:)]; %%% Combine into new CTYyyyy table
```

%%% 2002 >> 2038 %%%

```
NewYear = AUS2002(:,1);      %%% Pull date and time data from raw data
NewYear = table2array(NewYear); %%% Change format to array
NewYear = string(NewYear);   %%% Change format to string
NewYear = erase(NewYear, "2002"); %%% Delete real year data pulled from
NewYear = string(NewYear);   %%% Turn to string
Y01 = nan(height(NewYear),1); %%% Build empty array height of data for this year
Y01 = fillmissing(Y01, 'constant', 2038); %%% Fill empty array with "new" year
Y01 = string(Y01);          %%% Convert to string
NewYear = strcat(Y01,NewYear); %%% Concatenate into date/time data w/o year
NewYear = datetime(NewYear,'InputFormat','yyyy-MM-dd"T"HH:mm:ss');
NewYear = datetime(NewYear,'Format','yyyy-MM-dd"T"HH:mm:ss Z',
'TimeZone','America/Chicago'); %%% Convert to datetime
DOTY = day(NewYear,'dayofyear'); %%% Day of the year
DOTY = table(DOTY);
NewYear = table(NewYear); %%% Convert to table
AUS2038 = [NewYear(:,,:), DOTY, AUS2002(:,,:)]; %%% Combine into new CTYyyyy table
```

%%% 2003 >> 2039 %%%

```
NewYear = AUS2003(:,1);      %%% Pull date and time data from raw data
NewYear = table2array(NewYear); %%% Change format to array
NewYear = string(NewYear);   %%% Change format to string
NewYear = erase(NewYear, "2003"); %%% Delete real year data pulled from
NewYear = string(NewYear);   %%% Turn to string
Y01 = nan(height(NewYear),1); %%% Build empty array height of data for this year
```

```

Y01 = fillmissing(Y01, 'constant', 2039); %%% Fill empty array with "new" year
Y01 = string(Y01); %%% Convert to string
NewYear = strcat(Y01,NewYear); %%% Concatenate into date/time data w/o year
NewYear = datetime(NewYear,'InputFormat','yyyy-MM-dd"T"HH:mm:ss');
NewYear = datetime(NewYear,'Format','yyyy-MM-dd"T"HH:mm:ss Z',
'TimeZone','America/Chicago'); %%% Convert to datetime
DOTY = day(NewYear,'dayofyear'); %%% Day of the year
DOTY = table(DOTY);
NewYear = table(NewYear); %%% Convert to table
AUS2039 = [NewYear(:,:), DOTY, AUS2003(:,:)]; %%% Combine into new CTYyyyy table

```

%% 2004 >> 2040 %

```

NewYear = AUS2004(:,1); %%% Pull date and time data from raw data
NewYear = table2array(NewYear); %%% Change format to array
NewYear = string(NewYear); %%% Change format to string
NewYear = erase(NewYear, "2004"); %%% Delete real year data pulled from
NewYear = string(NewYear); %%% Turn to string
Y01 = nan(height(NewYear),1); %%% Build empty array height of data for this year
Y01 = fillmissing(Y01, 'constant', 2040); %%% Fill empty array with "new" year
Y01 = string(Y01); %%% Convert to string
NewYear = strcat(Y01,NewYear); %%% Concatenate into date/time data w/o year
NewYear = datetime(NewYear,'InputFormat','yyyy-MM-dd"T"HH:mm:ss');
NewYear = datetime(NewYear,'Format','yyyy-MM-dd"T"HH:mm:ss Z',
'TimeZone','America/Chicago'); %%% Convert to datetime
DOTY = day(NewYear,'dayofyear'); %%% Day of the year
DOTY = table(DOTY);
NewYear = table(NewYear); %%% Convert to table
AUS2040 = [NewYear(:,:), DOTY, AUS2004(:,:)]; %%% Combine into new CTYyyyy table

```

%% 2005 >> 2041 %

```

NewYear = AUS2005(:,1); %%% Pull date and time data from raw data
NewYear = table2array(NewYear); %%% Change format to array
NewYear = string(NewYear); %%% Change format to string
NewYear = erase(NewYear, "2005"); %%% Delete real year data pulled from
NewYear = string(NewYear); %%% Turn to string
Y01 = nan(height(NewYear),1); %%% Build empty array height of data for this year
Y01 = fillmissing(Y01, 'constant', 2041); %%% Fill empty array with "new" year
Y01 = string(Y01); %%% Convert to string
NewYear = strcat(Y01,NewYear); %%% Concatenate into date/time data w/o year
NewYear = datetime(NewYear,'InputFormat','yyyy-MM-dd"T"HH:mm:ss');
NewYear = datetime(NewYear,'Format','yyyy-MM-dd"T"HH:mm:ss Z',
'TimeZone','America/Chicago'); %%% Convert to datetime
DOTY = day(NewYear,'dayofyear'); %%% Day of the year
DOTY = table(DOTY);

```

```
NewYear = table(NewYear);          %%% Convert to table
AUS2041 = [NewYear(:,:), DOTY, AUS2005(:,:)]; %%% Combine into new CTYyyyyy table
```

```
%%% 2006 >> 2042 %%%
```

```
NewYear = AUS2006(:,1);          %%% Pull date and time data from raw data
NewYear = table2array(NewYear);  %%% Change format to array
NewYear = string(NewYear);       %%% Change format to string
NewYear = erase(NewYear, "2006"); %%% Delete real year data pulled from
NewYear = string(NewYear);       %%% Turn to string
Y01 = nan(height(NewYear),1);    %%% Build empty array height of data for this year
Y01 = fillmissing(Y01, 'constant', 2042); %%% Fill empty array with "new" year
Y01 = string(Y01);               %%% Convert to string
NewYear = strcat(Y01,NewYear);    %%% Concatenate into date/time data w/o year
NewYear = datetime(NewYear,'InputFormat','yyyy-MM-dd"T"HH:mm:ss');
NewYear = datetime(NewYear,'Format','yyyy-MM-dd"T"HH:mm:ss Z',
'TimeZone','America/Chicago'); %%% Convert to datetime
DOTY = day(NewYear,'dayofyear');  %%% Day of the year
DOTY = table(DOTY);
NewYear = table(NewYear);        %%% Convert to table
AUS2042 = [NewYear(:,:), DOTY, AUS2006(:,:)]; %%% Combine into new CTYyyyyy table
```

```
%%% 2007 >> 2043 %%%
```

```
NewYear = AUS2007(:,1);          %%% Pull date and time data from raw data
NewYear = table2array(NewYear);  %%% Change format to array
NewYear = string(NewYear);       %%% Change format to string
NewYear = erase(NewYear, "2007"); %%% Delete real year data pulled from
NewYear = string(NewYear);       %%% Turn to string
Y01 = nan(height(NewYear),1);    %%% Build empty array height of data for this year
Y01 = fillmissing(Y01, 'constant', 2043); %%% Fill empty array with "new" year
Y01 = string(Y01);               %%% Convert to string
NewYear = strcat(Y01,NewYear);    %%% Concatenate into date/time data w/o year
NewYear = datetime(NewYear,'InputFormat','yyyy-MM-dd"T"HH:mm:ss');
NewYear = datetime(NewYear,'Format','yyyy-MM-dd"T"HH:mm:ss Z',
'TimeZone','America/Chicago'); %%% Convert to datetime
DOTY = day(NewYear,'dayofyear');  %%% Day of the year
DOTY = table(DOTY);
NewYear = table(NewYear);        %%% Convert to table
AUS2043 = [NewYear(:,:), DOTY, AUS2007(:,:)]; %%% Combine into new CTYyyyyy table
```

```
%%% 2008 >> 2044 %%%
```

```
NewYear = AUS2008(:,1);          %%% Pull date and time data from raw data
NewYear = table2array(NewYear);  %%% Change format to array
NewYear = string(NewYear);       %%% Change format to string
```



```

NewYear = erase(NewYear, "2008");    %%% Delete real year data pulled from
NewYear = string(NewYear);          %%% Turn to string
Y01 = nan(height(NewYear),1);       %%% Build empty array height of data for this year
Y01 = fillmissing(Y01, 'constant', 2044); %%% Fill empty array with "new" year
Y01 = string(Y01);                  %%% Convert to string
NewYear = strcat(Y01,NewYear);       %%% Concatenate into date/time data w/o year
NewYear = datetime(NewYear,'InputFormat','yyyy-MM-dd"T"HH:mm:ss');
NewYear = datetime(NewYear,'Format','yyyy-MM-dd"T"HH:mm:ss Z',
'TimeZone','America/Chicago'); %%% Convert to datetime
DOTY = day(NewYear,'dayofyear');      %%% Day of the year
DOTY = table(DOTY);
NewYear = table(NewYear);             %%% Convert to table
AUS2044 = [NewYear(:,,:), DOTY, AUS2008(:,,:)]; %%% Combine into new CTYyyyy table

%% 2009 >> 2045 %

```

```

NewYear = AUS2009(:,1);              %%% Pull date and time data from raw data
NewYear = table2array(NewYear);      %%% Change format to array
NewYear = string(NewYear);           %%% Change format to string
NewYear = erase(NewYear, "2009");    %%% Delete real year data pulled from
NewYear = string(NewYear);           %%% Turn to string
Y01 = nan(height(NewYear),1);        %%% Build empty array height of data for this year
Y01 = fillmissing(Y01, 'constant', 2045); %%% Fill empty array with "new" year
Y01 = string(Y01);                   %%% Convert to string
NewYear = strcat(Y01,NewYear);       %%% Concatenate into date/time data w/o year
NewYear = datetime(NewYear,'InputFormat','yyyy-MM-dd"T"HH:mm:ss');
NewYear = datetime(NewYear,'Format','yyyy-MM-dd"T"HH:mm:ss Z',
'TimeZone','America/Chicago'); %%% Convert to datetime
DOTY = day(NewYear,'dayofyear');      %%% Day of the year
DOTY = table(DOTY);
NewYear = table(NewYear);             %%% Convert to table
AUS2045 = [NewYear(:,,:), DOTY, AUS2009(:,,:)]; %%% Combine into new CTYyyyy table

```

```

%% 2010 >> 2046 %

```

```

NewYear = AUS2010(:,1);              %%% Pull date and time data from raw data
NewYear = table2array(NewYear);      %%% Change format to array
NewYear = string(NewYear);           %%% Change format to string
NewYear = erase(NewYear, "2010");    %%% Delete real year data pulled from
NewYear = string(NewYear);           %%% Turn to string
Y01 = nan(height(NewYear),1);        %%% Build empty array height of data for this year
Y01 = fillmissing(Y01, 'constant', 2046); %%% Fill empty array with "new" year
Y01 = string(Y01);                   %%% Convert to string
NewYear = strcat(Y01,NewYear);       %%% Concatenate into date/time data w/o year
NewYear = datetime(NewYear,'InputFormat','yyyy-MM-dd"T"HH:mm:ss');

```

```

NewYear = datetime(NewYear,'Format','yyyy-MM-dd"T"HH:mm:ss Z',
'TimeZone','America/Chicago'); %%% Convert to datetime
DOTY = day(NewYear,'dayofyear'); %%% Day of the year
DOTY = table(DOTY);
NewYear = table(NewYear); %%% Convert to table
AUS2046 = [NewYear(:,:), DOTY, AUS2010(:,:)]; %%% Combine into new CTYyyyy table

```

```

%% 2011 >> 2047 %

```

```

NewYear = AUS2011(:,1); %%% Pull date and time data from raw data
NewYear = table2array(NewYear); %%% Change format to array
NewYear = string(NewYear); %%% Change format to string
NewYear = erase(NewYear, "2011"); %%% Delete real year data pulled from
NewYear = string(NewYear); %%% Turn to string
Y01 = nan(height(NewYear),1); %%% Build empty array height of data for this year
Y01 = fillmissing(Y01, 'constant', 2047); %%% Fill empty array with "new" year
Y01 = string(Y01); %%% Convert to string
NewYear = strcat(Y01,NewYear); %%% Concatenate into date/time data w/o year
NewYear = datetime(NewYear,'InputFormat','yyyy-MM-dd"T"HH:mm:ss');
NewYear = datetime(NewYear,'Format','yyyy-MM-dd"T"HH:mm:ss Z',
'TimeZone','America/Chicago'); %%% Convert to datetime
DOTY = day(NewYear,'dayofyear'); %%% Day of the year
DOTY = table(DOTY);
NewYear = table(NewYear); %%% Convert to table
AUS2047 = [NewYear(:,:), DOTY, AUS2011(:,:)]; %%% Combine into new CTYyyyy table

```

```

%% 2012 >> 2048 %

```

```

NewYear = AUS2012(:,1); %%% Pull date and time data from raw data
NewYear = table2array(NewYear); %%% Change format to array
NewYear = string(NewYear); %%% Change format to string
NewYear = erase(NewYear, "2012"); %%% Delete real year data pulled from
NewYear = string(NewYear); %%% Turn to string
Y01 = nan(height(NewYear),1); %%% Build empty array height of data for this year
Y01 = fillmissing(Y01, 'constant', 2048); %%% Fill empty array with "new" year
Y01 = string(Y01); %%% Convert to string
NewYear = strcat(Y01,NewYear); %%% Concatenate into date/time data w/o year
NewYear = datetime(NewYear,'InputFormat','yyyy-MM-dd"T"HH:mm:ss');
NewYear = datetime(NewYear,'Format','yyyy-MM-dd"T"HH:mm:ss Z',
'TimeZone','America/Chicago'); %%% Convert to datetime
DOTY = day(NewYear,'dayofyear'); %%% Day of the year
DOTY = table(DOTY);
NewYear = table(NewYear); %%% Convert to table
AUS2048 = [NewYear(:,:), DOTY, AUS2012(:,:)]; %%% Combine into new CTYyyyy table

```

```

%% 2013 >> 2049 %

```

```

NewYear = AUS2013(:,1);          %%% Pull date and time data from raw data
NewYear = table2array(NewYear);  %%% Change format to array
NewYear = string(NewYear);       %%% Change format to string
NewYear = erase(NewYear, "2013"); %%% Delete real year data pulled from
NewYear = string(NewYear);       %%% Turn to string
Y01 = nan(height(NewYear),1);    %%% Build empty array height of data for this year
Y01 = fillmissing(Y01, 'constant', 2049); %%% Fill empty array with "new" year
Y01 = string(Y01);               %%% Convert to string
NewYear = strcat(Y01,NewYear);   %%% Concatenate into date/time data w/o year
NewYear = datetime(NewYear,'InputFormat','yyyy-MM-dd"T"HH:mm:ss');
NewYear = datetime(NewYear,'Format','yyyy-MM-dd"T"HH:mm:ss Z',
'TimeZone','America/Chicago'); %%% Convert to datetime
DOTY = day(NewYear,'dayofyear');  %%% Day of the year
DOTY = table(DOTY);
NewYear = table(NewYear);        %%% Convert to table
AUS2049 = [NewYear(:,:), DOTY, AUS2013(:,:)]; %%% Combine into new CTYyyyy table

```

```

%% 2014 >> 2050 %

```

```

NewYear = AUS2014(:,1);          %%% Pull date and time data from raw data
NewYear = table2array(NewYear);  %%% Change format to array
NewYear = string(NewYear);       %%% Change format to string
NewYear = erase(NewYear, "2014"); %%% Delete real year data pulled from
NewYear = string(NewYear);       %%% Turn to string
Y01 = nan(height(NewYear),1);    %%% Build empty array height of data for this year
Y01 = fillmissing(Y01, 'constant', 2050); %%% Fill empty array with "new" year
Y01 = string(Y01);               %%% Convert to string
NewYear = strcat(Y01,NewYear);   %%% Concatenate into date/time data w/o year
NewYear = datetime(NewYear,'InputFormat','yyyy-MM-dd"T"HH:mm:ss');
NewYear = datetime(NewYear,'Format','yyyy-MM-dd"T"HH:mm:ss Z',
'TimeZone','America/Chicago'); %%% Convert to datetime
DOTY = day(NewYear,'dayofyear');  %%% Day of the year
DOTY = table(DOTY);
NewYear = table(NewYear);        %%% Convert to table
AUS2050 = [NewYear(:,:), DOTY, AUS2014(:,:)]; %%% Combine into new CTYyyyy table

```

```

%% Assemble into AusSet01 %

```

```

AusSet01 = [AUS2020; AUS2021; AUS2022; AUS2023; AUS2024; AUS2025; AUS2026;
AUS2027; AUS2028; AUS2029; AUS2030; AUS2031; AUS2032; AUS2033; AUS2034;
AUS2035; AUS2036; AUS2037; AUS2038; AUS2039; AUS2040; AUS2041; AUS2042;
AUS2043; AUS2044; AUS2045; AUS2046; AUS2047; AUS2048; AUS2049; AUS2050];

```

Preprocess Latitude and Longitude:

```
%%
%%%%%%%%%%%%%%%%%%%%%%%%%%%%%%%%%%%%%%%%%%%%%%%%%%%%%%%%%%%%%%%%%%%%%%%%
%%
%%
%%% Location (Latitude & Longitude) Data Preprocessing
%%%%%%%%%%%%%%%%%%%%%%%%%%%%%%%%%%%%%%%%%%%%%%%%%%%%%%%%%%%%%%%%%%%%%%%%
%%
%%

Lat01 = AusSet01(:, 'LATITUDE');    %%% Pull latitude data from raw data
Lat01 = table2array(Lat01);         %%% Change to array format
Long01 = AusSet01(:, 'LONGITUDE');  %%% Pull longitude data from raw data
Long01 = table2array(Long01);       %%% Change to array format
Elevation01 = AusSet01(:, 'ELEVATION'); %%% Pull elevation data from raw data
Elevation01 = table2array(Elevation01); %%% Change to array format
```

Preprocess Wind:

```
%%%%%%%%%%%%%%%%%%%%%%%%%%%%%%%%%%%%%%%%%%%%%%%%%%%%%%%%%%%%%%%%%%%%%%%%
%%
%%
%%% Wind Data Preprocessing
%%%%%%%%%%%%%%%%%%%%%%%%%%%%%%%%%%%%%%%%%%%%%%%%%%%%%%%%%%%%%%%%%%%%%%%%
%%
%%

Wind01 = AusSet01(:, 'WND');          %%% Pull wind data from the raw sample data
Wind01 = table2array(Wind01);         %%% Change from table to array
Wind01 = string(Wind01);              %%% Change to string format
Wind01 = split(Wind01, ',');          %%% Split the raw wind data using the delimiter ","
Wind01 = double(Wind01);              %%% Change to numerical format
Wind01(Wind01 == 999) = NaN;           %%% Replace nonsense values with blank cells
Wind01(Wind01 == 9999) = NaN;         %%% Replace nonsense values with blank cells
Wind01 = array2table(Wind01);         %%% Change to table format
WindDir01 = Wind01(:, 1);             %%% Create wind direction table
WindDir01 = table2array(WindDir01);   %%% Turn wind direction table into array
WindSpeed01 = Wind01(:, 4);           %%% Create wind speed table
WindSpeed01 = table2array(WindSpeed01); %%% Turn wind speed table into array
WindSpeed01 = WindSpeed01./10;        %%% Scale wind speed
```

Preprocess Ambient Temperature:

%%
%%
%%

%%% Temperature Data Preprocessing

%%
%%
%%

Temp01 = AusSet01(:, 'TMP');	%%% Pull temperature data from raw data
Temp01 = table2array(Temp01);	%%% Change to array format
Temp01 = string(Temp01);	%%% Change to string format
Temp01 = split(Temp01, ',');	%%% Separate based on "," delimiter
Temp01 = double(Temp01);	%%% Change to numerical format
Temp01(Temp01 == 9999) = NaN;	%%% Replace nonsense data with blank cells
Temp01 = array2table(Temp01);	%%% Change to table
T_Amb01 = Temp01(:, 1);	%%% Pull air temperature from raw data
T_Amb01 = table2array(T_Amb01);	%%% Change to array
T_Amb01 = T_Amb01./10;	%%% Change to correct units

Incident Solar Radiation:

%%
%%
%%
%%

%%% Incoming Solar Radiation

%%
%%
%%

G_Sun = 1.353; % kW/(m^2) Max amount of sunlight hitting the Earth's atmosphere

LT01 = AusSet01(:, 'NewYear');
LT01 = table2array(LT01);
LT01 = string(LT01);
LT01 = eraseBetween(LT01, 1, 20);
LT01 = string(LT01);
LT01 = str2double(LT01); % String containing JUST the local time HH:mm:ss, no other info
LSTM01 = LT01/100; % this is the UTC to local time difference
LSTM01 = 15*LSTM01;

DOTY01 = AusSet01(:, 'DOTY');
DOTY01 = table2array(DOTY01);

```

BB01 = (360/365)*(DOTY01-81); % in degrees
BBrad01 = BB01*pi/180; % in radians
EoT01 = 9.87*sin(2*BBrad01)-7.53*cos(BBrad01)-1.5*sin(BBrad01); % minutes (or radians)
TC01 = 4*(Long01-LSTM01)+EoT01; % time correction in minutes
LT01 = AusSet01(:, 'New Year');
LT01 = table2array(LT01);
LT01 = datetime(LT01, 'Format', 'yyyy-MM-dd"T"HH:mm:ss Z', 'TimeZone', 'America/Chicago' );
LST01 = LT01 + minutes(TC01);
LSThr01 = hour(LST01);
LSTmin01 = minute(LST01);
LSTdecm01 = LSTmin01/60;
LSTsec01 = second(LST01);
LSTdecs01 = LSTsec01/60/60;
LSThr01 = LSThr01 + LSTdecm01 + LSTdecs01;

HRAam01 = 15*(LSThr01);
HRApm01 = 15*(LSThr01-24);
HRA01 = zeros(numel(LSThr01),1);
for i = 1:numel(LSThr01) % Creating the morning and evening blended HRA array
    if LSThr01(i) < 12
        HRA01(i) = 15*LSThr01(i);
    else
        HRA01(i) = 15*(LSThr01(i)-24);
    end
end

DecMath01 = DOTY01 - 81;
DecMath01 = (360/365)*(DecMath01); % in degrees not radians
DecMath01 = DecMath01*pi/180; % in radians
Dec01 = 23.45*sin(DecMath01); % in degrees

SDec01 = sin(Dec01*pi/180);
SLat01 = sin(Lat01*pi/180);
CDec01 = cos(Dec01*pi/180);
CLat01 = cos(Lat01*pi/180);
CHRA01 = cos(HRA01*pi/180);
SC01 = SDec01.*CLat01;
CS01 = CDec01.*SLat01;
CSC01 = CS01.*CHRA01;
IntermA01 = SDec01.*SLat01;
IntermB01 = CDec01.*CLat01;
IntermB01 = IntermB01.*CHRA01;
IntermAB01 = IntermA01+IntermB01;
Elev01 = -asin(IntermAB01); % in radians
ElevDeg01 = (180/pi)*Elev01; % in degrees
CElev01 = cos(Elev01);

```

```

IntermAz1_01 = SC01 - CSC01;
IntermAz2_01 = zeros(numel(IntermAz1_01),1);
for i = 1:(numel(IntermAz1_01)-1)
    IntermAz2_01(i) = IntermAz1_01(i)/CElev01(i); % no units so radians
end

Azim01 = acos(IntermAz2_01);
AzimDeg01 = Azim01*180/pi;
AzimMax01 = 90 - Lat01 - Dec01;
Zenith01 = 90 - ElevDeg01; % Zenith Angle in degrees

Elev0Dark01 = zeros(numel(Elev01),1);
for i = 1:(numel(Elev01)-1)
    if Elev01(i) < 0
        Elev0Dark01(i) = NaN;
    else
        Elev0Dark01(i) = Elev01(i);
    end
end

RoofAngl = 0;
EWallAngl = pi/2;

GRoofSun01 = sin(Elev0Dark01);
GRoofSun01 = G_Sun*GRoofSun01; % this is the amount to subtract PV efficiency from!
GRoofSun01max = max(GRoofSun01);
GRoofSun01min = min(GRoofSun01);
GRoofSun01 = fillmissing(GRoofSun01,'constant', 0);

GEwallSun01 = cos(Elev0Dark01); % Base East wall solar irradiation; Needs to be split at the
90 degrees pt and turned to the WEST wall
GEwallSun01 = G_Sun*GEwallSun01; % this is how much would just generally be source
energy in
% Base East wall solar irradiation; Needs to be split at the 90 degrees pt and turned to the WEST
wall
GEwallSun01max = max(GEwallSun01);
GEwallSun01min = min(GEwallSun01);
GEwallSun01 = fillmissing(GEwallSun01,'constant', 0);

```

Cloud Cover Effects:

```

%% %%
%%%%%%%%%%
%%%%%%%%%%
%%

```

```

%%% Cloud Cover
%%%%%%%%%%%%%%%%%%%%%%%%%%%%%%%%%%%%%%%%%%%%%%%%%%%%%%%%%%%%%%%%%%%%%%%%
%%%%%%%%%%%%%%%%%%%%%%%%%%%%%%%%%%%%%%%%%%%%%%%%%%%%%%%%%%%%%%%%%%%%%%%%
%
```

```

CC01 = AusSet01(:, 'CIG');
CC01 = table2array(CC01);
CC01 = string(CC01);
CC01 = eraseBetween(CC01, 6, 11);
CC01 = str2double(CC01);
```

```

GccRoof01 = zeros(numel(GRoofSun01), 1);
GccEwall01 = zeros(numel(GEwallSun01), 1);
nrand = zeros(numel(GRoofSun01), 1);
N_cc01 = zeros(numel(GRoofSun01), 1);
for i=1:(numel(GRoofSun01)-1)
    if CC01(i) == 22000 % this means no clouds, so all incoming radiation reaches panel
        GccRoof01(i) = GRoofSun01(i);
        GccEwall01(i) = GEwallSun01(i);
    else
        nrand = rand;
        N_cc01 = 0.6 + 0.4*nrand;
        GccRoof01(i) = (1 - (N_cc01)).*GRoofSun01(i);
        GccEwall01(i) = (1 - (N_cc01)).*GEwallSun01(i);
    end
end
```

Calculate Relative Humidity:

```

%%
%%%%%%%%%%%%%%%%%%%%%%%%%%%%%%%%%%%%%%%%%%%%%%%%%%%%%%%%%%%%%%%%%%%%%%%%
%%%%%%%%%%%%%%%%%%%%%%%%%%%%%%%%%%%%%%%%%%%%%%%%%%%%%%%%%%%%%%%%%%%%%%%%
%
```

%%% Calculating the Relative Humidity from Available Data

```

%%%%%%%%%%%%%%%%%%%%%%%%%%%%%%%%%%%%%%%%%%%%%%%%%%%%%%%%%%%%%%%%%%%%%%%%
%%%%%%%%%%%%%%%%%%%%%%%%%%%%%%%%%%%%%%%%%%%%%%%%%%%%%%%%%%%%%%%%%%%%%%%%
%
```

```

Dew01 = AusSet01(:, 'DEW');
Dew01 = table2array(Dew01);
Dew01 = string(Dew01);
Dew01 = eraseBetween(Dew01, 6, 7);
Dew01 = str2double(Dew01);
```

```

Dew01 = Dew01/10; % Dewpoint Temperature in Celsius
```



```

RHtop01 = (17.625*Dew01)./(243.04+Dew01);
RHtop01 = exp(RHtop01);
RHbot01 = (17.625*T_Amb01)./(243.04+T_Amb01);
RHbot01 = exp(RHbot01);
RHdec01 = RHtop01/RHbot01; % RH in decimal %
RH01 = 100*RHdec01; % Relative Humidity in %

```

Increasing Ambient Temperatures:

```

%%
%%%%%%%%%%%%%%%%%%%%%%%%%%%%%%%%%%%%%%%%%%%%%%%%%%%%%%%%%%%%%%%%%%%%%%%%
%%%%%%%%%%%%%%%%%%%%%%%%%%%%%%%%%%%%%%%%%%%%%%%%%%%%%%%%%%%%%%%%%%%%%%%%
%%
%%% Ramping Ambient/Environmental Temperature
%%%%%%%%%%%%%%%%%%%%%%%%%%%%%%%%%%%%%%%%%%%%%%%%%%%%%%%%%%%%%%%%%%%%%%%%
%%%%%%%%%%%%%%%%%%%%%%%%%%%%%%%%%%%%%%%%%%%%%%%%%%%%%%%%%%%%%%%%%%%%%%%%
%%

```

```

TempRampRate01 = 3.04206E-8; %% 0.016 C/yr --> C/min
TempRampRate02 = 3.66948E-8; %% 0.0193 C/yr --> C/min
TempRampRate03 = 6.2172E-8; %% 0.0327 C/yr --> C/min
TempRampRate04 = 3.84463E-8; %% 0.036 C/yr --> C/min

```

```

DT01 = AusSet01(:,1);          %%% Pull date and time data from raw data
DT01 = table2array(DT01);      %%% Change format to array

```

```

%%% Assemble date and time arrays into the datetime format
%%% recognized by Matlab

```

```

DTDiff01 = diff(DT01);
DTDiff01 = [0; DTDiff01];
DTDiff01 = time2num(DTDiff01,'minutes');
DT01 = datetime(DT01,'InputFormat','yyyy-MM-dd"T"HH:mm:ss');

```

```

RampTemp01 = nan(height(DT01),1);
RampTemp02 = nan(height(DT01),1);
RampTemp03 = nan(height(DT01),1);
RampTemp04 = nan(height(DT01),1);
TempTbl01 = nan(height(DT01),1);
Time01 = nan(height(DT01),1);
t01 = 0;

```

```

for i = 1:(height(DT01)-1)
    Time01(i) = t01 + DTDiff01(i);
    RampTemp01(i) = T_Amb01(i) + Time01(i).*TempRampRate01;
    RampTemp02(i) = T_Amb01(i) + Time01(i).*TempRampRate02;

```

```

RampTemp03(i) = T_Amb01(i) + Time01(i).*TempRampRate03;
RampTemp04(i) = T_Amb01(i) + Time01(i).*TempRampRate04;
t01 = t01 + DTDiff01(i);
end

```

```

Time01(height(DT01))=Time01(height(DT01)-1) + DTDiff01(height(DT01)-1);

```

Panel Degradation Over Time:

```

%%
%%%%%%%%%%%%%%%%%%%%%%%%%%%%%%%%%%%%%%%%%%%%%%%%%%%%%%%%%%%%%%%%%%%%%%%%
%%
%% Panel Degradation Over Time
%%%%%%%%%%%%%%%%%%%%%%%%%%%%%%%%%%%%%%%%%%%%%%%%%%%%%%%%%%%%%%%%%%%%%%%%
%%
%%

```

```

HrDec01 = hour(LT01);
MinDec01 = minute(LT01);
MinDec01 = MinDec01/60;
SecDec01 = second(LT01);
SecDec01 = SecDec01/60/60;
HrDec01 = HrDec01 + MinDec01 + SecDec01;

```

```

DOTY01 = AusSet01(:,2);
DOTY01 = table2array(DOTY01);
DayCt01 = DOTY01-1;

```

```

YearDec01 = year(LT01);

```

```

YrCt01 = YearDec01 - 2020;
YrDegRt01 = -0.0095; % Degradation of 0.95% per year
DayDegRt01 = YrDegRt01/365.25;
HourDegRt01 = DayDegRt01/24;

```

```

LumosInitEff01 = nan(height(T_Amb01),1);
LumosInitEff01 = fillmissing(LumosInitEff01, 'constant', 0.1762); % Lumos LSX305 efficiency
is 17.62%

```

```

MS425InitEff01 = nan(height(T_Amb01),1);
MS425InitEff01 = fillmissing(MS425InitEff01, 'constant', 0.1930); % Mission Solar
MS#425SX6W efficiency is 19.30%

```

```

MS330InitEff01 = nan(height(T_Amb01),1);
MS330InitEff01 = fillmissing(MS330InitEff01, 'constant', 0.1953); % Mission Solar
MSE330SR8K efficiency is 19.53%

MS390InitEff01 = nan(height(T_Amb01),1);
MS390InitEff01 = fillmissing(MS390InitEff01, 'constant', 0.1935); % Mission Solar
MSE390SR9S efficiency is 19.35%

SolarTechInitEff01 = nan(height(T_Amb01),1);
SolarTechInitEff01 = fillmissing(SolarTechInitEff01, 'constant', 0.1930); % Solar Tech
PERC315 efficiency is 19.30%

LumosBaseEff01 = zeros(numel(LT01),1);
for i = 1:(numel(LT01))
    LumosBaseEff01(i) = (1+(YrDegRt01*YrCt01(i) + DayDegRt01*DayCt01(i) +
    HourDegRt01*HrDec01(i)))*LumosInitEff01(i);
end

MS425BaseEff01 = zeros(numel(LT01),1);
for i = 1:(numel(LT01))
    MS425BaseEff01(i) = (1+(YrDegRt01*YrCt01(i) + DayDegRt01*DayCt01(i) +
    HourDegRt01*HrDec01(i)))*MS425InitEff01(i);
end

MS330BaseEff01 = zeros(numel(LT01),1);
for i = 1:(numel(LT01))
    MS330BaseEff01(i) = (1+(YrDegRt01*YrCt01(i) + DayDegRt01*DayCt01(i) +
    HourDegRt01*HrDec01(i)))*MS330InitEff01(i);
end

MS390BaseEff01 = zeros(numel(LT01),1);
for i = 1:(numel(LT01))
    MS390BaseEff01(i) = (1+(YrDegRt01*YrCt01(i) + DayDegRt01*DayCt01(i) +
    HourDegRt01*HrDec01(i)))*MS390InitEff01(i);
end

SolarTechBaseEff01 = zeros(numel(LT01),1);
for i = 1:(numel(LT01))
    SolarTechBaseEff01(i) = (1+(YrDegRt01*YrCt01(i) + DayDegRt01*DayCt01(i) +
    HourDegRt01*HrDec01(i)))*SolarTechInitEff01(i);
end

```

Panel Degradation due to Temperature:

```
%%  
%%%%%%%%%%%%%%%%%%%%%%%%%%%%%%%%%%%%%%%%%%%%%%%%%%%%%%%%%%%%%%%%%%%%%%%%  
%%%%%%%%%%%%%%%%%%%%%%%%%%%%%%%%%%%%%%%%%%%%%%%%%%%%%%%%%%%%%%%%%%%%%%%%  
%%  
%% PV Panel Efficiency Decrease >> Due to Ambient Temp <<  
%%%%%%%%%%%%%%%%%%%%%%%%%%%%%%%%%%%%%%%%%%%%%%%%%%%%%%%%%%%%%%%%%%%%%%%%  
%%%%%%%%%%%%%%%%%%%%%%%%%%%%%%%%%%%%%%%%%%%%%%%%%%%%%%%%%%%%%%%%%%%%%%%%  
%%
```

EffDecTemp = -0.0008; % 0.08% = 0.0008 decimal percent LOSS of efficiency per degree C over 25C

```
LumosEffT01 = zeros(numel(T_Amb01),1);  
MS425EffT01 = zeros(numel(T_Amb01),1);  
MS330EffT01 = zeros(numel(T_Amb01),1);  
MS390EffT01 = zeros(numel(T_Amb01),1);  
SolarTechEffT01 = zeros(numel(T_Amb01),1);  
dTemp01 = zeros(numel(T_Amb01),1);  
for i=1:(numel(T_Amb01)-1)  
    if T_Amb01(i) < 25  
        LumosEffT01(i) = LumosBaseEff01(i);  
        MS425EffT01(i) = MS425BaseEff01(i);  
        MS330EffT01(i) = MS330BaseEff01(i);  
        MS390EffT01(i) = MS330BaseEff01(i);  
        SolarTechEffT01(i) = SolarTechBaseEff01(i);  
    else  
        dTemp01(i) = T_Amb01(i) - 25;  
        LumosEffT01(i) = LumosBaseEff01(i) + EffDecTemp*dTemp01(i);  
        MS425EffT01(i) = MS425BaseEff01(i) + EffDecTemp*dTemp01(i);  
        MS330EffT01(i) = MS330BaseEff01(i) + EffDecTemp*dTemp01(i);  
        MS390EffT01(i) = MS390BaseEff01(i) + EffDecTemp*dTemp01(i);  
        SolarTechEffT01(i) = SolarTechBaseEff01(i) + EffDecTemp*dTemp01(i);  
    end  
end
```

```
BestEff_Lumos = max(LumosEffT01);  
WorstEff_Lumos = min(LumosEffT01);
```

```
BestEff_MS425 = max(MS425EffT01);  
WorstEff_MS425 = min(MS425EffT01);
```

```
BestEff_MS330 = max(MS330EffT01);  
WorstEff_MS330 = min(MS330EffT01);
```

BestEff_MS390 = max(MS390EffT01);
WorstEff_MS390 = min(MS390EffT01);

BestEff_SolTch = max(SolarTechEffT01);
WorstEff_SolTch = min(SolarTechEffT01);

Panel Degradation due to Temperature:

%%% Pulling the extremes and medians from the hitorical data sets:

%%% Real-World Wind Speed

WS_Max_01 = max(WindSpeed01);
WS_50per_01 = WS_Max_01/2;
WS_75per_01 = (WS_Max_01 + WS_50per_01)/2;
WS_25per_01 = WS_50per_01/2;

%%% Non-Real-World Wind Speed:

WS_01 = 10;
WS_02 = 20;
WS_03 = 30;
WS_04 = 40;
WS_05 = 50;

%%%

WS00 = WS_05;

%%% Real-World Cloud Cover

CC_Max_01 = max(CC01);
CC_50per_01 = CC_Max_01/2;
CC_75per_01 = (CC_Max_01 + CC_50per_01)/2;
CC_25per_01 = CC_50per_01/2;

%%% Non-Real-World Cloud Cover:

CC_01 = 0.5;
CC_02 = 0.6;
CC_03 = 0.7;
CC_04 = 0.8;
CC_05 = 0.9;

%%%%%%%%

CC_00 = CC_01;

%%% Real-World Incident Solar Radiation - Extremes

GWall_Max_01 = max(GEwallSun01); % only when GRoof = 0

GWall_50per_01 = GWall_Max_01/2; % 45 degree angle, so 50/50 to wall and roof

GWall_75per_01 = (GWall_Max_01 + GWall_50per_01)/2; % goes with roof 25; Sun at 30 degree point

GWall_25per_01 = (GWall_50per_01)/2; % goes with roof 75

```

GINC_Roof_Max_01 = max(GRoofSun01); % only when GWall = 0
GINC_Roof_50per_01 = GINC_Roof_Max_01/2; % 45 degree angle, so 50/50 to wall and roof
GINC_Roof_75per_01 = (GINC_Roof_Max_01 + GINC_Roof_50per_01)/2; % goes with wall
25
GINC_Roof_25per_01 = (GINC_Roof_50per_01)/2; % goes with wall 75

```

```

%%% taking out CC:

```

```

Ginc_Wall_Max_01 = CC_00*GWall_Max_01; % Goes with roof = 0
Ginc_Wall_50per_01 = CC_00*GWall_50per_01; % Goes with roof = 50per
Ginc_Wall_75per_01 = CC_00*GWall_75per_01; % Goes with roof = 25per
Ginc_Wall_25per_01 = CC_00*GWall_25per_01; % Goes with roof = 75per

```

```

Ginc_Roof_Max_01 = CC_00*GINC_Roof_Max_01; % Goes with wall = 0
Ginc_Roof_50per_01 = CC_00*GINC_Roof_50per_01; % Goes with wall = 50per
Ginc_Roof_75per_01 = CC_00*GINC_Roof_75per_01; % Goes with wall = 25per
Ginc_Roof_25per_01 = CC_00*GINC_Roof_25per_01; %

```

```

%%% Ginc Wall and Roof to use in equations

```

```

Ginc_ROOF = 0;
Ginc_WALL = Ginc_Wall_Max_01;

```

```

%%%%%%%% Adjusting Panel Efficiency with RH
%%%%%%%% Real-World Calculated Relative Humidities

```

```

RH_Max_01 = max(RH01);
RH_50per_01 = RH_Max_01/2;
RH_75per_01 = (RH_Max_01 + RH_50per_01)/2;
RH_25per_01 = RH_50per_01/2;

```

```

%%%%%%%% Non-Real-World Estimated RH values:

```

```

RH_01 = 0.3;
RH_02 = 0.4;
RH_03 = 0.5;
RH_04 = 0.6;
RH_05 = 0.7;
RH_06 = 0.8;
RH_07 = 0.9;
RH_08 = 1;

```

```

%%%%%%%%

```

```

RH00 = RH_Max_01;

```

```

%%% RH Affecting Panel Efficiency

```

```

%%% 30% RH (0.3) starts affecting Panel Efficiency;
%%% 0.06% decrease in panel efficiency for every % change in RH

```

```

%%% Ambient Temp Inc. over 30 years due to Climate Temp Inc

```

```

TaRamp_01 = 30*0.016; %%%% 0.016 C/yr times 30 years + 273.15K/C = total K Tamb inc

```

TaRamp_02 = 30*0.0193; %%% 0.0193 C/yr times 30 years + 273.15K/C = total K Tamb inc
 TaRamp_03 = 30*0.0327; %%% 0.0327 C/yr times 30 years + 273.15K/C = total K Tamb inc
 TaRamp_04 = 30*0.036; %%% 0.036 C/yr times 30 years + 273.15K/C = total K Tamb inc
 %%%

TaRamp00 = TaRamp_03;

%%% Real-World Ambient Temperatures - NO CLIMATE CHG INCREASE

Ta_Max_01 = 273.15 + max(T_Amb01);
 Ta_Min_01 = 273.15 + min(T_Amb01);
 Ta_50per_01 = (Ta_Max_01+Ta_Min_01)/2;
 Ta_75per_01 = (Ta_Max_01 + Ta_50per_01)/2;
 Ta_25per_01 = (Ta_Min_01 + Ta_50per_01)/2;

%%%%%%%%%

%%% Real-World Ambient Temperatures - WITH Climate increase

Ta_Max_01_wCC = Ta_Max_01 + TaRamp00;
 Ta_Min_01_wCC = Ta_Min_01 + TaRamp00;
 Ta_50per_01_wCC = (Ta_Max_01+Ta_Min_01)/2 + TaRamp00;
 Ta_75per_01_wCC = (Ta_Max_01 + Ta_50per_01)/2 + TaRamp00;
 Ta_25per_01_wCC = (Ta_Min_01 + Ta_50per_01)/2 + TaRamp00;

%%% Simulated Ambient Temperatures

%%%%%%%%%

ta1 = 273.15; % 0C
 ta2 = 293.15; % 20C
 ta3 = 303.15; % 30C
 ta4 = 313.15; % 40 C
 ta5 = 323.15; % 50 C
 ta6 = 333.15; % 60 C

%%%%%%%%%

ta0 = ta5; % The ambient temperature in Kelvin - 0C

%%%%%%%%%

%%% PV Efficiency

%%%%%%%%%

BaseEff_Lumos = 0.1762;
 BaseEff_MS425 = 0.1930;
 BaseEff_MS330 = 0.1953;
 BaseEff_MS390 = 0.1935;
 BaseEff_SolTech = 0.1930;

%%%%%%%%%

%%% After 30 years of operation:

Eff_Lumos_30yr = 0.1762 - 0.0095*30;
 Eff_MS425_30yr = 0.1930 - 0.0095*30;
 Eff_MS330_30yr = 0.1953 - 0.0095*30;
 Eff_MS390_30yr = 0.1935 - 0.0095*30;
 Eff_SolTech_30yr = 0.1930 - 0.0095*30;

%%%%%%%%%

```

%%% Efficiency Decrease due to ambient temps:
%%%%%%%%
if ta0 > (25+273.15)
    EffLumosTemp = BaseEff_Lumos+((ta0-273.15)-25)*EffDecTemp;
    EffMS425Temp = BaseEff_MS425 +((ta0-273.15)-25)*EffDecTemp;
    EffMS330Temp = BaseEff_MS330 +((ta0-273.15)-25)*EffDecTemp;
    EffMS390Temp = BaseEff_MS390 +((ta0-273.15)-25)*EffDecTemp;
    EffSolTechTemp = BaseEff_SolTech +((ta0-273.15)-25)*EffDecTemp;
    EffLumosTemp30yr = Eff_Lumos_30yr+((ta0-273.15)-25)*EffDecTemp;
    EffMS425Temp30yr = Eff_MS425_30yr +((ta0-273.15)-25)*EffDecTemp;
    EffMS330Temp30yr = Eff_MS330_30yr +((ta0-273.15)-25)*EffDecTemp;
    EffMS390Temp30yr = Eff_MS390_30yr +((ta0-273.15)-25)*EffDecTemp;
    EffSolTechTemp30yr = Eff_SolTech_30yr +((ta0-273.15)-25)*EffDecTemp;
else
    EffLumosTemp = BaseEff_Lumos;
    EffMS425Temp = BaseEff_MS425;
    EffMS330Temp = BaseEff_MS330;
    EffMS390Temp = BaseEff_MS390;
    EffSolTechTemp = BaseEff_SolTech;
    EffLumosTemp30yr = Eff_Lumos_30yr;
    EffMS425Temp30yr = Eff_MS425_30yr;
    EffMS330Temp30yr = Eff_MS330_30yr;
    EffMS390Temp30yr = Eff_MS390_30yr;
    EffSolTechTemp30yr = Eff_SolTech_30yr;
end

%%% Less Relative Humid Efficiency Decrease:
%%%%%%%%
if RH00 > 0.3
    d_RH = RH00 - 0.3;
    EffDec_RH = EffDecRH*d_RH;
else
    EffDec_RH = 0;
end

EffLumos = EffLumosTemp + EffDec_RH;
EffMS425 = EffMS425Temp + EffDec_RH;
EffMS330 = EffMS330Temp + EffDec_RH;
EffMS390 = EffMS390Temp + EffDec_RH;
EffSolTech = EffSolTechTemp + EffDec_RH;
EffLumos_30 = EffLumosTemp30yr + EffDec_RH;
EffMS425_30 = EffMS425Temp30yr + EffDec_RH;
EffMS330_30 = EffMS330Temp30yr + EffDec_RH;
EffMS390_30 = EffMS390Temp30yr + EffDec_RH;
EffSolTech_30 = EffSolTechTemp30yr + EffDec_RH;
%%%%%%%%

```


Effic00 = EffLumos_30;

The Three-Box Model:

%%
%%
%%% Constants
%%
%%

stefanBoltz = 5.670373e-8; % Stefan-Boltzmann constant, W/(m^2-K^4)
H3 = Bldg_Z; % Height of shipping container in meters
thick1 = Bldg_Y_20; % Length of container in meters - 20' Container
thick2 = Bldg_Y_40; % Length of container in meters - 40' Container
width = Bldg_X;
A_Wall_Bldg1 = H3*thick1;
A_Wall_Bldg2 = H3*thick2;
V_Air_Bldg1 = H3*width*thick1;
V_Air_Bldg2 = H3*width*thick2;

%%
%%
%%% Features to Vary: Tamb, hCoeff, ...?
%%
%%

%%% PCM Layer Thickness

HPCM_01 = 0.05;
HPCM_02 = 0.1;
HPCM_03 = 0.2;
HPCM_04 = 0.3;
HPCM_05 = 0.4;
HPCM_06 = 0.5;
%%%%%%%%
H1a = HPCM_06;

%%% Channel Layer Thickness

HCh_01 = 0.05;
HCh_02 = 0.1;
HCh_03 = 0.2;
HCh_04 = 0.3;
HCh_05 = 0.4;
HCh_06 = 0.5;
%%%%%%%%
H2a = HCh_06;

%%% Roof and Wall Areas:

A_Roof1 = width*thick1;

A_Roof2 = width*thick2;

A_Wall_PCM1 = H1a*thick1;

A_Wall_PCM2 = H1a*thick2;

A_Wall_Chan1 = H2a*thick1;

A_Wall_Chan2 = H2a*thick2;

%%% PCM Volume

Vol_PCM1 = H1a*width*thick1;

Vol_PCM2 = H1a*width*thick2;

%%% Channel Volume

V_Air_Chan1 = A_Wall_Chan1*width;

V_Air_Chan2 = A_Wall_Chan2*width;

%%% Convection Coefficient

%%%%%%%%%

hCoeff1 = 5; % No wind

hCoeff2 = 10; % Light wind

hCoeff3 = 25;

hCoeff4 = 50;

hCoeff5 = 100;

hCoeff6 = 250; % Strong wind

%%%%%%%%%

hCoeff0 = hCoeff6; % Convection coefficient, $W/(m^2-K)$

%%%%%%%%%
%%%%%%%%%
%%

%%% Thermal Conductivity of Air as a function of Ambient Temperature

%%%%%%%%%
%%%%%%%%%
%%

k_Air = 0.0242; % k_air = ; from https://www.engineeringtoolbox.com/air-properties-viscosity-conductivity-heat-capacity-d_1509.html

rho_Air = 1.2; % Function of temperature, figured from

https://www.engineeringtoolbox.com/air-density-specific-weight-d_600.html?vA=40&units=C#

Cp_Air = 1;

%%%%%%%%%
%%%%%%%%%
%%

%%% PCM Choice

```

%%%%%%%%%%%%%%%%%%%%%%%%%%%%%%%%%%%%%%%%%%%%%%%%%%%%%%%%%%%%%%%%%%%%%%%%
%%%%%%%%%%%%%%%%%%%%%%%%%%%%%%%%%%%%%%%%%%%%%%%%%%%%%%%%%%%%%%%%%%%%%%%%
%
```

```

k_PCM_00 = k_Cand;
rho_PCM_00 = rho_Cand;
Cp_PCM_00 = Cp_Cand;
Lf00 = 0;
```

```

%%%%%%%%%%%%%%%%%%%%%%%%%%%%%%%%%%%%%%%%%%%%%%%%%%%%%%%%%%%%%%%%%%%%%%%%
%%%%%%%%%%%%%%%%%%%%%%%%%%%%%%%%%%%%%%%%%%%%%%%%%%%%%%%%%%%%%%%%%%%%%%%%
```

```

%%% PDE & Model
```

```

%%%%%%%%%%%%%%%%%%%%%%%%%%%%%%%%%%%%%%%%%%%%%%%%%%%%%%%%%%%%%%%%%%%%%%%%
%%%%%%%%%%%%%%%%%%%%%%%%%%%%%%%%%%%%%%%%%%%%%%%%%%%%%%%%%%%%%%%%%%%%%%%%
```

```

numberOfPDE = 1;
model = createpde(numberOfPDE);
```

```

g = decsg(gd, sf, ns);
geometryFromEdges(model,g);
```

```

%figure;
%pdegplot(model,"EdgeLabels","on");
%axis([-1 3 -1 3]);
%title("Geometry With Edge Labels Displayed")
```

```

%figure;
%pdegplot(model,"FaceLabels","on");
%axis([-1 3 -1 3]);
%title("Geometry With Face Labels Displayed")
```

```

%%%%%%%%%%%%%%%%%%%%%%%%%%%%%%%%%%%%%%%%%%%%%%%%%%%%%%%%%%%%%%%%%%%%%%%%
%%%%%%%%%%%%%%%%%%%%%%%%%%%%%%%%%%%%%%%%%%%%%%%%%%%%%%%%%%%%%%%%%%%%%%%%
```

```

%%% PDE Coefficients
```

```

%%%%%%%%%%%%%%%%%%%%%%%%%%%%%%%%%%%%%%%%%%%%%%%%%%%%%%%%%%%%%%%%%%%%%%%%
%%%%%%%%%%%%%%%%%%%%%%%%%%%%%%%%%%%%%%%%%%%%%%%%%%%%%%%%%%%%%%%%%%%%%%%%
```

```

% Face 1: PCM Layer
```

```

c1 = k_PCM_00*(A_Wall_PCM1+A_Roof1);
a1 = hCoeff0*(A_Roof1+2*A_Wall_PCM1); % + (stefanBoltz*Emis_Glass*A_Roof1 +
2*stefanBoltz*Emis_Al*A_Wall_PCM1).*state.u.^3;
f1 = -(1-Effic00)*Ginc_ROOF*A_Roof1 - Ginc_WALL + A_Roof1*hCoeff0*ta0 +
2*A_Wall_PCM1*hCoeff0*ta0 - rho_PCM_00*Vol_PCM1*Lf00; % -
stefanBoltz*Emis_Glass*A_Roof1*ta0^4 - 2*stefanBoltz*Emis_Al*A_Wall_PCM1*ta0^4;
d1 = rho_PCM_00*Cp_PCM_00*Vol_PCM1;
specifyCoefficients(model,"m",0,"d",0,"c",c1,"a",a1,"f", f1, "Face", 1);
```

```

% Face 2: Building
c2 = k_Air*(A_Wall_Bldg1+A_Roof1);
a2 = 2*A_Wall_Bldg1*hCoeff0; % +2*stefanBoltz*Emis_Cort*A_Wall_Bldg1.*state.u.^3;
f2 = -Ginc_WALL*A_Wall_Bldg1+2*A_Wall_Bldg1*hCoeff0*ta0; %-
2*stefanBoltz*Emis_Cort*A_Wall_Bldg1*ta0^4;
d2 = rho_Air*Cp_Air*V_Air_Bldg1;
specifyCoefficients(model,"m",0,"d",0,"c",c2,"a",a2,"f", f2, "Face", 3);

% Face 3: Channel between PV and Bldg
c3 = k_Air*(A_Wall_Chan1+A_Roof1);
a3 = rho_Air*A_Wall_Chan1*Cp_Air*WS00;
f3 = rho_Air*A_Wall_Chan1*Cp_Air*WS00*ta0;
d3 = rho_Air*Cp_Air*V_Air_Chan1;
specifyCoefficients(model,"m",0,"d",0,"c",c3,"a",a3,"f", f3, "Face", 2);

%%%%%%%%%%%%%%%%%%%%%%%%%%%%%%%%%%%%%%%%%%%%%%%%%%%%%%%%%%%%%%%%%%%%%%%%%%%%%%
%%%%%%%%%%%%%%%%%%%%%%%%%%%%%%%%%%%%%%%%%%%%%%%%%%%%%%%%%%%%%%%%%%%%%%%%%%%%%%
%% Boundary and Initial Conditions
%%%%%%%%%%%%%%%%%%%%%%%%%%%%%%%%%%%%%%%%%%%%%%%%%%%%%%%%%%%%%%%%%%%%%%%%%%%%%%
%%%%%%%%%%%%%%%%%%%%%%%%%%%%%%%%%%%%%%%%%%%%%%%%%%%%%%%%%%%%%%%%%%%%%%%%%%%%%%

% Bottom Edge: Constant 20C temperature
applyBoundaryCondition(model,"dirichlet","Edge",1,"h",1,"r",293.15);

% Top Edge: Ginc_perpendicular(*1-PVeff) + Qconv_glass + Qrad_glass
q_top = A_Roof1*hCoeff0; % + stefanBoltz*Emis_Glass*A_Roof1.*state.u.^3;
g_top = -(1-Effic00)*Ginc_ROOF*A_Roof1 + A_Roof1*hCoeff0*ta0; %-
stefanBoltz*Emis_Glass*A_Roof1*ta0^4;
applyBoundaryCondition(model,"neumann","Edge",2,"g",g_top,"q",q_top);

% L/R (East/West) Edges PCM Layer:
q_topLR = A_Wall_PCM1*hCoeff0; % + stefanBoltz*Emis_Al*A_Wall_PCM1.*state.u.^3;
g_topLR = -0.5*Ginc_WALL*A_Wall_PCM1 + A_Wall_PCM1*hCoeff0*ta0; % -
stefanBoltz*Emis_Al*A_Wall_PCM1*ta0^4;
applyBoundaryCondition(model,"neumann","Edge",6,"g",g_topLR,"q",q_topLR);
applyBoundaryCondition(model,"neumann","Edge",10,"g",g_topLR,"q",q_topLR);

% L/R (East/West) Edges Bldg Layer:
q_botLR = A_Wall_Bldg1*hCoeff0; % + stefanBoltz*Emis_Cort*A_Wall_Bldg1.*state.u.^3;
g_botLR = -0.5*Ginc_WALL*A_Wall_Bldg1 + A_Wall_Bldg1*hCoeff0*ta0; % -
stefanBoltz*Emis_Cort*A_Wall_Bldg1*ta0^4;
applyBoundaryCondition(model,"neumann","Edge",8,"g",g_botLR,"q",q_botLR);
applyBoundaryCondition(model,"neumann","Edge",4,"g",g_botLR,"q",q_botLR);

% L/R (East/West) Air Channel Bldg Layer:

```

```

q_mid_R = rho_Air*A_Wall_Chan1*WS00*Cp_Air;
g_mid_R = rho_Air*A_Wall_Chan1*WS00*Cp_Air*ta0;
h_mid_L = 1;
r_mid_L = ta0;

applyBoundaryCondition(model,"mixed","Edge",9,"h",1,"r",ta0,"g",g_mid_R,"q",q_mid_R);
applyBoundaryCondition(model,"neumann","Edge",5,"g",g_mid_R,"q",q_mid_R);

setInitialConditions(model,ta1);

% Meshing
hmax = 0.1; % element size
msh = generateMesh(model,"Hmax",hmax);

%figure;
%pdeplot(model);
%axis([-1 3 -1 3]);
%title("Plate With Triangular Element Mesh")
%xlabel("X-coordinate, meters")
%ylabel("Y-coordinate, meters")

%%% Solution

%endTime = 50;
%StepSize = endTime/5000;
%tlist = 0:StepSize:endTime;
p = msh.Nodes;
numNodes = size(p,2);

u0(1:numNodes) = 293.15;
setInitialConditions(model,293.15);

model.SolverOptions.RelativeTolerance = 1.0e-3;
model.SolverOptions.AbsoluteTolerance = 1.0e-4;
model.SolverOptions.MaxIterations = 100;

R = solvepde(model,tlist);
u = R.NodalSolution;

%figure;
%plot(tlist,u(3, :));
%grid on
%title(["Temperature Along the Top Edge of " ...
    %"the Plate as a Function of Time"])
%xlabel("Time, seconds")
%ylabel("Temperature, degrees-Kelvin")

```

```

figure;
pdeplot(model,"XYData",u(:,end),"Contour","on","ColorMap","jet");
title('Temperature In The Plate, Steady State Solution');
xlabel('X-coordinate, meters');
ylabel('Y-coordinate, meters');
axis equal;

nodestop = findNodes(msh,"region","Edge",2);
nodesbldg = findNodes(msh,"nearest",[1.22;1.3]);

fprintf(['\nTemperature at the Center of the Building = ','%5.1f degrees-K\n'],u(155,end));
fprintf(['\nTemperature at the Roof = ','%5.1f degrees-K\n'],u(870,end));
fprintf(['\nTemperature at the Roof = ','%5.1f degrees-K\n'],u(827,end));
fprintf(['\nTemperature at the Roof = ','%5.1f degrees-K\n'],u(4,end));
fprintf(['\nTemperature at the Roof = ','%5.1f degrees-K\n'],u(3,end));

fprintf(['\nPCM: XXPCM TypeXX ; Wind Speed: XX m/s ; Tambient: XX K ; hCoeff: XX ;
PCM: XXm ; Channel: XXm']);

```

REFERENCES

- [1] NASA, “Scientific Consensus: Earth’s Climate Is Warming,” *Global Climate Change. Vital Signs of the Planet*, 2021. <https://climate.nasa.gov/scientific-consensus/> (accessed Mar. 19, 2021).
- [2] K. Meyer and P. Newman, “The Science of Anthropogenic Climate Change,” in *Planetary Accounting: Quantifying How to Live Within Planetary Limits at Different Scales of Human Activity*, K. Meyer and P. Newman, Eds., 1st ed. Singapore: Springer, Singapore, 2020, pp. 11–33. doi: 10.1007/978-981-15-1443-2.
- [3] IPCC, “Global Warming of 1.5°C. An IPCC Special Report on the impacts of global warming of 1.5°C above pre-industrial levels and related global greenhouse gas emission pathways, in the context of strengthening the global response to the threat of climate change,” 2018.
- [4] Met Office, “2016: one of the warmest two years on record.” 2017.
- [5] Copernicus Climate Change Service, “2020 warmest year on record for Europe; globally, 2020 ties with 2016 for warmest year recorded.” 2021.
- [6] U.S. Global Change Research Program, “Climate Science Special Report: Fourth National Climate Assessment, Volume I,” Washington, DC, USA, 2017.
- [7] A. Lake, *Thirsting for a Future Water and children in a changing climate*. 2017.
- [8] O. Milman, ““Heating Arctic may be to blame for snowstorms in Texas, scientists argue,”” *The Guardian*, p. 1, Feb. 17, 2021.

- [9] R. Lindsey, “Preliminary analysis concludes Pacific Northwest heat wave was a 1,000-year event...hopefully,” *ClimateWatch Magazine*, 2021. <https://www.climate.gov/news-features/event-tracker/preliminary-analysis-concludes-pacific-northwest-heat-wave-was-1000-year>
- [10] B. Berwyn, “A Week After the Pacific Northwest Heat Wave, Study Shows it Was ‘Almost Impossible’ Without Global Warming,” *Inside Climate News*, 2021. <https://insideclimatenews.org/news/07072021/pacific-northwest-heat-wave-attribution-study-climate-change/>
- [11] B. Henson and J. Masters, “Central Europe staggers toward recovery from catastrophic flooding: more than 200 killed,” *Yale Climate Connections*, 2021. <https://yaleclimateconnections.org/2021/07/central-europe-staggers-toward-recovery-from-catastrophic-flooding-more-than-200-killed/>
- [12] R. Gray, “What would happen in an apocalyptic blackout?,” *bbc.com*, p. 1, Oct. 24, 2019.
- [13] H. Kretchmer, “Global hunger fell for decades, but it’s rising again,” *World Economic Forum*, 2020. <https://www.weforum.org/agenda/2020/07/global-hunger-rising-food-agriculture-organization-report/> (accessed Apr. 09, 2021).
- [14] MarketLine, “Vertical Farming: The Future of Agriculture,” 2020.
- [15] M. A. Clark *et al.*, “Global food system emissions could preclude achieving the 1.5° and 2°C climate change targets,” *Science* (1979), vol. 370, no. 6517, pp. 705–708, 2020, doi: 10.1126/science.aba7357.
- [16] M. Rodell *et al.*, “Emerging Trends in Global Freshwater Availability,” *Nature*, vol. 557, no. 7707, pp. 651–659.

- [17] K. Chipman, “California Water Futures Begin Trading Amid Fear of Scarcity,” *bloomberg.com*, p. 1, Dec. 06, 2020.
- [18] The World Bank, “Water in Agriculture,” *worldbank.org*, 2020.
<https://www.worldbank.org/en/topic/water-in-agriculture> (accessed Dec. 04, 2021).
- [19] A. McCrone *et al.*, “Global Trends in Renewable Energy Investment 2019,” *Bloomberg New Energy Finance*, p. 76, 2019.
- [20] C. B. Honsberg and S. G. Bowden, “Photovoltaics Education Website,” 2019.
www.pveducation.org
- [21] M. Roser, “Why did renewables become so cheap so fast? And what can we do to use this global opportunity for green growth?,” *ourworldindata.org*, 2020.
<https://ourworldindata.org/cheap-renewables-growth> (accessed Dec. 04, 2021).
- [22] R. Wang *et al.*, “Caffeine Improves the Performance and Thermal Stability of Perovskite Solar Cells,” *Joule*, vol. 3, no. 6, pp. 1464–1477, 2019, doi: 10.1016/j.joule.2019.04.005.
- [23] M. Hutchins, “A pinch of chili gives perovskites a kick,” *pv-magazine.com*, p. 1, Jan. 2021.
- [24] C. Lane, “Solar panel efficiency: The gap between the most efficient solar panels narrows in 2021,” *SolarReviews Blog*, 2021. <https://www.solarreviews.com/blog/what-are-the-most-efficient-solar-panels>
- [25] NREL, “Life Cycle Greenhouse Gas Emissions from Solar Photovoltaics,” *Renewable and Sustainable Energy Reviews*, vol. 50, no. 190, p. 80, 2012.

- [26] M. Tawalbeh, A. Al-Othman, F. Kafiah, E. Abdelsalam, F. Almomani, and M. Alkasrawi, “Environmental impacts of solar photovoltaic systems: A critical review of recent progress and future outlook,” *Science of the Total Environment*, vol. 759, 2021, doi: 10.1016/j.scitotenv.2020.143528.
- [27] A. R. Amelia, Y. M. Irwan, W. Z. Leow, M. Irwanto, I. Safwati, and M. Zhafarina, “Investigation of the effect temperature on photovoltaic (PV) panel output performance,” *Int J Adv Sci Eng Inf Technol*, vol. 6, no. 5, pp. 682–688, 2016, doi: 10.18517/ijaseit.6.5.938.
- [28] H. Yousuf *et al.*, “A Review on Degradation of Silicon Photovoltaic Modules,” *New & Renewable Energy*, vol. 17, no. 1, pp. 19–32, 2021, doi: 10.7849/ksnre.2021.2034.
- [29] D. C. Jordan, S. R. Kurtz, K. VanSant, and J. Newmiller, “Compendium of photovoltaic degradation rates,” *Progress in Photovoltaics: Research and Applications*, vol. 24, pp. 978–989, 2016, doi: 10.1002/pip.2744.
- [30] M. Theristis, A. Livera, C. B. Jones, G. Makrides, G. E. Georghiou, and J. S. Stein, “Nonlinear Photovoltaic Degradation Rates: Modeling and Comparison against Conventional Methods,” *IEEE J Photovolt*, vol. 10, no. 4, pp. 1112–1118, 2020, doi: 10.1109/JPHOTOV.2020.2992432.
- [31] FinancialNewsMedia, “Global Solar Power Market Size Expected to Exceed \$194 Billion By 2027,” *financialnewsmedia.com*, Feb. 23, 2021. <https://www.prnewswire.com/news-releases/global-solar-power-market-size-expected-to-exceed-194-billion-by-2027-301233068.html>
- [32] Association Solar Energy Industries, “U.S. Solar Market Insight,” *seia.org*, 2021. <https://www.seia.org/us-solar-market-insight>

- [33] Business & Human Rights Resource Centre, “Human Rights in the Mineral Supply Chains of Solar Panels,” <https://www.business-humanrights.org/en/>, 2021.
<https://dispatches.business-humanrights.org/human-rights-in-the-mineral-supply-chains-of-solar-panels/index.html>
- [34] The World Bank, “Climate-Smart Mining: Minerals for Climate Action,” *worldbank.org*, 2021. <https://www.worldbank.org/en/topic/extractiveindustries/brief/climate-smart-mining-minerals-for-climate-action>
- [35] E. Biyik *et al.*, “A key review of building integrated photovoltaic (BIPV) systems,” *Engineering Science and Technology, an International Journal*, vol. 20, no. 3, pp. 833–858, 2017, doi: 10.1016/j.jestch.2017.01.009.
- [36] M. Debbarma, K. Sudhakar, and P. Baredar, “Thermal modeling, exergy analysis, performance of BIPV and BIPVT: A review,” *Renewable and Sustainable Energy Reviews*, vol. 73, no. January, pp. 1276–1288, 2017, doi: 10.1016/j.rser.2017.02.035.
- [37] D. E. Attoye, K. A. T. Aoul, and A. Hassan, “A review on building integrated photovoltaic façade customization potentials,” *Sustainability (Switzerland)*, vol. 9, no. 12, 2017, doi: 10.3390/su9122287.
- [38] M. C. Browne, B. Norton, and S. J. McCormack, “Phase change materials for photovoltaic thermal management,” *Renewable and Sustainable Energy Reviews*, vol. 47, no. 244, pp. 762–782, 2015, doi: 10.1016/j.rser.2015.03.050.
- [39] Z. A. Qureshi, H. M. Ali, and S. Khushnood, “Recent advances on thermal conductivity enhancement of phase change materials for energy storage system: A review,” *Int J Heat Mass Transf*, vol. 127, no. December, pp. 838–856, 2018, doi: 10.1016/j.ijheatmasstransfer.2018.08.049.

- [40] K. Kant, A. Shukla, A. Sharma, and P. H. Biwole, “Heat transfer studies of photovoltaic panel coupled with phase change material,” *Solar Energy*, vol. 140, pp. 151–161, 2016, doi: 10.1016/j.solener.2016.11.006.
- [41] H. Li, H. Chen, X. Li, and J. G. Sanjayan, “Development of thermal energy storage composites and prevention of PCM leakage,” *Appl Energy*, vol. 135, pp. 225–233, 2014, doi: 10.1016/j.apenergy.2014.08.091.
- [42] R. Buchwald, M. D. Breed, and A. R. Greenberg, “The thermal properties of beeswaxes: Unexpected findings,” *Journal of Experimental Biology*, vol. 211, no. 1, pp. 121–127, 2008, doi: 10.1242/jeb.007583.
- [43] W. F. Tinto, T. O. Elufioye, and J. Roach, *Waxes*. Elsevier Inc., 2017. doi: 10.1016/B978-0-12-802104-0.00022-6.
- [44] V. Dossetti-Romero, J. A. Méndez-Bermúdez, and E. López-Cruz, “Thermal diffusivity, thermal conductivity and resistivity of candelilla wax,” *Journal of Physics Condensed Matter*, vol. 14, no. 41, pp. 9725–9732, 2002, doi: 10.1088/0953-8984/14/41/327.
- [45] IPCC, “Climate Change and Land,” 2019. doi: 10.4337/9781784710644.
- [46] IPCC, “Global Warming of 1.5°C. An IPCC Special Report on the impacts of global warming of 1.5°C above pre-industrial levels and related global greenhouse gas emission pathways, in the context of strengthening the global response to the threat of climate change,” 2018. [Online]. Available: <https://www.ipcc.ch/sr15/>
- [47] P. Zhao, R. Dai, W. Li, Q. Wang, and M. Zeng, “Modeling the mushy zone during the melting process under Neumann boundary condition using the improved enthalpy-porosity method,” *Numeri Heat Transf A Appl*, vol. 78, no. 8, pp. 1–20, 2020, doi: 10.1080/10407782.2020.1793540.

- [48] H. Asgharian and E. Baniasadi, “A review on modeling and simulation of solar energy storage systems based on phase change materials,” *J Energy Storage*, vol. 21, no. November 2018, pp. 186–201, 2019, doi: 10.1016/j.est.2018.11.025.
- [49] F. P. Incropera, D. P. Dewitt, T. L. Bergman, and A. S. Lavine, *Fundamentals of Heat and Mass Transfer*, 6th ed. John Wiley & Sons, Inc., 2007. doi: 10.1007/978-3-319-15793-1_19.
- [50] C. Kittel, *Introduction to Solid State Physics*, 7th ed. John Wiley & Sons.
- [51] P. Shewmon, *Diffusion in Solids*, Second. Warrendale: The Minerals, Metals & Materials Society, 1989.
- [52] J. Zhao, T. Ma, Z. Li, and A. Song, “Year-round performance analysis of a photovoltaic panel coupled with phase change material,” *Appl Energy*, vol. 245, no. January, pp. 51–64, 2019, doi: 10.1016/j.apenergy.2019.04.004.
- [53] K. Kant, A. Shukla, A. Sharma, and P. H. Biwale, “Heat transfer studies of photovoltaic panel coupled with phase change material,” *Solar Energy*, vol. 140, pp. 151–161, 2016, doi: 10.1016/j.solener.2016.11.006.
- [54] J. H. I. Lienhard and J. H. V Lienhard, *A Heat Transfer Textbook*, Fifth. Cambridge: Phlogiston Press, 2019.
- [55] W. M. Rohsenow, J. R. Hartnett, and Y. I. Cho, *Handbook of heat transfer*, Third. New York: McGraw-Hill, 1998. doi: 10.5860/choice.36-3347.
- [56] T. Stuetzle, N. Blair, J. W. Mitchell, and W. A. Beckman, “Automatic control of a 30 MWe SEGS VI parabolic trough plant,” *Solar Energy*, vol. 76, no. 1–3, pp. 187–193, 2004, doi: 10.1016/j.solener.2003.01.002.

- [57] A. Mohammed, A. Hanieh, and A. M. A. Hanieh, "Automatic Orientation of Solar Photovoltaic Panels AUTOMATIC ORIENTATION OF SOLAR PHOTOVOLTAIC PANELS TO INCREASE EFFICIENCY." [Online]. Available: <https://www.researchgate.net/publication/239840189>
- [58] NOAA - National Centers for Environmental Information and US Air Force - 14th Weather Squadron, "Federal Climate Complex Data Documentation for Integrated Surface Data." NOAA, Asheville, NC, p. 133, 2018. [Online]. Available: <http://www1.ncdc.noaa.gov/pub/data/ish/ish-format-document.pdf>
- [59] H. A. Kazem and M. T. Chaichan, "Effect of humidity on photovoltaic performance based on experimental study," *International Journal of Applied Engineering Research*, vol. 10, no. 23, pp. 43572–43577, 2015.
- [60] F. A. Touati, M. A. Al-Hitmi, and H. J. Bouchech, "Study of the effects of dust, relative humidity, and temperature on solar PV performance in Doha: Comparison between monocrystalline and amorphous PVS," *Int J Green Energy*, vol. 10, no. 7, pp. 680–689, Jan. 2013, doi: 10.1080/15435075.2012.692134.
- [61] National Oceanic and Atmospheric Administration, "Meteorological Conversions and Calculations," *National Weather Service: Weather Prediction Center*, Mar. 01, 2007. <https://www.wpc.ncep.noaa.gov/html/dewrh.shtml> (accessed Feb. 05, 2022).
- [62] B. McNoldy, "Calculate Temperature, Dewpoint, or Relative Humidity," *University of Miami*. <https://bmcnoldy.rsmas.miami.edu/Humidity.html> (accessed Feb. 05, 2022).
- [63] A. Phinikarides, N. Kindyni, G. Makrides, and G. E. Georghiou, "Review of photovoltaic degradation rate methodologies," *Renewable and Sustainable Energy Reviews*, vol. 40. Elsevier Ltd, pp. 143–152, 2014. doi: 10.1016/j.rser.2014.07.155.

- [64] United States Environmental Protection Agency, “Climate Change Indicators: Heat Waves,” Apr. 2021.
- [65] Washington State Department of Health, “Heat Wave 2021,” *Washington State Department of Health: Public Health Message*.
<https://www.doh.wa.gov/Emergencies/BePreparedBeSafe/SevereWeatherandNaturalDisasters/HotWeatherSafety/HeatWave2021> (accessed Feb. 05, 2022).
- [66] United States Environmental Protection Agency, “Climate Change Indicators: Heat Waves,” *United States Environmental Protection Agency: Climate Change Indicators*.
<https://www.epa.gov/climate-indicators/climate-change-indicators-heat-waves> (accessed Feb. 05, 2022).
- [67] World Weather Attribution, “Western North American extreme heat virtually impossible without human-caused climate change,” *World Weather Attribution*, Jul. 07, 2021.
<https://www.worldweatherattribution.org/western-north-american-extreme-heat-virtually-impossible-without-human-caused-climate-change/> (accessed Feb. 05, 2022).
- [68] C. Y. Sjoukje Philip *et al.*, “Rapid attribution analysis of the extraordinary heatwave on the Pacific Coast of the US and Canada June 2021.” [Online]. Available:
<https://public.wmo.int/en/media/news/june-ends-exceptional-heat>
- [69] D. Arndt, “It’s not the heat; it’s the humidity,” *Beyond the Data*, Sep. 20, 2018.
<https://www.climate.gov/news-features/blogs/beyond-data/its-not-heat-its-humidity> (accessed Feb. 05, 2022).
- [70] K. Willett, “Guest post: Investigating climate change’s ‘humidity paradox,’” *Carbon Brief: Clear on Climate*, Dec. 01, 2020. <https://www.carbonbrief.org/guest-post-investigating-climate-changes-humidity-paradox> (accessed Feb. 05, 2022).

- [71] Tuff Shipping Containers, “What Steel is Used to Make Shipping Containers,” *Tuff Shipping Containers: Steel Shipping Containers*. <https://tuffshippingcontainers.com/what-steel-is-used-to-make-shipping-containers/#:~:text=How%20Thick%20Is%20the%20Metal,the%20rest%20of%20the%20structure> (accessed Feb. 05, 2022).
- [72] Container Container, “Shipping Container Dimensions,” *Container Container: Container Info*. <https://www.containercontainer.com/shipping-container-dimensions/> (accessed Feb. 05, 2022).
- [73] backyardgardenlover.com, “Best Grow Room Temperature And Humidity,” *Backyard Garden Lover*, Oct. 14, 2021. <https://www.backyardgardenlover.com/grow-room-temperature-and-humidity/> (accessed Feb. 05, 2022).
- [74] A. Miller and K. Nemali, “Heating Requirements for Winter Hydroponic Lettuce Production.” [Online]. Available: https://iclimat.org/climate_fact_sheet/
- [75] aqua-calc.com, “Density of Soy wax (material).” <https://www.aqua-calc.com/page/density-table> (accessed Feb. 15, 2022).
- [76] S. Sinaringati, N. Putra, M. Amin, and F. Afriyanti, “THE UTILIZATION OF PARAFFIN AND BEESWAX AS HEAT ENERGY STORAGE IN INFANT INCUBATOR,” vol. 11, no. 2, 2016, [Online]. Available: www.arpnjournals.com
- [77] Z. Arifin *et al.*, “The Effect of Soybean Wax as a Phase Change Material on the Cooling Performance of Photovoltaic Solar Panel,” *International Journal of Heat and Technology*, vol. 40, pp. 326–332, Feb. 2022, doi: 10.18280/ijht.400139.
- [78] L. Cowan, “Eight Common Reasons Small Businesses Fail,” *Ellevest*, Oct. 24, 2019.

- [79] Strategyzer, “Business Model Canvas Explained,”
https://www.youtube.com/watch?v=QoAOzMTLP5s&ab_channel=Strategyzer, Sep. 01, 2011.
- [80] Minute Tools Content Team, “Business Model Canvas Explained with Examples,”
<https://expertprogrammanagement.com/2018/10/business-model-canvas-explained/>, Oct. 2018.
- [81] GaryFox.co, “The Business Model for Beginners: The Essential Step By Step Guide,”
<https://www.garyfox.co/business-model/>.
- [82] R. Alberdi, “The 9-Step Business Model Canvas Explained (2023 Update),”
<https://www.thepowermba.com/en/blog/business-model-canvas>.
- [83] Strategyzer, “The Business Model Canvas,”
<https://www.strategyzer.com/canvas/business-model-canvas>, 2020.
- [84] CFI Team, “Business Model Canvas Template: The executive summary of a business,”
<https://corporatefinanceinstitute.com/resources/management/business-model-canvas-template/>, Mar. 23, 2023.
- [85] Alanis Business Academy, “How to use the Business Model Canvas,”
https://www.youtube.com/watch?v=CV5AQ-aZRBw&ab_channel=AlanisBusinessAcademy, Oct. 05, 2020.
- [86] S. F. Dieffenbacher, “Customer Segments in Business Model Canvas,”
<https://digitalleadership.com/blog/customer-segments/>, Jun. 25, 2022.
- [87] T. J. Mierzwa, “Innovation for Entrepreneurs: From Idea to Marketplace - Customer Types,” *<https://www.coursera.org/lecture/innovative-entrepreneur/customer-types-Bf5fo>*, 2023.

- [88] R. Stetson, “Best Shipping Container Homes for Sale in Texas 2023,” https://www.containeraddict.com/shipping-container-homes-for-sale-in-texas/#Cost_of_Building_a_Container_Home_in_Texas, 2023.
- [89] D. Ozdemir, “Off-Grid Container House Has Its Own Wind Turbine and Solar Panels,” <https://interestingengineering.com/innovation/off-grid-container-house-has-its-own-wind-turbine-and-solar-panels>, Mar. 12, 2021.
- [90] Boxx Modular, “Boxx Modular,” <https://www.boxxmodular.com/>, 2023.
- [91] Container Xchange, “Container-XChange,” <https://www.container-xchange.com/blog/container-manufacturers-new-built-and-used-containers/>, Nov. 04, 2022.
- [92] Shipping Container Depot, “Top 10 Shipping Container Manufacturers in USA,” <https://www.shippingcontainerdepot.com/shipping-container-manufacturers-in-usa/>, 2023.
- [93] USA Containers Co., “USA Containers Co.,” <https://usacontainers.co>.
- [94] Lumos Solar, “Lumos,” <https://lumossolar.com/>, 2023.
- [95] Mission Solar, “Mission Solar Energy,” <https://www.missionsolar.com/>, 2021.
- [96] SolarTech Universal, “SolarTech Universal,” <https://www.solartechuniversal.com/>.
- [97] Thomas Publishing Company, “Thomas For Industry,” thomasnet.com, 2023.
- [98] Advanced Cooling Technologies, “Advanced Cooling Technologies The Thermal Management Experts,” <https://www.1-act.com/>, 2023.
- [99] Phase Change Solutions, “Phase Change Solutions,” <https://phasechange.com/>, 2022.
- [100] Micro Lab Farms, “Micro Lab Farms,” <https://www.micro-farms.co/>, 2022.
- [101] Freight Farms Inc., “Freight Farms,” <https://www.freightfarms.com>, 2023.

- [102] Farmbox Foods, “FarmBox Foods,” <https://farmboxfoods.com/>, 2023.
- [103] P. M. Voss, “Vertical Farming: An agricultural revolution on the rise,” *Environ Sci Technol*, pp. 1–21, 2012.
- [104] peter platt, “Vertical Farming: An Interview with Dickson Despommier,” *Gastronomica*, vol. 7, no. 3, pp. 80–87, 2007, doi: 10.1525/gfc.2007.7.3.80.
- [105] J. Bailey-Serres, J. E. Parker, E. A. Ainsworth, G. E. D. Oldroyd, and J. I. Schroeder, “Genetic strategies for improving crop yields,” *Nature*, vol. 575, no. 7781, pp. 109–118, 2019, doi: 10.1038/s41586-019-1679-0.
- [106] A. Raklami, N. Bechtaoui, A. I. Tahiri, M. Anli, A. Meddich, and K. Oufdou, “Use of rhizobacteria and mycorrhizae consortium in the open field as a strategy for improving crop nutrition, productivity and soil fertility,” *Front Microbiol*, vol. 10, no. MAY, pp. 1–11, 2019, doi: 10.3389/fmicb.2019.01106.
- [107] N. K. Fageria, V. C. Baligar, and Y. C. Li, “The role of nutrient efficient plants in improving crop yields in the twenty first century,” *J Plant Nutr*, vol. 31, no. 6, pp. 1121–1157, 2008, doi: 10.1080/01904160802116068.
- [108] N. Yeh and J. P. Chung, “High-brightness LEDs-Energy efficient lighting sources and their potential in indoor plant cultivation,” *Renewable and Sustainable Energy Reviews*, vol. 13, no. 8, pp. 2175–2180, 2009, doi: 10.1016/j.rser.2009.01.027.
- [109] D. A. Kopsell, C. E. Sams, and R. C. Morrow, “Blue wavelengths from led lighting increase nutritionally important metabolites in specialty crops,” *HortScience*, vol. 50, no. 9, pp. 1285–1288, 2015, doi: 10.21273/hortsci.50.9.1285.

- [110] S. Gao, X. Liu, Y. Liu, B. Cao, Z. Chen, and K. Xu, “Photosynthetic characteristics and chloroplast ultrastructure of welsh onion (*Allium fistulosum* L.) grown under different LED wavelengths,” *BMC Plant Biol*, vol. 20, no. 1, pp. 1–12, 2020, doi: 10.1186/s12870-020-2282-0.
- [111] G. D. Massa, H. H. Kim, R. M. Wheeler, and C. A. Mitchell, “Plant productivity in response to LED lighting,” *HortScience*, vol. 43, no. 7, pp. 1951–1956, 2008, doi: 10.21273/hortsci.43.7.1951.
- [112] H. M. Resh, *Hydroponic Food Production*, 7th ed. CRC Press, 2013.
- [113] J. Birkby, “Vertical Farming Issues,” *National Center for Appropriate Technology*, pp. 1–12, 2016.
- [114] C. Gerten, S. Fina, and K. Rusche, “The Sprawling Planet: Simplifying the Measurement of Global Urbanization Trends,” *Front Environ Sci*, vol. 7, no. September, pp. 1–20, 2019, doi: 10.3389/fenvs.2019.00140.
- [115] I. A. Lakhiar, J. Gao, T. N. Syed, F. A. Chandio, and N. A. Buttar, “Modern plant cultivation technologies in agriculture under controlled environment: A review on aeroponics,” *J Plant Interact*, vol. 13, no. 1, pp. 338–352, 2018, doi: 10.1080/17429145.2018.1472308.
- [116] S. Goddek, B. Delaide, U. Mankasingh, K. V. Ragnarsdottir, H. Jijakli, and R. Thorarinsdottir, “Challenges of sustainable and commercial aquaponics,” *Sustainability (Switzerland)*, vol. 7, no. 4, pp. 4199–4224, 2015, doi: 10.3390/su7044199.
- [117] L. Wood, “Insights on the Vertical Farming Global Market to 2027,” Dublin, 2020.
- [118] MarketLine, “Vertical-farm operator Infarm sees \$ 100m added to funding pot,” p. 1, Mar. 11, 2021.

- [119] L. Garfield, “Investors are sinking hundreds of millions into a technology that could revolutionize the way we eat,” *Businessinsider.com*, p. 1, Aug. 2017.
- [120] R. Nickel, “Investors seed indoor farms as pandemic disrupts food supplies,” *Reuters*, p. 1, Feb. 2021.
- [121] S. Villarreal, J. A. Jimenez, T. Jin, and M. Cabrera-Rios, “Designing a sustainable and distributed generation system for semiconductor wafer fabs,” *IEEE Transactions on Automation Science and Engineering*, vol. 10, no. 1, pp. 16–26, 2013, doi: 10.1109/TASE.2012.2214438.
- [122] T. Jin, J. Jimenez, and Z. Tian, “Managing demand response for manufacturing enterprises via renewable energy integration,” *IEEE International Conference on Automation Science and Engineering*, pp. 645–650, 2013, doi: 10.1109/CoASE.2013.6653961.
- [123] S. M. Bhagavathy and G. Pillai, “PV microgrid design for rural electrification,” *Designs (Basel)*, vol. 2, no. 3, pp. 1–22, 2018, doi: 10.3390/designs2030033.
- [124] O. M. Longe, K. Ouahada, H. C. Ferreira, and S. Chinnappen, “Renewable Energy Sources microgrid design for rural area in South Africa,” *2014 IEEE PES Innovative Smart Grid Technologies Conference, ISGT 2014*, pp. 3–7, 2014, doi: 10.1109/ISGT.2014.6816378.
- [125] Y. B. Aemro, P. Moura, and A. T. de Almeida, “Design and Modeling of a Standalone DC-Microgrid for Off-Grid Schools in Rural Areas of Developing Countries,” *Energies (Basel)*, vol. 13, no. 23, p. 6379, 2020, doi: 10.3390/en13236379.
- [126] D. T. Ton and M. A. Smith, “The U.S. Department of Energy’s Microgrid Initiative,” *The Electricity Journal*, vol. 25, no. 8, pp. 84–94, 2012, doi: <https://doi.org/10.1016/j.tej.2012.09.013>.

- [127] L. Cohn, “History of Microgrids in the US: From Pearl Street to Plug-and-Play,” *microgridknowledge.com*, p. 1, Jul. 22, 2019.
- [128] W. Bower, I. Llc, J. Reilly, and R. Associates, “The Advanced Microgrid Integration and Interoperability,” *Sandia Report*, no. March, pp. 1–56, 2014.
- [129] S. M. Bhagavathy and G. Pillai, “PV microgrid design for rural electrification,” *Designs (Basel)*, vol. 2, no. 3, pp. 1–22, 2018, doi: 10.3390/designs2030033.
- [130] D. Xue, “Microgrids Have a Role in the Global Energy Transition, If They Can Lower Costs,” *Engineering for Change*, 2020.
<https://www.engineeringforchange.org/news/microgrids-role-global-energy-transition-can-lower-costs/>
- [131] National Aeronautics and Space Administration, “Drought Conditions Continue in Spring 2021,” *NASA: Earth Observatory Blog*, Mar. 23, 2021.
- [132] National Oceanic and Atmospheric Administration, “Discussion for the Seasonal Drought Outlook,” *National Weather Service: Climate Prediction Center*, 2021.
- [133] S. York, “Smoke from California wildfires decreases solar generation in CAISO,” *U.S. Energy Information Administration*, Sep. 30, 2020.
- [134] California Air Resources Board: Research Division, “Inhalable Particulate Matter and Health (PM2.5 and PM10).”
- [135] G. Flaccus and S. Cline, “Wildfire smoke clouds sky, hurts air quality on East Coast,” *AP News*, Jul. 21, 2021.
- [136] J. Marder and L. Dauphin, “Which Way Will the Smoke Go?,” *NASA: Earth Observatory*, Aug. 06, 2018. <https://earthobservatory.nasa.gov/images/144190/which-way-will-the-smoke-go> (accessed Feb. 11, 2022).

- [137] “A Model that Predicts the Spread of Wildfire Smoke Becomes Operational,” *National Environmental Satellite Data and Information Service*, Jan. 08, 2021.
<https://www.nesdis.noaa.gov/news/model-predicts-the-spread-of-wildfire-smoke-becomes-operational> (accessed Feb. 11, 2022).
- [138] National Oceanic and Atmospheric Administration, “Forecasters are giving feedback to improve GSD’s experimental High Resolution Rapid Refresh-Smoke (HRRR-Smoke),” *Earth System Research Laboratories: Global System Laboratory*, Aug. 02, 2016.
<https://www.esrl.noaa.gov/gsd/learn/hotitems/2016/hrrr-smoke.html> (accessed Feb. 11, 2022).